Title

3D Interface-Engineered Transition Metal Oxide/Carbon Hybrid Structures for Efficient Bifunctional Oxygen Electrocatalysis in Alkaline and Acidic Environments

Author

Grewal, Simranjit Kaur

Publication Date

2021

Peer reviewed|Thesis/dissertation

UNIVERSITY OF CALIFORNIA, MERCED

3D Interface-Engineered Transition Metal Oxide/Carbon Hybrid Structures for Efficient Bifunctional Oxygen Electrocatalysis in Alkaline and Acidic Environments

Submitted to the School of Engineering
In Partial Fulfillment of the Requirements for
the degree of Doctor of Philosophy
May 2021

in

Materials and Biomaterials Science and Engineering

by

Simranjit Kaur Grewal

Committee in charge
Professor Ashlie Martini
Professor Christopher Viney
Professor Jessica (Yue) Wang
Professor Min-Hwan Lee

SIGNATURE PAGE

The Dissertation of Simranjit Grewal is approved, and it is acceptable in quality and form for publication on microfilm and electronically:

_____

Professor Ashlie Martini, Chair and Committee Member

_____

Professor Christopher Viney, Committee Member

_____

Professor Jessica (Yue) Wang, Committee Member

_____

Professor Min-Hwan Lee, Supervisor and Committee Member

I dedicate this dissertation to

My brother Balraj Grewal, who always inspire me to live every day like a gift.
My parents Gurinderjit Sanghera & Karamjit Grewal, who have always been by my side.
My grandparents Bupinderjit & Harcharan Sanghera, who are a second set of parents.
My late grandparents Rajinder & Harwant Grewal, who I remember lovingly.
My uncles Gurdeep, Gurmeet, Paramjit, & Rajbir families, for loving and supporting us.
My Friends, for believing in me when I did not.

I am who I am today because of you.

Always your sister, daughter, granddaughter, niece/cousin, and friend

Your Simranjit

QUOTE

"Fortunately science, like that nature to which it belongs, is neither limited by time nor by space. It belongs to the world, and is of no country and no age. The more we know, the more we feel our ignorance; the more we feel how much remains unknown."

-Sir Humphry Davy

TABLE OF CONTENTS

LIST OF FIGURES

LIST OF TABLES

PREFACE

The basis for this research stems from my passion for developing efficient methods of energy conversion devices. As the world moves towards renewable technologies, greater strategies are needed than what is currently available now. Many scientists across the world will need to work together to solve current issues and for this reason, a dissertation has been to possibly provide some help in the fight against the greatest threat to our generation, climate change. The reader is asked to keep an open mind to our approach and, explore the ways how science can provide solutions to the world's current problems.

ACKNOWLEDGMENT

Simranjit Grewal (SG) acknowledge the following individuals, organizers, and grants to make the contents of this dissertation possible.

This work was supported by the NASA MIRO Program NNX15AQ01A. SG also acknowledges the NASA ASTAR Fellowship NNX15AW57H. The use of TEM at the Molecular Foundry and DFT calculations performed using resources from the National Energy Research Scientific Computing Center were supported by the U.S. Department of Energy Contract No. DE-AC02-05CH11231. Thank you Lawrence Berkeley National Laboratory (LBNL).

SG acknowledges Dr. Eunseok Lee for his contributions DFT optimized structures and calculation of the energy profiles in Chapter 4. ACS granted SG to use copyrighted material.

Secondary use of TEM at the Molecular Foundry was supported by the U.S. Department of Energy Contract No. DE-AC02-05CH11231 at LBNL. SG would like to acknowledge the support by the U.S. Department of Energy, Office of Science, Office of Basic Energy Science, via Grant DE-SC0008685 to the SUNCAT Center of Interface Science and Catalysis and the use of the computer time allocation for the "Transition metal-oxide and metal surfaces: applications and reactivity trends in catalysis" at the National Energy Research Scientific Computing Center, a DOE Office of Science User Facility supported by the Office of Science of the U.S. Department of Energy under Contract No. DE-AC02-05CH11231.

SG acknowledges the DFT optimized structures and calculation of the overpotentials was provided by SUNCAT Staff Scientist Michal Bajdich, SLAC NL, Stanford. Wiley granted SG to use copyrighted material.

The text of this thesis/dissertation is a reprint of the material as it appears in ACS Publication and John Wiley & Sons, Inc. The co-authors listed in this publication directed and supervised research which forms the basis for the thesis/dissertation. Co-authors listed are as follows:
Angela Macedo Andrade of the University of California, Merced
Ziqi Liu of the University of California, Merced
Dr. Alireza of the University of California, Merced
Dr. Art Nelson of the Lawrence Livermore National Laboratory
Dr. Eunseok Lee of the University of Alabama
Kevin Thai of the University of Alabama
Dr. Jose Antonio Garrido Torres
Dr. Ambarish Kulkarni
Dr. Michal Bajdich
Dr. Min-Hwan Lee

SG has been granted permission by co-authors to use copyrighted material for the sole purpose of this dissertation. Special permission has also been granted by ACS Publications and John Wiley & Sons, Inc.

SG thanks the faculty of UC Merced: Prof. Vincent Tung and Prof. Ryan Baxter for their valuable discussions, and Prof. Anne Kelley and Dr. David Rice for their help with FTIR. SG also thanks Prof. Viney, Prof. Wang, and Prof. Valerie Leppert for their materials expertise in regard to this dissertation, materials characterization techniques, and general materials science principles.

SG would like to thank NASA technical advisor Dr. Jin-woo Han for his contributions towards SGs efforts of research at NASA.

Finally, SG wants to thank Prof. Min-Hwan Lee (MHL) for being her supervisor. Gratitude would not be enough to express his support, patience, and encouragement shown throughout graduate school. Many advisors would not tolerate nor provide the support MHL has given to problems and roadblocks that unavoidably came during the course of performing research. His technical and editorial advice led to success and completion of many manuscripts. More importantly, he has shown what excellence is and what it means to the bear the title Doctor of Philosophy. Thank you!

VITA

EDUCATION

Doctoral Degree of Materials and Biomaterials Science and Engineering *2015 – 2021*
University of California, Merced, Merced, CA, USA

Master Degree of Materials and Biomaterials Science and Engineering *2015 – 2020*
University of California, Merced, Merced, CA, USA

Dual Major: Bachelor of Science in Physics and Biological Sciences *2010 - 2015*
Stanislaus State, Turlock, CA, USA

Bachelor of Arts in Economics, Focus on Energy & Renewable Technologies *2010 - 2015*
Stanislaus State, Turlock, CA, USA

RESEARCH EXPERIENCE

Graduate Student Researcher *2015 - 2021*
University of California, Merced, Merced, CA, USA under Faculty of Dr. Min-Hwan Lee

- Conducted mechanistic study of surface synergy for energy conversion devices with 92% correlation.
- Successfully fabricated inorganic materials (organometallic, metalorganic): Ti, Zr, and Cr oxides with functionalized 3D carbon structures using atomic layer deposition (ALD).
- Characterization of thin-films (metal oxides) using electrical and material techniques.
- Designed, tested and prototyped supercapacitors to improve their wettability.
- Led research and development of ALD based Li-ion Batteries

Undergraduate Student Researcher *2013 - 2014*
Stanislaus State, Turlock, CA, USA under Faculty of Dr. Rose Zhang

- Conducted research to create more cost-effective superconductors.
- Successfully modeled (98.2% correlation) and fabricated YBCO, LCO and TBCCO superconductors for magnetic time relaxation.

PROFESSIONAL EXPERIENCE

Materials Research Society Student Engagement Subcommittee *2018 - Present*
Pittsburgh, PA USA

- Organized events for meetings (three) with an average of 100 attendees.
- Wrote procedures and held meetings to better facilitate communications within teams.
- Tasked and funded to be present for the Fall 2019 event in Boston.
- Provided two written reports for the Spring and Fall 2019 events.

NASA Ames Facility *2015 – 2020*
Mountain View, CA, USA under Faculty of Dr. Jin-Woo Han

- Fabricated energy conversion devices to better reduce weight and utilized material surfaces.
- Participated in teams to create materials to withstand extreme conditions.
- Volunteered to provide material expertise to other NASA based centers.

Executive Scribe and Panelist for the 2020 NASA Graduate Fellowship *2020*
NASA Headquarters, Washington D.C., USA

- Served on panels by providing both minutes and drafting feedback to proposals.
- Provided expertise based upon both technical and fellow experience.

Teaching Assistant *2015 & 2020*
University of California, Merced, Merced, CA, USA

- Engineering Service Learning: Assisted students with community-based projects
- The Unmanned Aerial Systems with Kearney Agricultural Research and Extension Center.
- The Project Protect for the Healthy House of Merced.

College Reading and Learning Association (CRLA) Certified Tutor *2011-2015*
Stanislaus State Tutoring Center, Turlock, CA, USA

- Provided academic tutoring for English, Economics, Chemistry, and Physics.
- Provided assistance and tutoring for remedial and non-native English writers.

Student Leader for the International Space Education Board (ISEB) *2018 - 2019*
NASA Headquarters, Washington D.C., USA

- Organized space related events for both national and international space programs (e.g. NASA, ESA, CSA, JAXA, and UAESA).
- Helped organizers for NASA's effort to plan, coordinate, and execute the "Student Program and Educator Professional Development Workshop."
- Moderated an Astronaut Symposium for school aged students
- Moderated Heads of Space Agency (twice) for an interview with NASA's administrator Jim Bridenstine and ESA's Director Johann-Dietrich Wörner.

Space Generation Congress Rapporteur *2018 - 2019*
Space Generation Advisory Council, Vienna, Austria

- Participated in meetings and dialogues to solutions towards space related problems.
- Recorded minutes of meetings and provided feedback to both sponsors and moderators.
- Helped submit a report to the U.N containing the groups solutions towards Common Space Areas (2018) and Utilization of the Lunar Surface Mission Objectives as sponsored by Lockheed Martin (2019).

AWARDS

Graduate Dean's Dissertation Award Fellowship *Fall 2020*
2015 - 2021
Merced Nanomaterials Center for Energy and Sensing (MACES) of NASA sponsorship for materials specific (silicon, ceramic, and carbon-based catalysts) SEM training by Zeiss officials.
Molecular Foundry Grant from the U.S Department of Energy for materials *2017 - Present*
specific (silicon, MOFs, GO, and ceramics (YSZ, GDC, LNF, & metal oxides) using TEM, HRTEM, and EFTEM
NASA Harriet G. Jenkins Graduate Fellowship *2015 – 2020*
Materials and Biomaterials Science and Engineering) Travel Award *2016 -2019*
ISEB NASA Scholarship Award to attend the Space Generation Congress *2018 - 2019*

2017 - 2019

NASA sponsorship to attend three International Astronautical Congress Conferences

K.C. & Izzy Hoddle Scholarship for Excellence in Economics *2013 - 2015*

PUBLICATIONS and CONFERENCES

Peer-reviewed Journal

L. Haoyu, H.-S. Kang, S. Grewal, A. Nelson, S.A Song, M.H. Lee "Atomic-scale metal oxide overcoat on decorated ceria nanoclusters for enhanced performance and durability of solid oxide fuel cell cathodes", *Journal of Materials Chemistry A,* 8, 15927, 2020-*2020 Emerging Investigators Themed Issue.*

S. Grewal, A. Macedo Andrade, Z. Liu, J. Antonio Garrido Torres, A. Nelson, A. Kulkarni, M. Bajdich, M.H. Lee "Highly Active Bifunctional Oxygen Electrocatalytic Sites Realized in Ceria Functionalized Graphene", *Journal of Advanced Sustainable Systems,* 4, 2000048, 2020.

H.-S. Kang, S. Grewal, H. Li, M.H. Lee "Effect of surface-specific treatment by infiltration into $LaNi_6Fe_4O_{3-d}$ cathodic backbone for solid oxide fuel cells", *Journal of The Electrochemical Society 166, F255, 2019*.

S. Grewal, A. Macedo Andrade, A. Nelson, A. Karimaghaloo, E. Lee, and M. H. Lee, "Critical impact of graphene functionalization for transition metal oxide/graphene hybrids on oxygen reduction reaction", *The Journal of Physical Chemistry C*, 122, April 2018.

A. Karimaghaloo, A. Macedo Andrade, S. Grewal, J. H. Shim, M. H. Lee, "Mechanism of Cathodic Performance Enhancement by a Few-Nanometer-Thick Oxide Overcoat on Porous Pt Cathodes of Solid Oxide Fuel Cells", *ACS Omega*, 2, 806, March 2017.

Conference Presentations

S. Grewal, A. Macedo Andrade, Z. Liu, and M. H. Lee, "Use of Functionalization on Bimetallic MOFs for Enhanced ORR and OER Performance, Materials Research Society, December 1 –6, 2019, Boston, MA

S. Grewal, A. Macedo Andrade, Z. Liu, and M. H. Lee, "Surface Functionalization of Graphene Prior to Nanoparticles Tethering for Tri-Functionality in both Acidic and Alkaline Media", 70th International Astronautical Congress, September 2018, Washington D.C

S. Grewal, A. Macedo Andrade, A. Karimaghaloo, and M. H. Lee, "Surface Functionalization of Metal-Organic Framework Prior to TiO_2 Tethering for Oxygen Reduction Catalyst in Alkaline Media", Electrochemical Conference on Energy & the Environment, July 2019, Glasgow, Scotland

S. Grewal, A. Macedo Andrade, Z. Liu, and M. H. Lee, "Surface Functionalization of Graphene Prior to CeO_2 Tethering for Oxygen Reduction Catalyst in Both Acidic and Alkaline Media, Materials Research Society, April 2 –6, 2019, Phoenix, AZ

S. Grewal, A. Macedo Andrade, A. Karimaghaloo, and M. H. Lee, "Graphene Functionalization using Transition Metal Oxide for Enhancing the Bifunctional Catalytic Ability of Nanoparticles", 69th International Astronautical Congress, September 2018, Bremen, Germany

S. Grewal, A. Macedo Andrade, Z. Liu, and M. H. Lee, "Enhanced Oxygen Reduction by Surface Functionalization of Carbon Prior to Metal Oxide Tethering", Material Research Society, April 2 –6, 2018, Phoenix, AZ

S. Grewal, A. Macedo Andrade, A. Karimaghaloo, and M. H. Lee, "Novel fabrication of Graphene Oxide supported TiO_2 catalyst using HTM and ALD", 68th International Astronautical Congress, September 2017, Adelaide, Australia

S. Grewal, A. Macedo Andrade, A. Karimaghaloo, and M. H. Lee, "TiO_2 Supported by Acid Treated Graphene Oxide As an Oxygen Reduction Catalysts", 231st Electrochemical Society Meeting, May 2017, New Orleans, LA

S. Grewal, B. Read, and M. H. Lee, "Functionalization of carbon with manganese oxide for enhanced wettability and capacitance in neutral aqueous electrolyte", 229th Electrochemical Society Meeting, May 9 – June 2, 2016, San Diego, CA

ADDITIONAL SKILLS and TRAINING

Software Tools

IBM SPSS Statistics, MAPLE

Materials Characterization Techniques for 3D Carbon structures, Ceramics, and Thin-Films

Transmission Electron Microscope (TEM) including: EDS & EELS, Scanning Electron Microscope (SEM), X-Ray Diffraction (XRD), X-Ray Photoelectron Spectroscopy (XPS), X-ray absorption near edge structure (XANES), Nuclear Magnetic Resonance (NMR), Fourier-Transform Infrared Spectroscopy (FT-IR), and
Rotating Disk Electrode (RDE)/Rotating Ring Disk Electrode (RRDE).

3D Carbon Structures: Graphene oxide, graphite, metal-organic frameworks, and carbon composites.
Ceramics: YSZ, GDC, LNF, TiO_{x-2}, ZrO_{x-2}, CeO_{x-2}.

Materials Fabrication Techniques

Chemical Vapor Deposition (formally, Atomic Layer Deposition) with Ti, Zr, Ce, and Pd precursors.
Solvothermal and Hydrothermal Synthesis with graphene oxide, metal-organic framework, and etc. Sputtering with Ti, Zr, Ce, Pd, and Au precursors.

ABSTRACT

3D Interface-Engineered Transition Metal Oxide/Carbon Hybrid Structures for Efficient Bifunctional Oxygen Electrocatalysis in Alkaline and Acidic Environments
by
Simranjit Grewal
Doctor of Philosophy in Materials and Biomaterials Science and Engineering
University of California, Merced
2021
Chair: Prof. Ashlie Martini

Use of regenerative fuel cells requires efficient bifunctionality in oxygen electrocatalysis: oxygen reduction reaction (ORR) and oxygen evolution reaction (OER). Commonly used noble metals like Pt and its alloys (Pt/Ir or Pt/Ru) are often used for their catalytic activity, selectivity and stability in harsh environments. However, Pt can degrade during operation from catalyst agglomeration and poisoning. Therefore, researchers have used non-precious transition metal oxides (TMO) including Fe_3O_4, MnO_x and Co_3O_4 and/or nanocarbon structures (NC) as potential catalyst. Composite structures where TMO nanoparticles are deposited onto a NC, derived from either graphene oxide (GO) or metal-organic frameworks (MOFs), have often been used. NCs have high surface area and excellent electronic conductivity, and while many studies assert these types of composite materials exhibiting synergistic effects in oxygen electrocatalysis, efforts to elucidate the origin of the synergy is lacking. This doctoral research explores how functional groups present on the surface of NCs affect synergy (reaction route and kinetics) of these electrocatalysis. To incur catalytically active sites between the metal oxides and carbon, the NCs basal plane were functionalized using acid treatments, after which various types of TMO/NC hybrids were synthesized using either wet process or vacuum deposition techniques.

The hydroxylated CeO_2/graphene hybrids showed the best ORR and OER performance in both alkaline and acidic media, in terms of onset/half-wave potential, electron transfer number, and current density when compared to the performance of benchmark catalysts: Pt/C (for ORR) and IrO_2 (for OER). From a series of material and electrochemical analyses, it was determined that a strong tethering of TMOs on graphene's basal plane prohibited restacking and particle-carbon interfaces dictates the performance and reaction route, as indicated in density functional theory calculations. In addition, a hybrid catalyst of TiO_2 nanodots, uniformly anchored on phosphorylated carbon by atomic layer deposition (ALD), showed even better ORR and OER performance in alkaline media when compared the aforementioned CeO_2/graphene hybrid. Materials characterization emphasized a strong adhesion of TMOs on MOF structures; thus providing ample surface interactions for a favorable reaction route. Therefore, an activation of catalytic sites can be realized by proper engineering of interfaces in each hybrid system.

Chapter 1: Objectives

Energy has been the source of mankind's advancement throughout the ages. However, clean energy is needed to mitigate climate change, which is a national security issue for the country. It is widely accepted that the surging CO_2 content over the last several decades has resulted in an increase by one degree to the average temperature of earth, which has caused an increased frequency of natural disasters. This has translated in rising costs of disaster relief in the US (Figure 1.1).[1] For this reason renewable energies such as wind, solar, and tidal are intensively explored as the main energy source for the future, and the importance of large scale energy storage schemes such as rechargeable batteries and regenerative fuel cells (RFC) is ever increasing to address the fluctuating and unreliable production of these energies.[2] Energy conversion from naturally formed states into a readily usable state continues to be extensively researched by scientists. Many examples of energy conversions exist, but the device of interest in this study involves the conversion of chemical energy to electrical energy and vice versa through the electrochemical processes. However, the performance of electrochemical energy devices such as fuel cells, electrolyzers, regenerative fuel cells (RFC) and metal-air batteries is often limited by the sluggish kinetics of oxygen electrocatalysis. This Dissertation addressed the challenge through better understanding the oxygen electrocatalytic processes and developing new catalysts to facilitate the process for these energy conversion devices and the likes.[3–5]

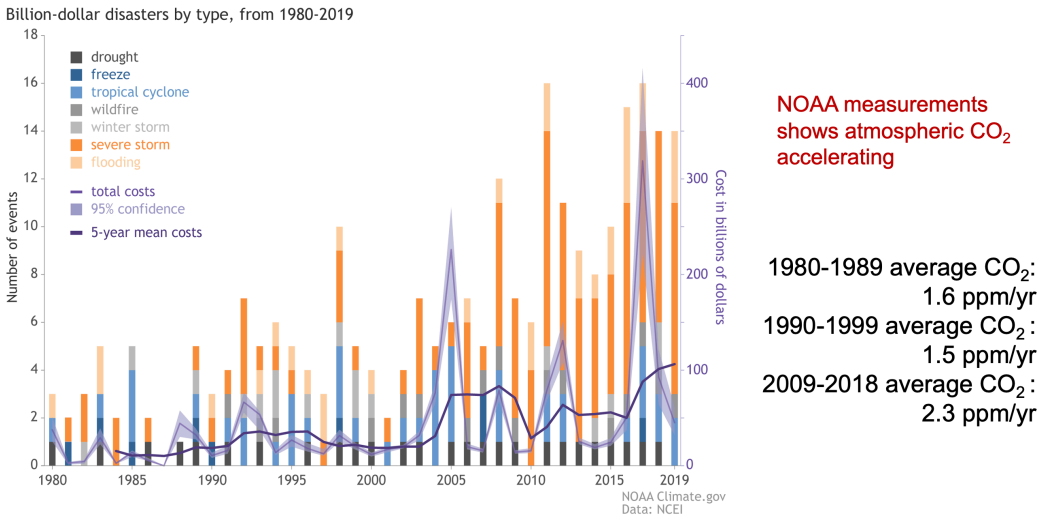

Figure 1.1: The number, type, and annual cost of U.S. billion-dolor disasters from 1980-2019. Running annual cost (depicted as a purple line and shade of 95% confidence interval) and five-year average costs (depicted as a black line). The frequency and significance of disasters have increased in recent years, indicating that the costs of disasters are increasing. Inland flooding and severe storms are contributing the most towards the number of U.S. billion-dollar disasters. NOAA Climate.gov image, based on NCEI data.

1.1 Background of Problem

The kinetically sluggish oxygen electrocatalytic processes includes oxygen reduction reaction (ORR) and oxygen evolution reaction (OER) processes the major cause of power losses in fuel cells, electrolyzers and metal-air batteries due to their sluggish kinetics. Activation overpotential is the voltage needed to drive electrochemical reactions such as ORR and OER at a desired rate. Figure 1.2 shows the multiple steps and resulting intermediates of ORR and OER.[3,6–8] More discussion is provided in Chapter 2 on the thermodynamics and kinetics of these reactions.

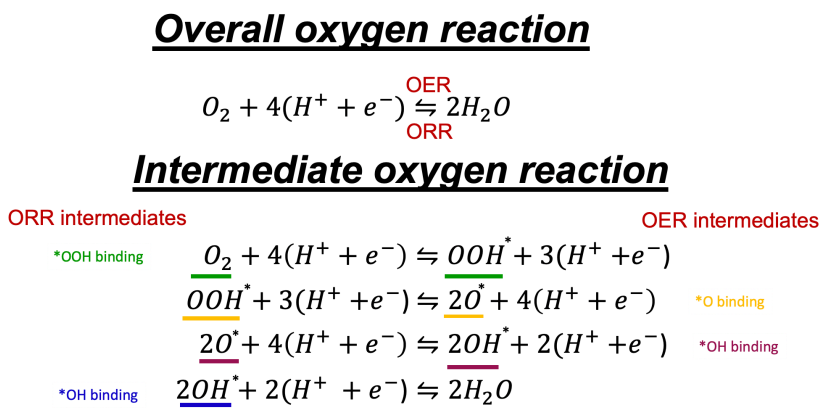

Figure 1.2: Overall oxygen reactions and their intermediates for ORR and OER in acidic media. An overpotential must pass the theoretical activation barrier to produce electrons (form water through ORR) and use electrons (split water through OER).

Scientists have minimized activation losses by using a noble metal-based catalyst whose activation barrier for ORR and OER process is significantly lower than other materials. However, many noble metals are expensive and susceptible to "poisoning" (deactivation with time). Among many, nonprecious transmission metal oxides (TMO) including Fe_3O_4 , MnO_x and Co_3O_4[9] have attracted significant attention as alternative catalysts. TMOs are often dispersed on a carbon nanostructure with a large surface area to supplement relative low electronic conductivity of TMOs and to maximize catalytically active sites per volume and mass.[10] Widely explored carbon nanostructures used TMO/carbon hybrid catalysts include graphene (2D carbon) and metal-organic frameworks (MOF)-derived 3D carbon.[11,12] Nanocarbon structures (NCs) and TMOs are combined together through functional oxygen groups (FOGs); a more exhaustive literature review is provided in Chapter 3. However, few studies have explored the role of FOGs in the catalytic activity of TMO/NC hybrids.[7,13–16]

1.2 Statement of Problem

The objectives of my study are:

(1) To study the effects of interfaces between NCs and TMOs on electrochemical performance and durability for ORR and OER.

(2) To develop high-performance NC/TMO hybrid electrocatalysts for ORR and OER based upon the studied property-performance correlation.

1.3 Research Design

To study the impact of interfacial properties on the electrocatalytic performance, we varied NCs, TMOs, and FOGs. Graphene oxide/TMO samples were fabricated using the hydrothermal process (Chapters 4 & 5) while metal-organic frameworks/TMO samples were made using the hydrothermal process, atomic-layer deposition, and heat treatment (Chapters 6). We utilized a potentiostat to perform typical electrochemical tests to determine the catalysts performance toward both ORR and OER. Additional materials characterization techniques were performed to correlate the property and performance.

1.4 Findings

As seen Table 1, 32 variations of the three NCs, FOGs, and TMOs were fabricated. Of these, only nine variations of graphene oxide-based hybrid catalysts and three variations of MOF-based ones were successfully fabricated using acid treatment to induce FOGs. These 16 catalysts were tested using both materials and electrochemical characterization techniques. The following includes a list of successfully fabricated catalyst in *italics bold*:

Table 1.0 Nanocarbon structures, functional oxygen groups, and transition metal oxides potential catalyst variations.

Nanoarbon Structures (NCs)	**Functional Oxygen Groups (FOGs)**	**Transition Metal Oxides (TMOs)**
Graphene Oxide (G)	Epoxy (e) ***-eG***	TiO_{2-x} (T) ***T-eG***, ***T-cG***, ***T-hG***, and ***T-pMOF***
Metal-Organic Framework-derived carbon (MOF) ***-MOF***	Carboxyl (c) ***-cG***	ZrO_{2-x} (Z) ***Z-eG***, ***Z-cG***, ***Z-hG***, and ***Z-pMOF***
	Hydroxyl (h) ***-hG***	CeO_{2-x} (C) ***C-eG***, ***C-cG***, and ***C-hG***
	Phosphate (p) ***-pMOF***	

Sample preparation, detailed in Chapters 4-6, for both G and MOF (i.e. MOF-derived carbon structures) allowed TMOs to be adsorbed onto them. Due to optimal chemisorption conditions for T-cG, Z-hG, C-hG, and T-pMOF, the catalyst within their own series outperformed others in OER/ORR as revealed by both density functional theory (DFT) calculations and electrochemical testing (Figure 1.2).

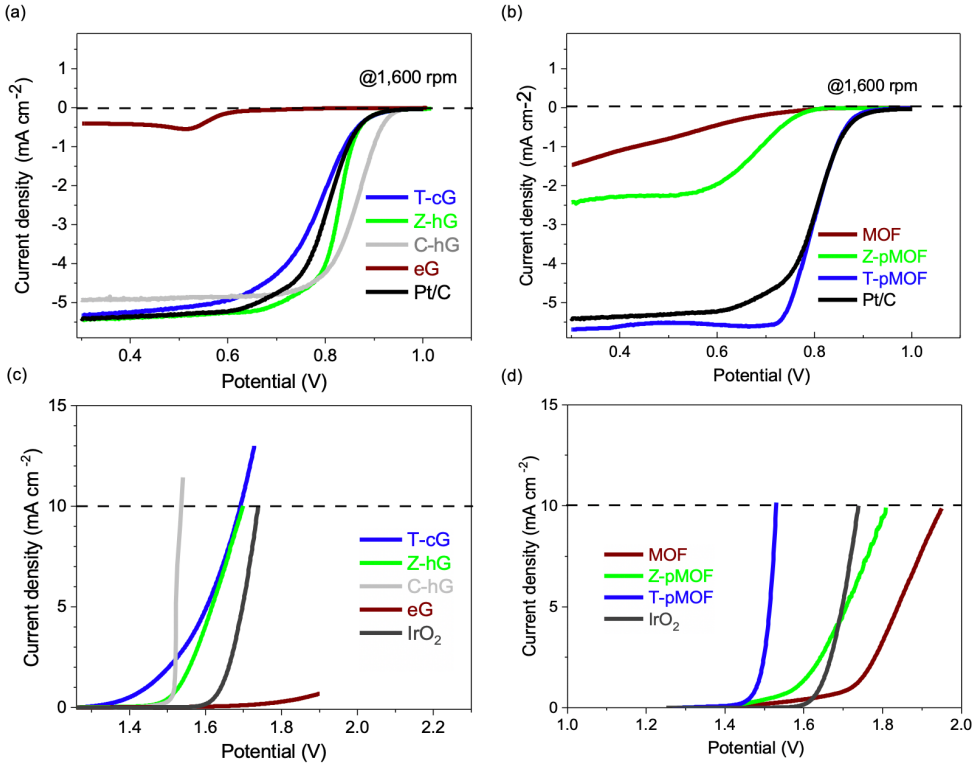

Figure 1.3: Voltammograms obtained in 0.1 M KOH for ORR under O_2-saturated linear sweep voltammetry (LSV) curves at 1600 rpm of (a) G samples and (b) MOF samples; OER was obtained using similar conditions under N_2-saturated LSV at 1600 rpm of (c) G samples (d) MOF samples. Curves have been IR-corrected.

Using onset potentials for our catalysts as seen in Figure 1.3 with accompanying DFT calculations to describe intermediate binding ΔG energy profiles and comparing them to other catalysts, the following volcano plot can be obtained (Figure 1.4). In general, those catalyst that are nearest the peak allow for the most "optimal binding" conditions. Platinum and iridium-based alloys tend to be nearest to the peaks, hence, are often the most favored catalyst; detailed discussion is provided in Chapters 3.

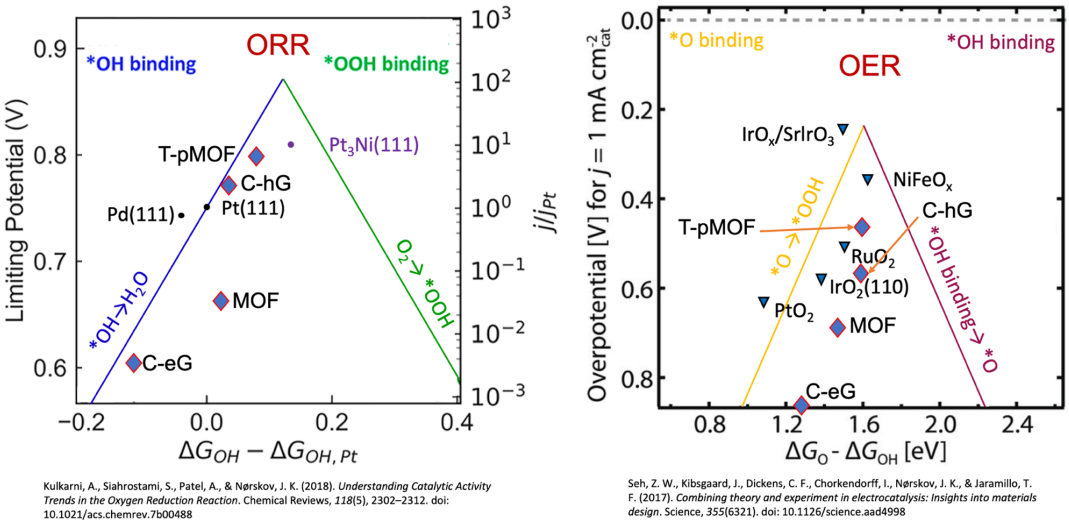

Kulkarni, A., Siahrostami, S., Patel, A., & Nørskov, J. K. (2018). *Understanding Catalytic Activity Trends in the Oxygen Reduction Reaction*. Chemical Reviews, *118*(5), 2302–2312. doi: 10.1021/acs.chemrev.7b00488

Seh, Z. W., Kibsgaard, J., Dickens, C. F., Chorkendorff, I., Nørskov, J. K., & Jaramillo, T. F. (2017). *Combining theory and experiment in electrocatalysis: Insights into materials design*. Science, *355*(6321). doi: 10.1126/science.aad4998

Figure 1.4: Volcano plots for both ORR (a) and OER (b) in terms of binding energy profiles (ΔG) for their respective intermediates (ORR: OH* & OHH* binding; OER: O* & OH* binding). More information is presented in Chapter 2. When taking two of the best catalyst from each nanocarbon structure (C-hG and T-pMOF), we can see an improvement in both limiting potential across and ΔG of intermediates.

The best performing graphene-based catalyst (C-hG) and MOF-based catalyst (T-pMOF) show close proximity to the peak when compared to the non-optimal chemisorption (C-eG and MOF) catalyst. Chapters 4-6, will provide further insight on how FOG affects the ORR/OER activity and reaction pathway of resulting carbon/TMO hybrid catalysts. An optimized combination of carbon structure, FOGs and TMOs enhances performance and durability as a result of effective interfacing between NCs and TMOs. A combination of experimental observations and DFT calculations leads to a design guideline for carbon/TMO hybrid catalysts for oxygen electrocatalysis. The significance of this discovery will enable scientists to create a library of optimal combinations along with their respective characterielies from which other scientists can access, provide help to achieve industrial and governmental efforts to realize cost-effective, durable and efficient energy conversion. Other applications of the TMO, NC, and FOG hybrids include the general field of electrochemistry, synthetic chemistry and nanotechnology in general, as most catalyst used for energy conversion devices are also used for other wider range of applications including biological cell pathways, water purification, fuel synthesis, etc.

The following chapters provide an explanation for the operation of conversion devices (Chapter 2), the progress scientist have made so far (Chapter 3) and the meaning and explanation of the Dissertation's findings (Chapter 4-6).

References

1. Smith, A. B. 2010-2019: A landmark decade of U.S. billion-dollar weather and climate disasters. *Climate News* 07–11 (2020).
2. Khalilpour, K. R. Stranded renewable energies, beyond local security, toward export: A concept note on the design of future energy and chemical supply chains. in *Polygeneration with Polystorage: For Chemical and Energy Hubs* 157–173 (Elsevier, 2018). doi:10.1016/B978-0-12-813306-4.00006-9
3. Ryan O'Hayre, Suk-Won Cha, Whitney Colella, F. B. P. *Fuel cell fundamentals*. (WILEY-VCH Verlag, 2009).
4. Vielstich, W., Lamm, A., Gasteiger, H. A. (Hubert A. & Yokokawa, H. *Handbook of fuel cells : fundamentals, technology, and applications*. (Wiley, 2003).
5. Montoya, J. H. *et al.* Materials for solar fuels and chemicals. *Nat. Mater.* **16**, 70–81 (2016).
6. Luo, Z. *et al.* Mn_3O_4 @$CoMn_2O_4$ –Co_xO_y Nanoparticles: Partial Cation Exchange Synthesis and Electrocatalytic Properties toward the Oxygen Reduction and Evolution Reactions. *ACS Appl. Mater. Interfaces* **8**, 17435–17444 (2016).
7. Sun, M., Liu, H., Liu, Y., Qu, J. & Li, J. Graphene-based transition metal oxide nanocomposites for the oxygen reduction reaction. *Nanoscale* **7**, 1250–1269 (2015).
8. Dong, C. *et al.* Modest Oxygen-Defective Amorphous Manganese-Based Nanoparticle Mullite with Superior Overall Electrocatalytic Performance for Oxygen Reduction Reaction. *Small* **13**, 1603903 (2017).
9. Wu, G. & Zelenay, P. Nanostructured nonprecious metal catalysts for oxygen reduction reaction. *Acc. Chem. Res.* **46**, 1878–1889 (2013).
10. Sun, Y., Wu, Q. & Shi, G. Graphene based new energy materials. *Energy Environ. Sci.* **4**, 1113 (2011).
11. Osgood, H., Devaguptapu, S. V., Xu, H., Cho, J. & Wu, G. Transition metal (Fe, Co, Ni, and Mn) oxides for oxygen reduction and evolution bifunctional catalysts in alkaline media. *Nano Today* **11**, 601–625 (2016).
12. Huang, Y. B., Liang, J., Wang, X. S. & Cao, R. Multifunctional metal-organic framework catalysts: Synergistic catalysis and tandem reactions. *Chemical Society Reviews* **46**, 126–157 (2017).
13. Rümmeli, M. H. *et al.* Graphene: Piecing it Together. *Adv. Mater.* **23**, 4471–4490 (2011).
14. Lee, K., Ahmed, M. S. & Jeon, S. Electrochemical deposition of silver on manganese dioxide coated reduced graphene oxide for enhanced oxygen reduction reaction. *J. Power Sources* **288**, 261–269 (2015).
15. Zhang, H. *et al.* Crucial role for oxygen functional groups in the oxygen reduction reaction electrocatalytic activity of nitrogen-doped carbons. *Electrochim. Acta* **292**, 942–950 (2018).
16. Shin, D. S. *et al.* Distribution of oxygen functional groups of graphene oxide obtained from low-temperature atomic layer deposition of titanium oxide. *RSC Adv.* **7**, 13979–13984 (2017).

Chapter 2: Oxygen Electrocatalysis and its Characterization

2.1 A Brief history of Fuel Cells and Electrolyzers

Fuel cells generate clean energy using pure H_2 with only one, non-lethal byproduct – water. Unlike conventional combustion engines, fuel cells convert chemical energy directly into electrical energy without an intermediate step (not to be confused with reaction intermediates) and moving parts, making the energy conversion intrinsically efficient. Unlike batteries, where the scaling of energy and power is separable, the scaling of energy and power in fuel cells can be separated. The scaling of energy and power are related to the fuel storage capacity and cell size, respectively.[1] Additionally, fuel cells can generate power continuously without a separate recharging phase, provided that fuel is supplied.

Electrolyzers are very similar to fuel cells with the exception that the direction of reaction is reversed; pure water is split into hydrogen and oxygen when using an external energy input. The reactant of a fuel cell is the product of an electrolyzer, and vice versa. Both a fuel cell and an electrolyzer can be integrated in a given cell to save space and weight, which is called a unitized regenerative fuel cell.[2]

Brief History: Fuel Cells

The Ancient Greeks (~600 BC) discovered how attraction (static electricity) could result from rubbing fur on amber and decided to "harvest" this energy to better serve the Greek society. However, it would be nearly 2,400 years until further progress would be made by British chemist Sir Humphry Davy. He pioneered the field of electrolysis by inducing a non-spontaneous chemical reaction using direct electric current to isolate various elements including potassium, sodium, magnesium and others. He compared the forces that were involved to separate these elements from compounds, thus creating the new field of electrochemistry.[3] Using a "reversed" reaction, Davy produced water from hydrogen and oxygen. It is noted that this is a point of contention, as some believe the physical chemist Sir William R. Grove generated electricity by a spontaneous process using water to create hydrogen and oxygen. Regardless, this would lead to Groves invention in 1839 of the first phosphoric acid fuel cell using zinc and platinum electrodes separated by a porous ceramic pot. Years later, Grove developed the first fuel cell that used both hydrogen and oxygen, which he termed gas voltaic batteries (Grove cell).[4]

Charles Langer and Ludwig Mond attempted to enhance Grove's fuel cell by using both air and coal gas that relied on a porous, non-conducting diaphragm. This, however, suffered from catalyst poisoning and was later discarded for the more practical and cheaper alternative at the time, the combustion engine.[5,6]

The first successful fuel cell was developed by Francis Thomas Bacon using alkaline electrolyte and nickel electrodes in 1932. Later, in 1955, W. Thomas Grubb replaced the alkaline electrolyte with the polymer ion-exchange membrane that would be termed the proton exchange membrane fuel cell (PEMFC). Later, Leonard Niedrach coated the membrane with platinum for a more efficient reaction that would be later used for the Gemini project (as developed by General Electric[7]), the second human controlled spaceflight program of NASA. Other missions using this technology included the provision of not only electricity, but portable water to the space shuttle.[8]

Brief History: Electrolyzers

Shortly after the discovery of electricity, J.R Deiman and A.P. van Troostwijk in 1789 used an electrostatic generator to discharge electricity through gold wires inserted into a tube filled with water, causing gasses to be evolved.[9,10] Sir Anthony Carlisle, a surgeon by trade, and William Nicholson discovered electrolysis by applying a potential through water and splitting it into oxygen and hydrogen in 1800. Later, in 1869, Zenobe Gramme used both Carlisle's and Davy's electrolysis to create the Gramme machine to cheaply produce hydrogen. A more industrial version to produce hydrogen and oxygen from water was developed by Dmitry Lachinov in 1888.[11] This would come after Michael Faraday's laws stating that the amount of material produced (or liberated) at an electrode during an electrochemical reaction is directly proportional to the total conducted charge.[12] By 1902, more than 400 water electrolyzers were already in operation. Industry would continue to improve this technology throughout the 1930-1970s.[9]

2.2 Fuel Cell Characteristics

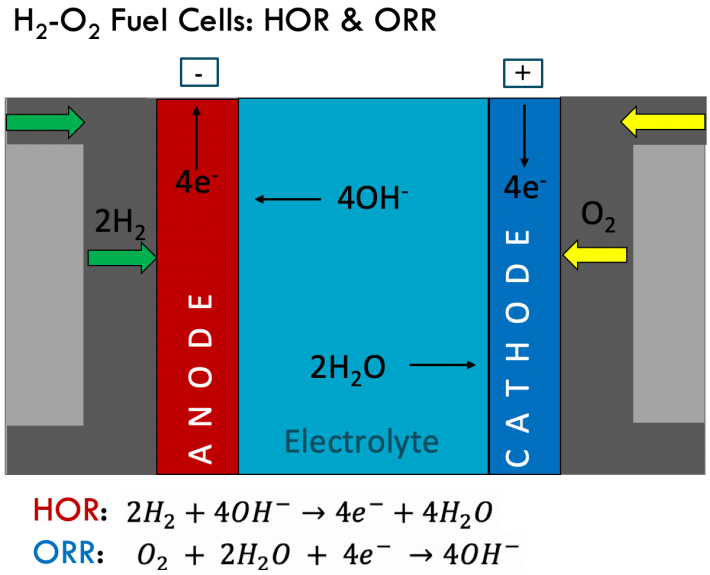

Figure 2.1: A simplified cross-sectional schematic diagram depicting the operation of a H_2-O_2 fuel cell. HOR stands for hydrogen oxidation reaction.

Fuel cells, like any other electrochemical devices, are made of three components: anode, electrolyte, and cathode. The anode splits H_2 and converts it into protons (H^+) and electrons. In the case of PEMFC, the protons pass through the electrolyte to recombine with oxygen at the cathode side and produce water while the electrons take a separate route before reaching the cathode. For alkaline fuel cells (AFC; Figure 2.1), oxygen is fed into the cathode side. The hydroxide ion, when passing through the electrolyte, will be recombine with protons at the anode side producing water as the final product. Note for both types of fuel cells, the anode generates electrons while the cathode consumes them.[1] The electrolyte of a PEMFC is based on a polymer backbone with side-chains containing

acidic moieties while alkaline fuel cells use neutral to alkaline media.[13,14,15] As for electrodes in both fuel cells, the following characteristics are required:

- High catalytic activity
- High surface area
- High triple phase boundary area
- High electronic conductivity
- High chemical stability/corrosion resistance
- Low cost; abundance of material

To maximize the catalytic activity per mass, most fuel cells utilize highly active catalyst nanoparticles (e.g. platinum) dispersed on a high-surface-area carbon.[1] Despite the benefits fuel cells can provide, they can suffer from: poisoning as a result of a sensitivity to fuel impurities, low temperature waste heat, and expensive materials such as platinum/platinum alloys used as the ORR catalyst.[8] While platinum may have extremely high activity due to its bond affinity to hydrogen, it can suffer from CO poisoning.[16–18] One way to prevent this is by making platinum particles extremely small or using a secondary component such as ruthenium, tin, tungsten or rhenium that are alloyed with platinum particles. Ruthenium is often used as an alloy with platinum due to its ability to create new absorption sites to remove CO poisoning[19] and must be small enough to increase the electrochemically active surface area. However, formidable cost has impeded further development of a platinum/ruthenium catalyst.[1] For this reason, extensive research has been directed towards the development of cathodes including Pt-Ni, Pt-Cr, Pt-Ti, Pt-Mn, Pt-Co and Pt-Fe.[20] For example, Pt-Co catalysts have attracted special attention due to their impressive catalytic behavior and smaller degradation rates than the favored platinum with carbon (Pt/C).[21] Metal oxides also have been widely studied as a replacement for platinum-based catalysts, due to their cost effectiveness and sufficient activity towards ORR.[22] Metal oxides can also leach (especially for PEMFC) into the electrolyte and poison the cell, which unfortunately adds to an already accelerated degradation, corrosion, and deactivation generally seen in platinum based catalysts.[23–27] Some researchers have designed a pre-leaching processes that alleviates the effects of leaching from a catalyst. This includes the removal of the base-metal/poorly bound particles on the carbon structures.[1] However, these techniques have not been entirely successful for all catalysts that are used in corrosive media.[1,12,28,29]

2.3 Fuel Cell Performance and Cell Losses

The cell potential is determined by the thermodynamically determined potential (reversible voltage) and cell voltage losses: $V = E_{thermo} - N_{act} - N_{ohmic} - N_{conc}$ where V is the actual output voltage of the fuel cell, E_{thermo} is the predicted reversible cell potential output, N_{act} is the activation loss originated from the activation barrier for electrochemical reactions, N_{ohmic} is the ohmic loss from both electronic and ionic conduction, and N_{conc} is the concentration loss due to limited mass transport. Activation loss (N_{act}) is due to the sacrificed potential used to overcome an activation barrier; an active catalyst will have a lower "barrier height" and thus, have a smaller activation loss. Ohmic loss originates from the "friction" that moving electronic and ionic charges experience during their migration under an electric field. Ionic conduction loss, which is

usually much larger than the ohmic loss from electronic conduction, occurs during the movement of ions through an electrolyte. Finally, the concentration loss is due to the limited availability of reactants and/or incomplete removal of products from the reaction sites. Mass transport is the process of supplying reactants and removing products. These uncharged species are affected by the convective and diffusive forces of movement rather than a voltage gradient. Figure 2.2 shows a typical current-voltage curve from an electrochemical cell.[1,30]

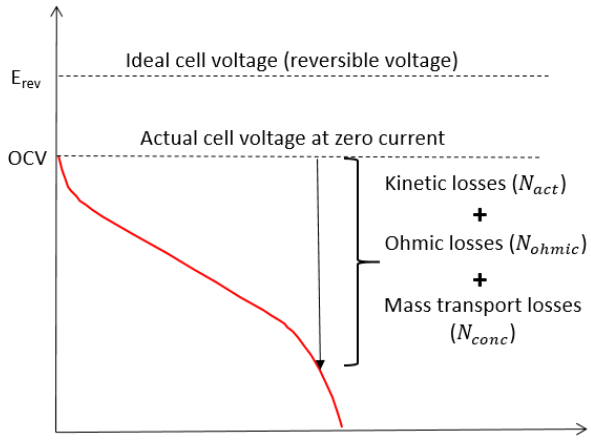

Figure 2.2: A typical current-voltage curve of fuel cells where the reversible voltage, open circuit voltage and three different types of voltage losses are depicted.

A major factor of N_{act} is the exchange current density, which is the equilibrium charge transfer rate at which reactants and products are exchanged without an activation overpotential. Therefore, a higher exchange current density represents an intrinsically faster reaction. To increase the exchange current density, a kinetically favorable catalytic material should be used. To minimize N_{ohmic} with a given electrolyte material, the thickness of the electrolyte, through which ions travel, should be minimized. However, when decreasing the thickness, one should ensure that the electrolyte is not subjected to:

- mechanical degradation
- short-circuiting
- high contact resistance (delamination; non-conformality)
- dielectric breakdown
- fuel crossover

When the electrolyte is too thin to endure the electric field, the electrolyte may suffer from a dielectric breakdown and also short-circuiting (massive uncontrolled electronic current) between two electrodes. Fuel can also cross a very thin electrolyte and reach the "air electrode" side, which leads to a Nernstian loss. To minimize the N_{conc}, both an efficient supply of reactants (e.g. oxygen or hydrogen) and removal of products (e.g. water) are necessary.

2.4 Thermodynamics and Reversible Voltages

To quantify the reversible voltage of a cell in various conditions, a brief discussion on related thermodynamics is necessary. The energy conservation requirement of a system leads to:

$$dU = dQ - dW \tag{2.1}$$

where dU is the internal energy of the closed system, dQ is the heat transferred to the system, and dW is the work done by the system. As the work is equal to the pressure times the volume change, assuming constant volume, the energy conversion is described as:

$$dU = dQ - pdV \tag{2.2}$$

In a reversible process, from the known relationship of $dQ = TdS$ from the second law of thermodynamics, the following equation is acquired:

$$dU = TdS - pdV \tag{2.3}$$

Using the Legendre transform and several substitutions, we derive Gibbs free energy of reaction (see Figure 2.3) as:

$$dG = -TdS + Vdp \tag{2.4}$$

Taking both equations (2.3) and (2.4), and considering mechanical and electrical work only ($dW = pdV + dW_{elec}$), we obtain:

$$dG = -dW_{elec} \tag{2.5}$$

where W_{elec} is the maximum amount of "useful work" in the form of electrical work extractable from the system.

On the other hand, the electrical current is:

$$i_e = nF\frac{dN}{dt} = iFk \tag{2.6}$$

where n is the moles of electrons generated per mole of reactant, F being Faraday's constant and k (dN/dt) being the rate of the electrochemical reaction (in mol/s). If we relate the potential difference to equation (2.5) and (2.6) the following is observed:

$$\Delta G = -nFE \tag{2.7}$$

where E is positive if the reaction is spontaneous.

The chemical potential (μ) as defined as:

$$\mu_{i,k} = \frac{dG}{dn_i}_{T,p,n,j\neq I} \tag{2.8}$$

where $\mu_{i,k}$is the chemical potential of species i in phase k, and (dG/dn_i) expresses the change in Gibbs free energy of the system by the incremental increase of i species amount under all else constant. If we consider a reaction having the following:

$$aA + bB \leftrightarrow eE + fF$$

where A and B are reactants, E and F are products, and their lowercased counterparts represents their number of moles. Solving for the differential in (2.8), we have

$$\Delta G = (e\mu_E + f\mu_F) - (a\mu_A + b\mu_B) + RTln\frac{X_E^{e*}X_F^f}{X_A^{a*}X_B^b} \tag{2.9}$$

where X is the mole fraction.

Recognizing that $(e\mu E + f\mu F) - (a\mu A + b\mu B)$ is the standard-state molar free-energy change for the reaction (E^0), we obtain the reversible potential, E, by applying equation (2.7)

$$E = E^0 - RTln\frac{X_E^e * X_F^f}{X_A^a * X_B^b} \quad (2.10)$$

The relation is known as the Nernst equation.[1,31,32]

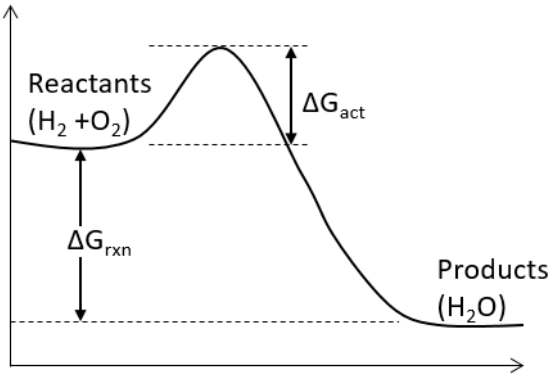

Figure 2.3: Free energy profile of reactants and products for H_2/O_2 fuel cells. The reversible voltage of the cell is determined by ΔGrxn while the reaction kinetics are affected by ΔGact.

2.5 Introduction to ORR

Oxygen reduction reaction (ORR) is an electrochemical reaction that occurs in the cathode of a fuel cell. Due to its sluggish kinetics compared to HER, intensive research has been performed to improve the ORR kinetics and understand the mechanism of ORR. The charge transfer route for ORR depends on the type of intermediates.[33]

Table 2.0: Selected list of standard electrode potentials in alkaline and acidic aqueous electrolytes.

Electrolyte	Pathway	ORR reactions	E^o_{NHE}, ($V_{vs.}$NHE)
Alkaline aqueous solution	Four-electron pathway	$O_2 + 2H_2O + 4e^- \rightarrow 4OH^-$	0.401 V
	Two-electron pathway	$O_2 + H_2O + 2e^- \rightarrow HO_2^- + OH^-$	-0.076 V
		$HO_2^- + H_2O + 2e^- \rightarrow 3OH^-$	0.878 V
Acidic aqueous solution	Four-electron pathway	$O_2 + 4H^+ + 4e^- \rightarrow 2H_2O$	1.229 V
	Two-electron pathway	$O_2 + 2H^+ + 2e^- \rightarrow H_2O_2$	0.695 V
		$H_2O_2 + 2e^- \rightarrow 2H_2O + O_2$	1.776 V

The ORR process on a catalyst can take multiple routes as shown in Figure 2.4 for two types of media: alkaline and acidic. In alkaline media, two general routes are possible. One is the production of an OH^- through a 4e- electron pathway, and the other is the production of the peroxide ion through a $2e^-$ pathway. In the desired $4e^-$ pathway route, an ORR catalyst reduces oxygen molecules into OH^- without going through an intermediate (peroxides).[1,8,33,34] Incomplete reduction of oxygen to the peroxide ion not only leads to a low energy conversion efficiency, but creates free radical species as a

reaction intermediate. As for acidic media, through a 4e- electron pathway, molecular oxygens are reduced directly to H_2O by combining with protons while the 2e- pathway produces hydrogen peroxides as a reaction intermediate.

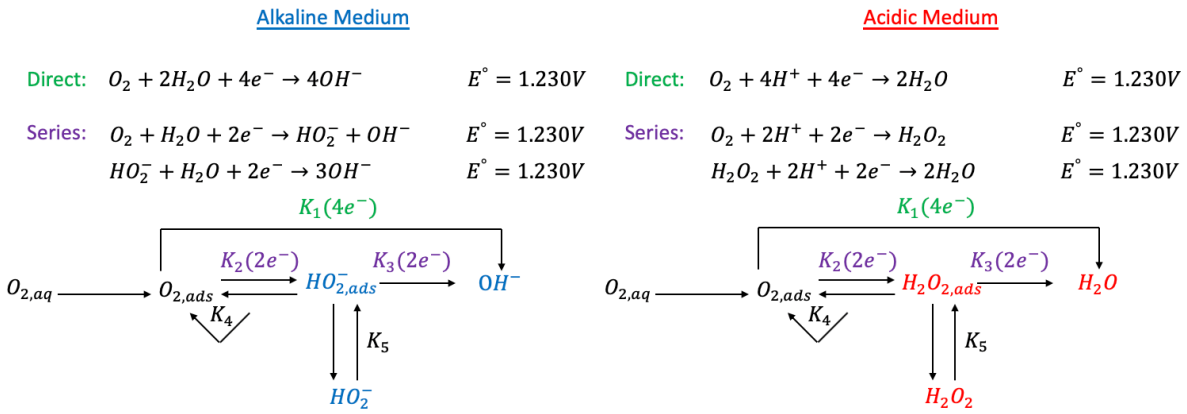

Figure 2.4: Charge transfer pathways and standard electrode potentials of ORR in alkaline and acidic media.

Nonequilibrium reactions are important as they can generate a net current in a fuel cell by sacrificing electric potential at both the cathode and anode components. An electric overpotential can change the activation barrier of the reaction. By providing an external energy (or by applying an overpotential) to a cell, the electrochemical potential of the cell deviates from the thermodynamically determined cell potential (galvani potential), and thus a net current is generated. The Butler-Volmer equation provides a means of quantifying a net current generated from an electrochemical reaction, which increases exponentially with the activation overpotential.[1,8,35] The Butler-Volmer equation is given as

$$j = j_0\left(e^{\frac{\alpha\eta FN}{RT}} - e^{\frac{-(1-\alpha)\eta FN}{RT}}\right) \qquad (2.11)$$

where j_0 (at equilibrium) is the current densities for the forward and reverse reactions, N is the activation overvoltage (sacrificed voltage to overcome a electrochemical reaction's barrier), and α is the transfer coefficient. The transfer coefficient depends on the symmetry of the activation barrier and expresses how the change in potential across the catalysts interfaces changes the size of the forward reaction vs the reverse reaction at a given j_0.

The produced net current can be increased by:

- Increasing reactant concentration
- Decreasing activation barrier (high activity catalysts)
- Increasing temperature
- Increasing electrolyte/electrode interfacial area.

2.6 Electrochemical characterization components

The ORR performance is mainly quantified by electrochemical characterization techniques, such as linear voltammetry and electrochemical impedance spectroscopy (EIS) in a static, rotating disk electrode (RDE) or rotating ring-disk electrode (RRDE) setup. RDE was first developed by Veniamin (Benjamin) Levich at the Institute of Electrochemistry at the Academy of Sciences of the USSR in 1952.[36] The disk rotation in RDE induces a continuous electrolyte flux toward the active electrode, thereby replenishing homogeneous and fresh electrolyte into what is known as the hydrodynamic boundary layer. This action of replacing electrolyte also follows a removal of the reacted species away from the electrode surface, making the overall reaction at the disk "less limited" by mass transport kinetics.[8,36,37] Therefore, a higher angular speed of disk warrants a higher flux of the electrolyte, making mass transport kinetics even "less limiting" to the overall reaction. Under a polarization, the potential of the electrode at the hydrodynamic boundary layer shifts away from its equilibrium, causing an electrochemical half reaction.[38] Using Fick's second law and fluid dynamics (convection-diffusion concepts),[33] the estimated diffusion layer thickness is:

$$\mathrm{D_{thickness}} = 1.61 \mathrm{D}_O^{1/3} \nu^{1/6} \omega^{-1/2} \tag{2.12}$$

where D_o is the diffusion coefficient of a particular gas in a specific molar concentration electrolyte, ν is of the kinematic viscosity of the electrolyte, and ω is the angular rotation rate of disk. Using Equation 2.12 and principles of a convection/diffusion system towards a rotating disk electrode, where the only oxidized form of the ion is initially present in the electrochemical cell, we arrive at the Levich equation of limiting current density,

$$J_L = 0.62 n F D_O^{2/3} \nu^{-1/6} \omega^{-1/2} \tag{2.13}$$

where n is the number of moles of electrons per reaction. Combined with the Koutecky equation:

$$J_k = nFKC_O \tag{2.14}$$

where J_k is the kinetic limiting current density and F is Faraday's constant, we arrive at the Koutecky-Levich equation[1]:

$$\frac{1}{J} = \frac{1}{J_K} + \frac{1}{J_L} \tag{2.15}$$

In an RDE setup, voltammetry can be performed by controlling either the current or voltage while measuring both. One particular form of voltammetry includes linear sweep voltammetry (LSV) where the following occur simultaneously:

(1) The current at the working electrode (WE) is measured,
(2) The potential between the WE and reference electrode (REF) is swept linearly in time at a specific rate ($\frac{dV}{dt}$),
(3) The counter electrode (CE) completes the charge circuit in the cell (not depicted).

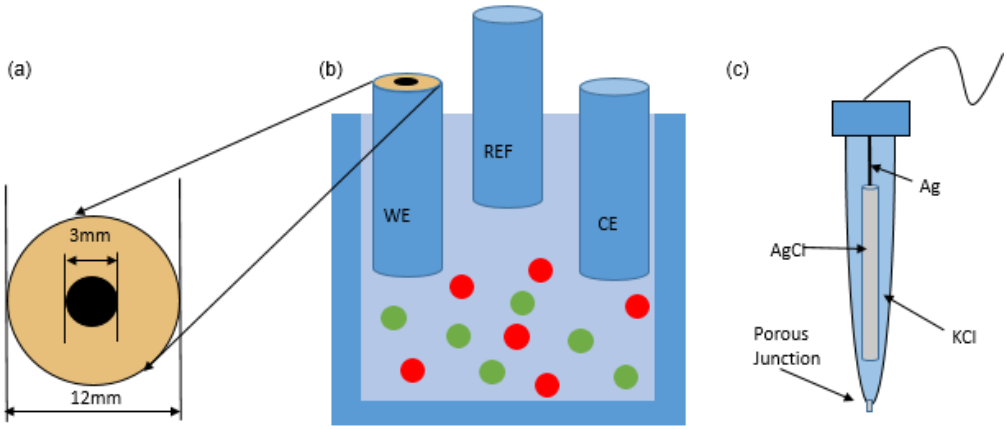

Figure 2.5: (a) RDE with a typical 3 mm diameter across the glassy carbon electrode and plastic holder (seen in light brown). A schematic diagram depicting (b) the three-electrode set-up during a half-reaction testing and (c) a Ag/AgCl reference electrode.

A common disk component used for RDE, as part of the WE as seen in Figure 2.5a, is glassy carbon. Glassy carbon is widely used due to its resistance against deformation in high temperature and corrosive environments while being impermeable to gases and liquids. By utilizing glassy carbon's ability, a well-defined hydrodynamic boundary layer can form when a catalyst is deposited onto the glassy carbon.[8]

The type of electrolyte used for electrolysis determines the type of REFs are used. For acidic electrolyte, the most frequently used reference electrode is the silver-silver chloride electrode (Ag/AgCl REF). Ag/AgCl REF contains a silver-rod (coated with silver chloride) inside a glass vial that is filled with potassium chloride (mostly in ~ 3.5 M), as seen in Figure 2.5c. When subjected to a large polarization in the WE, the Ag/AgCl REF can accommodate the high flux of redox reactions and remain in a quasi-equilibrium state between AgCl and Ag. This quasi-equilibrium state creates stability during measurements in acidic enviroments.[8] Also, Ag/AgCl performs well in acidic electrolyte due to the ions, such as Cl^- from a hydrochloric acid based media, having little to no impact on the concentration of chloride within the reference itself. If a basic electrolyte such as sodium hydroxide is used, the cations in the electrolyte would indirectly block some of the chlorides within the reference electrode itself (the frit), thus causing a change with the standardized reference potential. For alkaline electrolyte, Hg/HgO/1M NaOH REF is widely used. Hg/HgO/1 M NaOH REF performs more favorably in alkaline solutions due to its stability in a quasi-equilibrium state between Hg and HgO.[39,40] Like Ag/AgCl REF, if the Hg/HgO/1M NaOH REF is exposed to an acidic environment, the concentration of Hg/HgO would change thus changing the standardized reference potential. Special care is needed when deciding to use a reference electrode for a particular electrolyte. [12,33,41]

2.7 Electrochemical characterization of fuel cells

2.7.1 LSV Characterization

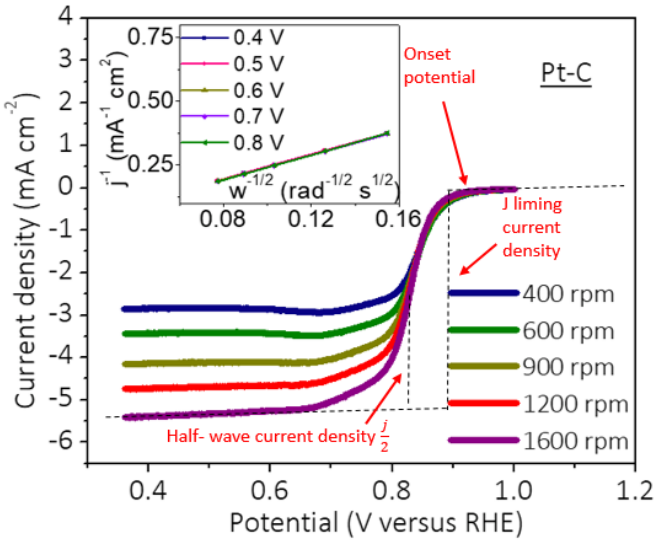

Figure 2.6: A typical set of LSV curves and the corresponding Koutechy-Levich plots at different disk potentials (inset). The data was obtained from Pt/C in O_2-saturated 0.1 M KOH

Linear sweep voltammetry (LSV) is a voltammetry technique where a sweep of electric potential in a direction relative to the standard electrode potential is applied in an RDE setup. The maximum current generated by this potential, restricted by how fast the oxidized form of species can arrive at the electrode surface interface, is termed the limiting current. In general, the overall reaction rate is co-limited by both mass transport and reaction kinetics, which is described and analyzed by the Koutecky-Levich equation (2.15). An electrochemical reaction with facile kinetics has an overall reaction that is limited by mass transport. Using a linear equation,

$$B = 0.62nFD_O^{2/3}\nu^{-1/6} \tag{2.16}$$

With equation (2.15), we have the following:

$$y = \frac{x}{B} + \frac{1}{J_k} \tag{2.17}$$

where we have the y as the resulting current density and x as the changing rpm ($\omega^{-1/2}$). Figure 2.6 is an example of LSV curves and corresponding Koutecky-Levich (K-L) plots obtained from a Pt/C catalyst in O_2-saturated 0.1 M KOH at a sweep of 5 mV s^{-1}. By determining the slope of the K-L plot, the number of electrons involved in the reaction (i.e. electron transfer number) can be determined (here it is 3.94). In the plot, it is also deduced that the ORR performance is limited by diffusion rather than the kinetics of the electrode itself by noticing that the $1/J_K$ value in the K-L equation is approaching zero, thereby $J \sim J_L$.

When analyzing the LSV curves, the onset potential, half-wave potential, and limiting current density can be determined (0.94 V, 0.82 V and ~5.5 mA cm^{-2}, respectively, from Figure 2.6). The onset potential is the potential where the current begins to increase by overcoming the thermodynamic and kinetic barriers. The half-wave potential is the point where the current is equal to one half of the limiting current density. Since Pt/C is the industrial standard, these values stand as "potential goal(s)" when developing new catalyst.[42,43]

Once the number of electronic moles per reaction is obtained, a Tafel plot can be drawn from the J_k value (Figure 2.7). A Tafel plot (potential versus kinetic current) can determine the Faradaic kinetics more explicitly by excluding the contribution from diffusion and ohmic transport. The kinetic current J_k is found by:

$$J_K = \frac{J_L \cdot J}{J_L - J} \tag{2.18}$$

The Tafel slope is an indication of the kinetics of the electrode; a smaller slope corresponds to faster kinetics.[1]

2.7.2 RRDE Characterization

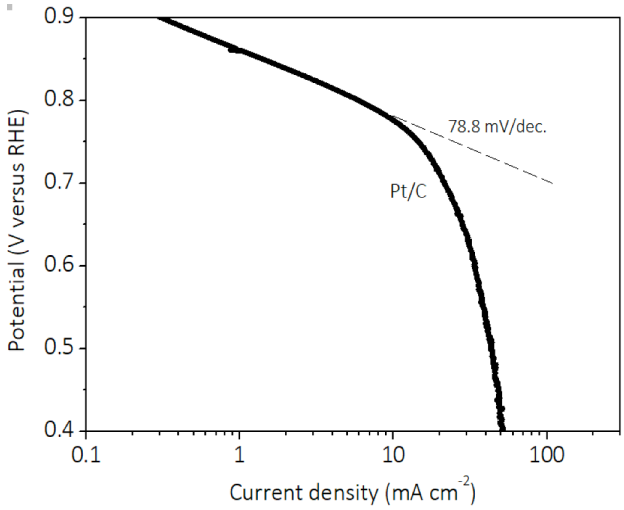

Figure 2.7: An example of a Tafel plot. Obtained from Pt/C in O_2-saturated 0.1 M KOH at 1,600 rpm.

The ORR electron transfer number is widely quantified by the rotating ring-disk electrode (RRDE). First successfully constructed by Lev Nekrasov and consequently mathematically developed by researchers at the University of Minnesota and Oxford University, RRDE allows researchers to better describe the types of reactions occurring on the surface of an electrode. Like RDE, reactants such as oxygen (for ORR analysis) are flowed to the disk electrode to be reduced. If the catalyst on the disk induces the $4e^-$ process (pathway [a] below in alkaline medium), the resultant solution that flows to the ring would not incur further reaction. For the $2e^-$ process, the disk would only reduce O_2 partially into a peroxide (reaction pathway [b] below), and the product will be further

reduced to OH^- (reaction pathway [c]) at the ring. Note that the electronic flow into the disk electrode incurs both a $4e^-$ and $2e^-$ reduction; i.e. both pathways [a] and [b], and those into the ring incur the completion of $2e^-$ process (pathway [c]). Therefore, by measuring both the disk and ring current, the relative amount of electrons contributing to the $2e^-$ and $4e^-$ processes can be quantified.[8,32,33]

$$O_2 + 2H_2O + 4e^- \rightarrow 4OH^- \quad [a]$$
$$O_2 + H_2O + 2e^- \rightarrow HO_2^- + OH^- \quad [b]$$
$$H_2O + HO_2^- + 2e^- \rightarrow 3OH^- \quad [c]$$

There is an important consideration to be made about RRDE: Not all of the products of reaction at the disk electrode reach the ring. Therefore, for an accurate quantification of the electron transfer number, we need to quantify the so-called collection efficiency (N). The collection efficiency is the fraction of reactants from the disk that eventually flows to the ring for reaction:

$$N = \frac{i_{[c]}}{i_{[a]} + i_{[b]}} \quad (2.19)$$

Since the fraction of reactants from the disk surface reaching the ring for further reaction (the collection efficiency is alternatively $N = i_{Ring}/i_{Disk}$) varies, each RRDE setup should undergo a prior characterization. This is achieved by reducing ferricyanide at the disk electrode in 0.1 M KOH containing 10 mM of $K_3Fe(CN)_6$ because the ferrocyanide / ferricyanide is a simple well-defined single-electron half-reaction. In the case shown in Figure 2.8 as an example, the collection efficiency is quantified to be 0.42 (N = 0.31/0.72).

Once the collection efficiency is found, the ratio of currents originating from the 2e- and 4e- processes can be quantified from LSV, using a RRDE setup. Note that the scan rate must be slow enough (typically < 10 mV s^{-1}) for an accurate measurement to avoid capacitive current behavior. The percentage of peroxide ion generation ($\%HO_2^-$) and n values can be obtained using two assumptions denoted in Equations (2.20) and (2.21):

$$i_{Disk} = i_{[a]} + i_{[b]} \quad (2.20)$$
$$\frac{i_{Disk}}{ne^-} = \frac{i_{[a]}}{4} + \frac{i_{[b]}}{2} \quad (2.21)$$

and,

$$ne^- = \frac{i_{Disk}}{\frac{i_{[a]}}{2} + \frac{i_{[b]}}{4}} \quad (2.22)$$

that leads to:

$$\%HO_2^-{}_{electronic} = \frac{i_{Disk}}{\frac{i_{[a]}}{2} + \frac{i_{[b]}}{4}} = \frac{4}{ne^-} - 1 \quad (2.23)$$

Since we are interested in the molar percentage of HO_2^- we have:

$$\%HO_2^-{}_{electronic} = \frac{\frac{i_{[a]}}{2}}{\frac{i_{[a]}}{2} + \frac{i_{[b]}}{4}} * 100\% = 4 - \frac{ne^-}{2} * 100\% \quad (2.24)$$

then using equations 2.19 and 2.22 we have

$$n_{e^-} = 4 * \frac{i_{Disk}}{i_{Disk} + \frac{i_{Ring}}{N}} \quad (2.25)$$

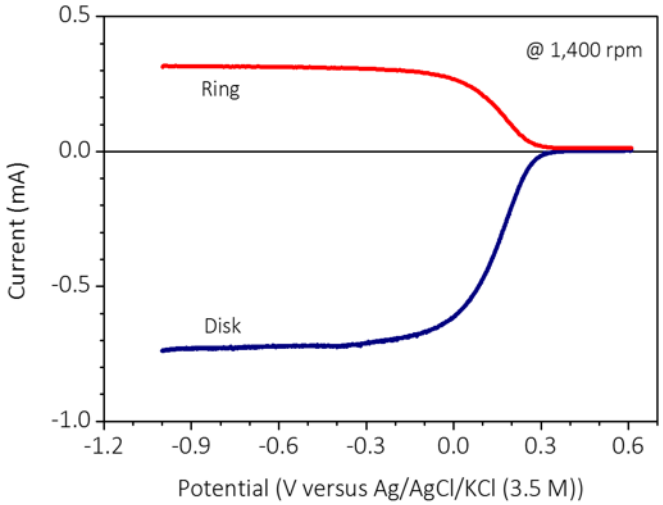

Figure 2.8: An example of RRDE curve obtained from the reduction of ferricyanide to quantify the collection efficiency.

2.7.2 CV Characterization

Cyclic voltammetry (CV) is widely used to study redox behavior. When a potential sweep in an increasing direction (oxidative direction) is applied (e.g. from **a** to **d** in Figure 2.9a), a positive voltammogram is obtained (e.g. from **a** to **d** in Figure 2.9b). During a positive scan**,** an anodic peak is formed at E_{pa} where the analyte is oxidized with a current of i_{pa}. As the analytes to be oxidized become depleted at point **c**, the anodic current decreases with higher potentials. On the other hand, when a potential is applied from **d** to **g** in Figure 2.9a, a negative scan of **d** to **g** (reduction) is seen in Figure 2.9b. A move from **d** to **g** results in reduction, with the cathodic current of i_{pc} where the analyte at the surface of the electrode, forming a characteristic peak potential of E_{pc}. The unstirred (stationary) solution makes the introduction of reactants and removal of products solely dependent on diffusion according to Fick's Law.[12,33,35]

2.7.3 Quantification of electrochemical active surface area (ECSA)

The ECSA can be quantified by assuming the area of electrochemical double-layer is proportional to the electrochemically active surface area. Experimentally, it is characterized in each solvent of cell operation (mostly in 0.1 M KOH) by cycling a CV within a narrow potential window free of a redox reaction (e.g. from -0.7 to -0.8 V vs. Ag/AgCl/KCl 3.5 M). This is to ensure to obtain a linear relationship between anodic and cathodic current by avoiding any artifact caused by Faradaic current.[44] In our study, the CV was mostly performed at different scan rates of 12 to 48 mV s^{-1} at intervals of 4 mV s^{-1} to acquire the slope and calculate the ECSA using the following equation:

$$ECSA = \frac{A*C_{area}}{C_{ref}} \quad (2.26)$$

where A is the geometric area of the sample, C_{area} is the areal capacitance, and C_{ref} is the referential areal capacitance of a flat electrode (80 μF cm^{-2}).[45]

To measure ECSA, a Ni-foam can be employed as the substrate for catalyst loading. Ni-foam is carefully cleaned using HCl solution (37 wt%) in an ultrasonic bath for 30 min, rinsed in a 1:10 ratio between ethanol and DI water, and later ultrasonicated for an additional 10 min. Once prepared, the catalyst slurry is drop-casted on Ni-foam.

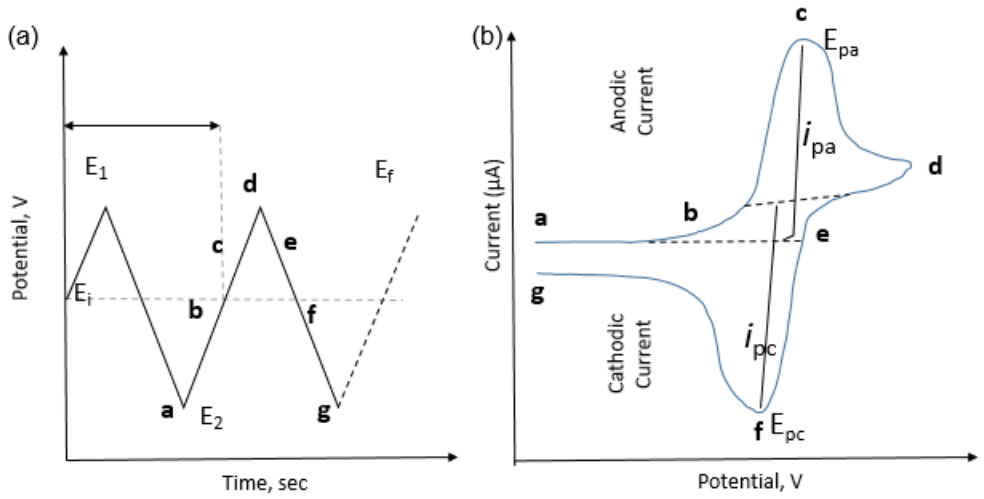

Figure 2.9: (a) Triangular potential waveform provided to the working electrode for CV measurements. (b) A CV curve obtained by the application of triangular potential waveform.

2.7.3 Assumptions for electrochemical testing

When analyzing RDE, RRDE and CV data, we assume: the deposited electrode material is evenly distributed on the surface, different samples of comparison have the same number of grams in each deposit, and the absence of a dipole concentration gradient in the bulk solution (electrolyte). To check for an even distribution of the catalyst, a microscope is used to make sure the deposition is both uniform and even as depicted in Figure 2.10. If the surface is non-uniform, then many ions will flow improperly over the glassy carbon causing the catalyst to underperform.[32] To make sure the same number of grams are deposited with every use of the pipette, deposits of the catalytic solution can be placed inside multiple thermogravimetric analysis (TGA) vessels. TGA is a method of analyzing the percentage mass change as both temperature and time increase. After the heating process using TGA, the amount of material left after evaporation of ethanol/water can be measured. Therefore, if the percentages of the catalytic material in the vessels are similar after increasing the temperature for all vessels, the catalyst is consistent in weight while depositing electrode material on a surface. To eliminate the effects of a concentration gradient caused by movement in the bulk solution, we can use temperature

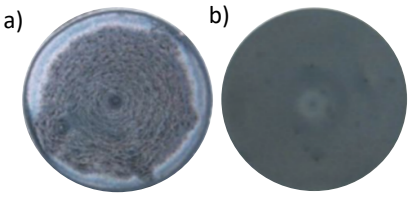

Figure 2.10: (a) A non-uniform and (b) uniform catalyst deposition on glassy carbon electrode examined under an optical microscope.

control devices and leveled surfaces for conducting experiments. Temperature control is imperative as basic kinetics suggest that an imbalance of temperature within the bulk solution causes an uneven flow of ions to the RDE, thereby creating unreliable results. Using the same principle, if the contents within the bulk solution are tilted, then an uneven flow of the catalytic material will create unreliable results as well. The use of distilled water is critical as tap (hard) water contains many ions such as sodium, potassium, calcium, magnesium and iron that could change the reactions occurring on the surface of the catalytic material. Therefore, making sure the resistance within the DI water machine is > 18 MΩ cm at 25°C and a total organic carbon (TOC) value below 5ppb will decrease the amount of hard water.[8,12] When using DI water, the use of fresh DI water is important. As time elapses, the CO_2 in the air will make the DI water more acidic, thereby changing the predicted flow of ions. This small difference (>0.5 pKa) may not seem significant, but when used for electrochemical testing, can affect the measured potentials of electrochemical reactions.

2.8 Introduction to Electrolyzers

Electrolyzers, also known as water-splitting devices, generate fuels which again can be used to generate electricity using a galvanic cell (i.e. fuel cells). Water splitting was demonstrated first by the Dutch merchants Jan Rudloph Deiman and Adriaan Paets van Troostwijk in 1789 using an electrostatic generator. An electrostatic generator induces water splitting by an electrostatic discharge between two gold electrodes immersed in water.[10] Later development by Johann Wilhelm Ritter, battery technology was "thought" to separate the produced gasses and by 1802, Ritter designed an electrochemical cell demonstrating this phenomenon.[46] Nearly a century later in 1888, Russian engineer Dmitry Lachinov industrialized the synthesis of hydrogen and oxygen via electrolysis,[11] and by 1902, more than 400 industrial water electrolyzers were in use.[47]

2.8.1 Catalysis of OER/HER

In an electrolyzer, hydrogen evolution reaction (HER) and oxygen evolution reaction (OER) occur and split water into hydrogen and oxygen. The two half-reactions (oxidation and reduction, respectively) and overall reaction are described in Table 2.

Table 2.1: Reactions of an electrolyzer

Reaction	Reaction Equation	E^0_{NHE} ($V_{vs.}$ NHE)
HER	$4H^+(aq) + 4e^- \rightarrow 2H_2$ (g)	(0 - 0.059 × pH)

OER	$2H_2O\ (l) \rightarrow O_2\ (g) + H_2\ (aq) + 4e^-$	(1.23 - 0.059 × pH)
Combined (OER + HER)	$2H_2O\ (l) \rightarrow 2H_2\ (g) + O_2\ (g)$	(1.23 - 0.059 × pH)

As is the case for fuel cell electrodes, the electrodes of an electrolyzer are required to have high surface area, electronic conductivity and stability/corrosion resistance.[48,49] Like any other electrochemical cells, electrolyzers need an overpotential to drive a net water splitting reaction. The thermodynamic potential for water splitting can be presented as ($E°$)

$$E° = \frac{\Delta G°}{nF} \qquad (2.27)$$

where n denotes number of moles of electron transfer and F is Faraday's constant. OER involves 4 moles of electron transfer per mole of O_2 whereas HER consumes 2 moles of

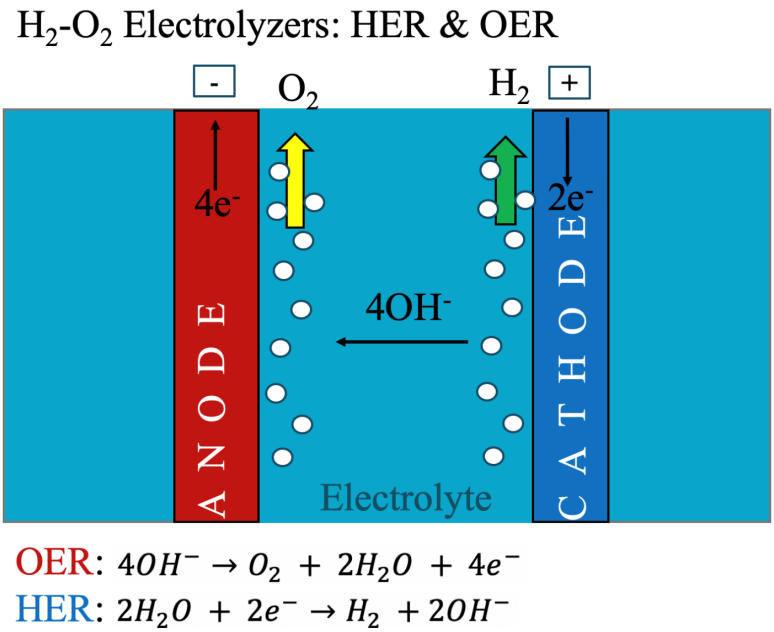

Figure 2.11: A simplified cross-sectional schematic diagram depicting the operation of a H_2-O_2 water splitting.

electron per mole of H_2. The overall voltage (E) to split water is:

$$E = E° + \eta_{OER} + abs(\eta_{HER}) + \eta_{ohmic} \qquad (2.28)$$

$E°$ is the thermodynamically determined reversible voltage for water splitting, which requires 237 kJ of electric energy to dissociate each mole of water; Gibbs free energy to form water is 237 kJ.

At standard conditions, the reversible voltage for oxygen electrolysis is 1.23 V. The total overpotential ($\eta_{OER} + abs(\eta_{HER}) + \eta_{ohmic}$) is the amount of voltage loss needed to drive the system. η_{OER} and $abs(\eta_{HER})$ are the activation overpotentials for OER and HER, respectively. η_{ohmic} is the ohmic overpotential. An external DC voltage bias, which is equal to the overpotential, is supplied to split water.

While both OER and HER are required for water splitting, OER (anode) is kinetically more sluggish as it necessitates a four proton-coupled redox processes and formation of two oxygen-oxygen bonds. Acidic and alkaline reactions of O_2 generation follows as seen in Figure 2.12.[50]

2.8.2 Electrochemical Characterization of Electrolyzers

The methods of characterizing overall kinetics and electron transfer route are very

Alkaline Medium

$$4OH^- \rightarrow 2H_2O + 4e^- + O_2 \qquad E^\circ = 1.230V$$

Acidic Medium

$$2H_2O(l) \rightarrow O_2 + 4H^+ + 4e^- \qquad E^\circ = 1.230V$$

Figure 2.12 OER in alkaline and acidic media.

similar to those for fuel cells. However, linear voltammetry for OER in an RDE setup is performed at an electrode potential relevant for OER (e.g. 1.3 – 1.8 V vs. RHE). In addition, the onset potential for OER is usually quantified at 10 mA cm^{-2} as seen in Figure 2.12.

The voltage difference between the onset potentials of ORR and OER (alternatively between the onset potential of OER and the half-wave potential of ORR) is used to discuss the bifunctional activity for both ORR and OER of the catalyst. Catalysts that perform both ORR and OER are applicable to metal-air batteries and unified regenerative fuel cells (URFC).[43]

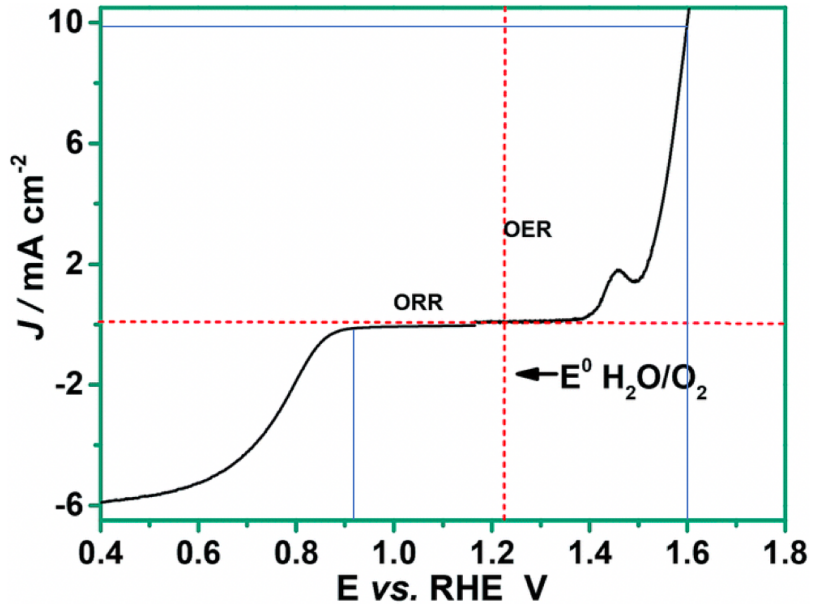

Figure 2.13: A typical LSV curve to show both ORR and OER.

2.9 Binding Conditions

As aforementioned in Chapter 1, for both ORR and OER, there are oxygen intermediates (O, OH and OOH), which are bound to the catalyst surface during the reaction. According to the Sabatier principle, the catalyst should bond reactants and their intermediates at an optimum bond strength for maximized catalytic activity; that is, not too weak to efficiently adsorb the reactant in each step, but not too strong to desorb the product. As depicted in the so-called volcano plot that displays the chemisorption free energies of intermediates (ΔG) vs. potential of either ORR or OER (Figure 2.13),[51] there is a clear correlation between the bonding free energy and electrocatalytic activity.

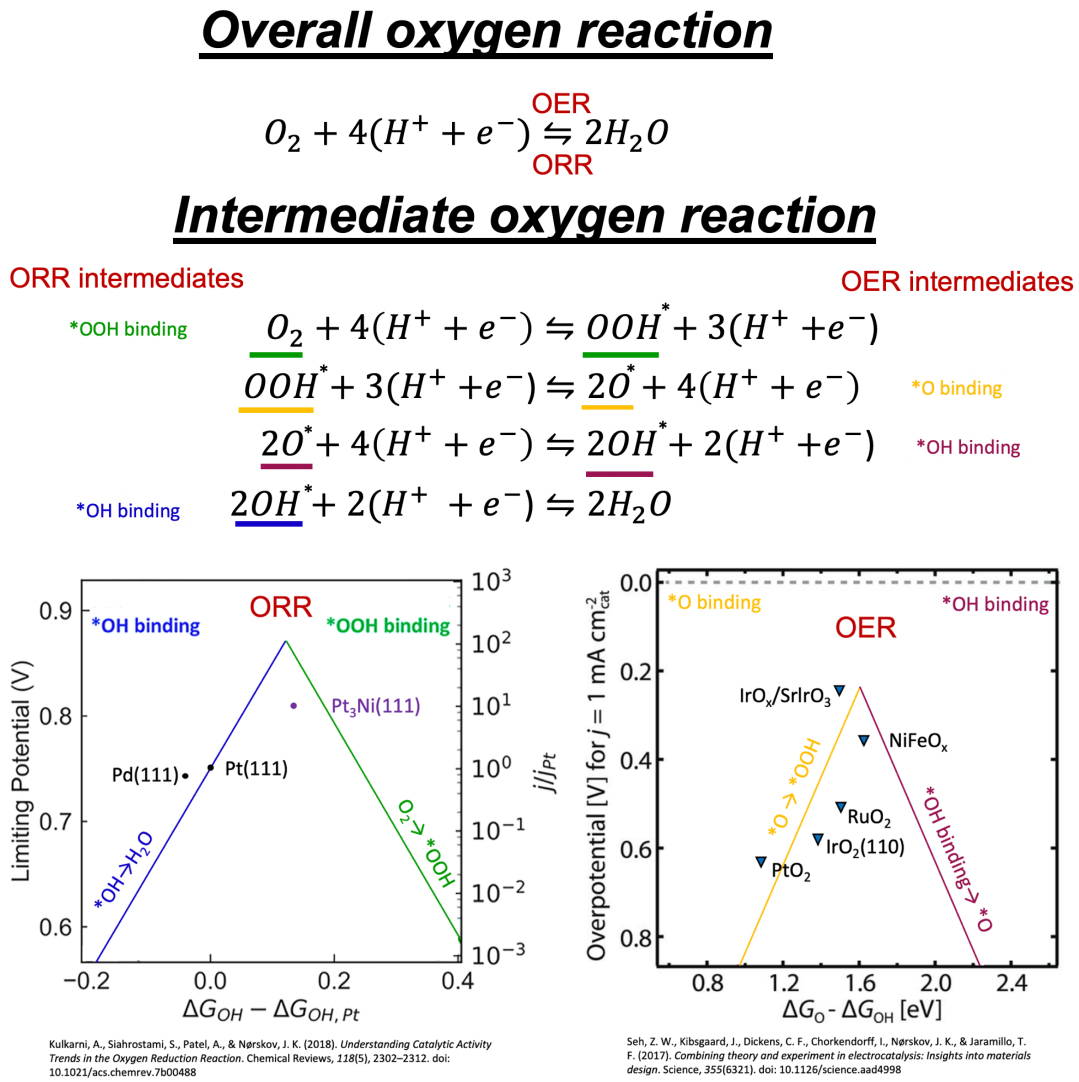

Figure 2.14: Overall oxygen reactions and its intermediates for ORR and OER. An overpotential must pass the theoretical activation barrier to produce electrons (form water through ORR) and use electrons (split water through OER). Second image includes volcano plots for both ORR (a) and OER (b) in terms of binding energy profiles (ΔG) for their respective intermediates (ORR: OH* & OHH* binding; OER: O* & OH* binding). When taking two of the best catalysts from each NCs (C-hG and T-pMOF), we can see an improvement in both potential and ΔG intermediates.

2.10 Materials Characterization

Researchers who work within the interdisciplinary field of materials science often piece together the form and function of materials.[52] This often requires examination for material's characteristic using high resolution magnification especially for energy storage properties at the nanotechnology level.[53] The next few sections will discuss some of the materials characterization devices used for energy storage materials.

2.10.1. TEM

The TEM (transmission electron microscope) produces images at higher resolution than light microscopes, by generating electrons to interact with ultra-thin

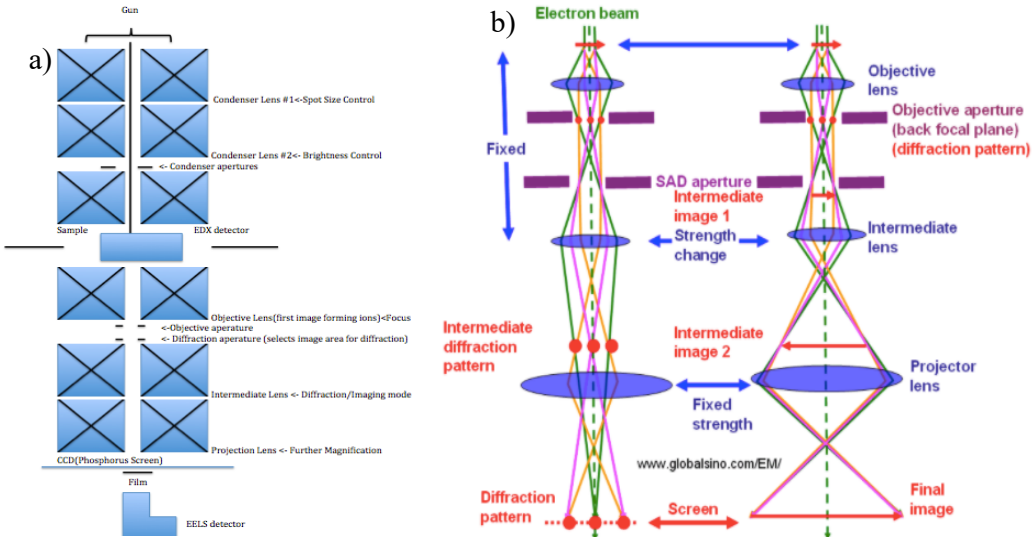

Figure 2.15 (a) Schematic of the transmission electron microscope b) comparison lens conditions between TEM imaging mode and TEM diffraction. Figure 2.15b is from the Practical Electron Microscopy and Database.

specimens resulting in the small de Broglie wavelengths of the generated electrons.[54]

2.10.1.1. TEM procedures

Beginning at the top of Figure 2.15a, the gun provides an intense beam of high-energy electrons. Specifically, a field emission electron gun creates a strong electric field to extract electrons from a filament to form an electron beam that travels down the column, passing through the magnetic fields of the first and second condenser lenses. The first condenser lens controls the approximate size of the beam, while the second condenser lens controls the sample area with which it interacts. A more condensed beam results in less interaction area and a higher beam intensity in that area. After the beam passes through the condenser lenses the aperture is used to improve resolution by excluding electrons travelling further off the optic axis which tend to contribute the most to image aberrations that reduce resolution. The beam then encounters the specimen of <100 nm thickness, where electron scattering occurs. Portions of the sample oriented at the Bragg condition or with greater mass-thickness scatter more electrons, leading to contrast in the resulting image. The objective lens then collects electrons from the

sample to form the first magnified image. In standard TEM bright-field imaging, an objective aperture placed between the objective lens and its image (in the objective lens back focal plane) excludes scattered electrons from contributing to the image. Bragg-diffracting, thick areas and areas with higher atomic number elements appear darker in the image, as a result.

In standard TEM dark-field imaging, the objective aperture excludes unscattered electrons, so that Bragg-diffracting, thick areas and areas with higher atomic number elements appear brighter. In high-resolution TEM, an objective aperture is not used, so that unscattered and Bragg-scattered electrons recombine to form a phase contrast image based on phase differences introduced by the scattering process and lens system. The intermediate lens further magnifies the objective lens image and its current can also be adjusted to magnify the sample diffraction pattern formed by the objective lens (found in the objective lens back focal plane) rather than its image. The projector lens system then provides further magnification for the final image, which can be observed on a phosphorescent screen or collected by a charge-coupled device (CCD) camera.

Some instruments are equipped with an electron energy loss spectrometer to exclude from the image electrons that have undergone inelastic collisions in the sample and have different focal planes from elastically scattered electrons, improving image resolution. Describing each component of TEM is important because knowing the nature of TEM can provide solutions to problems that may arise while imaging. For example, if a beam light fails to make a perfect circle, then an "unbalanced" condenser stigmator is more likely at fault.

Energy-filtered transmission electron microscopy (EFTEM) imaging techniques can utilize properties of loss spectrum energy to increase contrast, reduce chromatic aberration, and increase depth perception. Contrast is made with images and diffraction patterns when the TEM removes inelastically scattered electrons, which can produce a fog-like image. Mapping, using a form of EFTEM, creates an elemental/chemical maps at nanometer resolution by forming images with inelastically scattered electrons. Some types of mapping include a 2- and 3-window elemental mapping/jump-ratio to create fine structures. Please refer to Figure 2.15b for how lens changes between TEM imaging and TEM diffraction can occur.[54]

2.10.1.3. TEM Theory

As mentioned before, TEM can image samples at a high resolution. When an electron of charge e passes through a potential difference V, its kinetic energy will be given by the energy of the field

$$\frac{mv^2}{2} = eV \tag{2.29}$$

where m is mass and v is velocity and eV is energy in electron volts. Then using de Broglie's wavelength equation and relating it to kinetic energy we have

$$\lambda = \frac{h}{p} = \frac{h}{mv} \tag{2.30}$$

where λ is the de Broglie wavelength, h is Planck's constant and p is the momentum of the particle. Combining equations 2.29 and 2.30, we have

$$\lambda = \frac{h}{(2meV)^{\frac{1}{2}}} \tag{2.31}$$

However, due to the relativistic effects of electrons the incorporation of relativistic kinetic energy E_k is needed, therefor we use

$$E_k = mc^2 - m_0c^2 \tag{2.32}$$

where m_o is an electon's rest mass, and c is the speed of light. Noting that E_k is equal to eV and using equation 2.32 we have

$$\lambda = \frac{h}{[2m_0eV(1+\frac{eV}{2m_0c^2})]^{\frac{1}{2}}} \tag{2.33}$$

TEMs typically operate at an accelerating voltage of 200 kV and wavelength of ~2.51 pm, therefore, the electron beam can reach the theoretical resolution limit smaller than atoms.[55,56]

2.10.1.4. TEM Aberrations

An ideal TEM is able to provide a perfect image of a sample, however, this is not always the case due to aberrations (spherical and chromatic) and astigmatism. Rays, that pass through a spherical aberrated lens at a high angle to the optic axis, are focused closer to the lens than rays passing along (or at a smaller angle) to the optic axis create spherical aberrated lens. As a result, the angle rays that are incorrectly focused rays produce a "smearing" in the lens as seen in Figure 1a. Another way of describing spherical aberrations is that electrons passing through the periphery of a lens are refracted more than rays passing through the center of a lens. The electrons, therefore, do not reach a common focal point. If we block, using a suitable aperture in the back focal plane, the rays scattered to a high angle then an image without "smearing" will form as depicted below Figure 2.16a.

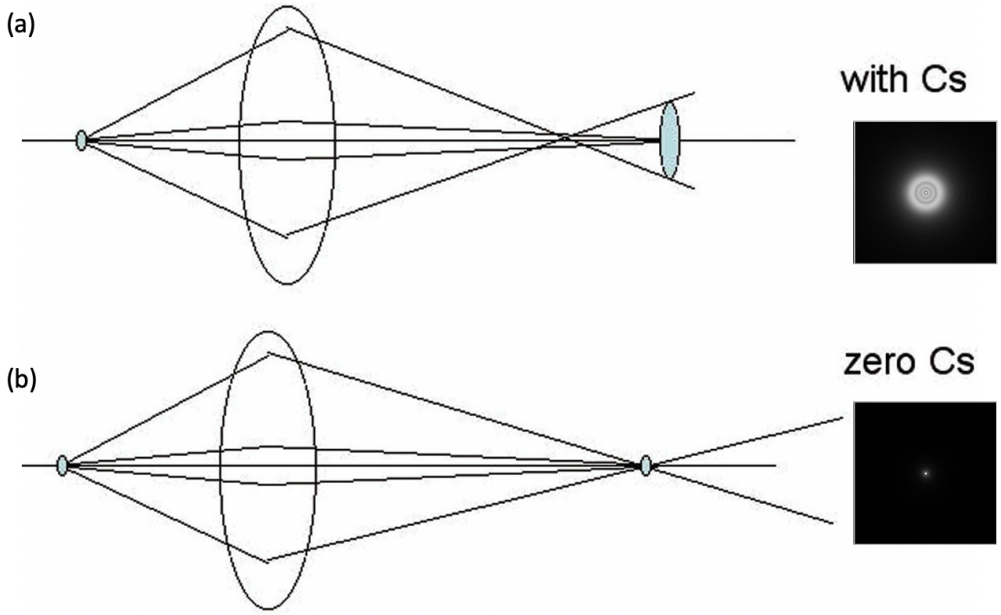

Figure 2.16: Depicted above includes standard electron lens with spherical aberrations. (a) Rays at different angles to optic axis are focused on different points. TEM image shows the effects of spherical aberration (b) By blocking scattered rays, the spherical aberration is minimized with all rays being

focused on the same point. *Crispin Hetherington, Materials Today. 2004, 7:12.*

Spherical aberration (C_s) where the diameter of the distorted disk of intensity d_{sph} is given as

$$d_{sph} = \frac{1}{2} C_s \beta^3 \tag{2.34}$$

where β is the collection semi angle of the lens.

Another common aberration is known as chromatic aberration (C_c) that can cause a disk rather than ideal point for rays to be focused. However, unlike spherical aberrations, chromatic aberrations are caused by electromagnetic radiation of different energies converging at different focal planes. Chromatic aberration diameter of the disk (d_{chr})can be expressed as

$$d_{chr} = C_c \frac{\Delta E}{E_0} \beta \tag{2.35}$$

where ΔE is the energy loss. E_0 the incident energy and C_c is the chromatic aberration coefficient of the lens. If the ΔE is large, the image will be blurry as seen in the C_c TEM image compared to Little C_c in Figure 2.17a.

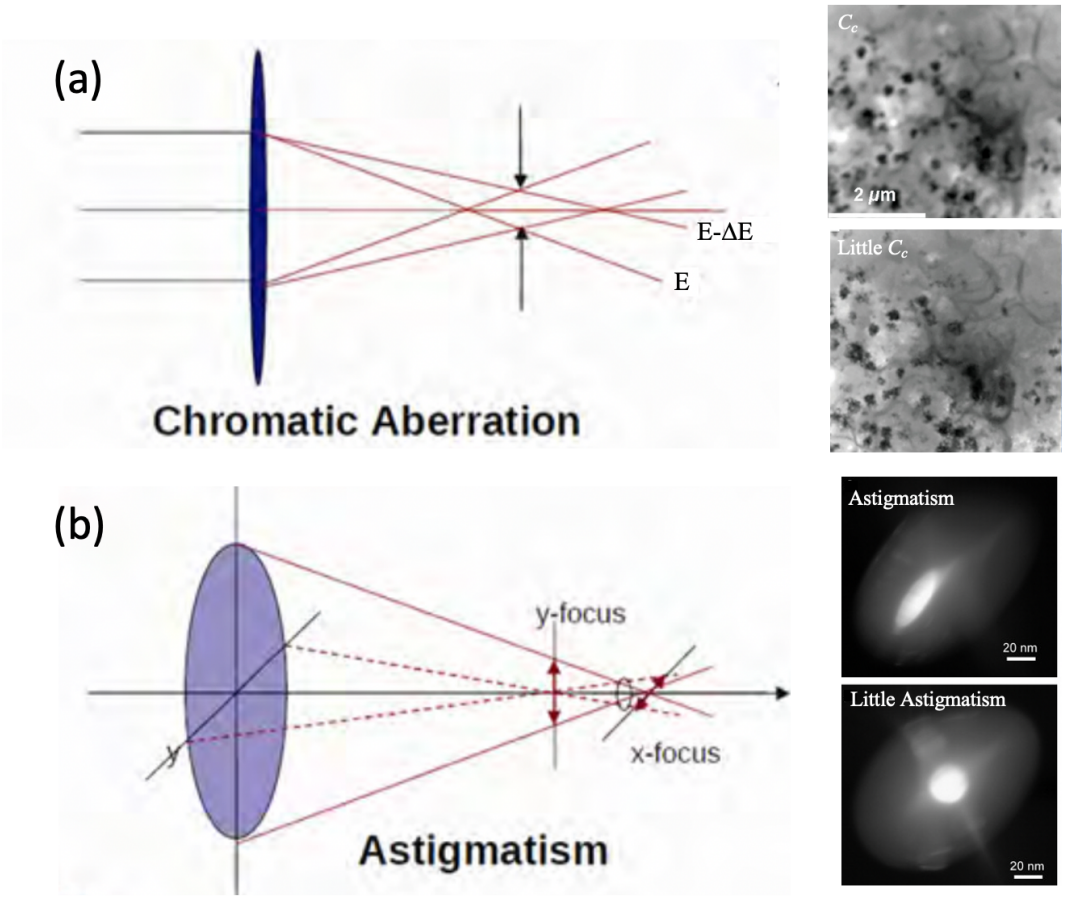

Figure 2.17: Schematic of (a) Chromatic aberration as a result of differential focusing of electrons of varying energies (b) Astigmatism effects as a result of non-isotropic directional focusing. Dominik Green et al. Biomedical Applications of Biophysics. 2010, 7:155-183 and Q. Xing et al. Ultrmicrocopy, 2008, 4:109

and Rafel Dunin-Borkowski et al. Cambridge University Press 2016, 434-455.

Another type of aberration of TEM called astigmatism. Inhomogeneities in polepieces, machining errors, asymmetry in lens winding, and dirty apertures can lead to lens that is astigmatic rather cylindrical. Astigmatic means that electrons diverging from a point will produce two separate line foci at right angles to each other (y-focus vs. x-focus). The TEM image of Figure 2.2b labeled Astigmatism has a distorted x-focus compared to the Little Astigmatism TEM image.[57]

2.10.1.2. HRTEM

HRTEM has the ability to image atomic lattices, and position of lattice fridges, for the purposes of the dissertation, through an analysis of the atomic planes in samples. This is very helpful for thin film metal oxides whose crystallinity can be determined based upon the spacing of these crystal lattice structures. Although useful, caution when interpreting HRTEM images is necessary as the image can be inaccurate in terms of its d-spacing. Also, if the sample is too thick, the image resolution decreases and aberrations in the astigmatism, objective lens, defocus can occur. For this reason alone, TEM diffraction and/or XRD will be tied with a catalysts facet in Chapters 4,5, and 6 of this dissertation. Also, please refer to the XRD section for more on how crystallinity can be determined.[58]

2.10.1.2. EDX

Energy-dispersive X-ray spectroscopy relies on the interaction of x-ray and excitation sample to analyze the elemental or chemical composition of a sample. Each element has a “finger-print” electromagnetic emission spectrum. Some of the limitation of EDX include element detection for heavy elements. Modern EDX detectors have ultrathin or windowless detectors which can lead to a limited energy resolution of the EDX detector, thereby leading to a peak-overlap problem. Also, finite time for the detector to process each X-ray can create a dead zone where another X-ray cannot be recorded. If the arrival rate of X-rays is large, then no X-rays will be recorded. Therefore, improving a detectors energy resolution can reduce peak overlapping.[54,59]

2.10.1.2. SAED

Selected area electron diffraction (SAED) is an experimental technique to obtain a diffraction pattern in the reverse space of lattice planes. This is often used to determine d-spacing of crystal planes, please refer to the XRD materials section in this Chapter. In other words, a selected area is used to obtain a diffraction pattern in which the reciprocal lattices are projected, with lattice reflections shown as sharp diffraction spots.[54]

A diffraction experiment uses a known crystalline sample (gold polycrystalline standard), an alignment of TEM, an area of diffraction aperture (SAD), and under diffraction mode. When placing the gold polycrystalline sample at the eucentric height, a diffraction pattern is collected to determine the camera length. Please note that the eucentric height is the position, within the objective lens, on a reference plane. With the camera length (λL), the d-spacing can be determined as

$$Rd = \lambda L \quad (2.36)$$

where R is the distance of the diffracted beam from the central, non-diffracted beam on the image plane, L is the distance between the image plane and sample. The equation above is determined by using Bragg's law assuming small scattering angles

$$n\lambda = 2d \sin\theta \Rightarrow (n = 1) \quad (2.37)$$

$$\lambda = 2d\theta \quad (2.38)$$

and that

$$\frac{R}{L} = \tan\theta \sim 2\theta \quad (2.39)$$

Camera length can be determined using a standard (gold polycrystalline sample) inside the TEM and measuring the R distance from the resulting diffraction pattern.[60,61]

Limitations

Limitations and errors can arise from sample preparation and image distortions/irregulates. A sample primary particle must be dispersed in a monolayer on a substrate, otherwise, the beam may not transmit through it. Also, without proper care of the TEM grid, contamination such as oils render the TEM analysis useless for high resolution TEM (HRTEM).[62,63]

2.11.3 FT-IR

Infrared spectroscopy studies the interaction of matter with infrared light. Light, having dual nature of a particle (electric) and wave (magnetic), move together in perpendicular planes through space. The electric vector interacts with molecules while the magnetic vector interacts with light. The wavenumber of the magnetic vector is the reciprocal of a wavelength that measures the number waves that exist in a centimeter. The wavenumber of the magnetic vector can be defined by its energy where E is light energy, c is the speed of light, h is planck's constant, and W is wavenumber

$$E = hcW \quad (2.40)$$

where a high wavenumber light has more energy (infrared) than a low wavenumber light.[64] This infrared energy (infrared radiation) is present in all matter that is above 0 kelvin. When infrared radiation is absorbed by matter, the chemical bonds within the material begin to vibrate. Chemical structural fragments within molecules, known as functional groups, absorb infrared radiation in the same "wavenumber range." This absorption can be tied to the structure of the unknown molecules to be later identified from an infrared spectrum. Beer's Law, which relates concentration absorbance can be defined as

$$A = \varepsilon l c \quad (2.41)$$

where A is absorbance, ε is absorptivity, l is pathlength, and c is concentration. Using these principles, a plot of infrared radiation intensity vs. wavenumber can be plotted.[65]

Fourier-transform infrared spectroscopy (FTIR) is used to understand carbon-based materials in a solid, liquid or gas. An interferometer takes a beam of light (400-4000 cm^{-1}) and splits it into two beams, and makes one beam of light travel a different distance than the other. This difference between the two beams is called the optical path difference (optical retardation) δ. These beams go into the Michelson interferometer. The Michelson interferometer has a configuration of mirrors that either blocks or transfers a wavelength. More specially, light from a black-body radiator (infrared source) is directed towards a beam splitter in which half of the light is refracted while the other is transmitted to a moving mirror. The Michelson interferometer has four parts. The first part contains the source of infrared light, the second part contains the stationary mirror, the third part contains a moving mirror, and the fourth part is the opening for the sample placement. The intersection of the four parts (Figure 2.18) is the beam splitter that transmits half of the radiation that impinges on it and reflect nearly half. The light transmitted by the beam splitter strikes the fixed mirror and reflects onto the moving mirror. These two beams recombine towards the beam splitter and leave the interferometer to the fourth part to interact with the sample and strikes the detector.[66]

2.11.3.1 Optics

If the distance by two beams (the moving mirror and fixed mirror beams) are the same, this means there is zero path difference (ZPD). If the beams have a difference, the mirror displacement is defined as Δ. Since the moving mirror and fixed mirror have an optical retardation, with the moving mirror light length being longer than fixed, we can define the extra distance as 2Δ and define the following

$$\delta = 2\Delta \tag{2.42}$$

If a monochromatic light source has a wavelength of λ, the beams have recombined from the beam splitter, and they are both in phase then their (recombined beams) crests and tough will overlap. Though their amplitudes add, the constructive inference causes an intense light beam to leave the interferometer and allows it to equal a multiple λ.

$$\delta = n\lambda \tag{2.43}$$

where n= 0,1,2,3…

When destructive interference takes place the intensity of the light beam is less due to the "half wavelength" adding, which provides the following equation

$$\delta = (n + \tfrac{1}{2})\lambda \tag{2.44}$$

If the mirror is moved at a constant velocity, the detector measures the intensity in a cosine wave, and modulated light beams are denoted by the number of times per second they switch between light and dark, we can describe

$$F_v = 2VW \tag{2.45}$$

where F_v is the modulation frequency, V is the moving mirror velocity i, and W is the wavenumber of the light in the interferometer. Once the light leaves the interferometer (part four) passes through the sample compartment and focused on the detector. The detector takes signal and has the Fourier transform simply calculate the infrared spectrum from the sum of cosine waves in the interferogram. Though the Fourier transform is not

rigorously correct, it allows for the optical path length and collects finite number of datapoints to obtain an interferogram (truncation).[67]

2.11.3.2 Bond Stretching and Bending

Lightly touched upon, the exact reason why molecules can be detected by FT-IR is due to their bond stretching and bending. This, consequently, can also be used to distinguish molecules. Depending on the wavenumber absorption, bond stretching and bending depends on (1) bond strength and (2) masses of the atoms sharing the bond. The impact of these two factors can be explained using Hooke's Law, enabling us to approximate frequency of vibration for a bond between two atoms of mass

$$\upsilon = (\frac{1}{2\pi c})(\frac{f}{m_{red}})^{\frac{1}{2}} \quad (2.46)$$

where is υ vibration, c is speed of light, f is the force constant (bond strength), and m_{red} is the reduced mass of the system (treating both atoms as one system). This means, smaller atoms give bonds that vibrate at higher frequencies, a higher wavenumber of absorption. For example, a carbon attached to a hydrogen provides a larger wavelength value (~3000 cm^{-1}) than chloride (~700 cm^{-1}). This equation also means, a large force constant will cause the molecule to vibrate at higher frequencies, thereby, corresponding to a higher wavenumber of absorption. For example, a carbon triple bonded to a nitrogen will have a larger wavenumber (~2200 cm^{-1}) than a single bond (~1100 cm^{-1}). Another way to distinguish molecules includes the effects of hybridization states on wavenumber absorption. A C-H bond that has a hybridization that has C_{sp}-H bond produces the highest (~3300 cm^{-1}) compared to a C_{sp3}-H (~2900 cm^{-1}) in terms of wavenumber. *sp* orbitals have more *s* character than other hybridized atomic orbitals and will therefore more closely resemble *s* orbitals. The electron density of *sp* orbitals is closest to the nucleus. Therefore, comparing the shapes of other hybridized atomic orbitals, the sp^3 bond length is larger than the sp^2 bond length. A smaller bond length translates to a stronger bond, therefore C_{sp}-H will have a larger wavelength number.[68]

Limitations

FT-IR cannot detect atoms or monatomic ions. Single atomic entities contain no chemical bond nor posses any vibrational motion and therefore, not absorbed by infrared radiation. FT-IR uses a single beam in which the background spectrum, an accumulation of instrument or the environment, can lead to artifacts being misinterpreted and perhaps, mask sample absorbance. Finally, sample preparation (depending on the techniques used) plays a large part on making sure certain spectra are distinguishable.[69]

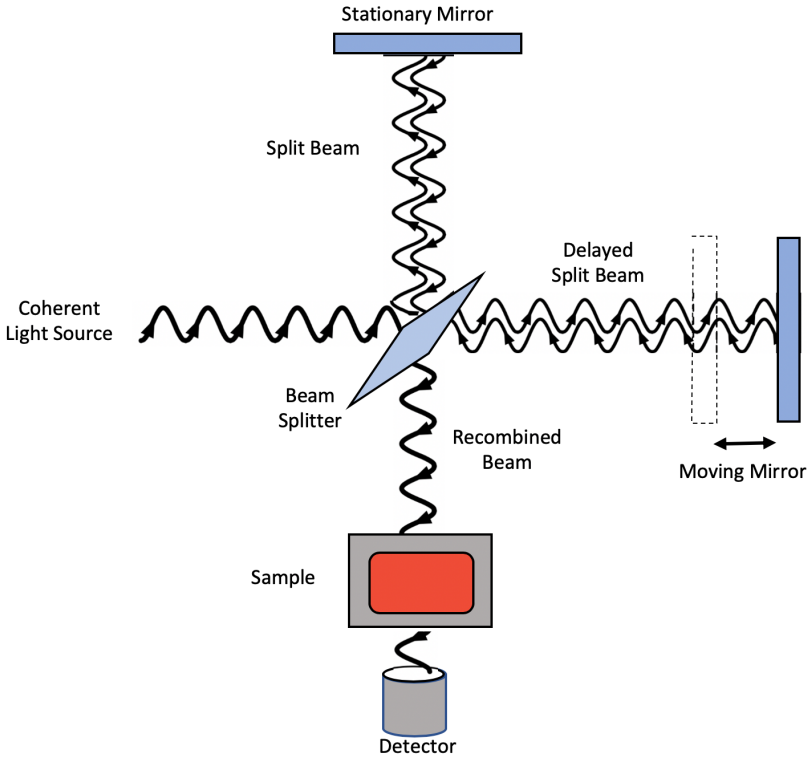

Figure 2.18: Schematic of the Michelson Interferometer.

2.12.4 XRD

2.12.4.1 XRD Spectra

X-ray Diffraction (XRD) can determine crystallographic structures for materials using X-ray beams. The collision of incident x-rays and core electrons causes two outcomes to occur: Compton or Thomson scattering. Compton scattering is when the x-ray collision with the electron yields a smaller photon energy (result of inelastic scattering), thereby increasing the wavelength. Thomson scattering occurs when the x-ray is elastically scattered, by a free particle, thereby keeping the same wavelength. Please note, the incident x-ray's energy is greater than the valence electron's energy. When using Thomson scattering, we can use what is known as the Braggs law where the materials periodic spacing, scattering angle (related to periodic spacing), and X-ray wavelength are related. The derivation is as follows, if we assume two parallel planes denoted as A and B are separated by a distance d and that, two ray vectors s/λ and s_0/λ of the same wavelength incident upon the aforementioned planes, the path difference between two beams should be equal to $s\text{-}s_0/\lambda$ vector (See Figure 2.19).

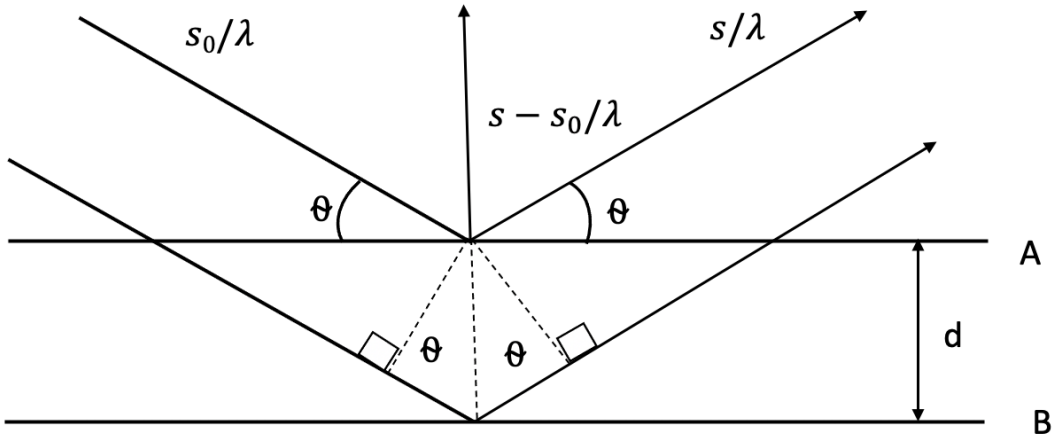

Figure 2.19: Diffraction of X-rays in accordance with Bragg's Law where s_0/λ is the incident wave vector and s/λ is the scattered wave vector.

However, before further discussion can be made on how Thomson scattering provides crystalline information, an explanation of crystal lattice structure is needed.

Crystalline materials are made of repeating basic structures called unit cell. Unit cells help describe planes using Miller indices to specify directions and planes in crystals. Notations often used include

- (h,k,l) represents a point
- [hkl] represents a direction
- <hkl> represents a family of directions
- (hkl) represents a plane
- {hkl} represents a family of planes

as demonstrated in Figure 2.20 below.

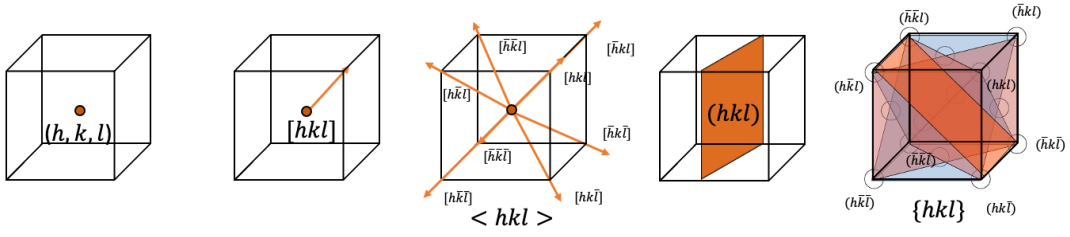

Figure 2.20: Notations often used for miller indices.

A plane denoted as (h k l) plane, that is closest to the origin, will have intercepts of

$$\frac{a_1}{h}, \frac{a_2}{k}, \frac{a_3}{l}$$

where a_1, a_2, and a_3 are the magnitudes. Use of these describing Miller indices is very useful as each plane within a family are spaced equally and contains the same density of lattice points. The spacing (d_{hkl}) can therefore be determined as

$$d_{hkl} = \frac{a}{\sqrt{h^2+k^2+l^2}} \quad (2.47)$$

where a is a constant.

Going back to Thomson scattering, the use of vectors can be difficult, therefore a switch from reciprocal space from normal space allows the vector to be defined in terms of Miller indices which is perpendicular to the hkl family of planes, $\mathbf{H}_{hkl}$. $\mathbf{H}_{hkl}$ is inversely related to the d-spacing as seen

$$d_{hkl} = \frac{1}{|hb_1+kb_2+lb_3|} = \frac{1}{|\boldsymbol{H}_{hkl}|} = \left|\frac{\lambda}{s-s_0}\right| \quad (2.48)$$

where b_1, b_2, and b_3 are reciprocal space vectors.

Please note, not all plane structures give a Bragg reflection. A prediction of which family will give us reflections can be done by calculating the structure factor. This is dependent on the atomic position of atoms within the unit cell. The structure factor can be thought as the scattering amplitude for any given plane.

When analyzing thin films, a specular scan is used to observe these reflections peaks. A sample, placed at an angle of ω (kept at half of 2θ), can be consistently rotated allowing x-rays to sufficiently scatter so that most of the crystallographic phases are detected.[70]

2.12.4.2 XRD Experimental

X-rays are generated from a x-ray tube (usually copper) and limited by the anode. The potential applied to the anode can cause melting, therefore, cooling is used to avoid anode melting. Electrons are then essentially boiled off the cathode and accelerated through a strong electric potential of ~50 kV. The electrons are then collided with the metal plate thus emitting bremsstrahlung. Bremsstrahlung are then filtered to a single wavelength (monochromatic) and collimated in a single direction towards the crystal. The intensities of the scattered x-rays are then collected with a photographic film or charge-coupled device image sensor. After this, standards are used to determine the sample's , crystallinity based upon the spectrum provided. We can also quantify the ratio between two crystals (e.g anatase and rutile) and quantify the particle size.[71]

2.12.4.3 Quantification of mass ratio

While using XRD, we can also measure the mass ratio between two phases (e.g. anatase and rutile phase of TiO_2) samples can be calculated from the relative intensities of the strongest diffraction peaks of the two phases ((101) peak of anatase and (110) peak of rutile) from the following equation:

$$f_r = \frac{1.26\, I_r}{I_a + 1.26\, I_r} \quad (2.49)$$

where f_r is the mass fraction of rutile, and I_a and I_r are the intensities of anatase (101) and rutile (110) diffraction peaks.[72]

2.12.4.4 Quantification of particle size from XRD

From the broadening of a diffraction peak, the average size of sub-micrometer particles can be quantified by the Scherrer equation:

$$d = \frac{0.9\lambda}{\beta cos\theta} \tag{2.50}$$

where λ is the beam wavelength (1.78897 Å; Co Kα radiation), β is the full width at half maximum (FWHM) and θ is the Bragg angle.[73]

2.12.4.3 Limitations

As a crystal's repeating unit cell becomes larger/complex the XRD crystallography decreases in resolution over a given number of observations. Hence, to fully quantify the crystal structure, XPS is needed to confirm such crystals.[60]

2.13.5 XPS

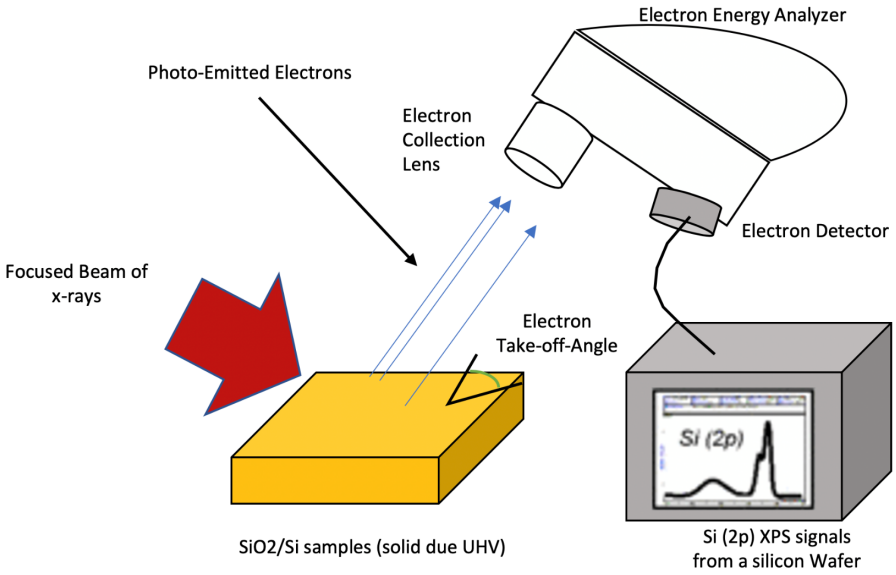

Figure 2.21: Schematic of XPS.

X-ray photoelectron spectroscopy (XPS), also known as Electron Spectroscopy for Chemical Analysis (ESCA), has been used to quantitatively measure the elemental composition of a surface. This surface-sensitive spectroscopic technique allows the analysis of metal and semiconductor surfaces using a focused monochromatic Al Kα x-

ray (1486.7 eV) source for excitation and a spherical section analyzer in a Mu-metal shielded stainless steel ultra-high vauum (UHV) chamber. The monochromatic AlKα x-rays obtained by diffracting and focusing a beam of x-rays onto a thin disc of crystalline-quartz in the <1010> direction. The beam of x-rays is focused onto the sample in which photo-emitted electrons (<1.5 kV) escape from the top of sample and thus analyzed by their electron binding energy (Figure 2.18). Theoretically, the binding energy of the photo-emitted electron is equal to the energy of photon (hν) minus the sum of kinetic energy of the electron measured and work function (ϕ) which is dependent on both the spectrometer and material.

$$\mathrm{BE} = h\upsilon - KE - \phi_s \tag{2.51}$$

Thus, by measuring the counts (parts per thousand) vs. binding energy we can characterize the sample from the top ≤3nm.[74]

When working with metal oxides, the effect of electronegativity is large as result of the electronegative oxygen atoms. Electronegative atoms not only attract the electron's host atom, but an additional electron. Therefore, the required energy to emit an electron from a host atom increases resulting in the binding energy for the host atoms to be shifted to a slightly higher energy. This is important as the spin-orbital coupling in XPS, all orbitals except s yield a doublet with two possible states.

2.13.5.1 Deconvolution of cerium based XPS

Ce 3d: By taking the method detailed by Maslakov et al.[75] the mole fraction of Ce^{3+} and Ce^{4+} can be quantified from Ce $3d_{5/2}$ peaks using the following equation:

$$f(Ce^{3+}) = \frac{1-a_0\cdot\frac{3}{2}\frac{I(u''')}{I(v)+I(v')+I(v'')}}{1-\frac{3}{2}\frac{I(u''')}{I(v)+I(v')+I(v'')}} \text{ and } f(Ce^{4+}) = 1 - f(Ce^{3+}) \tag{2.52}$$

$$\text{where } a_0 = \frac{I(v)+I(v'')}{\frac{3}{2}I(u''')} \tag{2.53}$$

I values (unit: a.u.) are obtained by taking the area under each spectrum.

O 1s: *I* values (unit: a.u.) are obtained by taking the area under each spectrum and tabulated below. The fraction of each bonding was quantified simply by:

$$f(\text{O-Ce}^{3+}) = \frac{I(O-Ce^{3+})}{I(O-Ce^{4+})+I(O-Ce^{3+})} \text{ and } f(\text{O-Ce}^{4+}) = 1 - f(O-Ce^{3+}) \tag{2.54}$$

Limitations

Like the other techniques, sample preparation can cause limitations when analyzing the material. Sample flatness is very important as height variations will cause the angle to vary so much, the angular dependence of the intensity ratio of the overlayer and substrate signals is no longer constant. To help with this the use of a silicon wafer is utilized as a substrate to deposit an ethanol based colloidal; ethanol is used instead of water as the surface tension for ethanol is low, thus the colloid can spread more evenly. Another source of error due to sample preparation is the lack of removal of various gases (O_2, CO) and liquids (water, solvents, alcohols, etc.) that will cause the chemistry and

morphology of the top surface to change continuously as gases/liquids are volatile in a vacuum chamber, thus causing intensity ratio to no longer be constant.[76]

2.14.5 Titration

To better compare chemical concentrations quantitively, scientists use a technique called titration. More specifically, the titrant a reagent (titrant) is prepared, with a known concentration and volume, and reacted in solution with analyte (to be analyzed substance) to determine the concentration. This technique, if applied properly, can also be used to determine the concentration of functional groups. The following includes a procedure and calculation to determine certain functional groups.[77]

2.14.5.1 Quantifying epoxides

When working with graphene oxide, a suppression of other groups before titration measurement is needed to prohibit false positives:

To suppress hydroxyl group: Add hydrogenation (water) + methanesulfonic acid

To suppress carboxyl group: Addition of NaOH + methanol iodine

In a conical flask with a ground glass stopper, add 10 ml of 33 wt% HCl and acetone in a flask. Add 3-5 drops of indicator (methyl violet). Using a Burette pipette flask, continue to add NaOH until color appears.

Measure the values:

$$\text{Epoxide value } (EV) = \frac{((V_0 - V) * N)}{(W * 10)} \tag{2.55}$$

V_0: Volume of NaOH with no dissolved sample

V: Volume of NaOH with dissolved sample

N: Concentration of NaOH

W: Mass of sample

2.14.5.2 Quantifying carboxyls

Weigh 0.5 – 1.0 g into a 200 ml glass stopper flask. Add Murexide as the metalchromic indicator with 100 ml of acetone. Slowly add NaOH.

$$\text{Carboxyl value } (EV) = \frac{((V_0 - V) * N)}{(W * 10)} \tag{2.56}$$

V_0: Volume of NaOH with no dissolved sample

V: Volume of NaOH with dissolved sample

N: Concentration of NaOH

W: Mass of sample

2.14.5.3 Quantifying hydroxyls

Weigh 0.5 – 1.0 g into a 200 ml glass stopper flask. Then 5 g of Toluene diisocyanate and 250 ml of anhydrous acetone. Add three drops of Dipropyltryptamine. This was reacted at 60 °C. During this reaction, 10 ml solution was drawn off and added into an iodine flask once every hour. The extracted solution is then cooled to room temperature and reacted with 0.4996 g n-butylamine for 15 – 20 min at room

temperature. The resultant solution had bromocresol green added to it. Then in the iodine flask, titration with hydrochloric acid was done until a slight yellow was seen.

$$\text{Hydroxyl value } (EV) = \frac{((V_0 - V) * N)}{(W * 10)} \quad (2.57)$$

V_0: Volume of NaOH with no dissolved sample
V: Volume of NaOH with dissolved sample
N: Concentration of NaOH
W: Mass of sample

Limitations

Due to the pose of human error the mass of the sample must be greater than 3 grams and the value of the functional group must be greater than 3-5% of the sample weight. Therefore, any substance smaller than the quantities mentioned above cannot be quantified using titration. Other factors that can influence readings include temperature, balance (weighing error), and handling. It is therefore important the experiment should be conducted at the same time and conditions.

2.11: Reproducibility

Reproducibility is the ability to which consistent results are obtained after repeated experimentation. Checking this allows scientific results to not only be verified but increases the chance of reusing the results or extending the work. To ensure the reproducibility of a scientific result, detailed documentation and specification of the involved scientific work is needed. The following section will explain how reproducibility was checked for this Dissertation.

2.11.1 Electrochemistry Reproducibility

To test the reproducibility of catalyst, at least seven batches were prepared for each type of sample. Each batch usually produces three samples worth for electrochemical testing. Before electrochemical characterization, each sample is cycled at least fifty times where the first ten is to activate the sample while the rest is to determine the extent of variability. Each sample is used for one set of fifty testing, ten LSV cycles (400-1600 rpm), and five RRDE cycles within a predefined potential range. The half-width is used to determine the variability for each set and, based upon a small degree of variability, a data set is used.

2.11.2 Materials Reproducibility

Each materials characterization technique uses seven batches of catalysts. For FT-IR, seven batches can produce 21 samples (after electrochemical samples have been set aside) to test. Each sample is tested at least three times, therefore, a total of 63 data sets are given for every catalyst. XPS is done in a similar way. XRD, due to the amount of material that is necessary, only one sample from each batch was tested. Due to the time needed for XRD scan (ca. 1 h for each), the test is run only twice. Therefore, a total of 14 data sets are given for every catalyst. For TEM, roughly 15 pictures were taken for each catalyst from two batches.

Many materials characterizations are used to “internally” check for certain characteristics. Particle size is determined using both TEM and XRD (using the Scherrer

equation), for comparison reasons. To check for elemental characterization XPS, TEM including elemental mapping, and to a certain extent FT-IR are used. Each sample is used once with the exception of where the effects of electrochemical durability testing is related to the (1) structural integrity, (2) chemical composition, and (3) effects of "binding conditions." To determine the degree of variability, each peak is checked using the half-width for each data in a similar manner that electrochemical data was done.

References

1. Ryan O'Hayre, Suk-Won Cha, Whitney Colella, F. B. P. *Fuel cell fundamentals*. (WILEY-VCH Verlag, 2009).
2. NASA. NASA Technology Roadmaps TA 3: Space Power and Energy Storage. *NASA Technol. Roadmaps* (2015). doi:10.1021/es802371n
3. Goldman, L. Oxford dictionary of national biography of Davy, Sir Humphry. x, 1268 p. (2009).
4. Goldman, L. Oxford dictionary of national biography of Grove, Sir William Robert. x, 1268 p. (2009).
5. VISHNYAKOV, V. Proton exchange membrane fuel cells. *Vacuum* **80**, 1053–1065 (2006).
6. Shao, M., Chang, Q., Dodelet, J.-P. & Chenitz, R. Recent Advances in Electrocatalysts for Oxygen Reduction Reaction. *Chem. Rev.* **116**, 3594–3657 (2016).
7. Zavasky. No Title. 1–2 (1962).
8. Qi, Z. Electrochemical methods for catalyst activity evaluation. *PEM Fuel Cell Electrocatal. Catal. Layers Fundam. Appl.* 547–607 (2008). doi:10.1007/978-1-84800-936-3_11
9. Zeng, K. & Zhang, D. Recent progress in alkaline water electrolysis for hydrogen production and applications. *Progress in Energy and Combustion Science* **36**, 307–326 (2010).
10. Levie, R. de. The electrolysis of water. *J. Electroanal. Chem.* 92–93 (1999). doi:0.1016/S0022-0728(99)00365-4
11. Kreuter, W. & Hofmann, H. Electrolysis: The important energy transformer in a world of sustainable energy. *Int. J. Hydrogen Energy* **23**, 661–666 (1998).
12. Bagotsky, V. S. *Fundamentals of Electrochemistry.* (John Wiley & Sons, 2005).
13. Zhang, H. *et al.* Single Atomic Iron Catalysts for Oxygen Reduction in Acidic Media: Particle Size Control and Thermal Activation. *J. Am. Chem. Soc.* **139**, 14143–14149 (2017).
14. Roth, C., Bleith, P., Schwöbel, C. A., Kaserer, S. & Eichler, J. Importance of fuel cell tests for stability assessment-suitability of titanium diboride as an alternative support material. *Energies* **7**, 3642–3652 (2014).
15. McLean, G. F., Niet, T., Prince-Richard, S. & Djilali, N. An assessment of alkaline fuel cell technology. *Int. J. Hydrogen Energy* **27**, 507–526 (2002).
16. Yao, W., Yang, J., Wang, J. & Nuli, Y. Chemical deposition of platinum nanoparticles on iridium oxide for oxygen electrode of unitized regenerative fuel cell. *Electrochem. commun.* **9**, 1029–1034 (2007).
17. Morozan, A. *et al.* Low-platinum and platinum-free catalysts for the oxygen

reduction reaction at fuel cell cathodes. *Energy Environ. Sci.* **4**, 1238 (2011).
18. Liu, Y., Ishihara, A., Mitsushima, S., Kamiya, N. & Ota, K. Transition Metal Oxides as DMFC Cathodes Without Platinum. *J. Electrochem. Soc.* **154**, B664 (2007).
19. J. W. Long, R. M. Stroud, K. E. Swider-Lyons, and D. R. R. How to make electrocatalysts more active for direct methanol oxidation—Avoid PtRu bimetallic alloys. *J. Phisical Chem. B* **104**, 9772–9776 (2000).
20. Antolini, E., Salgado, J. R. C. & Gonzalez, E. R. The stability of Pt–M (M = first row transition metal) alloy catalysts and its effect on the activity in low temperature fuel cells: A literature review and tests on a Pt–Co catalyst. *J. Power Sources* **160**, 957–968 (2006).
21. Vinayan, B. P. *et al.* Catalytic activity of platinum–cobalt alloy nanoparticles decorated functionalized multiwalled carbon nanotubes for oxygen reduction reaction in PEMFC. *Int. J. Hydrogen Energy* **37**, 412–421 (2012).
22. Goswami, C., Hazarika, K. K. & Bharali, P. Transition metal oxide nanocatalysts for oxygen reduction reaction. *Mater. Sci. Energy Technol.* **1**, 117–128 (2018).
23. V. R. Stamenkovic, B. Fowler, B. S. Mun, G. Wang, P. N. Ross, C. A. Lucas, N. M. M. Improved oxygen reduction activity on Pt3Ni(111) via increased surface site availability. *Science (80-.).* **315**, 493–497 (2007).
24. N. S. Porter, H. Wu, Z. Quan, J. F. Shape-control and electrocatalytic activity-enhancement of Pt-based bimetallic nanocrystals. *Acc. Chem. Res* **46**, 1867–1877 (2013).
25. J. Wu, H. Y. Platinum-based oxygen reduction electrocatalysts. *Acc. Chem. Res* **46**, 1848–1857 (2013).
26. Y. J. Wang, N. Zhao, B. Fang, H. Li, X. T. Bi, H. W. Carbon-supported Pt-based alloy electrocatalysts for the oxygen reduction reaction in polymer electrolyte membrane fuel cells: Particle size, shape, and composition manipulation and their impact to activity. *Chem. Rev* 3433–3467 (2015).
27. Z. Peng, H. Y. Designer platinum nanoparticles: Control of shape, composition in alloy, nanostructure and electrocatalytic property. *Nano Today* **4**, 143–164 (2009).
28. Senanayake, G., Childs, J., Akerstrom, B. D. & Pugaev, D. Reductive acid leaching of laterite and metal oxides — A review with new data for Fe(Ni,Co)OOH and a limonitic ore. *Hydrometallurgy* **110**, 13–32 (2011).
29. Markovic, N. M., Gasteiger, H. A. & Ross, P. N. Oxygen reduction on platinum low-index single-crystal surfaces in sulfuric acid solution. Rotating ring - Pt(hkl) disk studies. *J. Phys. Chem.* **99**, 3411–3415 (1995).
30. Hassel, B. van, Pasini, J. & Limarga, A. IV. D. 6 Advancement of Systems Designs and Key Engineering Technologies for Materials Based-Hydrogen Storage. *Hydrogen.Energy.Gov* 1–6 (2010).
31. Sánchez-Sánchez, C. M. & Bard, A. J. Hydrogen peroxide production in the oxygen reduction reaction at different electrocatalysts as quantified by scanning electrochemical microscopy. *Anal. Chem.* **81**, 8094–8100 (2009).
32. Lee, S.-J., Pyun, S.-I., Lee, S.-K. & Kang, S.-J. L. Fundamentals of Rotating Disc and Ring-Disc Electrode Techniques and their Applications to Study of the Oxygen Reduction Mechanism at Pt/C Electrode for Fuel Cells. *Isr. J. Chem.* **48**,

215–228 (2008).
33. Carl H. Hamann, Andrew Hamnett, W. vielstich. *Electrochemistry*. (WILEY-VCH Verlag, 2007).
34. Brownson, D. A. C. & Banks, C. E. *The Handbook of Graphene Electrochemistry*. *The Handbook of Graphene Electrochemistry* (2014). doi:10.1007/978-1-4471-6428-9
35. Vielstich, W., Lamm, A., Gasteiger, H. A. (Hubert A. & Yokokawa, H. *Handbook of fuel cells : fundamentals, technology, and applications*. (Wiley, 2003).
36. Levich, V. G. (Veniamin G. & Spalding, D. B. (Dudley B. *Physicochemical hydrodynamics : V.G. Levich festschrift*. (Advance Publications, 1977).
37. Bard, A. J. & Faulkner, L. R. *Electrochemical methods : fundamentals and applications*. (Wiley, 2001).
38. Schmidt, T. J. Characterization of High-Surface-Area Electrocatalysts Using a Rotating Disk Electrode Configuration. *J. Electrochem. Soc.* **145**, 2354 (1998).
39. Kim, W. & Park, J. *Preparation and Characterization of a Surface Renewable Solid State Hg/HgO Reference Electrode Utilizing Gold Amalgam*. *Surface Renewable Hg/HgO Reference Electrode Bull. Korean Chem. Soc* **28**, (2007).
40. Rius-Ruiz, F. X. *et al.* Solid-state reference electrodes based on carbon nanotubes and polyacrylate membranes. *Anal. Bioanal. Chem.* **399**, 3613–3622 (2011).
41. Lukaszewski, M., Soszko, M. & Czerwiński, A. Electrochemical methods of real surface area determination of noble metal electrodes - an overview. *Int. J. Electrochem. Sci.* **11**, 4442–4469 (2016).
42. Gorlin, Y. & Jaramillo, T. F. A bifunctional nonprecious metal catalyst for oxygen reduction and water oxidation. *J. Am. Chem. Soc.* **132**, 13612–13614 (2010).
43. Patel, P. P. *et al.* Noble metal-free bifunctional oxygen evolution and oxygen reduction acidic media electro-catalysts. *Sci. Rep.* **6**, 1–14 (2016).
44. Kou, T. *et al.* Ni Foam-Supported Fe-Doped β-Ni(OH) 2 Nanosheets Show Ultralow Overpotential for Oxygen Evolution Reaction. *ACS Energy Lett.* **4**, 622–628 (2019).
45. Stevens, M. B. *et al.* Measurement techniques for the study of thin film heterogeneous water oxidation electrocatalysts. *Chem. Mater.* **29**, 120–140 (2017).
46. Ritter, J. W. & Holland, J. *Key texts of Johann Wilhelm Ritter (1776-1810) on the science and art of nature*. (Brill, 2010).
47. Liu, R.-S. & Wiley InterScience (Online service). *Electrochemical technologies for energy storage and conversion. [Volume 1 & 2]*. (John Wiley & Sons, 2012).
48. Martin, D. J. *Investigation into High Efficiency Visible Light Photocatalysts for Water Reduction and Oxidation*. (2015). doi:10.1007/978-3-319-18488-3
49. Grigoriev, S. A., Porembsky, V. I. & Fateev, V. N. Pure hydrogen production by PEM electrolysis for hydrogen energy. *Int. J. Hydrogen Energy* **31**, 171–175 (2006).
50. Suen, N. T. *et al.* Electrocatalysis for the oxygen evolution reaction: Recent development and future perspectives. *Chem. Soc. Rev.* **46**, 337–365 (2017).
51. Kulkarni, A., Siahrostami, S., Patel, A. & Nørskov, J. K. Understanding Catalytic Activity Trends in the Oxygen Reduction Reaction. (2018).

doi:10.1021/acs.chemrev.7b00488
52. Functional Material - an overview | ScienceDirect Topics. Available at: https://www.sciencedirect.com/topics/materials-science/functional-material. (Accessed: 24th February 2020)
53. Baidakova, M., Vul' -, A., Iakoubovskii, K., Mitsuishi, K. & Furuya, K. High-resolution electron microscopy of detonation nanodiamond. *IOP Publ. Nanotechnol. Nanotechnol.* **19**, 5 (2008).
54. Bonnamy, S. & Oberlin, A. Transmission Electron Microscopy. Materials Science and Egnineering of Carbon. *Methods Mol. Biol.* 45–70 (2016). doi:10.1016/b978-0-12-805256-3.00004-0
55. Frabboni, S. *et al.* The Young-Feynman two-slits experiment with single electrons: Build-up of the interference pattern and arrival-time distribution using a fast-readout pixel detector. *Ultramicroscopy* **116**, 73–76 (2012).
56. Harada, K. *et al.* Interference experiment with asymmetric double slit by using 1.2-MV field emission transmission electron microscope. *Sci. Rep.* **8**, 1–10 (2018).
57. Hetherington, C. Aberration correction for TEM. *Mater. Today* **7**, 50–55 (2004).
58. STOYANOV PA. *TRANSMISSION ELECTRON MICROSCOPES. Bull Acad Sci USSR Phys Ser (Columbia Tech Transl)* **32**, (Springer, Boston, MA, 1968).
59. Williams, D. B., Carter, C. B., Williams, D. B. & Carter, C. B. Scattering and Diffraction. in *Transmission Electron Microscopy* 23–38 (Springer US, 2009). doi:10.1007/978-0-387-76501-3_2
60. Bendersky, L. A. & Gayle, F. W. Electron Diffraction Using Transmission Electron Microscopy. *J. Res. Natl. Inst. Stand. Technol.* **106**, 997–1012 (2001).
61. Williams, D. B. & Carter, C. B. Scattering and Diffraction. in *Transmission Electron Microscopy* 23–38 (Springer US, 2009). doi:10.1007/978-0-387-76501-3_2
62. Vorob'ev, A. B., Gutakovskiĭ, A. K., Prinz, V. Y. & Seleznev, V. A. Preparation of monolayers of nanoparticles for transmission electron microscopy. *Tech. Phys.* **45**, 783–785 (2000).
63. Kim, Y.-W. *Artifacts in Sample Preparation of Transmission Electron Microscopy*. *METALS AND MATERIALS International* **7**, (2001).
64. Klein, D. R. *Organic chemistry*.
65. Fradkin, E. *Field theories of condensed matter physics*.
66. Brenner, I. J. Inductively coupled plasma mass spectrometry applications. in *Encyclopedia of Spectroscopy and Spectrometry* 229–235 (Elsevier, 2016). doi:10.1016/B978-0-12-803224-4.00057-1
67. Larkin, P. J. General Outline for IR and Raman Spectral Interpretation. in *Infrared and Raman Spectroscopy* 135–151 (Elsevier, 2018). doi:10.1016/b978-0-12-804162-8.00007-0
68. Griffiths, P. R. & De Haseth, J. A. *Fourier Transform Infrared Spectrometry: Second Edition*. *Fourier Transform Infrared Spectrometry: Second Edition* (wiley, 2006). doi:10.1002/047010631X
69. Larkin, P. J. IR and Raman Spectra–Structure Correlations. in *Infrared and Raman Spectroscopy* 85–134 (Elsevier, 2018). doi:10.1016/b978-0-12-804162-8.00006-9
70. Dorset, D. L. X-ray Diffraction: A Practical Approach. *Microsc. Microanal.* **4**,

513–515 (1998).
71. Vos, W. L. *et al.* Influence of Optical Band Structures on the Diffraction of Photonic Colloidal Crystals. in *Photonic Band Gap Materials* 107–118 (Springer Netherlands, 1996). doi:10.1007/978-94-009-1665-4_7
72. Zhou, X. *et al.* XRD-based quantitative analysis of clay minerals using reference intensity ratios, mineral intensity factors, Rietveld, and full pattern summation methods: A critical review. *Solid Earth Sci.* **3**, 16–29 (2018).
73. Monshi, A., Foroughi, M. R. & Monshi, M. R. Modified Scherrer Equation to Estimate More Accurately Nano-Crystallite Size Using XRD. *Artic. World J. Nano Sci. Eng.* **2**, 154–160 (2012).
74. van der Heide, P. *X-Ray Photoelectron Spectroscopy: An Introduction to Principles and Practices*. *X-Ray Photoelectron Spectroscopy: An Introduction to Principles and Practices* (John Wiley and Sons, 2011). doi:10.1002/9781118162897
75. Maslakov, K. I. *et al.* XPS study of ion irradiated and unirradiated CeO_2 bulk and thin film samples. *Appl. Surf. Sci.* **448**, 154–162 (2018).
76. Hofmann, S. *Auger- and X-Ray Photoelectron Spectroscopy in Materials Science : a User-Oriented Guide*. (Springer Berlin, 2013).
77. Salim, E. F. Ionic equilibria in analytical chemistry. By Henry Freiser and Quintus Fernando. John Wiley & Sons Inc., 605 Third Avenue, New York, N.Y., 1963. *J. Pharm. Sci.* **53**, 1435 (1964).

Chapter 3: Literature Review

3.1. Hybrid catalyst for oxygen electrocatalysis

Oxidation reduction reaction (ORR) and oxidation evolution reaction (OER) are the most widely studied reactions because they are often the rate determining steps for many electrochemical energy conversion devices such as fuel cells, electrolyzers and metal-air batteries.[1,2] To maximize their kinetics, noble metals such as iridium, Pt, or Pt-alloys have been utilized due to their excellent catalytic activity. However, these noble metals have major issues including prohibitive cost, scarcity and fast degradation.[3,4,5] Transition metal oxides (TMOs) have garnered attention as a highly promising alternative for electrocatalyst[6] due to their high ORR/OER activity, cost competitiveness and abundance.[7,8] The exact understanding of TMOs' role in ORR is not fully understood, but their ability to shift their oxidation states is believed to facilitate and better tolerate repeated charge transfer.[9] In addition, their existence in various crystallographic structures provide ample room for improving their catalytic activities.[9] Examples of TMOs used in these reactions include MnO_2, Co_3O_4, Fe_2O_4, NiO, TiO_2, ZrO_2, and CeO_2.

Due to their low electrical conductivity, TMOs have been incorporated into electronically conducting material such as metal-organic framework (MOF)-derived carbon, polyaniline (PANI), highly oriented pyrolytic graphite (HOPG), and graphene.[10] In particular, low-dimensional carbonaceous nanostructures such as graphene[7] have been widely employed for this purpose. Graphene maximizes the catalytically active sites for ORR owing to its high surface area[11] and suppresses the agglomeration of TMO nanoparticles (NPs) by immobilizing the NPs on their surface.[7] The ORR/OER activity of TMO/graphene hybrids can be further improved by forming 3-dimensional graphene structures or doping graphene with heteroatoms.[12–16] In addition to the expected merits, the excellent ORR/OER performance of TMO/graphene has often been attributed to an alleged synergetic effect by the chemical coupling between TMOs and graphene.[17–21] However, the origin of the synergistic effect between TMO, NC, and FOG is largely unrevealed, and relevant study is scarce. Wu et al. recently reported a mechanistic study of the synergistic ORR using Mn_3O_4/graphene hybrids.[22] They asserted that C–O–Mn^{3+} linkage is responsible for lowering the activation barrier for the initial O_2/HO_2^- reduction and assisting Mn_3O_4 NPs with the subsequent peroxide reduction. More recently, Ryabova et al. also reported the role of carbon in Mn_2O_3/carbon systems to act as a co-catalyst accelerating the initial reduction of O_2 into H_2O_2.[23]

The performance of an electrocatalyst for energy conversion devices is dependent upon its electronic conductivity,[24] that is dictated by interfacial charge transport through the dissimilar materials such as TMO, NC, and FOG. The increase in charge transport, controlled mostly by "binding" conditions, will be demonstrated in Chapters 4-6. To better understand Chapters 4-6, an understanding of the types of materials and research that has been done is needed. The next few sections will describe the structure, fabrication, and overall use as an ORR/OER catalyst of graphene oxide (GO), TMO/GO, and TMO/MOF-derived carbon.

3.2. Graphene oxide

To maximize the catalytically active surface area per mass, it is necessary to decrease the particle size of a catalyst and improve their distribution/dispersion.[25] To achieve this, researchers have employed conductive nanostructures with a large surface areas as their backbone. Carbon-based 3D structures such as reduced GO (rGO) have been widely used to leverage their extremely high surface area and excellent electronic conductivity.[24,26–28] Being mostly carbon, GO is a readily available resource supplied abundantly in nature with its mass production of graphene. Industry markets have already enabled its scalability and cost competitiveness.[29]

3.2.1. Synthesis methods of GO

Nearly 160 years ago, British chemist Brodie treated graphite with potassium chloride, fuming nitric acid, and water to create graphitic acid. This method was modified by the chemists from the Institute of Industrial Research in Mellon by Hummer and Offerman to create GO using sulfuric acid, potassium permanganate and sodium nitrate. This method, which resulted in more oxygen-based groups, was later termed the Hummer's method.[28]

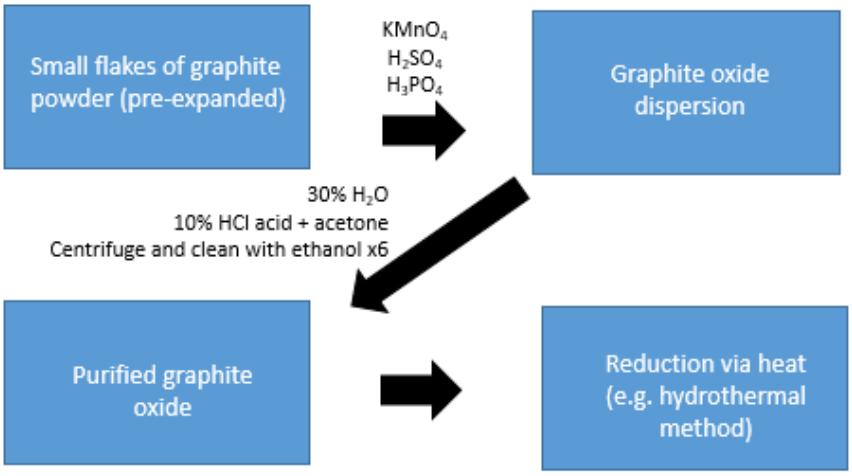

Figure 3.1: Schematic diagram depicting the Tour's method

However, as other scientist realized, the core GO sheets were incompletely oxidized when using the Hummer's method (i.e. the addition of oxygen-based groups is incomplete). To completely oxidize the oxygen-based groups, Koutyukhova[30] introduced H_2SO_4, $K_2S_2O_8$, and P_2O_5 to pretreat graphite in theory. However, this pretreatment of graphite was later discarded as smaller or thermally expanded graphite flakes could more readily add oxygen-based groups to GO. Despite the advancement, safety concerns over the Hummer's methods using $NaNO_3$ began to rise. The byproduct of using the acid caused toxic gases such as NO_2, N_2O_4 and ClO_2, thus inhibiting its industrial application. To combat this issue, researchers from Rice University eliminated the use of $NaNO_3$ and also, reduced the number of steps from over 25 to roughly 8 using a 9:1 mixture of

H_2SO_4/H_3PO_4 (Figure 3.1).[31] Furthermore, the use of H_3PO_4 provided more interactions of the sp^2 carbon domains in the basal planes, thereby producing a larger yield than the Hummer's method. Another advantage of this approach is a further oxidation of diols which are known to be unreactive, as result of the five-membered phosphor ring in H_3PO_4.[28,31–33]

3.2.2 Theoretical Structure of GO

Researchers initially theorized the chemical composition of GOs as a 6-edge ring structure with oxygen groups attached.[34] Later in 1959, Hofmann and Holst found epoxy groups are attached to the basal plane of GOs.[35] In 1946, Ruess modified this structure by introducing hydroxyl groups and corrugating the basal plane. His model added the 1,3-ether on the cyclohexane ring with the four-position hydroxylated and described graphene oxide as "stoichiometrically uniform".[36] Mermoux in 1991 supported this observation and accounted for the large hydrogen content within GO.[37] In 1957, Clauss and Boehm introduced the C=C bonds, ketone, cholic groups, and carboxylic groups on the very edges of GO.[38] Later, Boehm and Scholz modified the this theory by introducing layers into a conjugated GO layers. This layers would have alternating linked quinone structure, opened cyclohexanes ring in chair conformation, epoxy/ether structures, and hydroxyl groups in the four-position of 1,2-oxidized cyclohexane rings.[39] Moving forward to 2012, Dimiev described GO as having a "dynamic structure model" in regards to water. Dimiev theorized, as time progresses, water gradually degrades GO and converts it into a humid acid-like structure.[40] To combat this, researchers like Kim et. al. indicated how GO's liquid crystallinity could be maintained with the addition of nanoparticles or polymers.[41] Unfortunately, the exact structure of GO still eludes many within the field. This lack of understanding is mostly due to the variability within sample-to-sample fabrication.[28,33,42]

3.2.3. Functionalization of GO

Functionalization of GO is the process of adding new functional groups by changing the surface chemistry of GO for enhanced properties. Forms of functionalization include covalent attachments with amides,[43] hydroxyl groups, and epoxides. Hydroxyl groups can be combined with nitriles by an aqueous solution to maintain tunability and functionalities for electronic transport.[44] Epoxides, which occupy the basal plane, could be opened for greater utilization via S_N2 reactions.[45] S_N2 reactions are nucleophilic reactions in which a bond formation is due to another bond breaking and ion dispensing, possible if and only if the backside route is not sterically hindered by substitutes on the aliphatic sp^3 carbon center.[46] Therefore, using a S_N2 reaction can open ring conformation within GO, and thus adding amines using 3-aminopropyltriethoxysilane (ATPS). The idea of using epoxides for basal utilization via non-covalent bonding can increase catalytic behavior will be discussed in later Chapters.[47,28]

3.2.4 Heteroatom doping into GO

Heteroatom is strictly defined as atoms other than carbon or hydrogen. When describing heteroatoms doping GO, we describe the typical 6-ring structure having an

atom that is typically nitrogen, boron, a transition metal, or TMO. In this section, nitrogen and boron heteroatom doping into GO will be explained briefly. In section 3.5, transition metal and TMO doped GO (and MOF) will be extensively explained as a catalyst for ORR and OER performance.

Boron Heteroatom Doped GO

Electron-deficient boron is used for effective chemical doping due to it having three valence electrons, allowing it to functionalize to the inert sp2 carbon structure. This allows abundant free ‑ flowing π electrons and possibly improve the conductivity of carbon materials by increasing the density of holetype charge carriers.[48,49] Several studies show its ability to compete with Pt ($\eta = 7.98 \pm 0.05\%$).[50] Others showed increased capacitance using reduced GO (termed rGO) with the introduction of boron (B-rGO), which was the result of boron's valences and ability to adhere.[51] Other types of boron heteroatom includes nitrides, in which nanotubes are use as carbon source, where researcher reported a stable hydrogen storage catalysts.[52] They attributed, like the other studies mention, the interaction between carbon and boron.

Nitrogen Heteroatom Doped GO

GO heteroatoms, such as nitrogen, can be doped into the graphitic basal plane and change both the electronic and structural properties. As seen Figure 3.2, three major types of bonding exists: (a) graphitic N are substituted on the inner surface of graphene, (b) pyrollic, and (c) pyridinic both found at the edge defects that donate two and one p electrons to pi system respectively. Pyridinic N hybridization is sp^2 whereas pyrollic N is sp^3.[53,54]

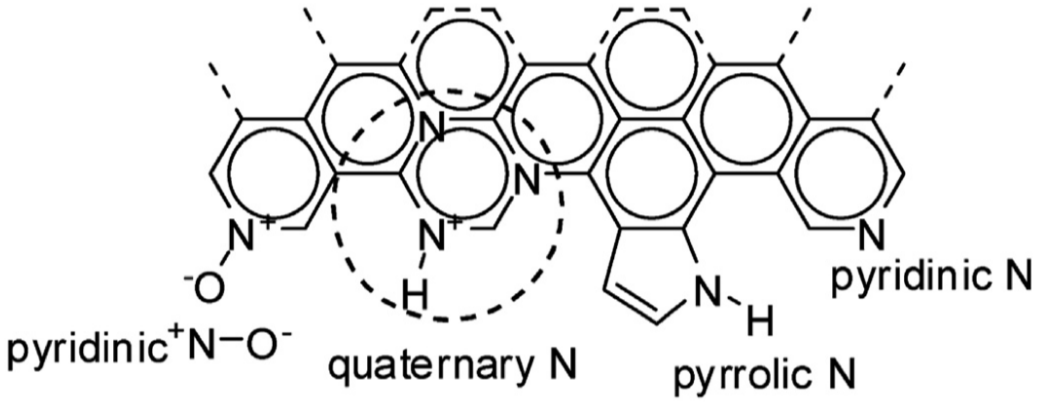

Figure 3.2: Three types of nitrogen bonding upon graphene: pyridinic, pyrrolic, and graphitic N. Schematic was used from Nitrogen-doped graphene and graphene quantum dots: A review on synthesis and applications in energy, sensors and environment.[55]

At lower temperatures, it is observed that the pyrrolic form of nitrogen is more dominant.[56] Graphitic nitrogen doping can lead to a nonuniform electron distribution that can shorten the C-N bond, thus facilitating more O_2 adsorption and subsequent dissociation of the O-O bonds. Other studies, for pyrindinic N, have shown without the

use of metal oxides, high performance activity was achieved due the change of morphology and structure of rGO rather than the electron distribution.[28,57]

Extensive research has been made on the ORR mechanism of N-graphene in which earlier studies showed how oxygen could be reduced either the direct four-electron pathway or two-electron pathways. Huang et al. showed a graphene model possessing two neighbor N atoms in a zigzag edge following a two-electron pathway.[58] Zhang et al. was able to reach a four-electron pathway with the introduction of graphene in an acidic environment[59] while Yu et. al used an alkaline environment.[59] Dissociative and associative mechanism show that ORR was more energetically favored following a four-electron pathway with the introduction of N-graphene.[60]

3.3 Metal Organic Frameworks

Metal organic framework (MOF) is a type of supporting structure (framework) that links polyatomic clusters (secondary building blocks) using strong directional covalent bonds. A point of contention often comes from this definition, as some researchers define MOFs as the coordination of polymers.[61] SBUs are commonly a carboxylate that can be categorized as ditopic, polytopic, or with just one branch point. The metal framework can be a finite cluster of a polygonal shape or infinite cluster like an octahedra. The shapes of metal frameworks are defined as *points of extension* where they are linked to an organic linker at a specific point which creates a specific framework with a desired pore, chemistry, and geometric shape. The branch of chemistry that covers MOFs is known as reticular chemistry. Reticular chemistry is the study of design and synthesis of materials targeted symmetrical structures by linking together SBUs using a chemical bond.[62–64]

MOFs have extraordinarily high surface areas (ca. 6000 m^2 g^{-1}), tunable pore size, and changeable surface properties. Early examples of a MOF include a two-periodic net made of zinc-benzenedicarboxylate (MOF-2). This structure containing two zinc atoms that are linked in a periodic square array shows high microporsity and surface area. MOF-3 (now known as MOF-4) has a framework of zinc-1,3,5-benzenetricarboxylate whose metal ions had a triangular shape, specifically, the chiral cubic net known as $SrSi_2$-type net. Shortly after the MOF-3 (MOF-4) was created, the MOF-5 with the zinc carboxylate cluster with six carboxylate carbons forming a regular octahedron with tetrahedral symmetry was created. This was very important linkage as the cavity within the actual structure could be formed without much degradation, thus providing enhanced surface area, porosity, and stability. These few examples of early MOFs were only possible because of the work by O'Keeffe and Yaghi that deconvoluted the MOFs underlying topological nets, thereby, beginning the first subsequent descriptions/designs for other MOF structures.[65] This helped with the fabrication of other MOFs using HKUST-1 ($Cu_3(btc)_2$, btc=1,3,5-benezenetricarboxylate) with high porosity and low pressure gas sorption. Then the development of chromium(III) terephthalate (MIL-101) with high chemical stability, MOF-74 (Zn_2(dhbdc), dhbdc=2,4-dihydroxy-1,4-benzenedicarboxylate) with low pressure adsorption of CO_2, were made. Various other types of MOFs have been made with different types of metal clusters and organic linkers. However, the effects of the metal clusters and organic linkers to effect synergy (binding conditions as mentioned in Chapter 2) has yet to be studied extensively.[66]

3.4 Methods of fabricating TMO-NC hybrids

3.4.1 CVD

CVD involves a chamber in which one or more heated objects are coated with a flowing precursor. Chemical reactions between the precursor and the heated objects results in the deposition of a thin film on the surface, accompanied by the products of such reactions.[67] CVD has the advantage of depositing relatively uniform thin films on a substrate with a high-aspect ratio and/or severe corrugation. One of the most favorable aspects of CVD is its ability to deposit a variety of materials with a very high purity and high deposition rates.[54,68,69]

For carbon substrates in general, CVD can decompose carbon feedstock via heat to provide a source of carbon coatings which can rearrange to form sp^2 carbon species on a catalyst.[70] For example, hydrocarbons gasses can form from NCs. Many researchers utilize precursors such TMOs to prevent hydrocarbons from forming.[71,72]

However, carbon coatings can lead to interfacial stress of dissimilar layers due to their incompatible thermal expansion coefficients causing mechanical instabilities.[73–75] This is especially true for hybrids of NCs and TMOs as their thermal expansion rates are substantially different (roughly $60x10^{-6}$ vs. $4x10^{-6}$, respectively).[76]

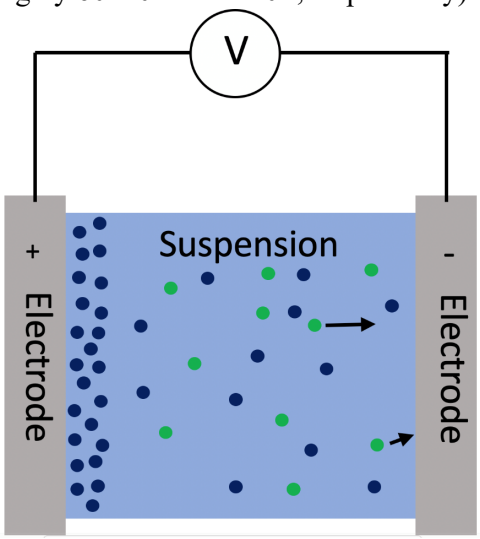

Figure 3.3: Depicts electrodeposition with a two-electrode system in suspension with an applied DC voltage. The green circles represents anions and the blue circles represent the metal cations that will be reduced and coated on a substrate during electrodeposition.

3.4.2 Electrodeposition

Electrophoretic deposition includes electrophoretic coating, electrocoating, electrophoretic painting, and electrodeposition.[77] As shown in Figure 3.3, under a DC bias, metal ions (blue circles) are attracted to the negatively charged substrate, electrochemically reduced and deposited as a metal film while anions (green circles) are directed to the other electrode for charge compensation. A major disadvantage of the electrodeposition is the non-uniform and inconsistent deposition, causing general

decrease of catalytic activity within the material and between the base metal and coating metal.[78] Since a large positive potential delaminates GO from its substrate, a low potential has to be utilized for GO-based samples.[69] This is also true for other types of carbon-based electrodes.

3.4.3 Hydrothermal reaction

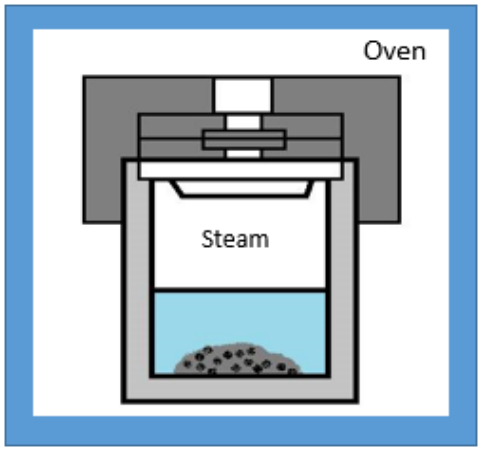

Figure 3.4: Precursors are placed inside an HTM vessel. The HTM vessel is then placed inside an autoclave where two temperature zones exist. The precursors dissolve inside the hotter zone and the saturated aqueous solution at the bottom is moved to the top by convection. The cooler part of the autoclave acts as a counterflow of the solution. This becomes supersaturated, thus allowing the temperature to decrease for crystallization to occur.

The hydrothermal method (HTM) is an approach of creating crystals from aqueous solutions under a high-pressure condition. Three HTM modes exist: metastable-phase, temperature-reduction, and temperature-difference.[79] The metastable-phase method is performed at temperatures below the supercritical temperature of water. This process, however, can produce both unreacted material and crystalline structures.[80] The temperature-reduction method is a process where a crystallization occurs without a temperature gradient between growth and the dissolution zones. Instead, supersaturation occurs when the temperature of the solution decreases, resulting in an uneven growth.[81] The temperature-difference method is favored due to its ability to reach supersaturation by reducing the temperature in the crystal growth zone (See Figure 3.4). This is important as many nanocarbon structures like GO and MOF-derived 3D carbon require supersaturation after adsorbing crystalline metal oxides. HTM also provides an environment for dissolved ions to nucleate while inside the HTM vessel. Therefore, it is suitable to use the HTM to fabricate a hybrid electrode of crystalline metal oxides and carbon.[82–85]

3.5. TMO/NC for ORR and OER

To better understand how the interactions between TMOs and NC affect the performance of ORR and OER, a summary of relevant catalysis based upon several representative TMOs is provided below. The research below will demonstrate how, most research is mainly focused on heteroatom dopants.

Cobalt oxide (CoO_x)

Cobalt oxides are the most prominently used oxides for fuel cells due to its low-cost, flexible valence shifts,[86] and activity as an electrocatalyst towards ORR[87,88]. The high activity towards ORR often found in Co_3O_4 (spinel structure) where Co^{2+} and Co^{3+} occupy the tetrahedral and octahedral sites, facilitate electron transfer.[89,90] However, cobalt oxide does not perform well in acidic media and tends to agglomerate thus exhibiting poor durability.[91,92] Researchers combat poor conductivity and severe agglomeration of metal oxides by dispersing them in nanoparticles using a carbon structure.[93–95] Examples of such materials were found in many reports. Dai et al. demonstrated that Co_3O_4 with rGO doped with nitrogen show an excellent activity towards both ORR (comparable to Pt/C) and OER.[18] They attributed this performance with the Co-O-C and Co-N-C bond formation that caused a synergistic effect of the interfaces towards catalytic activity. Studies have shown that a strong covalent interaction between N and Co_3O_4 partially reduces the Co^{3+} (in the Co_3O_4) to Co^{2+}. A strong covalent interaction, as a result of a reduction in valence state, can lead to enhanced catalytic performance.[96] Wang et al. used a similar interaction between MOF-cobalt derived, carbon cloth and nitrogen using thermal treatment. This enabled both mechanical stability and electrochemical performance significantly enhanced.[97]

The addition of dopants like N, Br, P, etc. into a carbon structure can change the charge distribution and spin density of nearby carbon atoms creating more active sites for ORR.[98] Tung et al. demonstrated a hybrid of Br and N doping into graphene enriches oxygen vacancies and Co-N-C active sites,[99] resulting in the onset potential of 0.95 V vs. RHE in 0.1 M KOH and an electron charge transfer number close to 4. A similar study was performed in an MOF-derived carbon to enrich oxygen vacancies and create active sites.[100]

A study using a different type of NC called graphitic carbon nitride (G-C_3N_4) demonstrated how the shell is used to generate active sites. Generation of active sites were demonstrated by trapping cobalt ions and GO sheet in the G-C_3N_4, thereby collecting the electron by covalently supporting the core-shell structures (changing the interface).[101] They theorized that the high stability of this catalyst was due to the releasing of Co ions from the cobalt core that would have "regenerated" active sites. One study argues that the charge transfer between graphene and Co_3O_4 nanosheets to be the primary reason for electrocatalytic properties based upon DFT analysis, where they experimented on the doped hybride Co-S/G microwave argon plasma sample.[102]

Iron oxide (FeO_x)

Iron oxide is economical, abundant and highly selective towards ORR.[103] Iron oxide however, suffers from poor mechanical characteristics to be used for catalysis: uncontrollable growth and agglomeration.[104] To better address this, Zhao et. al. created nano-Fe_3O_4/graphene and FeO(OH) nanoflake/graphene composites. The latter was found to have efficient catalytic activity for both ORR and OER.[105] Zhao attributed the

enhanced performance to the positive synergistic coupling effects at the interface between iron oxide and graphene. Similarly, a MOF based study using iron phosphide and iron oxide created a positive electronic synergistic effect between the Fe and P with high porosity, thus providing both easy diffusion and efficient electron transfer.[106]

Copper oxide (CuO_x)

Copper oxide has received significant attention as a electrocatalysis for ORR.[107] By mixing CuO_x with doped carbon, increasing activity towards the reduction of HOO- intermediate at the interface was seen. More specifically, when GO is doped with a N-based ligand, Cu^{2+} ions have a greater affinity to form N-based ligand with GO. This can improve ORR activity in terms of current density, onset potential, and four-electron process.[7] Another example includes the use of copper oxide/N-rGO synthesized via aqueous coprecipitation method,[108] where an enhanced electron transfer number was seen as a result of mixing copper oxide and N-rGO. Another study using a similar hybrid and technique showed enhanced stability and ORR activity, accrediting to the synergistic effect at the interface between high graphitization and their encapsulated structures.[109] For MOF based samples, further calcination of hybrid samples lead to improved performance.[110]

Manganese oxide (MnO_x)

Manganese oxide has high stability, low cost, variable oxidation states and has effective catalytic performance towards ORR. Oxygen defects have been introduced to Mn-based oxides using thermal reduction (Mn^{4+} to Mn^{3+}) to improve electrical conductivity which has, in turn, been proven to be catalytically more active than Pt/C.[111] One study by Shao-Hon et. al. suggested that a mix of $Mn^{3+/4+}$ and $Mn^{3+/4+}$ >1 valence created a four electron pathway and improved overall kinetics.[112] Mn^{3+} is an active intermediate state that can greatly improve catalytic performance.[113] This behavior is due to the presence of the electron resulting in the John-Teller distortion.[114]

However, when using Mn_3O_4 for its mixed valency studies showed poor structural stability, and low electrical conductivity impacting ORR.[115,116] Therefore, to improve both morphology and electrocatalytic activity, a carbonaceous substrate (graphene) was added to MnO_x. Difficulties can arise when using a carbon substrate as the valence diversity will decrease.[92,117–121] Cao et al. was able to combat the difficulty by synthesizing a new hybrid of carbon and MnO_x without compromising the flexibility in the valence states of Mn (Mn^{2+} and Mn^{3+}).[122] Li et. al also demonstrated how the combination between manganese oxide and graphene oxide accelerated ORR and decreased overall resistance.[123] The decrease in overall resistance occurred because of the enlarged contact area between oxygen and electrode catalyst.[124] Other studies, Bag et. al, demonstrated how N-rGO and Mn_3O_4 could be combined using hydrazine, a common reagent to functionalize rGO as a result of increasing contact area.[125] This functionalization increased ORR performance in alkaline solution in which the onset potential was -0.075 V vs. Ag/AgCl (~0.90 V vs. RHE). Wu et. al. demonstrated how nanowires of MnO_2 in a 3D compound with graphene changed the crystalline phase that enabled a four-electron ORR pathway.

Transition metals specifically for OER

Electrocatalyst using TMOs have been studied extensively due in part to their chemical stability for water oxidation reaction.[126–128] Research has indicated that iridium and

ruthenium oxides are the most active catalysts for water splitting in acidic media.[127,129,130] Iridium oxide is favored for its long term stability in acid-based electrolysis.[5,131] However, using iridium oxide for industrial purposes is not desirable as the commodity is in short supply, causing it to be prohibitively expensive for large-scale applications. Cheaper alternatives exist for the electrochemical oxidation of water such as abundant 3d transition metal oxides that have high catalytic activity towards OER.[129,132–136] As seen before, the use of a carbon source, such as graphene oxide, with a transition metal enhances the OER activity (cobalt oxide with N-GO created the Co-O-C and Co-N-C bond).

Table 3.0: Table of GO with particular metal oxides, fabrication method, and performance/stability.

GO / Metal Oxide	Fabrication Method	Onset potential	Durability
GO/ Pt/SnO_2	Self-assembly	0.95 V vs. RHE	82% of Pt[137]
GO-CNT/ Pt/SnO_2	Self-assembly	0.99 V vs. RHE	21.5% of Pt[138]
GO/Co_3O_4	HTM	0.3 V vs. SHE	110% of Pt[139]
GO/Fe_2O_3	HTM	-0.01 V vs. Hg/HgO	90% of itself[140]
GO/Fe_3O_4	HTM	-0.2 V vs. Hg/HgO	88% of itself[140]
GO/Mn_3O_4	Electrodeposition	0.86 V vs. RHE	Not avaliable[141]
GO/MnO_2	Electrodeposition	-0.35 V vs. SCE	141% of MnO only[142]
GO/NiO	HTM	0.92 V vs. RHE	Not avaliable[143]
GO/CuO	Self-assembly	-0.1 V vs. RHE	Not avaliable[108]
GO/Pd-CeO	HTM	0.95 V vs. RHE	Not available[144]
GO/MoO_2	HTM	0.86 V vs. RHE	174% of Pt[145]
GO/V_2O_5	Self-assembly	0.8 V vs. RHE	97% of Pt[146]

References

1. Wu, G. & Zelenay, P. Nanostructured nonprecious metal catalysts for oxygen reduction reaction. *Acc. Chem. Res.* **46**, 1878–1889 (2013).
2. Jaouen, F. *et al.* Recent advances in non-precious metal catalysis for oxygen-reduction reaction in polymer electrolyte fuel cells. *Energy Environ. Sci.* **4**, 114–130 (2011).
3. Morozan, A. *et al.* Low-platinum and platinum-free catalysts for the oxygen reduction reaction at fuel cell cathodes. *Energy Environ. Sci.* **4**, 1238 (2011).
4. Topalov, A. A. *et al.* Dissolution of Platinum: Limits for the Deployment of Electrochemical Energy Conversion. *Angew. Chemie Int. Ed.* **51**, 12613–12615 (2012).
5. Antolini, E. Iridium As Catalyst and Cocatalyst for Oxygen Evolution/Reduction in Acidic Polymer Electrolyte Membrane Electrolyzers and Fuel Cells. *ACS Catal.* **4**, 1426–1440 (2014).
6. Zhu, C. & Dong, S. Recent progress in graphene-based nanomaterials as advanced electrocatalysts towards oxygen reduction reaction. *Nanoscale* **5**, 1753 (2013).
7. Sun, M., Liu, H., Liu, Y., Qu, J. & Li, J. Graphene-based transition metal oxide nanocomposites for the oxygen reduction reaction. *Nanoscale* **7**, 1250–1269 (2015).
8. Liang, Y. *et al.* Co_3O_4 Nanocrystals on Graphene as a Synergistic Catalyst for

Oxygen Reduction Reaction. *Nat. Mater.* **10**, 780–786 (2011).
9. Osgood, H., Devaguptapu, S. V., Xu, H., Cho, J. & Wu, G. Transition metal (Fe, Co, Ni, and Mn) oxides for oxygen reduction and evolution bifunctional catalysts in alkaline media. *Nano Today* **11**, 601–625 (2016).
10. McCreery, R. L. Advanced Carbon Electrode Materials for Molecular Electrochemistry. *Chem. Rev.* **108**, 2646–2687 (2008).
11. Pumera, M. Graphene-based nanomaterials for energy storage. *Energy Environ. Sci.* **4**, 668 (2011).
12. Liang, Z. *et al.* Edge-Abundant Porous Fe_3O_4 Nanoparticles Docking in Nitrogen-Rich Graphene Aerogel as Efficient and Durable Electrocatalyst for Oxygen Reduction. *ChemElectroChem* **4**, 2442–2447 (2017).
13. Mao, S., Wen, Z., Huang, T., Hou, Y. & Chen, J. High-performance bi-functional electrocatalysts of 3D crumpled graphene–cobalt oxide nanohybrids for oxygen reduction and evolution reactions. *Energy Environ. Sci.* **7**, 609–616 (2014).
14. Sun, Y. *et al.* Ultrafine Co-doped ZnO nanoparticles on reduced graphene oxide as an efficient electrocatalyst for oxygen reduction reaction. *Electrochim. Acta* **224**, 561–570 (2017).
15. Wang, Y. *et al.* Nanoconfined nitrogen-doped carbon-coated MnO nanoparticles in graphene enabling high performance for lithium-ion batteries and oxygen reduction reaction. *Chem. Sci.* **7**, 4284–4290 (2016).
16. Pendashteh, A., Palma, J., Anderson, M. & Marcilla, R. $NiCoMnO_4$ nanoparticles on N-doped graphene: Highly efficient bifunctional electrocatalyst for oxygen reduction/evolution reactions. *Appl. Catal. B Environ.* **201**, 241–252 (2017).
17. Guo, S., Zhang, S., Wu, L. & Sun, S. Co/CoO Nanoparticles Assembled on Graphene for Electrochemical Reduction of Oxygen. *Angew. Chemie Int. Ed.* **51**, 11770–11773 (2012).
18. Liang, Y. *et al.* Co_3O_4 nanocrystals on graphene as a synergistic catalyst for oxygen reduction reaction. *Nat. Mater.* **10**, 780–6 (2011).
19. Yu, J., Liu, Z., Zhai, L., Huang, T. & Han, J. Reduced graphene oxide supported TiO_2 as high performance catalysts for oxygen reduction reaction. *Int. J. Hydrogen Energy* **41**, 3436–3445 (2016).
20. Wu, Z. *et al.* 3D nitrogen-doped graphene aerogel-supported Fe_3O_4 nanoparticles as efficient electrocatalysts for the oxygen reduction reaction. *J. Am. Chem. Soc.* **134**, 9082–5 (2012).
21. Ratha, S., Samantara, A. K., Rout, C. S. & Jena, B. K. Synergistic electrocatalytic activity of a spinel $ZnCo_2O_4$/reduced graphene oxide hybrid towards oxygen reduction reaction. *J. Solid State Electrochem.* **20**, 285–291 (2016).
22. Wu, K.-H. *et al.* Structural Origin of the Activity in Mn_3O_4 -Graphene Oxide Hybrid Electrocatalysts for the Oxygen Reduction Reaction. *ChemSusChem* **8**, 3331–3339 (2015).
23. Ryabova, A. S. *et al.* Further insights into the role of carbon in manganese oxide/carbon composites in the oxygen reduction reaction in alkaline media. *Electrochim. Acta* **246**, 643–653 (2017).
24. Carl H. Hamann, Andrew Hamnett, W. vielstich. *Electrochemistry*. (WILEY-VCH Verlag, 2007).

25. Wang, Z.-L., Li, C. & Yamauchi, Y. Nanostructured nonprecious metal catalysts for electrochemical reduction of carbon dioxide. *Nano Today* **11**, 373–391 (2016).
26. Ruoff, R., Dreyer, D. R., Park, S., Bielawski, W. & Ruoff, R. S. *The chemistry of graphene oxide The chemistry of graphene oxide*. **1**, (2016).
27. Dikin, D. A. *et al.* Preparation and characterization of graphene oxide paper. *Nature* **448**, 457–460 (2007).
28. Chem, J. M. *Graphene Oxide †*. (2012). doi:10.1039/c2jm32231e
29. Ryan O'Hayre, Suk-Won Cha, Whitney Colella, F. B. P. *Fuel cell fundamentals*. (WILEY-VCH Verlag, 2009).
30. Nina I. Kovtyukhova, *,† *et al.* Layer-by-Layer Assembly of Ultrathin Composite Films from Micron-Sized Graphite Oxide Sheets and Polycations. (1999). doi:10.1021/CM981085U
31. Marcano, D. C. D. *et al.* Improved synthesis of graphene oxide. *ACS Nano* **4**, 4806–4814 (2010).
32. Cao, X., Yin, Z. & Zhang, H. Three-dimensional graphene materials: preparation, structures and application in supercapacitors. *Energy Environ. Sci.* **7**, 1850–1865 (2014).
33. Yang, X., Cheng, C., Wang, Y., Qiu, L. & Li, D. Liquid-mediated dense integration of graphene materials for compact capacitive energy storage. *Science (80-.).* **341**, 534–7 (2013).
34. Staudenmaier, L. Verfahren zur Darstellung der Graphitsäure. *Berichte der Dtsch. Chem. Gesellschaft* **31**, 1481–1487 (1898).
35. Hofmann, U. & Holst, R. Über die Säurenatur und die Methylierung von Graphitoxyd. *Berichte der Dtsch. Chem. Gesellschaft (A B Ser.* **72**, 754–771 (1939).
36. G, R. Über das Graphitoxyhydroxyd (Graphitoxyd). *Monatsch Chem* **76**, 381–417 (1947).
37. Mermoux M, Chabre Y, R. A. FTIR and C-13 NMR-study of graphite oxidee. *Carbon N. Y.* 469–474 (1991).
38. Boehm HP, Clauss A, Hofmann U, F. G. Dunnste Kohlenstoff-Folien. Z Naturforschg. 150–157 (1962).
39. Scholz W, B. H. Graphite oxide. 6. Structure of graphite oxide. *Z Anorg Allg Chem* 327–340 (1969).
40. Dimiev, A. M., Alemany, L. B. & Tour, J. M. Graphene Oxide. Origin of Acidity, Its Instability in Water, and a New Dynamic Structural Model. *ACS Nano* **7**, 576–588 (2013).
41. Kim, S. *et al.* Room-temperature metastability of multilayer graphene oxide films. *Nat. Mater.* **11**, 544–549 (2012).
42. Chen, J., Yao, B., Li, C. & Shi, G. An improved Hummers method for eco-friendly synthesis of graphene oxide. *Carbon N. Y.* **64**, 225–229 (2013).
43. Stankovich, S., Piner, R. D., Nguyen, S. T. & Ruoff, R. S. Synthesis and exfoliation of isocyanate-treated graphene oxide nanoplatelets. *Carbon N. Y.* **44**, 3342–3347 (2006).
44. Gonçalves G, Marques PAAP, Barros-Timmons A, Bdkin I, Singh MK, Emami N, G. J. Graphene oxide modifi ed with PMMA via ATRP as a reinforcement filler. *J*

Mater Chem 9927–9934 (2010).
45. Kasprzak, A., Zuchowska, A. & Poplawska, M. Functionalization of graphene: does the organic chemistry matter? *Beilstein J. Org. Chem.* **14**, 2018–2026 (2018).
46. Chua, C. K. & Pumera, M. Chemical reduction of graphene oxide: A synthetic chemistry viewpoint. *Chem. Soc. Rev.* **43**, 291–312 (2014).
47. Becerril, H., Mao, J., Liu, Z. & Stoltenberg, R. Evaluation of solution-processed reduced graphene oxide films as transparent conductors. *Acs.* **2**, 463–470 (2008).
48. Han, J. *et al.* Generation of B-doped graphene nanoplatelets using a solution process and their supercapacitor applications. *ACS Nano* **7**, 19–26 (2013).
49. Chiang, W. H. *et al.* C/BCN core/shell nanotube films with improved thermoelectric properties. *Carbon N. Y.* **109**, 49–56 (2016).
50. Yeh, M. H. *et al.* Boron-doped carbon nanotubes as metal-free electrocatalyst for dye-sensitized solar cells: Heteroatom doping level effect on tri-iodide reduction reaction. *J. Power Sources* **375**, 29–36 (2018).
51. Li, S. *et al.* Plasma-induced highly efficient synthesis of boron doped reduced graphene oxide for supercapacitors. *Chem. Commun.* **52**, 10988–10991 (2016).
52. Li, S. *et al.* Highly Compressive Boron Nitride Nanotube Aerogels Reinforced with Reduced Graphene Oxide. *ACS Catal.* **2**, 141–149 (2018).
53. Sheng, Z. H. *et al.* Catalyst-free synthesis of nitrogen-doped graphene via thermal annealing graphite oxide with melamine and its excellent electrocatalysis. *ACS Nano* **5**, 4350–4358 (2011).
54. Tetana, Z. N., Mhlanga, S. D., Bepete, G. & Coville, N. J. The synthesis of nitrogen-doped multiwalled carbon nanotubes using an Fe-Co/CaCO3 Catalyst. *South African J. Chem.* **65**, 39–49 (2012).
55. Kaur, M., Kaur, M. & Sharma, V. K. Nitrogen-doped graphene and graphene quantum dots: A review onsynthesis and applications in energy, sensors and environment. *Adv. Colloid Interface Sci.* **259**, 44–64 (2018).
56. Chen, D., Feng, H. & Li, J. Graphene oxide: Preparation, functionalization, and electrochemical applications. *Chem. Rev.* **112**, 6027–6053 (2012).
57. Tans, S., Verschueren, A. & Dekker, C. Room-temperature transistor based on a single carbon nanotube. *Nature* **672**, 669–672 (1998).
58. Vayner, E. & Anderson, A. B. Theoretical predictions concerning oxygen reduction on nitrided graphite edges and a cobalt center bonded to them. *J. Phys. Chem. C* **111**, 9330–9336 (2007).
59. Zhang, L. & Xia, Z. Mechanisms of oxygen reduction reaction on nitrogen-doped graphene for fuel cells. *J. Phys. Chem. C* **115**, 11170–11176 (2011).
60. Groves, M. N., Chan, A. S. W., Malardier-Jugroot, C. & Jugroot, M. Improving platinum catalyst binding energy to graphene through nitrogen doping. *Chem. Phys. Lett.* **481**, 214–219 (2009).
61. Delgado-friedrichs, O., Keeffe, O. & Yaghi, O. M. Taxonomy of periodic nets and the design of materials. *Phys. Chem. Chem.* **9**, 1035–1043 (2007).
62. Sun, T., Xu, L., Wang, D. & Li, Y. Metal organic frameworks derived single atom catalysts for electrocatalytic energy conversion. *Nano Res.* **12**, 2067–2080 (2019).
63. Frost, H. & Snurr, R. Q. Design requirements for metal-organic frameworks as hydrogen storage materials. *J. Phys. Chem. C* **111**, 18794–18803 (2007).

64. Sun, L., Campbell, M. G. & Dincă, M. Electrically Conductive Porous Metal-Organic Frameworks. *Angew. Chemie - Int. Ed.* **55**, 1–29 (2016).
65. Furukawa, H., Cordova, K. E., O'Keeffe, M. & Yaghi, O. M. The chemistry and applications of metal-organic frameworks. *Science* **341**, (2013).
66. O'keeffe, M. Design of MOFs and intellectual content in reticular chemistry: A personal view. *Chem. Soc. Rev.* **38**, 1215–1217 (2009).
67. *Chemical Vapor Deposition*. (ASM International, 2001).
68. Arod, P. & Shivashankar, S. A. Single-step synthesis of carbon nanotubes/iron/iron oxide composite films through inert-ambient CVD using ferric acetylacetonate as a precursor. *RSC Adv.* **5**, 59463–59471 (2015).
69. Zhu, B. Y. *et al.* Enhanced stability of Cu-BTC MOF via perfluorohexane plasma-enhanced chemical vapor deposition. *J. Am. Chem. Soc.* **134**, 8683–8690 (2009).
70. Rümmeli, M. H. *et al.* Graphene: Piecing it Together. *Adv. Mater.* **23**, 4471–4490 (2011).
71. Chen, X., Wu, G., Jiang, Y., Wang, Y. & Chen, X. Graphene and graphene-based nanomaterials: the promising materials for bright future of electroanalytical chemistry. *Analyst* **136**, 4631 (2011).
72. Li, Xuesong; Cai, Weiwei; Colombo, Luigi; Ruoff, R. S. *Evolution of Graphene Growth on Ni and Cu by Carbon Isotope Labeling*. (American Chemical Society, 2000).
73. Obraztsov, A. N., Obraztsova, E. A., Tyurnina, A. V. & Zolotukhin, A. A. Chemical vapor deposition of thin graphite films of nanometer thickness. *Carbon N. Y.* **45**, 2017–2021 (2007).
74. Zhu, W. *et al.* Structure and Electronic Transport in Graphene Wrinkles. *Nano Lett.* **12**, 3431–3436 (2012).
75. Yoon, D., Son, Y.-W. & Cheong, H. Negative Thermal Expansion Coefficient of Graphene Measured by Raman Spectroscopy. *Nano Lett.* **11**, 3227–3231 (2011).
76. Deng, S. & Berry, V. Wrinkled, rippled and crumpled graphene: an overview of formation mechanism, electronic properties, and applications. *Mater. Today* **19**, 197–212 (2016).
77. Qi, Z. Electrochemical methods for catalyst activity evaluation. *PEM Fuel Cell Electrocatal. Catal. Layers Fundam. Appl.* 547–607 (2008). doi:10.1007/978-1-84800-936-3_11
78. Ali, G. A. M., Yusoff, M. M., Ng, Y. H., Lim, H. N. & Chong, K. F. Potentiostatic and galvanostatic electrodeposition of manganese oxide for supercapacitor application: A comparison study. *Curr. Appl. Phys.* **15**, 1143–1147 (2015).
79. Yang, D. *Titanium Dioxide - Material for a Sustainable Environment*. (2018). doi:10.5772/intechopen.70290
80. Zhao, Y. *et al.* Hydrothermal route to metastable phase $FeVO_4$ ultrathin nanosheets with exposed {010} facets: synthesis, photocatalysis and gas-sensing. *CrystEngComm* **16**, 270–276 (2014).
81. Xiang, X. *et al.* Improving the low-temperature hydrothermal stability of Cu-SAPO-34 by the addition of Ag for ammonia selective catalytic reduction of NO_x. *Appl. Catal. A Gen.* **551**, 79–87 (2018).
82. Lightcap, I. V., Kosel, T. H. & Kamat, P. V. Anchoring semiconductor and metal

nanoparticles on a two-dimensional catalyst mat. storing and shuttling electrons with reduced graphene oxide. *Nano Lett.* **10**, 577–583 (2010).
83. Ratha, S. & Rout, C. S. Supercapacitor Electrodes Based on Layered Tungsten Disulfide-Reduced Graphene Oxide Hybrids Synthesized by a Facile Hydrothermal Method. *ACS Appl. Mater. Interfaces* **5**, 11427–11433 (2013).
84. Naguib, M. *et al.* One-step synthesis of nanocrystalline transition metal oxides on thin sheets of disordered graphitic carbon by oxidation of MXenes. *Chem. Commun.* **50**, 7420–7423 (2014).
85. Wang, Q. H., Kalantar-Zadeh, K., Kis, A., Coleman, J. N. & Strano, M. S. Electronics and optoelectronics of two-dimensional transition metal dichalcogenides. *Nat. Nanotechnol.* **7**, 699–712 (2012).
86. Shahid, M. M., Rameshkumar, P., Basirun, W. J., Juan, J. C. & Huang, N. M. Cobalt oxide nanocubes interleaved reduced graphene oxide as an efficient electrocatalyst for oxygen reduction reaction in alkaline medium. *Electrochim. Acta* **237**, 61–68 (2017).
87. Liang, Y. *et al.* Oxygen reduction electrocatalyst based on strongly coupled cobalt oxide nanocrystals and carbon nanotubes. *J. Am. Chem. Soc.* **134**, 15849–15857 (2012).
88. Wang, D. *et al.* The influence of manganese–cobalt oxide/graphene on reducing fire hazards of poly(butylene terephthalate). *J. Hazard. Mater.* **278**, 391–400 (2014).
89. Zhang, T. *et al.* Co_3O_4 nanoparticles anchored on nitrogen-doped reduced graphene oxide as a multifunctional catalyst for H_2O_2 reduction, oxygen reduction and evolution reaction. *Sci. Rep.* **7**, 43638 (2017).
90. Xiao, J. *et al.* Surface Structure Dependent Electrocatalytic Activity of Co_3O_4 Anchored on Graphene Sheets toward Oxygen Reduction Reaction. *Sci. Rep.* **3**, 2300 (2013).
91. Hamdani, M., Singh, R. N. & Chartier, P. *Co_3O_4 and Co-Based Spinel Oxides Bifunctional Oxygen Electrodes*. *International Journal of ELECTROCHEMICAL SCIENCE* **5**, (2010).
92. Liang, Y. *et al.* Covalent hybrid of spinel manganese-cobalt oxide and graphene as advanced oxygen reduction electrocatalysts. *J. Am. Chem. Soc.* **134**, 3517–3523 (2012).
93. Yang, S. *et al.* Fabrication of Cobalt and Cobalt Oxide/Graphene Composites: Towards High-Performance Anode Materials for Lithium Ion Batteries. *ChemSusChem* **3**, 236–239 (2010).
94. Hao, Y., Xu, Y., Liu, J. & Sun, X. Nickel–cobalt oxides supported on Co/N decorated graphene as an excellent bifunctional oxygen catalyst. *J. Mater. Chem. A* **5**, 5594–5600 (2017).
95. Xie, G. *et al.* High catalytic activity of Co_3O_4 nanoparticles encapsulated in a graphene supported carbon matrix for oxygen reduction reaction. *RSC Adv.* **6**, 50349–50357 (2016).
96. Wang, Jian; Zhou, Jigang; Hu, Yongfeng; Regier, T. Chemical interaction and imaging of single Co3O4/graphene sheets studied by scanning transmission X-ray microscopy and X-ray absorption spectroscopy. *R. Soc. Chem.* **6**, 926–934 (2013).

97. Guan, C. *et al.* Cobalt oxide and N-doped carbon nanosheets derived from a single two-dimensional metal-organic framework precursor and their application in flexible asymmetric supercapacitors. *Nanoscale Horizons* **2**, 99–105 (2017).
98. Yang, N., Li, L., Li, J., Ding, W. & Wei, Z. Modulating the oxygen reduction activity of heteroatom-doped carbon catalysts via the triple effect: charge, spin density and ligand effect. *Chem. Sci.* **9**, 5795–5804 (2018).
99. Pascone, P.-A., Berk, D. & Meunier, J.-L. A stable and active iron catalyst supported on graphene nano-flakes for the oxygen reduction reaction in polymer electrolyte membrane fuel cells. *Catal. Today* **211**, 162–167 (2013).
100. Zhao, M. *et al.* Two-dimensional metal-organic framework nanosheets: synthesis and applictions. *Chem. Soc. Rev.* **47**, 6267–6295 (2018).
101. Wang, M. *et al.* Co_3O_4 nanorods decorated reduced graphene oxide composite for oxygen reduction reaction in alkaline electrolyte. *Electrochem. commun.* **34**, 299–303 (2013).
102. Xu, J. *et al.* Co_3O_4 nanocubes homogeneously assembled on few-layer graphene for high energy density lithium-ion batteries. *J. Power Sources* **274**, 816–822 (2015).
103. Ma, Y. *et al.* Ultrafine iron oxide nanoparticles supported on N-doped carbon black as an oxygen reduction reaction catalyst. *Int. J. Hydrogen Energy* **39**, 14777–14782 (2014).
104. Sharma, G. *et al.* Iron oxide nanoparticle agglomeration influences dose rates and modulates oxidative stress-mediated dose-response profiles in vitro. *Nanotoxicology* **8**, 663–75 (2014).
105. Zhao, B. *et al.* Multifunctional Iron Oxide Nanoflake/Graphene Composites Derived from Mechanochemical Synthesis for Enhanced Lithium Storage and Electrocatalysis. *ACS Appl. Mater. Interfaces* **7**, 14446–14455 (2015).
106. Chandra Shit, S. *et al.* MOF-Derived Bifunctional Iron Oxide and Iron Phosphide Nanoarchitecture Photoelectrode for Neutral Water Splitting. *ChemElectroChem* **5**, 2056–2063 (2018).
107. Davis, Danae J.; Lambert, Timothy N.; Vigil, Julian A.; Rodriguez, Mark A.; Brumbach, Michael T.; Coker, Eric N.; Limmer, S. J. Role of Cu-Ion Doping in Cu-α-MnO_2 Nanowire Electrocatalysts for the Oxygen Reduction Reaction. *J. Phys. Chem.* **118**, 17342–17350 (2014).
108. Zhou, R., Zheng, Y., Hulicova-Jurcakova, D. & Qiao, S. Z. Enhanced electrochemical catalytic activity by copper oxide grown on nitrogen-doped reduced graphene oxide. *J. Mater. Chem. A* **1**, 13179 (2013).
109. Song, J. *et al.* Encapsulated $NdCuO_x$ bimetallic nanoparticles with nitrogen doped carbon as an efficient electrocatalyst for oxygen reduction reaction. *Electrochim. Acta* **258**, 1404–1412 (2017).
110. Gong, X. *et al.* Metal-organic framework derived controllable synthesis of mesoporous copper-cerium oxide composite catalysts for the preferential oxidation of carbon monoxide. *Fuel* **229**, 217–226 (2018).
111. Dong, C. *et al.* Modest Oxygen-Defective Amorphous Manganese-Based Nanoparticle Mullite with Superior Overall Electrocatalytic Performance for Oxygen Reduction Reaction. *Small* **13**, 1603903 (2017).

112. Stoerzinger, K. A., Risch, M., Han, B. & Shao-Horn, Y. Recent Insights into Manganese Oxides in Catalyzing Oxygen Reduction Kinetics. *ACS Catal.* **5**, 6021–6031 (2015).
113. Risch, M. *et al.* Redox Processes of Manganese Oxide in Catalyzing Oxygen Evolution and Reduction: An in Situ Soft X-ray Absorption Spectroscopy Study. *J. Phys. Chem. C* **2**, 34 (2017).
114. Mosa, I. M. *et al.* Tunable mesoporous manganese oxide for high performance oxygen reduction and evolution reactions. *J. Mater. Chem. A* **4**, 620–631 (2016).
115. Zhao, A. *et al.* Spinel Mn–Co Oxide in N-Doped Carbon Nanotubes as a Bifunctional Electrocatalyst Synthesized by Oxidative Cutting. *J. Am. Chem. Soc.* **136**, 7551–7554 (2014).
116. Roche, I., Chainet, E., Chatenet, M. & Vondrak, J. Carbon-supported manganese oxide nanoparticles as electrocatalysts for the Oxygen Reduction Reaction (ORR) in alkaline medium: Physical characterizations and ORR mechanism. *J. Phys. Chem. C* **111**, 1434–1443 (2007).
117. Tang, Q., Jiang, L., Liu, J., Wang, S. & Sun, G. Effect of Surface Manganese Valence of Manganese Oxides on the Activity of the Oxygen Reduction Reaction in Alkaline Media. *ACS Catal.* **4**, 457–463 (2014).
118. Qian, Y., Lu, S. & Gao, F. Synthesis of manganese dioxide/reduced graphene oxide composites with excellent electrocatalytic activity toward reduction of oxygen. *Mater. Lett.* **65**, 56–58 (2011).
119. Ramírez, A. *et al.* Evaluation of MnO_x, Mn_2O_3, and Mn_3O_4 Electrodeposited Films for the Oxygen Evolution Reaction of Water. *J. Phys. Chem. C* **118**, 14073–14081 (2014).
120. Wen, Q. *et al.* MnO_2–graphene hybrid as an alternative cathodic catalyst to platinum in microbial fuel cells. *J. Power Sources* **216**, 187–191 (2012).
121. Wu, J., Zhang, D., Wang, Y. & Wan, Y. Manganese oxide–graphene composite as an efficient catalyst for 4-electron reduction of oxygen in alkaline media. *Electrochim. Acta* **75**, 305–310 (2012).
122. Cao, Y. L., Yang, H. X., Ai, X. P. & Xiao, L. F. The mechanism of oxygen reduction on MnO2-catalyzed air cathode in alkaline solution. *J. Electroanal. Chem.* **557**, 127–134 (2003).
123. Li, T. *et al.* Tubular Monolayer Superlattices of Hollow Mn_3O_4 Nanocrystals and Their Oxygen Reduction Activity. *J. Am. Chem. Soc.* **139**, 12133–12136 (2017).
124. Li, M., Zhou, S. & Xu, M. Graphene oxide supported magnesium oxide as an efficient cathode catalyst for power generation and wastewater treatment in single chamber microbial fuel cells. *Chem. Eng. J.* **328**, 106–116 (2017).
125. Bag, Sourav; Roy, Kanak; Gopinath, Chinnakonda S.; Raj, C. R. Facile Single-Step Synthesis of Nitrogen-Doped Reduced Graphene Oxide-Mn_3O_4 Hybrid Functional Material for the Electrocatalytic Reduction of Oxygen. *ACS Appl. Mater. Interfaces* **6**, 2692–2699 (2014).
126. Dau, H. *et al.* The Mechanism of Water Oxidation: From Electrolysis via Homogeneous to Biological Catalysis. *ChemCatChem* **2**, 724–761 (2010).
127. Matsumoto, Y. & Sato, E. Electrocatalytic properties of transition metal oxides for oxygen evolution reaction. *Mater. Chem. Phys.* **14**, 397–426 (1986).

128. Trasatti, S. Electrocatalysis by oxides — Attempt at a unifying approach. *J. Electroanal. Chem. Interfacial Electrochem.* **111**, 125–131 (1980).
129. McCrory, C. C. L., Jung, S., Peters, J. C. & Jaramillo, T. F. Benchmarking Heterogeneous Electrocatalysts for the Oxygen Evolution Reaction. *J. Am. Chem. Soc.* **135**, 16977–16987 (2013).
130. Lee, Y., Suntivich, J., May, K. J., Perry, E. E. & Shao-Horn, Y. Synthesis and Activities of Rutile IrO_2 and RuO_2 Nanoparticles for Oxygen Evolution in Acid and Alkaline Solutions. *J. Phys. Chem. Lett.* **3**, 399–404 (2012).
131. Davidson, L., Quinn, Y. & Steele, D. F. Ruthenium-mediated electrochemical destruction of organic wastes. *Platin. Met. Rev.* **42**, 90–98 (1998).
132. Gong, M. & Dai, H. A mini review of NiFe-based materials as highly active oxygen evolution reaction electrocatalysts. *Nano Res.* **8**, 23–39 (2015).
133. Gong, M. *et al.* An Advanced Ni–Fe Layered Double Hydroxide Electrocatalyst for Water Oxidation. *J. Am. Chem. Soc.* **135**, 8452–8455 (2013).
134. Grimaud, A. *et al.* Double perovskites as a family of highly active catalysts for oxygen evolution in alkaline solution. *Nat. Commun.* **4**, 2439 (2013).
135. Lu, Z. *et al.* Three-dimensional NiFe layered double hydroxide film for high-efficiency oxygen evolution reaction. *Chem. Commun. (Camb).* **50**, 6479–82 (2014).
136. Suntivich, J. *et al.* Design principles for oxygen-reduction activity on perovskite oxide catalysts for fuel cells and metal-air batteries. *Nat. Chem.* **3**, 546–550 (2011).
137. Kinumoto, Taro Nagano, Keita Tsumura, Tomoki Toyoda, M. A Novel Durable Electrode Catalyst of Pt/Ketjen Black Decorated with SnO_2 Nanoparticles for Polymer Electrolyte Fuel Cells. *Electrochemistry* **76**, 333–336 (2010).
138. Ignaszak, A., Teo, C., Ye, S. & Gyenge, E. Pt-SnO_2 −Pd/C Electrocatalyst with Enhanced Activity and Durability for the Oxygen Reduction Reaction at Low Pt Loading: The Effect of Carbon Support Type and Activation. *J. Phys. Chem. C* **114**, 16488–16504 (2010).
139. Shi, P. *et al.* Synergistic catalysis of Co_3O_4 and graphene oxide on Co_3O_4/GO catalysts for degradation of Orange II in water by advanced oxidation technology based on sulfate radicals. *Chem. Eng. J.* **240**, 264–270 (2014).
140. Liu, X. & Hu, W. Iron oxide/oxyhydroxide decorated graphene oxides for oxygen reduction reaction catalysis: a comparison study. (2016). doi:10.1039/c5ra28038a
141. Gorlin, Y., Chung, C.-J., Nordlund, D., Clemens, B. M. & Jaramillo, T. F. Mn_3O_4 Supported on Glassy Carbon: An Active Non-Precious Metal Catalyst for the Oxygen Reduction Reaction. *ACS Catal.* **2**, 2687–2694 (2012).
142. Basirun, W. J. *et al.* Graphene oxide electrocatalyst on MnO2 air cathode as an efficient electron pump for enhanced oxygen reduction in alkaline solution. *Sci. Rep.* **5**, 9108 (2015).
143. Yung, T.-Y. *et al.* Synthesis and characterizations of Ni-NiO nanoparticles on PDDA-modified graphene for oxygen reduction reaction. *Nanoscale Res. Lett.* **9**, 444 (2014).
144. Carrillo-Rodríguez, J. C. *et al.* High Performance Pd-$CeO_{2\text{-}NR}$ Supported on Graphene and N-Doped Graphene for the ORR and Its Application in a Microbial

Fuel Cell. *ECS Trans.* **77**, 1359–1365 (2017).
145. Li, P. *et al.* Nitrogen-doped graphene-supported molybdenum dioxide electrocatalysts for oxygen reduction reaction. (1972). doi:10.1007/s10853-017-1972-y
146. Du, X., Huang, G., Qin, Y. & Wang, L. Solvothermal synthesis of GO/V_2O_5 composites as a cathode material for rechargeable magnesium batteries † RSC Advances. (2015). doi:10.1039/c5ra15284d

Chapter 4: Critical Impact of Graphene Functionalization for Transition Metal Oxide/Graphene Hybrids on Oxygen Reduction Reaction

4.1 Introduction

As described in Chapter 3, the excellent ORR performance of TMO/graphene hybrid catalyst has often been ascribed to a synergetic effect by the chemical coupling between TMOs and graphene. However, a detailed mechanistic study about the synergy is scarce. In this Chapter, we address the question of how the difference in chemical coupling between graphene and TMO NPs affects the route and kinetics of ORR. Specifically, the impact of graphene functionalization, which is performed prior to TMO incorporation, on the ORR behavior of resulting TMO/graphene hybrid catalysts are studied. Oxygen-containing groups such as epoxide (–O–), hydroxyl (–OH), and carboxyl groups (–COOH) are major adsorption sites of TMO NPs on graphene.[1] To the best of our knowledge, there has not been a report about the dependency of ORR performance on the type of oxygen-containing functional group linking between TMOs and carbon. For the study, graphene flakes were treated with different acids to populate their surface with a specific functional oxygen group (FOG) before incorporating TMO NPs on them. Two different TMOs (commercial TiO_2 NPs (P25) and solvothermally synthesized ZrO_2 NPs) are considered in this study. In addition to a comparative study of ORR performances in these hybrid catalysts, factors of ORR activity and electron transfer pathway are discussed based upon a series of ex-situ physical characterization, electrochemical analyses and density functional theory (DFT) calculations.

4.2 Methods

4.2.1 Preparation of TMO/graphene Hybrid Catalysts.

First, graphene oxide (GO) was synthesized by a modified Hummers method.[2] Briefly, 45 mm flake graphite powder (3 g) and $KMnO_2$ (18 g) were mixed in 0.98 M H_2SO_4 (360 ml) and 0.75 M H_2PO_4 (14 ml) for 12 h at 50 °C. Afterwards, 400 ml of ice cubes were added to the solution. Once ice is melted, 3 ml of H_2O_2 and 50 ml of de-ionized (DI) water were added sequentially. The resulting GO solution was centrifuged, filtered slowly with 200 ml of 0.1M HCl and 200 ml of deionized (DI) water, and allowed to dry.[3]

Subsequently, acid treatments were performed on the GOs to functionalize the surface. 30 mg of GO, 3 ml of ethanol, and 27 ml of DI water were ultrasonicated for 0.5 h, and 2 ml of hydrobromic acid (HBr) was then added and stirred for 14 h. The resulting solution was filtered with 200 ml of DI water and allowed to dry under a house vacuum to produce hG (hydrobromic acid-treated GO). Additional 600 mg of oxalic acid was added into the solution of hG, which was then stirred for 5 h and dried in vacuum to generated oG (oxalic acid-treated G).

To synthesize TMO/graphene hybrids, hydrothermal reaction was performed. For TiO_2/graphene, 10 mg of dry GO (we call the non-treated GO as G hereafter), hG or oG was added to a solution of TiO_2 (P25; 600 mg), DI water (60 ml) and ethanol (30 ml). The suspension was stirred for 2 h and underwent a hydrothermal reaction at 160°C for 24 h in a 90 ml Teflon-sealed autoclave to produce TiO_2/graphene hybrids: T-G, T-hG and T-oG, respectively. The same process was used for ZrO_2/graphene hybrids with exception of using 0.3 M of $ZrOCl_2 \cdot 8H_2O$ instead of P25 and the hydrothermal reaction being performed at 220°C for 18 h, to produce Z-G, Z-hG and Z-oG.

4.2.2 Material Characterization

The morphology and size of NPs were characterized by transmission electron microscopy (TEM; Philips CM300 FEG system, 300 kV). TEM samples were prepared by drop-casting a catalyst suspension in ethanol (sonicated for 2 h with a concentration of 1 mg ml^{-1}) upon a 3 mm Lacey carbon 400 mesh grid (Ted Pella), followed by an ambient drying. X-ray photoelectron spectroscopy (XPS) was performed on a PHI Quantum 2000 system using a focused, monochromatic Al Kα X-ray (1486.6 eV) source for excitation and a spherical section analyzer (200 μm diameter X-ray beam incident to the surface normal; detector set at 45°). The collected data were referenced to an energy scale with binding energies for Cu $2p_{3/2}$ at 932.7 ± 0.1 eV and Au $4f_{7/2}$ at 84.0 ± 0.1 eV. For XPS, catalysts were dispersed in ethanol and drop-cast onto a cleaned Si wafer. X-ray diffraction (XRD) pattern was recorded by a PANalytical X'Pert PRO with Co Kα radiation (λ = 1.78897 Å) at the step size of 0.02° and scan rate of 0.04 ° s^{-1}. For XRD, a solution of 5 ml ethanol per 10 mg catalyst was sonicated for 2 h, drop-casted upon an aluminum disk, and dried in ambient air. Fourier transform infrared spectroscopy (FT-IR) samples were dried under vacuum for 10 h and placed on a diamond crystal before spectra were recorded (Nicolet 380 system, Thermo Scientific).

4.2.3 Electrochemical Characterization

The ORR activity of the catalysts was evaluated in 0.1 M KOH with cyclic voltammetry (CV), rotating disk electrode (RDE) and rotating ring disk electrode (RRDE) on a SP-200 system (Bio-Logic Science Instruments) with a rotator (RRDE-3A, ALS Co. Ltd.) in a three-electrode setup where an Ag/AgCl/KCl (3.5 M) electrode and a Pt wire were used as the reference and counter electrode, respectively; a comparison using a graphitic rod (instead of a Pt wire) as the counter electrode is presented in Scheme 3.1. All electrochemical data were expressed with respect to the reversible hydrogen electrode (RHE) after a calibration in saturated H_2 environment. The working electrode was prepared by drop-casting each electrode ink onto a 4 mm glassy carbon disk electrode. The ink was prepared by immersing 15 mg of TiO_2/graphene or ZrO_2/graphene catalyst material into 2.21 ml of ethanol along with 3.75 mg of carbon black and 73 μl of 5 wt. % Nafion (Nafion D-521, Alfa Aesar). 23 μl of solid phase substance (TMO/graphene, additional carbon black and Nafion) was loaded on the glassy carbon working electrode (~0.18 mg cm^{-2}). To prepare for Pt/C ink, 15 mg of commercial Pt/C (20 wt. % Pt supported on Vulcan XC72) was added instead of TiO_2/graphene or ZrO_2/graphene by having the amount of solvents and additives unchanged. Therefore, all electrodes have a total solid loading of ~0.18 mg cm^{-2}, and a catalyst/carbon (TiO_2/graphene,

ZrO_2/graphene or Pt/C) loading of ~0.12 mg cm^{-2}. After catalysts were placed, they were dried on the electrode under N_2 at 32 sccm rotating at 750 rpm. O_2 and N_2-saturated environment for electrochemical characterization was implemented by flowing high-purity O_2 and N_2 gas at 32 sccm into 30 ml of electrolyte for > 30 min. To check if any difference came between using a graphitic rod versus a pt wire, a side by side test was conducted as seen in Figure 4.1.

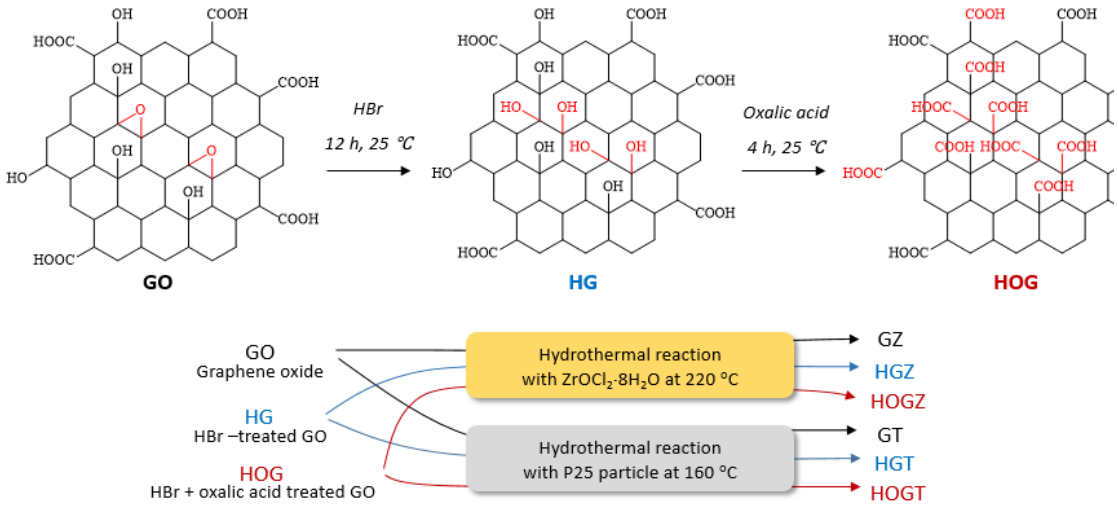

Scheme 4.1 Schematic drawing depicting surface functionalization of graphene oxide by acid treatments and hydrothermal reaction-based synthesis of TiO_2/GO and ZrO_2/GO hybrid catalysts.

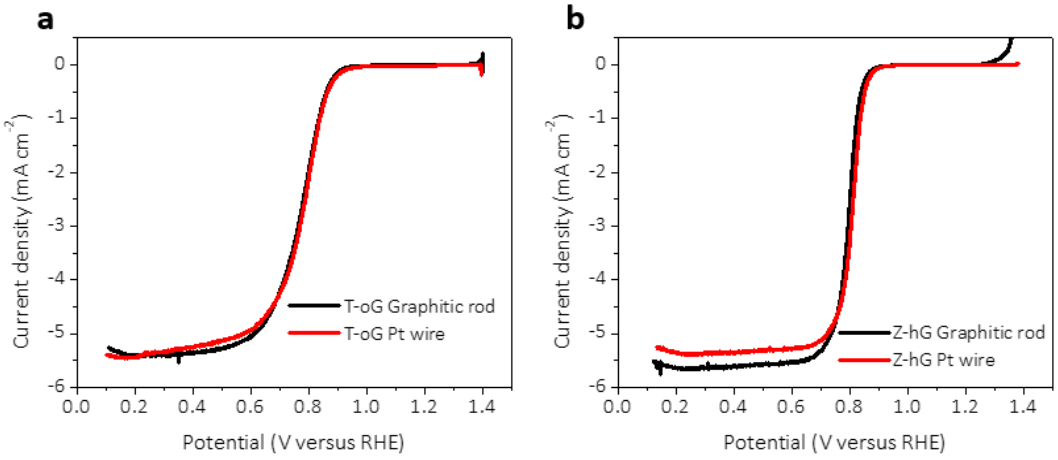

Figure 4.1 Graphitic rod versus Pt wire as the counter electrode. RDE voltammograms of (a) T-oG and (b) Z-hG in O_2-saturated 0.1 M KOH at a sweep at of 5 mV s^{-1}. No appreciable difference is found in the curve.

4.2.4 Modeling and Computation

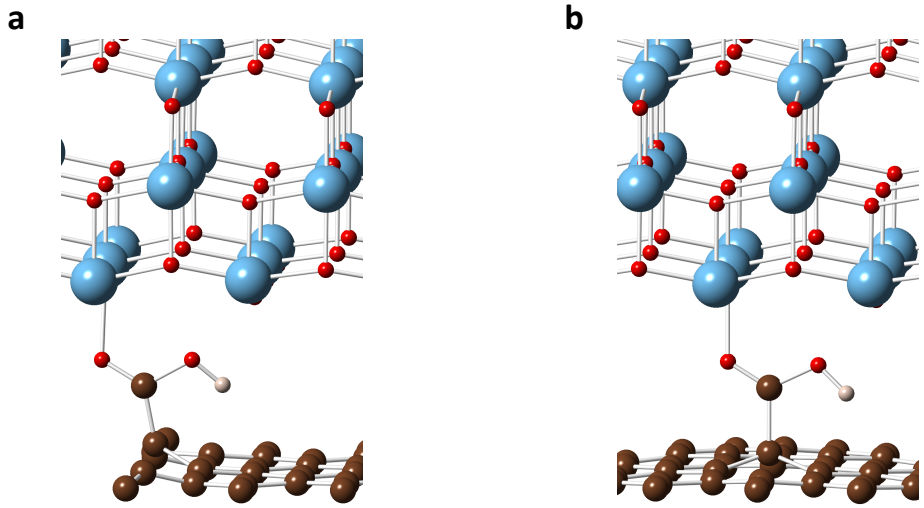

Figure 4.2: The structures of functionalized graphenes and TiO_2 slab, with a carboxyl group attached on (a) the edge site of graphene and (b) the basal plane site of graphene.

The stability of TiO_2/graphene and ZrO_2/graphene interfaces and the preferred electron transfer pathways of ORR were assessed by calculating the electronic energy of each interface structure and intermediate structures during the ORR. DFT calculations were performed within Perdew-Burke-Ernzerhof parameterization[4,5] of Generalized Gradient Approximation (GGA) with Projector Augmented Wave (PAW) potentials[6] as implemented in the Vienna Ab initio Simulation Package (VASP).[7–9] Both the volume and the shape of the supercell were optimized during the relaxation. 520 eV of cutoff energy together with a *k*-space mesh, which was adjusted depending on the size of supercell, ensured an energy convergence of 1 meV per atom. A total of six interface structures were examined: TiO_2-epoxy-graphene (TEG), TiO_2-hydroxyl-graphene (THG), TiO_2-carboxyl-graphene (TCG), ZrO_2-epoxy-graphene (ZEG), ZrO_2-hydroxyl-graphene (ZHG), and ZrO_2-carboxyl-graphene (ZCG). Each interface structure was modeled by one 8-layer TiO_2 or ZrO_2 slab structure, one layer of graphene, and one functional group molecule linking the slab and the graphene. {001} and {111} facets were adopted for the TiO_2 and ZrO_2 slab structures, respectively. The modeled interface structure was placed in a computational supercell and surrounded by empty space (~15 Å) along the direction normal to the interface to exclude the influence from its self-images. The distance between the slab and the graphene was adjusted to produce the lowest enthalpy of formation, E_f, which was defined as $E_f = E_{int} - (E_{slab} + E_{gr} + E_{fg})$ where E_{int} is the electronic energy of the interface, and E_{slab}, E_{gr}, and E_{fg}, are the electronic energy of the slab, the graphene and the function group composing the interface structure, respectively. Two different sites on graphene were examined for bonding to the functional groups: the edge site and the basal-plane site of graphene as illustrated in Figure 4.2 (referred hereafter as edge-bonded and plane-bonded interfaces, respectively).

The electron transfer pathway was studied by calculating the electronic energy of the intermediate states that could occur during the ORR in alkaline solution[10,11] and obtaining the change in the enthalpy of formation (ΔE_f) with respect to the interface structure, oxygen molecules, and water molecules. For the dissociation process of one O_2 molecule, interface structures with two oxygen atoms attached were examined and thus ΔE_f was calculated by $\Delta E_f = E_{int\text{-}2O^*} - (E_{int} + E_{O2})$, where $E_{int\text{-}2O^*}$ and E_{O2} are the electronic energy of interface structure with two dissociated oxygen atoms (O^*) and one O_2 molecule, respectively. Interestingly, the "edge-bonded" interfaces exhibited a positive ΔE_f, which implied the dissociation in this structure would be unfavorable. Hence, we examined only the "plane-bonded" interfaces for further study of the ORR. The association process of one water molecule was modeled based on the dissociated interface structures. In case of the ORR in alkaline solution, two (4- and 2-electron transfer) pathways are suggested for the association process. In the association via 4-electron transfer pathway, one O^* will be detached from the dissociated interface to combine with one proton, which will be dissociated from a water molecule, to form a hydroxide. Hence the ΔE_f for the 4-electron transfer pathway was obtained by $\Delta E_f = E_{int\text{-}O^*} + 2E_{OH} - (E_{int} + E_{O2} + E_{H2O})$, where E_{OH} and E_{H2O} are the electronic energy of a hydroxide and a water molecule. In case of the association via 2-electron transfer pathway, one proton from a water molecule is attached to the O^*s on the interface to form $O^*O^*H^-$, and hence, the ΔE_f was obtained by $\Delta E_f = E_{int\text{-}O^*O^*H} + E_{OH} - (E_{int} + E_{O2} + E_{H2O})$.

To complete the association process, another water molecule needs to be associated to produce the 4 hydroxides per the dissociation of one O_2. However, we will focus on ΔE_f during the first step of the association (the association of one water molecule as described above), because it will be more significant to determine the preferred electron transfer way – the ΔE_f simply increased to zero during the second step of the association (the association of one additional water molecule) in either pathway. The calculated ΔE_f will correspond to the one from the ORR with gaseous phase water and oxygen molecules, and thus, it should be calibrated to obtain the voltage for the ORR in alkaline solution. However, such a calibration was not made in this study, because the primary goal of this study is to determine the preferred electron transfer pathway by comparing the ΔE_f between different intermediate states, not to calculate the potential of ORR. The activation energy barrier for breaking a bond between a functional group and graphene, which was observed to occur prior to the dissociation of O_2, was obtained by calculating the change of electronic energy while manually translating the graphene by the increment of 0.08 Å from its optimal position in the interface.

4.3 Results and Discussion

4.3.1 Functionalization of Graphene Surface.

Three different kinds of GOs were prepared before tethering TiO_2 or ZrO_2 NPs onto them: as-synthesize GO (G), hydrobromic acid-treated G (hG) and GOs treated with both hydrobromic and oxalic acid (oG). Chemically exfoliated graphene oxide sheets are known to have their basal planes functionalized predominantly with epoxy and some hydroxyl groups while carboxyl groups are mostly located at the edges.[12,13] A hydrobromic acid treatment is intended to form more hydroxyl group via a ring-opening of epoxide groups, and an additional treatment with oxalic acid is expected to convert hydroxyl groups to carboxyl groups, by which a significant amount of carboxyl groups can be present on the basal plane as well;[14] a conceptual schematic diagram is provided in Schematic 4.1. FT-IR spectra presented in Figure 3.3(a) shows that hG has a more pronounced C–OH stretching of hydroxyl groups (1220 cm^{-1}) than G with a slightly lowered C–O stretching adsorption of epoxy groups (1060 cm^{-1}). This suggests a partial conversion of epoxide groups into hydroxyl groups on the GO sheet. In addition, oG has a larger C=O absorbance (1710 cm^{-1}) than G and hG indicating a carboxylation by the additional oxalic acid treatment. High resolution XPS was additionally performed to compare the relative amount of oxygen-containing functional groups. Figure 4.3(b) and Figure 4.3(c) show that oG has a stronger C=O/O–C=O peak (287.9 eV in C 1s and 531.3 eV in O 1s) than hG and thus a higher concentration of carboxyl groups, in accordance with the FT-IR observation.

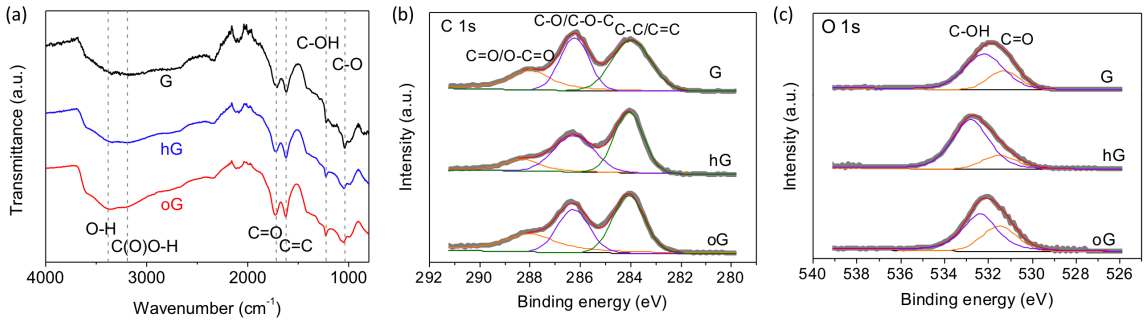

Figure 4.3 (a) FT-IR spectra of G, hG and oG. All measured after being dried. (b) XPS C 1s spectra of G, hG and oG. Binding energies of 284.0, 286.3 and 287.9 eV correspond to C-C/C=C, C-O/C-O-C and C=O/O-C=O bonding, respectively. (d) XPS O 1s spectra of G, hG and oG. Binding energies of 531.3 and 532.2 eV correspond to C=O and C-OH bonding, respectively.

While the G and oG are found to have a comparable amount of C=O, the oG is believed to have a significant portion of the carboxyl groups on its basal planes unlike the G where the C=O bonding is known to be mostly concentrated along the edges and wrinkles.[12,13]

4.3.2 Physical Characterization of Hybrid Catalysts.

The TEM images in Figure 4.4 show that the TiO_2 NPs in the three TiO_2/graphene electrodes spans 10 – 30 nm in size while the size of ZrO_2 NPs in the three ZrO_2/graphene samples are 3 – 10 nm. Both NPs tends to be more populated along the edge of graphene while a significant amount of NPs are also present on the basal plane. As noted in the Method section, TiO_2/graphene and ZrO_2/graphene hybrids made of G, hG and oG are denoted as T-G, T-hG and T-oG, and Z-G, Z-hG and Z-oG, respectively (Schematic 4.1).

Table 4.1: Calculated mass ratio of rutile (fr) computed from the signal counts of (101) peak of anatase and (110) peak of rutile for all Ti based samples. See the section entitled "Quantification of mass ratio between anatase and rutile" above for the equation used to quantify these.

Parameter	P25	GT	HGT	HOGT
I_r (counts)	2,083	2,133	2,104	1,268
I_a(counts)	11,528	13,000	14,638	7,746
f_r (%)	18.5%	17.1%	14.8%	17.1%

The XRD patterns of TiO_2/graphene hybrids (Figure 3.5(a)) reveals that the TiO_2 is a mixture of anatase and rutile as expected in P25.[15] The mass fractions of rutile phase in all the TiO_2/graphene samples were quantified to be 15 – 18% from the relative intensities of the strongest diffraction peaks of the two phases: (101) peak of anatase and

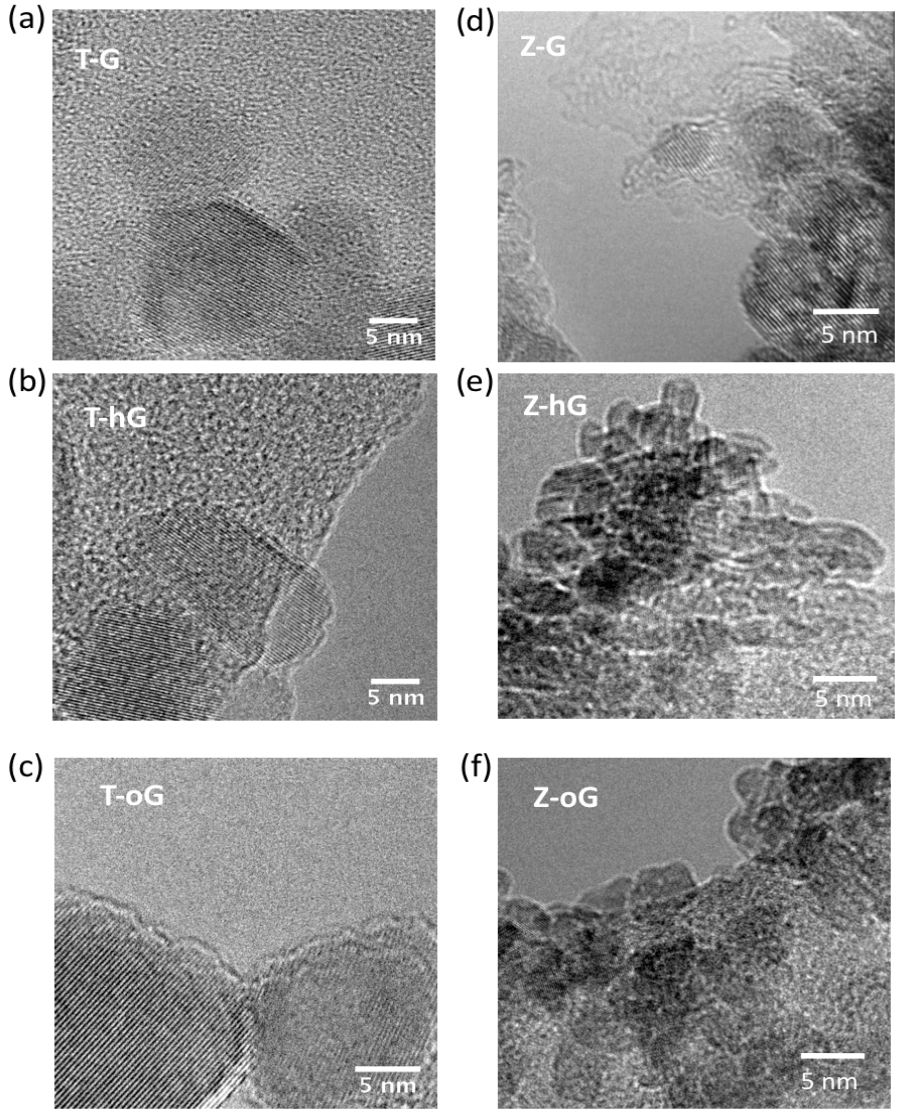

Figure 4.4 TEM images of (a) T-G, (b) T-hG, (c) T-oG (d) Z-G, (e) Z-hG and (f) Z-oG

(110) peak of rutile (see Table 4.1).

There is little appreciable differences in the rutile percentage between TiO_2/graphene variants. On the other hand, the crystal structure of ZrO_2 in the

ZrO_2/graphene hybrids (Figure 3.5b) was found monoclinic as expected; tetragonal and cubic phases are known to be unstable at ambient conditions.[16,17] The average particle sizes of TiO_2 and ZrO_2 NPs were obtained using the Scherrer equation[18] based upon anatase (101) peak for TiO_2 and monoclinic ($\bar{1}11$) peak for ZrO_2. The calculated NP sizes were T-G: 17.6, T-hG: 19.2, T-oG: 15.1, Z-G: 5.7, Z-hG: 4.7, and Z-oG: 9.3 nm in agreement with the TEM images.

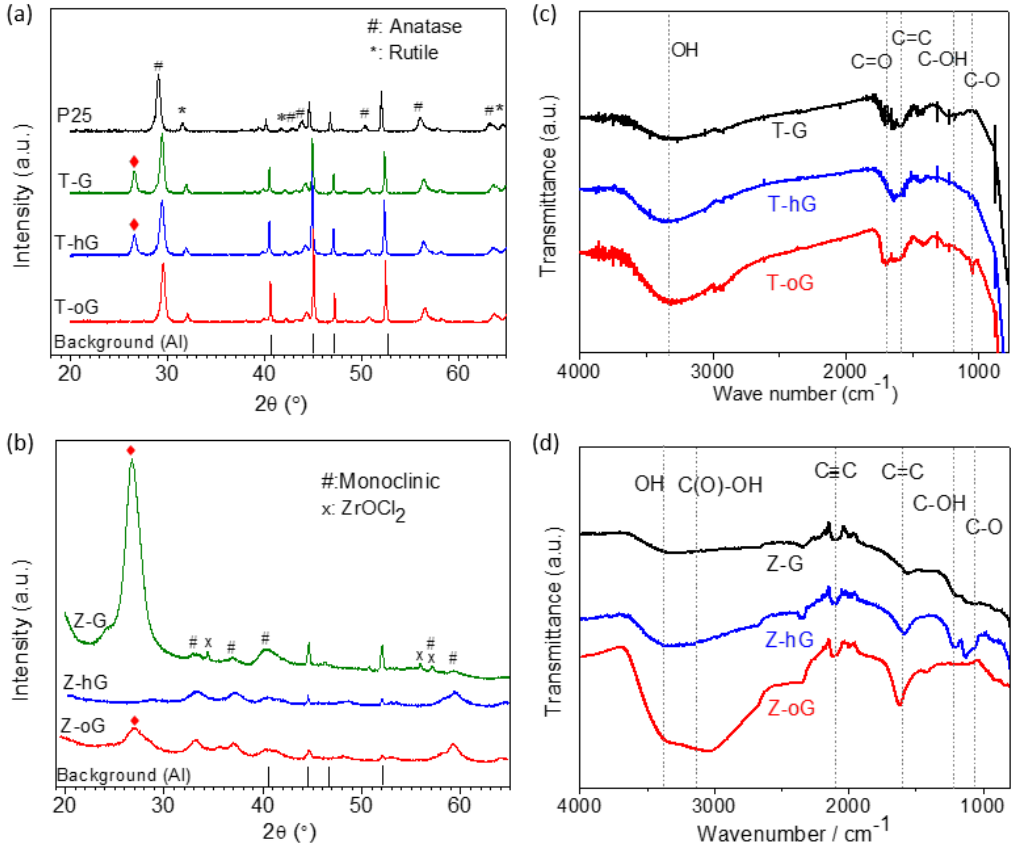

Figure 4.5: XRD spectra of (a) T-G, T-hG, T-oG and P25, and (c) Z-G, Z-hG and Z-oG. Co Kα radiation (λ = 1.78897 Å) was used. Note the peak locations of background is marked in the bottom. JCPDS Card No. 21-1272 and 21-1276 for TiO_2; ICDD Code No. 01-086-1451 for ZrO_2. FT-IR spectra of (b) T-G, T-hG and T-oG, and (d) Z-G, Z-hG and Z-oG.

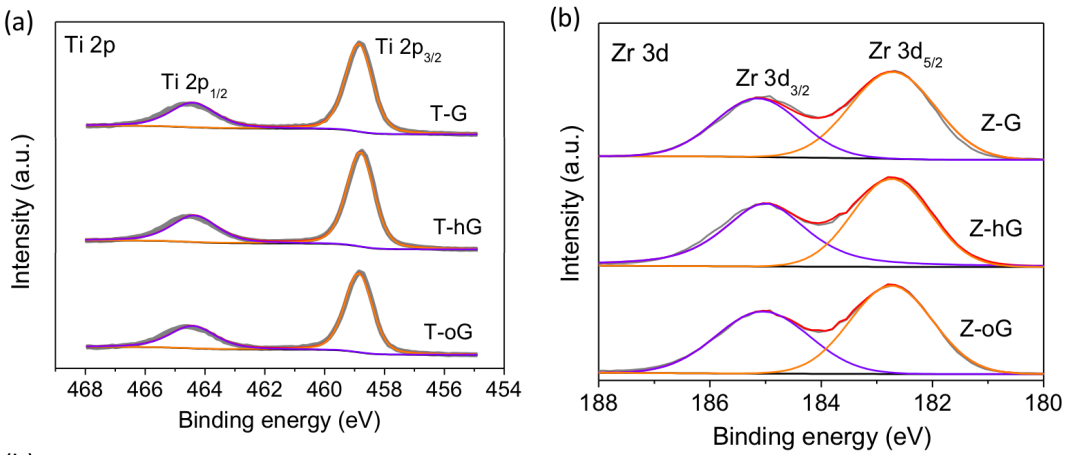

Figure 4.6: (a) XPS Ti 2p spectra of T-G, T-hG and T-oG. (b) Zr 3d spectra of Z-G, Z-hG and Z-oG. For standard TiO_2 and ZrO_2 spectra

An interesting XRD result is about the peak at 26.5°, which corresponds to the (002) diffraction of graphene (d-spacing of 0.39 nm) formed by graphene sheet restacking.[19,20] Graphene sheets tend to restack upon each other due to π-π stacking interaction and van der Waals attraction between their basal planes.[1,21] If there were a stable spacer between graphene layers, however, it would suppress the restacking of graphene sheets. In this sense, the absence of 26.5° peak in the T-oG (TiO_2 on carboxylated graphene) and Z-hG (ZrO_2 on hydroxylated graphene) is likely due to a stable anchoring of their TMO NPs on the graphene surfaces. On the other hand, a distinct diffraction peak at ~26.5° found in all the other hybrid samples (T-G, T-hG, Z-G and Z-oG) implies a significant restacking between their graphene layers probably due to an unstable anchoring of NPs. It was reported that the adsorption of TiO_2 on graphene is calculated to be most stable on carboxylate sites,[22] which is well aligned with the absence of (002) peak from T-oG. The FT-IR spectra shown in Figure 4.5(c) and Figure 4.5(d) support the XRD analysis. In comparison to the spectra of G, hG and oG (Figure 4.3(a)), those for TiO_2/graphene (Figure 4.5(c)) and ZrO_2/graphene hybrids (Figure 4.5(d)) show that oxygen-containing functional groups (C–O, C–OH and C=O) were largely removed after anchoring TMO NPs, except for the C=O stretching in T-oG and the C–OH stretching in Z-hG. This indicates that only the TiO_2 NPs on carboxyl groups and ZrO_2 NPs on hydroxyl group are still tethered on the graphene surface while all other unbound functional groups were removed during the hydrothermal reaction. This corroborates the aforementioned analysis on the ~26.5° XRD peak. On the other hand, the adsorption at low frequency region < 1000 cm^{-1} is ascribed to the vibration of Ti–O stretching in TiO_2,[15] and Zr–O stretching in ZrO_2.[23]

Figure 4.6 presents the Ti 2p XPS core-level spectra for TiO_2/graphene and the Zr 3d spectra of ZrO_2/graphene hybrids. The Ti 2p3/2 and Ti 2p1/2 peaks of T-G, T-hG and T-oG are located ~0.3 eV lower than the reported binding energies of the stoichiometric TiO_2 (459.1 and 465.0 eV, respectively),[24] indicating the existence of lower valence states (e.g. Ti^{3+}) in the P25 NPs. Likewise, the Zr $3d_{5/2}$ peaks of the three samples are

located ~0.3 eV lower than the reported binding energies of the stoichiometric ZrO_2 (182.6 eV)[25]. The slightly lower value also indicates an existence of lower Zr valence states.[26] More importantly, there is little difference in the peak locations of Ti $2p_{3/2}$, Ti $2p_{1/2}$, Zr $3d_{5/2}$ and Zr $3d_{1/2}$ (and thus in the stoichiometry of TiO_2 and ZrO_2 NPs) between the samples of each kind (TiO_2/graphene or ZrO_2/graphene). Therefore, the differences in ORR activity of hybrid catalysts (to be shown below) are not originated from any changes in valence state while the presence of low valence states may be a prerequisite for a high ORR activity. The wide scan XPS spectra of functionalized GOs and TiO_2/graphene and ZrO_2/graphene variants are provided in Figure 4.7.

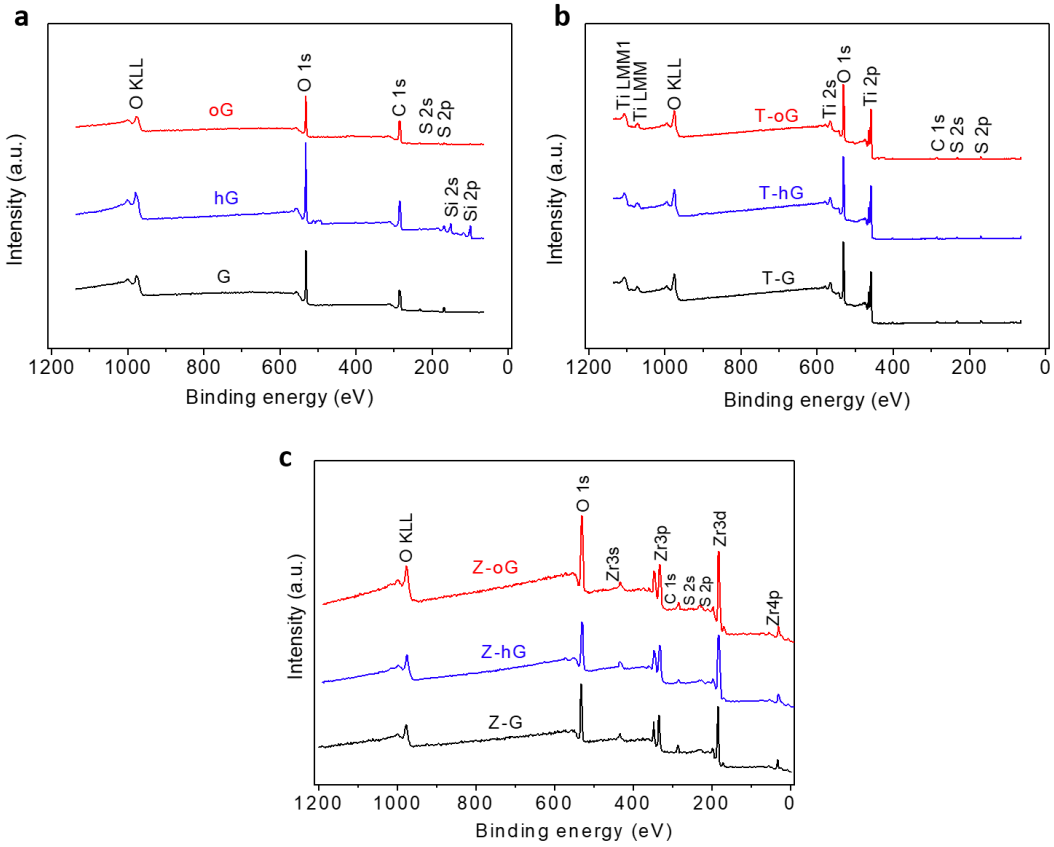

Figure 4.7: Wide scan XPS spectra of (a) functionalized graphene (G, hG and oG) and (b) TiO_2/graphene and (c) ZrO_2/graphene hybrid variants. Samples were drop-casted on a cleaned Si chip for the XPS analysis.

4.3.3 Electrochemical Characterization of Hybrid Catalysts

To assess the ORR activities of TiO_2/graphene and ZrO_2/graphene hybrid catalysts, CV, RDE and RRDE were performed in an aqueous solution of 0.1 M KOH. All samples have a solid loading of 0.18 mg cm^{-2} Pt/C (20 wt. % Pt) with the same mass loading (0.18 mg cm^{-2}) was also characterized for a comparison purpose. To probe the ORR activity of these catalysts, linear sweep voltammogram (LSV) was first performed in an O_2-saturated 0.1 M KOH solution at 1,600 rpm. Among the TiO_2/graphene hybrids, *carboxylated* graphene-based sample (i.e., T-oG) exhibited the highest onset potential (0.92 V versus RHE; all potentials versus RHE hereafter), half-wave potential (0.79 V) and current density (5.44 mA cm^{-2} at 0.2 V), close to those of Pt/C (0.92 V, 0.80 V and 5.54 mA cm^{-2} at 0.2 V, respectively) as shown in Figure 4.8(a). As for ZrO_2/graphene hybrids, however, *hydroxylated* graphene-based sample (i.e., Z-hG) showed the best performance with the onset and peak potentials of 0.92 V and 0.83 V, respectively, and the limiting current density of 5.39 mA cm^{-1} at 0.2 V, outperforming the other hybrids by a significant margin (Figure 4.8(b)). The other hybrid catalysts (other than T-oG and Z-hG) exhibited significantly poorer ORR performances. On the other hand, it was reported that the location (basal versus edge sites) and types (C=O, C–OH, COOH, epoxide, etc.) of surface oxygen groups has an impact on the ORR activity.[27] To check if the surface oxygen groups play a deterministic role in ORR activity before anchoring NPs, LSV curves of functionalized graphenes themselves without NP incorporation (G, hG and oG) are also provided in Figure 4.9. Their performances are found much poorer than the hybrid counterparts, proving that the high ORR activity of hybrid catalysts is not originated from the functionalized graphene itself. The two hybrids exhibiting excellent ORR performance in 0.1 M KOH, T-oG and Z-hG, were found to perform well in an acid medium as well. Both T-oG and Z-hG afforded high current densities in O_2-saturated 0.5 M H_2SO_4 with decent onset potentials of 0.77 V and 0.85 V, respectively (see Figure 4.10).

The LSV curves at different rotating speeds and corresponding Koutecky−Levich (K−L) plots (inset) are shown for T-oG (Figure 4.8(c)) and Z-hG (Figure 4.8(d)); those for the other hybrids are presented in Figure 4.11 and Figure 4.12. All the K−L plots exhibit linear slopes indicating a first-order ORR kinetics with respect to oxygen activity. The ORR kinetics were also quantified from the Tafel plots of mass transport-corrected kinetic currents for TiO_2 and ZrO_2-based NP/graphene hybrids (Figure 4.8(e) and Figure 4.8(f), respectively). Tafel slopes of T-oG and Z-hG were 87 mV and 75 mV per decade, close to that of Pt/C (76 – 78 mV per decade) and significantly smaller than those of T-G, Z-G, T-hG and Z-oG (225, 235, 108 and 98 mV per decade, respectively). It is reminded that the two high-performance hybrids (i.e. T-oG and Z-hG) are the aforementioned catalysts with decent TMO-graphene bonds and without an appreciable restacking of graphene layers. CV curves of the hybrid catalyst are presented in Figure 4.13 showing the same trend in the onset potential and activity.

In Figure 4.14(a) and Figure 4.14(b), the peroxide yield and electron transfer number (n) are presented based upon RRDE voltammograms (see Figure 4.15) obtained at a disk sweep rate of 5 mV s^{-1} while fixing the ring potential at 1.3 V. The peroxide yield was < 1.2% for T-oG and < 4.2% for Z-hG, and n was 3.96 for T-oG and 3.94 for Z-hG on average in a wide potential range of 0.35 – 0.85 V, suggesting a 4-electron

pathway dominated ORR process. The T-G, Z-G, T-hG and Z-oG, however, exhibited much lower averaged n values of 3.21, 3.09, 3.51 and 3.12, respectively, in the potential window of 0.35 – 0.75 V. Similar n values were maintained only up to ~0.7 V, above which n started plunging. (A summary of ORR performance is provided in Table 4.2.). In addition, a durability of T-oG and Z-hG was compared to that of Pt/C in O_2-saturated 0.1 M KOH via a chronoamperometric measurement at 0.4 V (Figure 4.14(c)). The T-oG and Z-hG exhibited a better durability than Pt/C, retaining 81.7% and 83.6% of their original catalytic activity after ~12 h of operation (Pt/C: 76.5%). In a separate characterization in 1 mM H_2O_2-containing KOH, it was found that T-oG and Z-hG showed a significant activity toward peroxide reduction (Figure 4.16), suggesting the possibility that the ORR activity was partially contributed by the associative ORR pathway. GO variants or P25 NPs alone exhibited little activity for peroxide reduction.

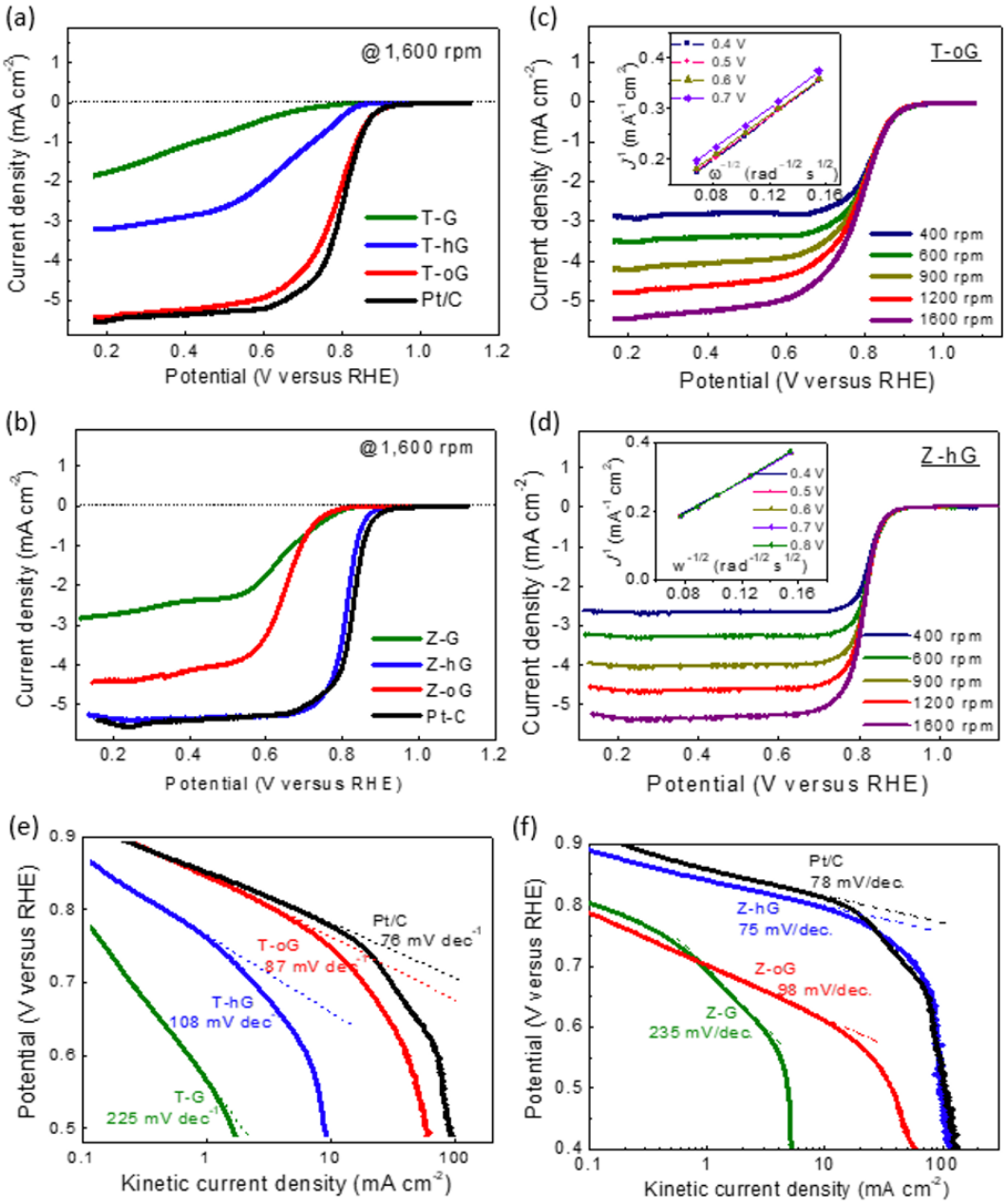

Figure 4.8: LSV curves of (a) TiO_2/graphene and (d) ZrO_2/graphene variants obtained at a rotating rate of 1,600 rpm in O_2-saturated 0.1 M KOH solution. RDE LSV curves of (b) T-oG and (e) Z-hG in O_2-saturated 0.1 M KOH at a sweep rate of 5 mV s^{-1}. Inset: the corresponding Koutechy-Levich plot at various disk potentials. Mass-transport corrected Tafel plots of (c) TiO_2/graphene and (f) ZrO_2/graphene variants derived from the LSV curves at 1,600 rpm. All voltammograms presented are IR-compensated.

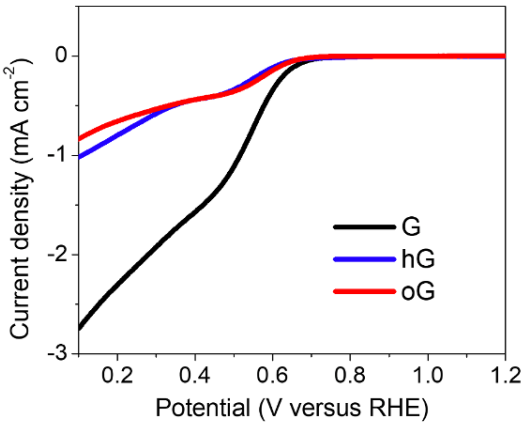

Figure 4.9: Rotating disk voltammograms of G, hG and oG in O_2-saturated 0.1 M KOH at a rotating speed of 1600 rpm and a sweep rate of 5 mV s^{-1}. Note that all the samples include black carbon additives for electrical conductivity.

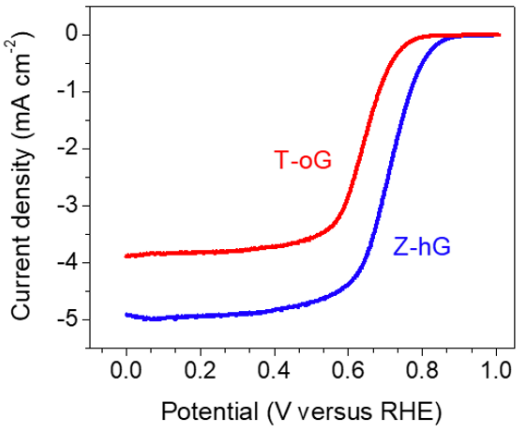

Figure: 4.10 Rotating disk voltammograms of T-oG, Z-hG in O_2-saturated 0.5 M H_2SO_4 at a rotating speed of 1600 rpm and a sweep rate of 5 mV s^{-1}. The onset potentials of T-oG and Z-hG are 0.77 V and 0.85 V versus RHE, respectively.

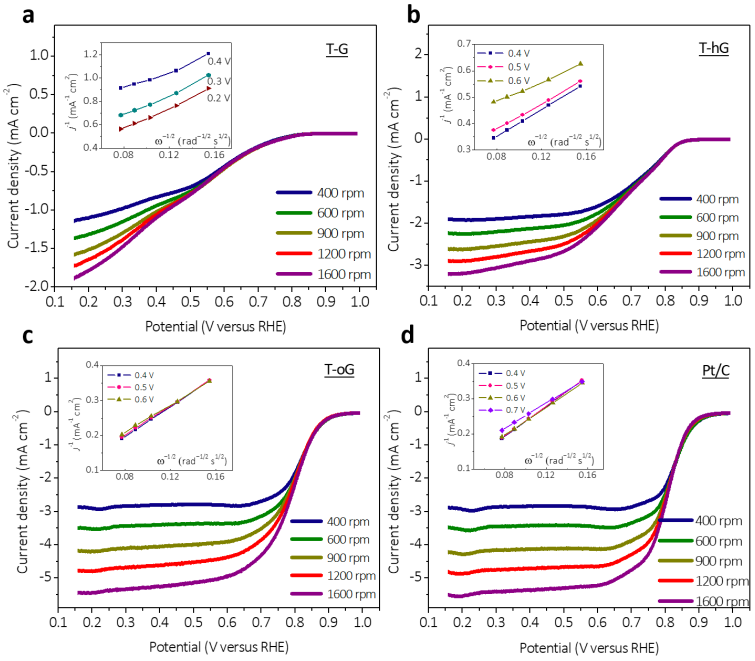

Figure 4.11: Rotating disk voltammograms of (a) T-G, (b) T-hG, (c) T-oG and (d) Pt/C in O_2-saturated 0.1 M KOH at a sweep rate of 5 mV s^{-1}. The inset shows the corresponding Koutechy-Levich plots at different disk potentials.

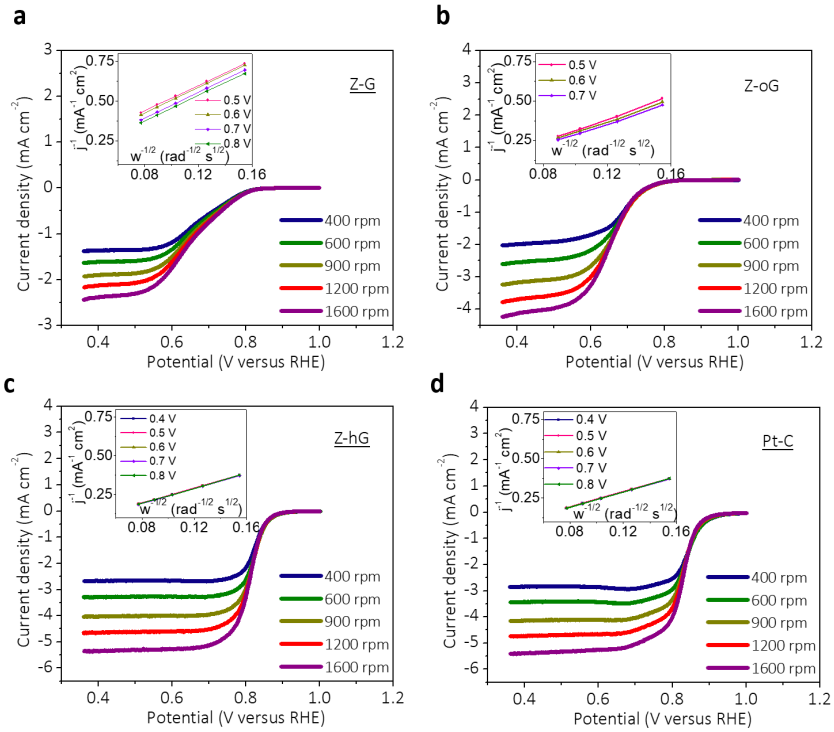

Figure 4.12: Rotating disk voltammograms of (a) Z-G, (b) Z-hG, (c) Z-oG and (d) Pt/C in O_2-saturated 0.1 M KOH at a sweep rate of 5 mV s^{-1}. The inset shows the corresponding Koutechy-Levich plots at different disk potentials.

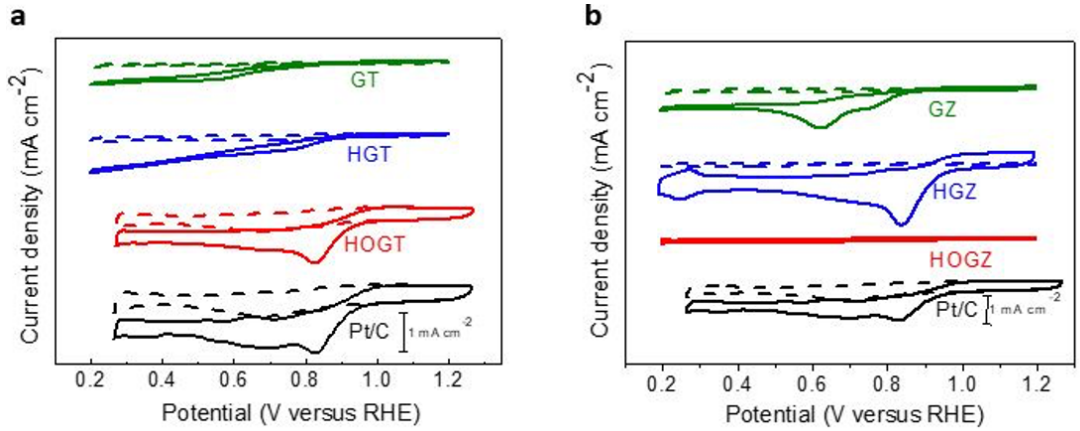

Figure 4.13: CV sweeps of (a) TiO_2/graphene and (b) ZrO_2/graphene hybrids at a scan rate of 50 mV cm^{-1} in N_2 (dotted) and O_2-saturated (solid) 0.1 M KOH solution.

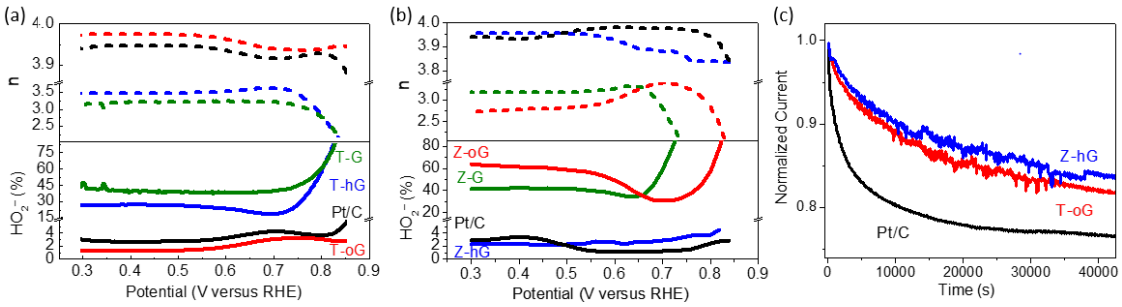

Figure 4.14: The electron transfer number n (upper) and peroxide generation in percentage (lower) TiO_2/graphene and (b) ZrO_2/graphene variants deduced from the RRDE data. (c) Relative ORR current nor by the initial current; based upon chronoamperometric voltammograms of T-oG, Z-hG and Pt/C at 0.4 V vs 1,600 rpm over ~12 h in O_2-saturated 0.1 M. KOH.

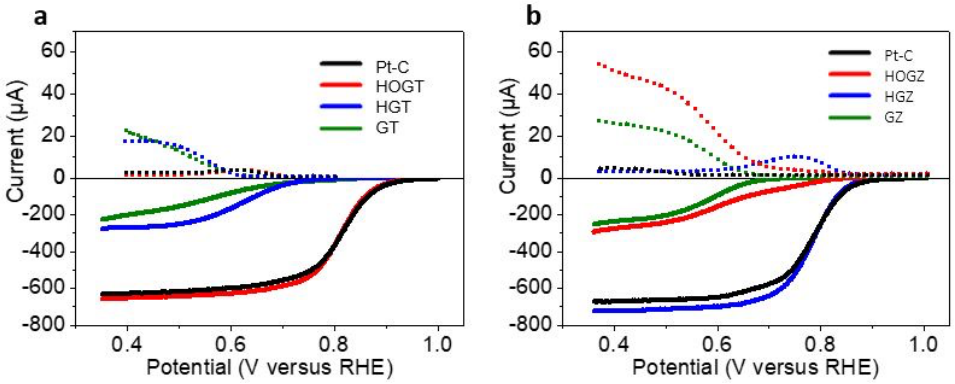

Figure 4.15: RRDE voltammograms of (a) TiO_2/graphene. (b) ZrO_2/graphene hybrids obtained in O_2-saturated 0.1 M KOH at 1600 rpm. Ring current (upper graph) and disk current (lower graph) are shown in dotted and solid lines, respectively. The disk potential was scanned at 5 mV s^{-1} while the ring potential was fixed at 1.3 V vs RHE. Presented after IR-compensation.

Table 4.2: A summary of ORR performance quantified in O_2-saturated 0.1 M KOH at a rotating rate of 1600 rpm. The RRDE for electron transfer number was performed at 1400 rpm.

		T-G	T-G	T-hG	Z-oG	T-oG	Z-hG	Pt/C
Onset potential[†] (V vs. RHE)		0.75	0.84	0.84	0.80	0.92	0.90	0.92
Half-wave potential (V vs. RHE)		0.61	0.66	0.62	0.66	0.79	0.76	0.80
Tafel slope (mV/decade)		225	235	108	98	87	75	76
Current density at 0.2V[‡] (mA/cm^2)		1.78	1.78	3.20	4.40	5.44	5.39	5.54
Mass activity[§] (A/g)	@ 0.90 V	0.05	0.05	0.07	0.08	1.96	4.13	2.44 (12.2)
	@ 0.85 V	0.22	0.22	0.18	0.61	9.78	34.35	11.3 (56.5)
	@ 0.80 V	0.70	0.70	0.51	4.16	46.5	210.4	47.0 (235.3)
Electron transfer number[*]		3.21	3.09	3.51	3.12	3.96	3.94	3.94

[†] Chosen to be the potential reaching 0.1 mA/cm^2.
[‡] IR-compensated current densities quantified at 0.2 V vs. RHE.
[§] Kinetic current per TiO_2/graphene, ZrO_2/graphene or Pt/C mass (excluding additives such as Nafion and additional carbon black); 123.2 $\mu g/cm^2$ for all samples. The values in the parenthesis is based upon the mass of Pt only (24.6 $\mu g/cm^2$).
[*] Averaged values within the potential window of 0.35 – 0.75 V vs. RHE. Quantified based upon the RRDE data.

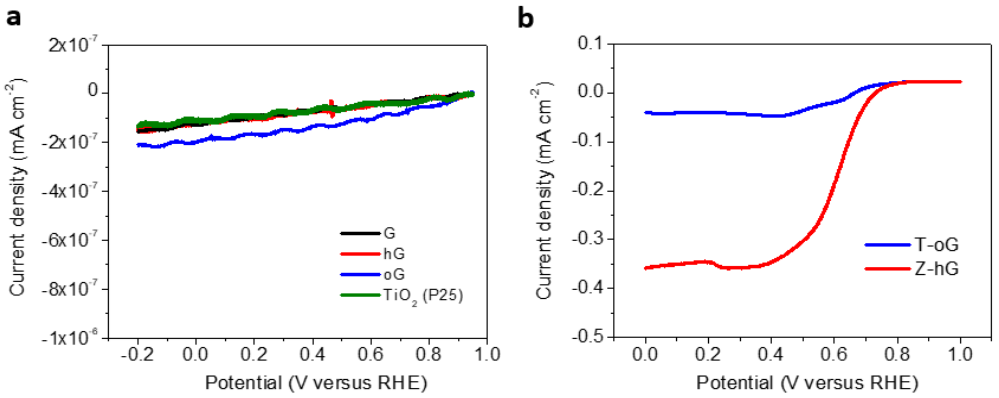

Figure 4.16: Rotating disk voltammograms of (a) G, hG, oG and P25 and (b) T-oG and Z-hG in 1mM H_2O_2-containing Ar-saturated 0.1 M KOH at a sweep at of 5 mV s^{-1}. Only T-oG and Z-hG in 1mM

In addition, a durability of T-oG and Z-hG was compared to that of Pt/C in O_2-saturated 0.1 M KOH via a chronoamperometric measurement at 0.4 V (Figure 4.14(c)). The T-oG and Z-hG exhibited a better durability than Pt/C, retaining 81.7% and 83.6% of their original catalytic activity after ~12 h of operation (Pt/C: 76.5%). In a separate characterization in 1 mM H_2O_2-containing KOH, it was found that T-oG and Z-hG showed a significant activity toward peroxide reduction (Figure 4.16), suggesting the possibility that the ORR activity was partially contributed by the associative ORR pathway. GO variants or P25 NPs alone exhibited little activity for peroxide reduction.

4.3.4 DFT Computational Results

DFT calculations were performed as described in Method section. The interfaces to be explained hereafter are meant the "plane-bonded" interfaces, because the ORR was inactive in the "edge-bonded" interfaces. The calculated E_f of each TiO_2/graphene interface was -1.29, -3.16, and -1.22 eV for TEG, THG, and TCG, respectively, indicating that all three functional groups create a stable bond between TiO_2 and graphene basal plane (illustration in Figure 4.17). The gap between TiO_2 and graphene was observed to be 3.5 – 4.6 Å depending on the functional groups, which will provide

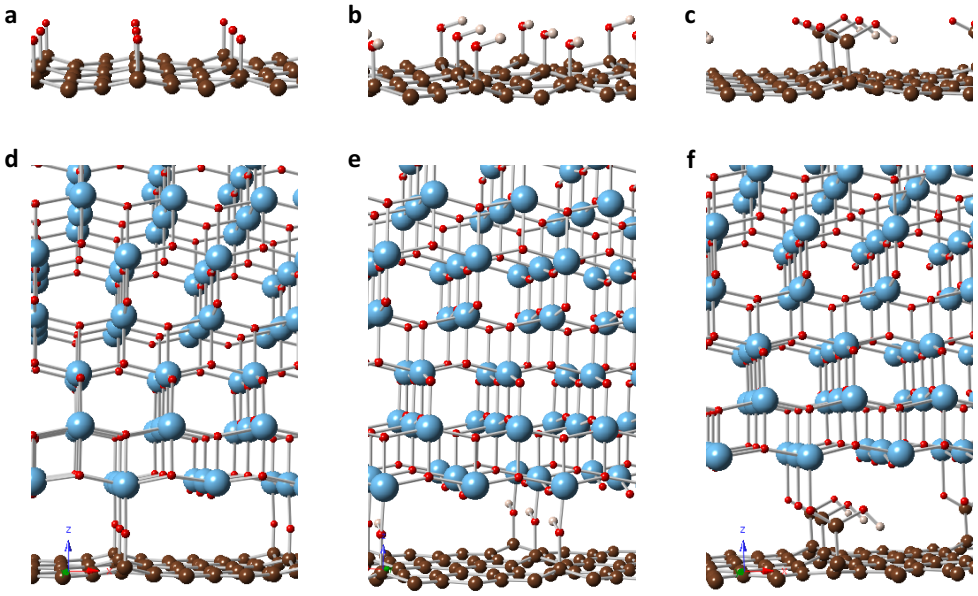

Figure 4.17: The structures of functionalized graphenes with (a) epoxy group, (b) hydroxyl group, and (c) carboxyl group on their basal planes. Their interface with {001}-TiO_2 through (d) epoxy, (e) hydroxyl, and (f) carboxyl group. Each color represents an element; Blue: Ti, Red: O, Brown: C, Grey: H.

acceptable space for the diffusion of oxygen molecules along the interface. The stable structures of ORR intermediates were also obtained. It was observed that all three functional

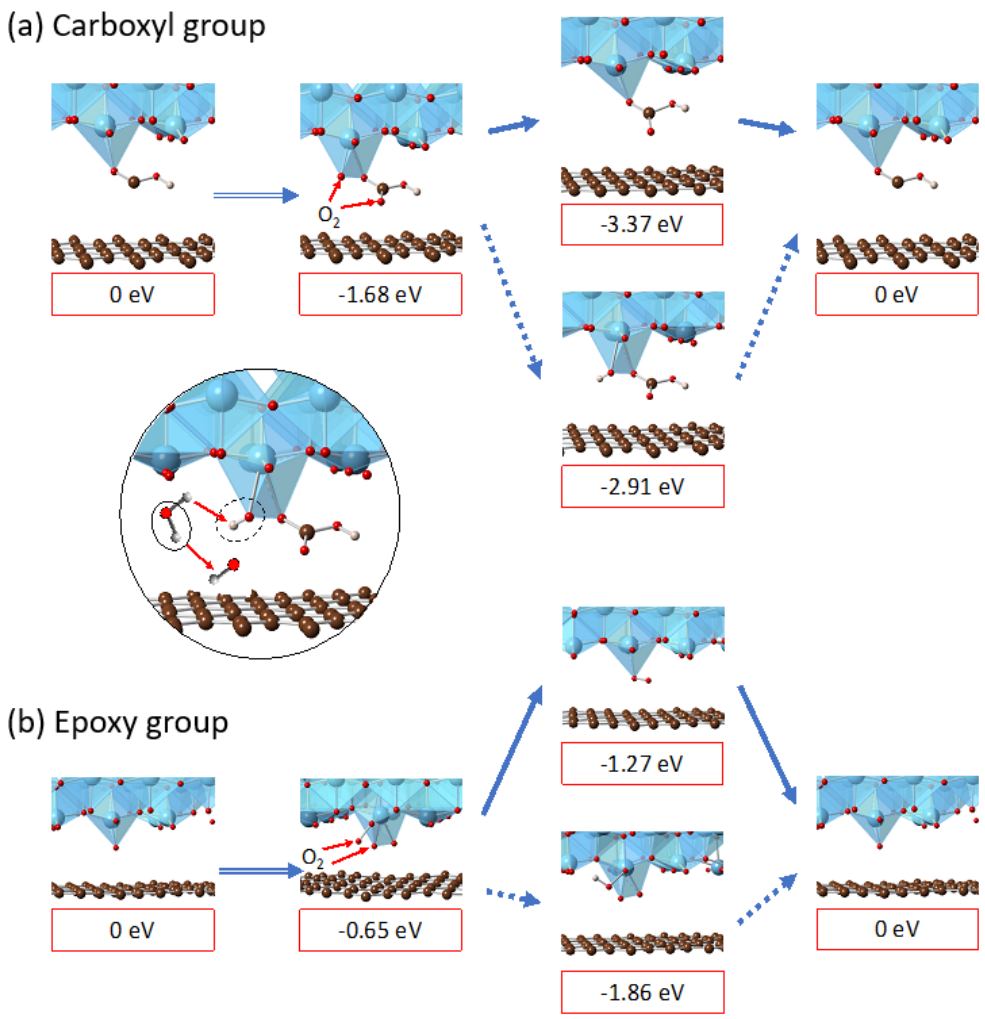

Figure 4.18: The ORR process in the (a) TCG and (b) TEG interface. Double arrows correspond to the dissociation of oxygen molecules. Continuous and dashed lines represent the 4-electron and 2-electron transfer pathways, respectively. Note that the bonds between functional groups and graphene were omitted intentionally for better visibility (refer to Supplemental Information for the illustration of the bonds). The circular Inset figure shows a zoom-in illustration of the first-step of the 2-electron transfer – one H_2O molecule disproportionate to one H atom, which forms a bond to a dissociated O and one OH. In the 4-electron transfer pathway, the formed OH (enclosed by the dashed oval) is detached from the functional group producing another OH^- in the solution. Credit: Dr. Eunseok Lee at the University of Alabama, Huntsville.

groups break the bonds to the graphene basal plane (while keeping the bonds to TiO_2) during the dissociation of oxygen molecule and form a new bond with the dissociated oxygen atom. Note that such bond-breakings occur as a result of the dissociation, and the

electron transfer from graphene will occur before the bonds are broken. Due to an activation energy barrier of 0.4 – 0.8 eV for the bond-breaking, only a portion of functional groups will participate in the ORR while the others retain the bond with the graphene. The structural change and ΔE_f during the ORR for TiO_2/graphene interfaces are presented in Figure 3.18. A comparison of ΔE_f indicates that TCG prefers the 4-electron transfer pathway while TEG favors the 2-electron transfer pathway, in an excellent accordance with the experimental observations, in which the T-oG exhibited an electron transfer number very close to 4 unlike T-G. In both TEG and TCG, two oxygen atoms dissociated from a molecular O_2 preferred to exist close to each other making bonds to a single functional group. In THG, on the other hand, such a configuration was slightly unfavorable (ΔE_f = 0.13 eV), and one O^* atom tends to make a bond to a hydroxyl group while the other was likely bound to a Ti. In this case, the formation of peroxide ion (OOH^-) is impeded, leaving the 4-electron transfer

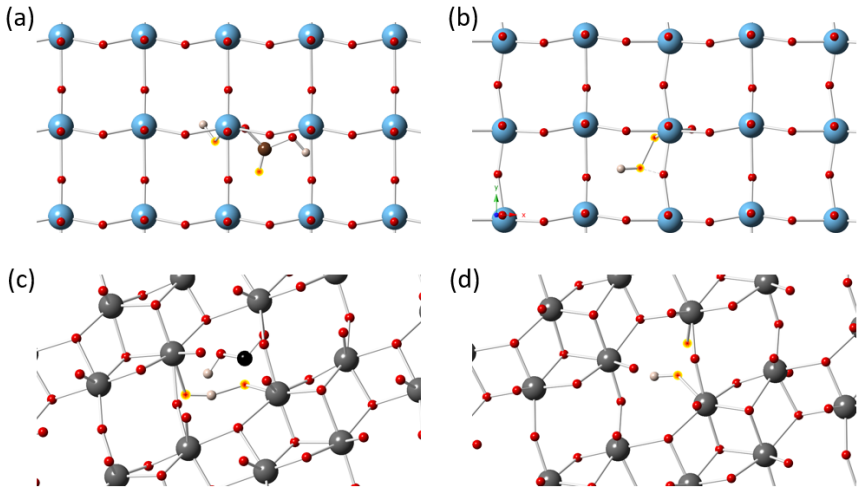

Figure 4.19: Illustration of (a) TCG, (b) TEG, (c) ZCG, and (d) ZEG after one O_2 molecule is dissociated and one water molecule is associated subsequently. The blue, grey, black, white, and red spheres correspond to Ti, Zr, C, H, and O. The yellow highlighted spheres indicate the dissociated oxygen (O*). For better visibility, only the bottom layer of slab structures, functional groups, O*s, and protons are displayed. Note that the structures in (a) and (b) are also shown in Figure 3.18. Credit: Dr. Eunseok Lee at the University of Alabama, Huntsville.

the only viable pathway. This explains the experimental observation that the T-hG showed an electron transfer number higher than that of the T-G.

A similar DFT study for ZrO_2/graphene interfaces was also performed. The calculated E_f was -2.44, -1.77, and -0.46 eV for ZEG, ZHG, and ZCG, respectively, indicating that all three functional groups also create a stable bond between ZrO_2 and graphene basal plane. The ΔE_f after
the association of one water molecule was -1.84 eV for ZEG, -1.58 eV for ZHG, -2.05 eV for ZCG, respectively, via 4-electron transfer pathway, while it was -0.32 eV for ZEG, -1.31 eV for ZHG, -2.64 eV for ZCG, respectively, via 2-electron transfer pathway.

Interestingly, this result indicates ZEG and ZHG prefer 4-electron transfer to 2-electron transfer while ZCG prefers 2-electron transfer to 4-electron transfer, which is the opposite to the tendency for TiO_2/graphene interfaces as well as agrees with the experimental result. We speculate that such a different preference on the electron transfer pathway originates from the structural difference between {001}-TiO_2 and {111}-ZrO_2 and the corresponding difference on the preferred sites for O^* attachment. Figure 4.18 compares the structures of intermediate states after the first step of the association via 2-electron transfer pathway between TCG, TEG, ZCG, and ZEG – for better visibility only the bottom layer of slab structures, functional groups, O^*s, and protons are displayed. It is seen that two O^*s attach to one Ti and the carbon of carboxyl group, respectively, in TCG and one Ti and one oxygen, respectively, in TEG, while both O^*s attach to Zr in ZCG and ZEG. This result is in line with the fact that Zr allows higher coordination number than Ti. The coordination number of metal center was 5 and 6 for Ti and Zr, respectively without a functional group attachment, and it increased to 6 and 7 with the functional groups attached. In TCG, the formation of $O^*O^*H^-$ is suppressed due to the long distance between two O^*s and hence the state becomes more favorable when the O^*H is detached from the interface, while a stable $O^*O^*H^-$ forms in ZCG. On the other hand, in TEG, two O^*s are located in close vicinity of each other forming a stable $O^*O^*H^-$ while two O^*s in ZEG are far apart suppressing the formation of a stable $O^*O^*H^-$. This difference in the formability of a stable $O^*O^*H^-$ can explain the preference to 4-electron transfer pathway in TCG and ZEG, and 2-electron transfer pathway in TEG and ZCG.

4.4 Conclusion

We demonstrated the critical impact of a proper priori graphene functionalization on the ORR performance of resulting TMO/graphene hybrid catalysts. Acid treatment was performed on GOs to induce more hydroxyl or carboxyl groups before anchoring TMO NPs (either TiO_2 or ZrO_2) by a hydrothermal reaction. First, among TiO_2(P25)/graphene hybrids, the T-oG (P25 NPs anchored on carboxylated graphene) showed the best ORR performance, close to that of Pt/C of an equal mass loading, in terms of onset potential, half-wave potential and Tafel slope with a 4-electron transfer dominated process. A similar observation was made for ZrO_2/graphene hybrids except for the fact that the Z-hG (ZrO_2 NPs anchored on hydroxylated graphene, not carboxylated graphene) exhibited the best performance, again very closed to that of Pt/C, with a 4-electron transfer process. All the other hybrid catalysts performed much worse than these two hybrids (T-oG and Z-hG) and their electron transfer numbers were significantly lower than 4, spanned between ~3.1 and ~3.5. As the size, phase and stoichiometry of NPs themselves were not different appreciably among hybrid catalyst variants, the significant differences in the ORR activity and charge transfer route are believed originated from the interface of NP/graphene, not from the NPs per se.

The excellent ORR performance of T-oG and Z-hG are surprising in that both TiO_2 and ZrO_2 have been considered to be relatively inert against ORR catalysis. While stoichiometric TiO_2 and ZrO_2 have an insulating nature with wide bandgaps (~3 – 5 eV),[28,29] they exhibit n-type semiconducting properties with anionic vacancies.[28,30] Probable presence of localized oxygen defects at their interface with graphene may have lowered/narrowed the electrical energy barrier and/or generated intermediate energy

levels, facilitating electronic tunneling or hopping through the interface.[31] The possible introduction of ionic defects and associated changes in valence states at the *interface* would not likely have been detected by the aforementioned XPS analysis because the interfaces are supposed to be hidden below TMO NPs.

From a series of characterization, it was found that P25 NPs tend to be anchored on graphene surfaces mostly through carboxyl groups while ZrO_2 NPs were bound through hydroxyl groups. A stable anchoring of NPs on graphene surface is conjectured to have prevented the restacking of graphene layers, providing more active sites (NP/graphene interface) available for reactant access. In addition, DFT calculations showed that oxygen dissociation is much less active at the interface of TMO NPs with graphene *edges* than the interface with *basal planes* of graphene. Electrochemical analyses are well aligned with the reasoning/information since the high performance hybrids (T-oG and Z-hG), unlike the other hybrids, are expected to provide a fluent reactant access to the highly active interfaces on the basal planes.

A series of DFT calculations is also supportive of the electrochemical results in that TiO_2 NPs anchored on carboxylated graphene and ZrO_2 NPs tethered on hydroxylated graphene surface favor the 4-electron transfer ORR pathway unlike other TMO/graphene catalysts. Such a different preference on the electron transfer pathway is ascribed to the structural difference of NPs interfacing with the graphene and functional groups, and the corresponding preferred sites for the oxygen dissociation.

References

1. Wu, Z.-S. *et al.* Graphene/metal oxide composite electrode materials for energy storage. *Nano Energy* **1**, 107–131 (2012).
2. Hummers, W. S. & Offeman, R. E. Preparation of Graphitic Oxide. *J. Am. Chem. Soc.* **80**, 1339–1339 (1958).
3. Marcano, D. C. D. *et al.* Improved synthesis of graphene oxide. *ACS Nano* **4**, 4806–4814 (2010).
4. Perdew, J. P., Burke, K. & Ernzerhof, M. Generalized Gradient Approximation Made Simple. *Phys. Rev. Lett.* **77**, 3865–3868 (1996).
5. Perdew, J. P., Burke, K. & Ernzerhof, M. Generalized Gradient Approximation Made Simple [Phys. Rev. Lett. 77, 3865 (1996)]. *Phys. Rev. Lett.* **78**, 1396–1396 (1997).
6. Kresse, G. & Joubert, D. From ultrasoft pseudopotentials to the projector augmented-wave method. *Phys. Rev. B* **59**, 1758–1775 (1999).
7. Kresse, G. & Furthmüller, J. Efficiency of ab-initio total energy calculations for metals and semiconductors using a plane-wave basis set. *Comput. Mater. Sci.* **6**, 15–50 (1996).
8. Kresse, G. & Hafner, J. Ab initio molecular-dynamics simulation of the liquid-metal–amorphous-semiconductor transition in germanium. *Phys. Rev. B* **49**, 14251–14269 (1994).
9. Kresse, G. & Hafner, J. Ab initio molecular dynamics for liquid metals. *Phys. Rev. B* **47**, 558–561 (1993).
10. Ge, X. *et al.* Oxygen Reduction in Alkaline Media: From Mechanisms to Recent Advances of Catalysts. *ACS Catal.* **5**, 4643–4667 (2015).

11. Pei, D.-N. *et al.* Defective titanium dioxide single crystals exposed by high-energy {001} facets for efficient oxygen reduction. *Nat. Commun.* **6**, 8696 (2015).
12. Chen, S., Zhu, J., Wu, X., Han, Q. & Wang, X. Graphene Oxide−MnO_2 Nanocomposites for Supercapacitors. *ACS Nano* **4**, 2822–2830 (2010).
13. Xu, Y. & Shi, G. Assembly of chemically modified graphene: methods and applications. *J. Mater. Chem.* **21**, 3311 (2011).
14. Liu, Y., Deng, R., Wang, Z. & Liu, H. Carboxyl-functionalized graphene oxide–polyaniline composite as a promising supercapacitor material. *J. Mater. Chem.* **22**, 13619 (2012).
15. Zhang, H., Lv, X., Li, Y., Wang, Y. & Li, J. P25-Graphene Composite as a High Performance Photocatalyst. *ACS Nano* **4**, 380–386 (2010).
16. Sternik, M. & Parlinski, K. Lattice vibrations in cubic, tetragonal, and monoclinic phases of ZrO_2. *J. Chem. Phys.* **122**, 064707 (2005).
17. Mirgorodsky, A., Smirnov, M. & Quintard, P. Lattice-dynamical study of the cubic-tetragonal-monoclinic transformations of zirconia. *Phys. Rev. B - Condens. Matter Mater. Phys.* **55**, 19–22 (1997).
18. Patterson, A. L. The Scherrer Formula for X-Ray Particle Size Determination. *Phys. Rev.* **56**, 978–982 (1939).
19. Yang, X. *et al.* Ordered Gelation of Chemically Converted Graphene for Next-Generation Electroconductive Hydrogel Films. *Angew. Chemie Int. Ed.* **50**, 7325–7328 (2011).
20. Yang, X., Cheng, C., Wang, Y., Qiu, L. & Li, D. Liquid-mediated dense integration of graphene materials for compact capacitive energy storage. *Science (80-.).* **341**, 534–7 (2013).
21. Cao, X., Yin, Z. & Zhang, H. Three-dimensional graphene materials: preparation, structures and application in supercapacitors. *Energy Environ. Sci.* **7**, 1850–1865 (2014).
22. Ayissi, S. *et al.* Interaction of Titanium Oxide Nanostructures with Graphene and Functionalized Graphene Nanoribbons: A DFT Study. *J. Phys. Chem. C* **117**, 25424–25432 (2013).
23. Berger, T., Monllor-Satoca, D., Jankulovska, M., Lana-Villarreal, T. & Gómez, R. The electrochemistry of nanostructured titanium dioxide electrodes. *ChemPhysChem* **13**, 2824–2875 (2012).
24. Xing, M., Zhang, J. & Chen, F. New approaches to prepare nitrogen-doped TiO_2 photocatalysts and study on their photocatalytic activities in visible light. *Appl. Catal. B Environ.* **89**, 563–569 (2009).
25. Ardizzone, S. & Bianchi, C. L. XPS characterization of sulphated zirconia catalysts: The role of iron. *Surf. Interface Anal.* **30**, 77–80 (2000).
26. Basahel, S. N., Ali, T. T., Mokhtar, M. & Narasimharao, K. Influence of crystal structure of nanosized ZrO_2 on photocatalytic degradation of methyl orange. *Nanoscale Res. Lett.* **10**, 73 (2015).
27. Wu, K.-H., Wang, D.-W. & Gentle, I. R. Revisiting oxygen reduction reaction on oxidized and unzipped carbon nanotubes. *Carbon N. Y.* **81**, 295–304 (2015).
28. Soriano, L., Abbate, M., Faber, J., Morant, C. & Sanz, J. . The electronic structure of ZrO_2: Band structure calculations compared to electron and x-ray spectra. *Solid*

State Commun. **93**, 659–665 (1995).
29. Scanlon, D. O. *et al.* Band alignment of rutile and anatase TiO_2. *Nat. Mater.* **12**, 798–801 (2013).
30. Kwon, D.-H. *et al.* Atomic structure of conducting nanofilaments in TiO_2 resistive switching memory. *Nat. Nanotechnol.* **5**, 148–153 (2010).
31. Lee, M. H. *et al.* Study on the electrical conduction mechanism of bipolar resistive switching TiO_2 thin films using impedance spectroscopy. *Appl. Phys. Lett.* **96**, 152909 (2010).

Chapter 5: Highly Active Bifunctional Oxygen Electrocatalytic Sites Realized in Ceria Functionalized Graphene

5.1 Introduction

The widely accepted benchmark catalysts use noble metals: Pt for ORR and IrO_2 or RuO_2 for OER as mentioned in previous chapters. Since these materials are good catalysts for one reaction, not for both, they are not suitable for metal-air batteries[1,2] or unitized regenerative fuel cells (URFCs)[3] that require efficiency for both ORR and OER in each given device. Furthermore, their limited availability, high cost, and poor operational stability prohibits them from widespread commercial applications.[4,5] Generally, materials and configurations tuned for ORR, are not optimal for OER. Thus, the development of high-performance bifunctional oxygen electrocatalysts remains an ongoing challenge in the community.[2]

Metal oxides (MOs) including Co_3O_4,[6–8] Mn_3O_4,[9–11], Fe_3O_4[12,13] and their hydroxide analogs such as FeNiOOH[14,15] have been widely considered as an alternative to the noble metal-based oxygen electrocatalysts owing to their high catalytic activity, good stability, earth-abundance, and low cost.[16,17] To supplement for their low electronic conductivity, MO nanoclusters (NCs) are often anchored onto a conductive substrate, most notably, carbon nanostructures such as graphene, carbon nanotube and porous 3D carbon.[16] By incorporating a conductive substrate, one can leverage their high surface area while suppressing the agglomeration of MO by strongly anchoring them to the carbon nanostructure. These hybrid MO/carbon materials demonstrate a synergistic effect that achieves an unexpectedly high catalytic activity,[18–21] however, the exact mechanism for this enhancement remains largely unknown.[19–21] Wu and colleagues studied the origins of ORR synergy between Mn_3O_4 and graphene oxide (GO) nanoribbons and concluded that $>C-O-Mn^{3+}$ junction at the interface played a significant role in lowering the activation barrier against the initial O_2/HO^{2-} reduction and facilitating peroxide reduction.[22] Leng et al. revealed that the Co-O-C bond in Co_3O_4/graphene plays a critical role in OER activity by promoting surface charge transfer and assisting in the deprotonation of hydroxides on the catalyst surface.[8]

We demonstrated that chemical coupling between graphene and MO nanoclusters improves ORR kinetics.[23] Specifically, ZrO_2/hydroxylated graphene and TiO_2/carboxylated graphene showed excellent ORR performance in alkaline media, similar to that of Pt/C as seen in Chapter 4. The performance was surprising as both TiO_2 and ZrO_2 are inert for ORR. Interestingly, all other combinations of MO/graphene results in significantly lower performance compared to the two hybrid catalysts. The high performance was attributed to a stable anchoring of nanoparticles that was established through a specific type of oxygen-containing functional groups on graphene, thereby maximizing reactant access (by preventing graphene restacking).[23] In addition, the type of bonding affected the preferred sites for oxygen dissociation, which consequently determines the electron transfer pathway.

Inspired by our previous results, we focused on ceria (CeO_2) as the metal oxide to be composited with reduced graphene oxide for oxygen electrocatalysts. The facile transitions between Ce^{3+} and Ce^{4+} provide surface redox capability, reversible oxygen

exchange, and high oxygen storage capacity, all of which are expected to enhance catalytic activity.[24,25] While the use of CeO_2 as an oxygen electrocatalysis is much less common than other transition MOs, it was recently employed as the ORR/OER catalyst in combination with hydroxides[26,27] and carbon[28–30], or as a support of noble metal catalyst to extend oxygen storage capacity.[31–33]

In this work, we demonstrate that an appropriate functionalization of GO prior to anchoring CeO_2 NCs results in hybrid CeO_2/graphene catalysts with significantly improved ORR and OER performance, comparable to or even better than that of noble metal-based benchmark catalysts. Most notably, this enhancement is observed not only in alkaline solutions but also in acidic media. A mechanistic interpretation of this surprising performance is also presented through a combination of experimental analyses and density functional theory (DFT) calculations. We identify a common structural motif of the activated graphene responsible for bifunctional activity. While it is widely known that most non-noble metal oxide catalysts degrade rapidly in acidic conditions,[17] we additionally demonstrate that CeO_2/graphene-based catalyst can operate in an acidic environment with excellent stability if mixed with nitric and sulfuric acid-treated activated carbon (AC).

5.2 Methods

5.2.1 Preparation of hybrid catalysts

Hybrid catalysts made of CeO_2 NCs and functionalized graphene oxide (fGO) were synthesized through a hydrothermal reaction process at 180°C. Three different kinds of fGOs were prepared before the hydrothermal reaction: as-synthesized GO (eG; graphene functionalized mostly with epoxy group), hydroxylated GO (hG) and carboxylated GO (cG). For hG sample, 30 mg of GO, 3 ml of ethanol, and 27 ml of DI water were ultrasonicated for 0.5 h. Then, 2 ml of hydrobromic acid was added and stirred for 14 h. The resulting solution was filtered/washed with 200 ml of DI water and allowed to dry under a house vacuum. For a cG sample, an additional 600 mg of oxalic acid was added and stirred for 5 h after mixing HBr for 14 h. These acid treatments to generate hG and cG were intended to further create hydroxyl and carboxyl groups, respectively in GO.[34] After these acid treatments, the GO solution was filtered, washed with DI water and dried. The resulting 100 mg of dry GO was added to a solution made of 0.1 M of cerium (III) nitrate hexahydrate that was created three days prior in DI water (100 ml). This was then heated at 80 ºC for 3 h and allowed to cool at room temperature, during which DI water (~15 ml) was added to maintain the same level of water before heating. The suspension was stirred for 2 h and placed in a 90 ml Teflon-sealed dry-oven for a hydrothermal reaction. The reaction was performed at 180°C for 18 h and the resulting CeO_2-fGO hybrid materials starting with eG, hG and cG were named C-eG, C-hG and C-cG. A hybrid of C-hG and AC was synthesized by mixing 3.75 mg of activated carbon, 2 ml of a 1:1 ratio of 0.1 M HNO_3 and 0.1 M H_2SO_4, and 10 ml of ethanol with 15 mg of C-hG. This slurry was stirred for 4 h at 80 °C and dried under house vacuum.

5.2.2 Material Characterization

Transmission electron microscopy (TEM) and scanning transmission electron microscopy (STEM) images were recorded on a 200 kV FEI monochromated F20 UT Tecnai system. The STEM image was acquired with a convergence angle of 10 mrad and a detection angle of 30 mrad. Energy filtered transmission electron microscopy (EFTEM) in association with STEM was used to visualize elemental distribution. Sample preparation for TEM samples included drop-casting sonicated ethanol-suspended catalyst upon a 3 mm Lacey B Carbon 400 mesh grid from Ted Pella, followed by ambient drying. X-ray photoelectron spectroscopy (XPS) was performed on a PHI Quantum 2000 system using a focused, monochromatic Al Kα X-ray (1486.6 eV) source for excitation and a spherical section analyzer (200 μm diameter X-ray beam incident to the surface normal; detector set at 45°). The collected data were referenced to an energy scale with binding energies for Cu $2p_{3/2}$ at 932.7 ± 0.1 eV and Au $4f_{7/2}$ at 84.0 ± 0.1 eV. For XPS, catalysts were dispersed in ethanol and drop-cast onto a cleaned Si wafer. X-ray diffraction (XRD) pattern was recorded by a PANalytical X'Pert PRO with Co Kα radiation (λ = 1.78897 Å) at a step size of 0.02º and scanning rate of 0.04º s^{-1}. Sample preparation for XRD included 10 mg of catalyst sonicated with 5 ml in ethanol and then drop-casted upon an aluminum disk to dry in ambient conditions. Fourier transform infrared spectroscopy (FT-IR) samples were dried under vacuum for 36 h and placed on a diamond crystal. A silicon wafer was placed on top of the sample before spectra was recorded (Nicolet 380 system, Thermo Scientific). NMR characterization was employed to quantify the amount of each functional group. Breifly, 10 μL of 0.081 mmol of eG, hG and cG is dissolved in 0.4 ml of acetone-d6. After dissolution, transfer mixture into NMR tube that can withstand 500MHz for ^{19}F NMR was made. Then an additional 10 μL α,α,α-trifluorotoluene and 20 μL 4-flourophenyl isocyanate were added. The reaction mixture was left for 15 min at room temperature in the NMR tube to react completely. Once NMR tubes have been made, an additional acetone-d6 is added to make all the samples of the same volume/height. Then the ^{19}F NMR was recorded using 500 MHZ. Peaks at ~ -60, -116, -120, and -121 ppm were integrated. -60 was the internal standard.

5.2.3 Electrochemical Characterization

The ORR activity of the catalysts was evaluated using similar techniques as shown in Chapter 4.

5.2.4 Modeling and Computation

The ORR and OER activities are computed using the thermodynamic limiting potential framework using density functional theory (DFT). For all systems, we have employed PBE-DFT[35] functional PAW potentials, 500 eV plane-wave cutoff, using the Vienna Ab initio Simulation Package[36–38] (VASP, version 5.4.4) and 5.3 eV Hubbard-U correction applied to f-electrons of Ce-atoms as described previously.[39–41] Our simulation cells for ceria surfaces were contained a minimum of 3 layers with a 2×2 periodicity. The two topmost layers were always allowed to relax until the forces were lower than 0.02 eV A^{-1} using a 5×5×1 k-point mesh. Equivalent precision was also used for graphene unit cells.

The theoretical limiting potentials for ORR and OER were calculated directly from free energies of OH*, O* and OOH* intermediates assuming the most common 4-

electron associative single-site mechanism.[42,43] Details of this approach are presented in our recent ORR and OER reviews.[43,44] Less common dissociative ORR mechanism, [42,45] which bypasses OOH* step but also requires low barrier for binuclear bond breaking,[46] was not considered in this screening study. Using standard conditions (T = 298.15 K, p = 1 bar, pH = 0), it requires 1.23 eV for each elementary step, and 4.92 eV in total for an ideal catalyst to perform ORR. For ORR, the elementary reactions are:

$$O_2 + * + (H^+ + e^-) \longrightarrow OOH^* \quad (1)$$

$$OOH^* + (H^+ + e^-) \longrightarrow H_2O + O^* \quad (2)$$

$$O^* + (H^+ + e^-) \longrightarrow OH^* \quad (3)$$

$$OH^* + (H^+ + e^-) \longrightarrow H_2O + * \quad (4)$$

and the theoretical ORR limiting potentials and overpotentials are defined based upon the free energies of Equations 1-4 as:

$$U_{L,ORR}[V] = max[\Delta G_1, \Delta G_2, \Delta G_3, \Delta G_4\ ]/e \quad (5)$$

$$\eta_{ORR}[V] = max[\Delta G_1, \Delta G_2, \Delta G_3, \Delta G_4\ ]/e + 1.23\ V \quad (6)$$

For OER, the equivalent elementary equations for the 4e- OOH-based mechanism[47–49] can be written as the reverse of Equations (1-4), and the theoretical OER limiting potentials and overpotentials are again defined simply as:

$$U_{L,OER}[V] = max[-\Delta G_4, -\Delta G_3, -\Delta G_2, -\Delta G_1\ ]/e \quad (7)$$

$$\eta_{OER}[V] = max[-\Delta G_4, -\Delta G_3, -\Delta G_2, -\Delta G_1\ ]/e - 1.23\ V \quad (8)$$

The Gibbs free reaction energies are calculated as $\Delta G_i = \Delta E_i + \Delta ZPE_i - T\Delta S_i$. The differences between zero-point energy, ΔZPE_i and entropy, $T\Delta S_i$ is calculated through vibrational frequencies of adsorbates on the surface, and the adsorption energies ΔE_i are calculated relative to $H_2O(g)$ and $H_2(g)$ references as:

$$\Delta E_{OH} = E(OH^*) - E(*) - [E(H_2O) - \frac{1}{2}E(H_2)] \quad (9)$$

$$\Delta E_O = E(O^*) - E(*) - [E(H_2O) - E(H_2)] \quad (10)$$

$$\Delta E_O = E(O^*) - E(*) - [E(H_2O) - E(H_2)] \quad (11)$$

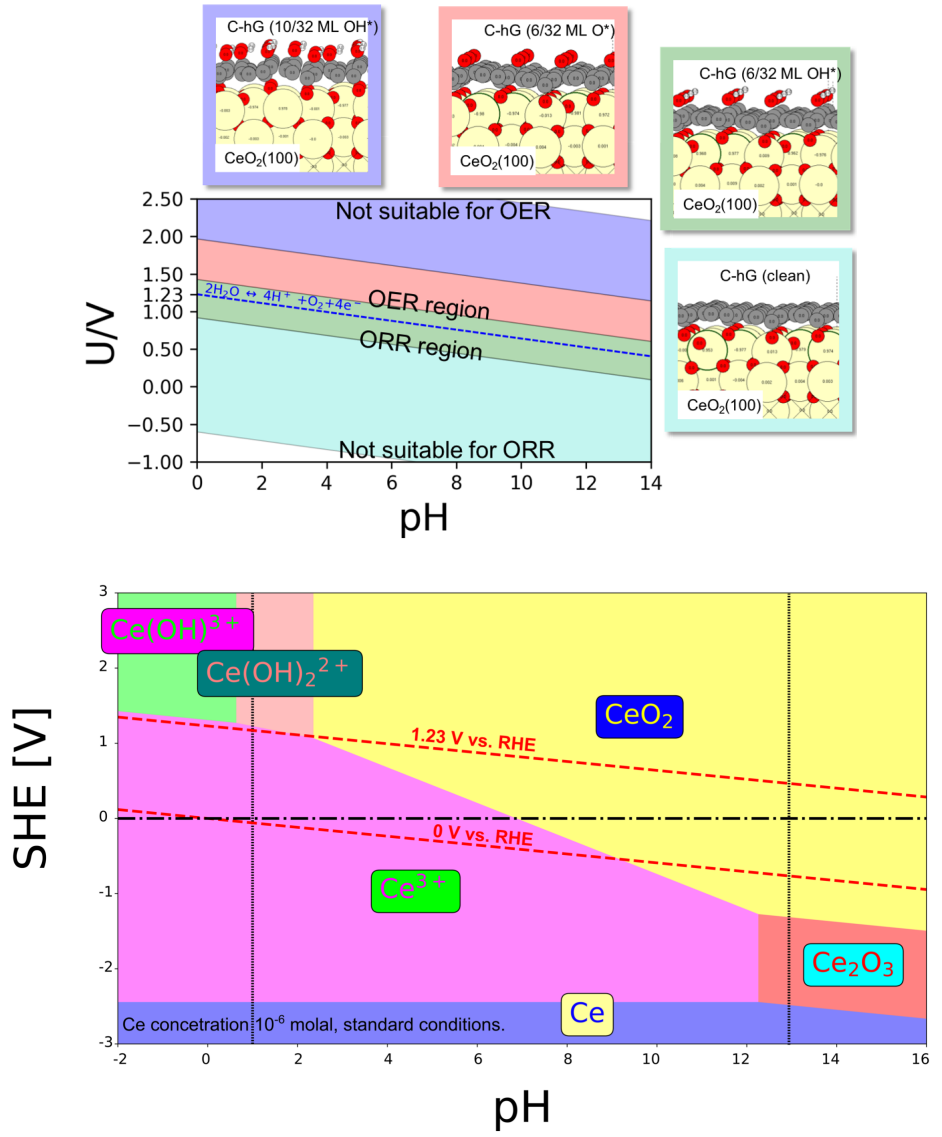

Figure 5.1: (a) Calculated surface Pourbaix diagram for the activated C-hG system. Four most stable coverages of OH/O on graphene (8x2) supported on CeO_2 (100) surface (6x1) were considered. For the main ORR and OER results shown in Figures 5.5 and 5.6 only the C-hG (clean) and C-hG (6/32 ML O*) were used. (b) Bulk Pourbaix diagram constructed from experimental free energies of Ce-H2O system at 10-6 molal concentration of Ce and standard conditions. The experimental free energies are taken from Barin Thermochemical Tables [50].

Whenever applicable, the coverage of the surfaces under applied voltage is incorporated by the calculation of the surface Pourbaix plots (Figure 5.1). The calculated energies involving adsorption on graphene or GO have been corrected by solvation corrections calculated with explicit water (Figure 5.2). Finally, all calculated ΔE_i are

released as part of the Catalysis-hub.org repository[51] at https://www.catalysis-hub.org/publications/GrewalHighly2019.

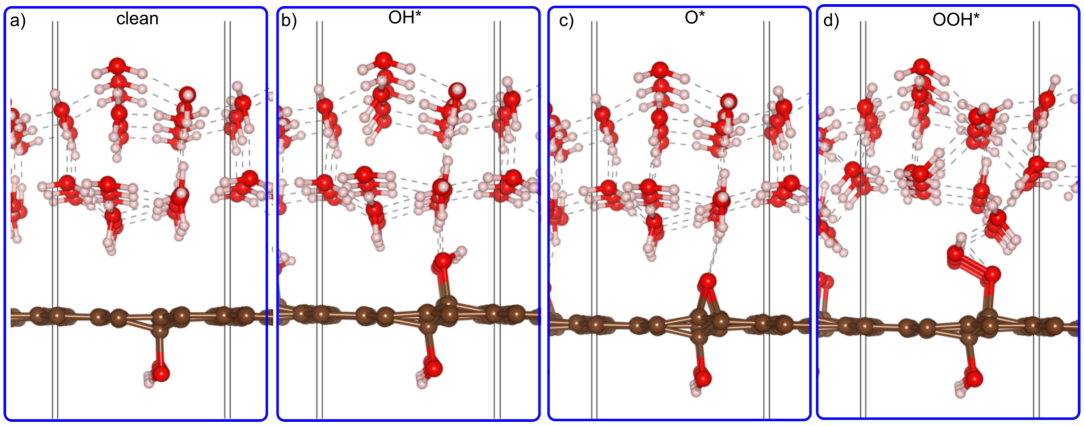

Figure 5.2: Solvation corrections obtained using global optimization of two layers of hexagonal H_2O taken from Pt(111) and graphene solvation studies [52,53] on top of C-hG-model. The simplified C-hG-model was used for computational efficiency. The calculated solvation corrections for this model relative to non-solvated structures for b) OH*, c) O* and d) OOH* adsorbates are -0.116 eV, -0.083 eV and -0.327 eV, respectively.

5.3 Results and Discussion

5.3.1 Physical characterization of CeO_2-fGO variants

Three different kinds of GOs (eG, hG and cG) were prepared before anchoring CeO_2 NCs onto them. The basal planes of chemically exfoliated graphene oxides (named as eG in this report) are decorated with mostly epoxy groups (–O–).[54,55] hG was prepared by treating eG with hydrobromic acid to convert the epoxy groups into hydroxyl groups, and cG was prepared by further adding oxalic acid, which converted hydroxyl groups into carboxyl groups.[23,56] A quantification by the titration method[57,58] indicates that hG has the largest amount of hydroxyl group, and eG and cG have the highest content of epoxy and carboxyl groups, respectively (Table 5.1).

Table 5.1: Molar percentages of epoxy, hydroxyl and carboxyl groups in each GO variant quantified by the nitration method.

Groups	eG	hG	cG
Epoxy	6.25	4.71	4.91
Hydroxyl	4.72	8.81	4.43
Carboxyl	4.52	4.42	9.17

Additionally, a nuclear magnetic resonance (NMR)[59] characterization was performed on eG having negligible OH content (0.001 mmol/g) while hG and cG having larger (0.853 and 0.875 mmol/g, respectively) OH content (Figure 5.2). Percentages of

hydroxyls for both non- and incorporated of cerium oxide are seen Table 5.1 and Table 5.2. The high OH content of cG is reasonable considering that each carboxyl group has a hydroxyl group in it. The FT-IR peak intensity of R-OH and R=O of CeO_2-fGO hybrid samples (Figure 5.4a) are significantly lower than those without CeO_2 incorporation (FT-IR on fGOs in Ref. [23]), suggesting the graphene sheets were highly reduced by losing most of their oxygen-containing functional groups during the hydrothermal reaction. It is also noted C-hG showed distinct Ce-O bond stretching (~1300 cm^{-1}; indicative of CeO_2 incorporation on graphene[60]) unlike the other two hybrids.

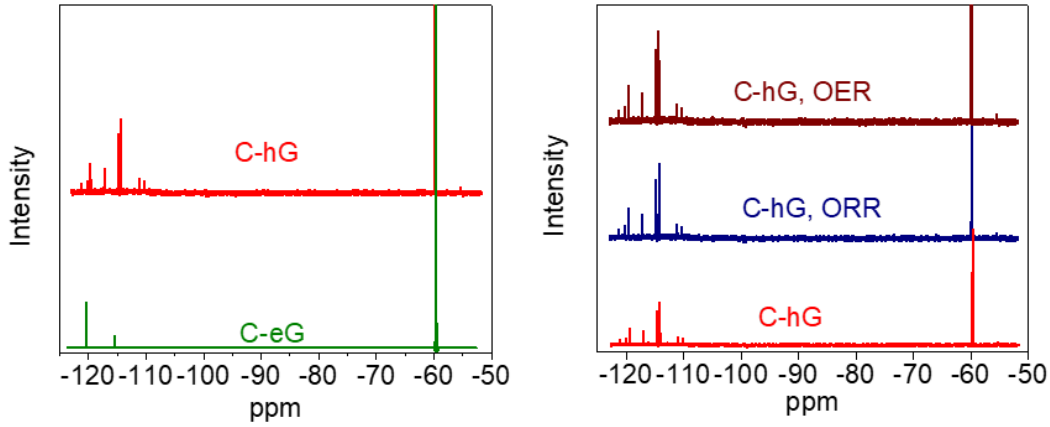

Figure 5.2: NMR spectra of C-hG and C-eG. C-hG was additionally characterized after an ORR scan and an OER scan in 0.1 M KOH solution for comparison. The quantified values are tabulated in Table 5.3.

Table 5.2: Content of hydroxyl group in each GO variant obtained based upon the NMR spectra. The OH content is in mmol per gram of each GO variant.

Samples	OH content (mmol/g)
eG	0.001
hG	0.853
cG	0.875 (in carboxyl group)

Table 5.3: Content of hydroxyl group in each CeO_2-GO variant obtained based upon the NMR spectra.

Samples	OH content (mmol/g)
C-hG, as-prepared	0.902
C-hG, after ORR	0.869
C-hG, after OER	0.883
C-eG, as-prepared	0.009

The X-ray diffraction (XRD) spectra in Figure 5.4b show peaks characteristic to CeO_2 in a cubic structure including the (111) fringe at 33.5°. An important observation is that C-eG and C-cG show a distinct carbon (002) peak at 26.5º while the peak is absent from C-hG. Since its appearance is ascribed to graphene sheet restacking, the absence of (002) peak from C-hG suggests that the binding of CeO_2 particles on the basal plane of

graphene is likely strong enough to deter the restacking of graphene flakes, which makes it advantageous to widen the accessible catalytic sites. The conjecture is in agreement with the electrochemically active surface areas (ECSA) that were separately quantified.

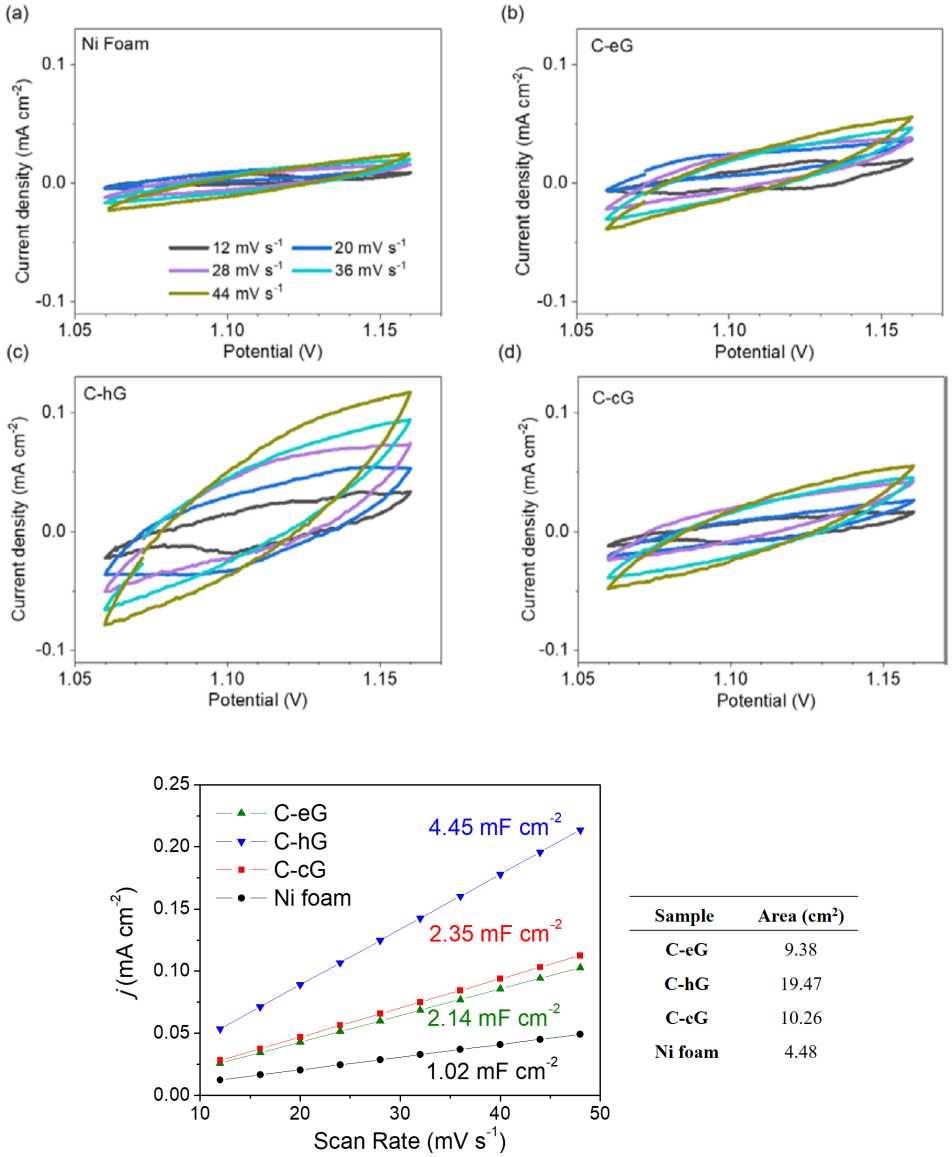

Sample	Area (cm²)
C-eG	9.38
C-hG	19.47
C-cG	10.26
Ni foam	4.48

Figure 5.3: Cyclic Voltammetry with various scan rates for the ECSA quantification (a) Ni foam, (b) C-eG, (c) C-hG and (d) C-cG in 0.1 M KOH (e) Plot of difference of anodic and cathodic current density as a function of scan rate for C-G, C-hG, C-oG, and Glassy carbon (GC) in 0.1 M KOH. For visual clarity, CV curves obtained at only 5 selected scan rates (12, 20, 28, 36 and 44 mV s^{-1}) are provided.

The measured ECSA values of C-eG, C-hG, C-cG and bare Ni foam were 9.4, 19.5, 10.3 and 4.5 cm^2 as calculated from Figure 5.3e, confirming that C-hG exhibits the largest surface area.

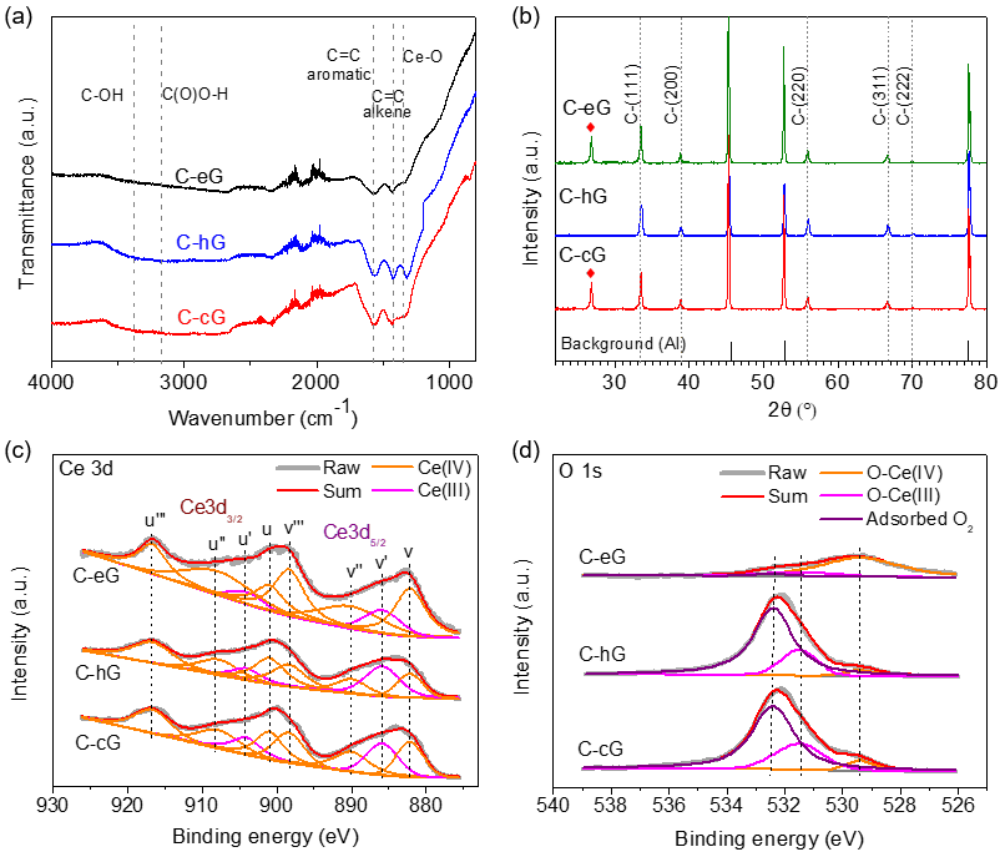

Figure 5.4: (a) FT-IR and (b) XRD spectra of C-eG, C-hG and C-cG. Co Kα radiation (λ = 1.78897 Å) was used for XRD. Both C-eG and C-cG show the (200) diffraction of graphene sheet restacking at 26.5°, which is missing from C-hG. (c) XPS Ce 3d and (d) O 1s spectra of CeO_2-fGO hybrid catalysts.

Figure 5.4c-d show x-ray photoelectron spectroscopy (XPS) spectra of the samples. The survey spectra (Figure 5.5) shows O 1s, C 1s, and Ce 3d peaks. The Ce 3d level (Figure 5.4c) has two series of peaks, v and u, corresponding to the $3d_{5/2}$ and $3d_{3/2}$ spin-orbit pair, respectively.

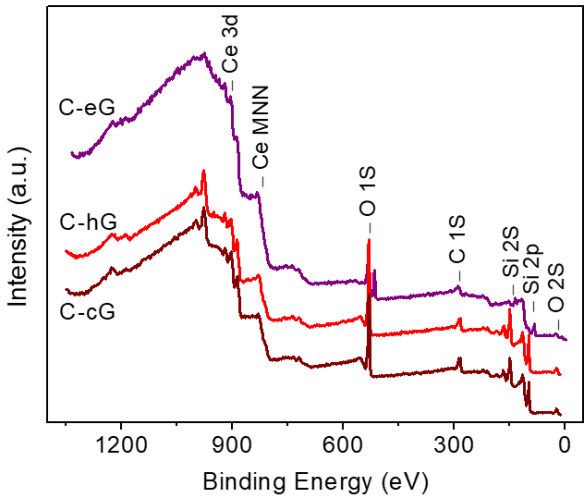

Figure 5.5: Wide survey scan XPS spectra of GO-CeO_2 hybrid catalysts. Si peaks are detected from the substrate on which the hybrid catalysts were placed.

The doublet (v′, u′) corresponds to Ce^{3+} and all the other peaks are assigned to Ce^{4+}.[29,61,62] By applying Maslakov et al.'s approach,[62] the molar ratios of Ce^{3+} with respect to the sum of Ce^{3+} and Ce^{4+} in C-eG, C-hG and C-cG were quantified to be 13.8%, 29.8% and 23.3%, respectively (Table 5.4). Quantification from Figure 5.4c of O 1s molar ratio for cerium based samples were done as well as seen in Table 5.5.

Table 5.4. XPS Ce 3d peak analysis. *I* values and calculated mole fraction of Ce^{3+} and Ce^{4+}.

Peaks	**C-G**	**C-hG**	**C-oG**
$\boldsymbol{v}$	8671.5	2733.9	4182.7
$\boldsymbol{v'}$	3728.5	5145.7	4480.6
$\boldsymbol{v''}$	6808.5	2340.3	3937.0
$\boldsymbol{v'''}$	8260.5	4276.8	4262.5
$\boldsymbol{u}$	5022.3	4829.9	4404.7
$\boldsymbol{u'}$	1784.0	2071.5	2981.1
$\boldsymbol{u''}$	6965.6	3042.7	3840.9
$\boldsymbol{u'''}$	5251.7	4708.4	4400.7
$\boldsymbol{f(Ce^{3+})}$	13.8%	29.8%	23.3%
$\boldsymbol{f(Ce^{4+})}$	86.2%	70.2%	76.7%

Table 5.5 XPS O 1s peak analysis. I values and calculated fraction of O-Ce^{3+} and O-Ce^{4+}.

Peaks	**C-G**	**C-hG**	**C-oG**
O-Ce^{4+}	3277.1	343.8	517.6
O-Ce^{3+}	570.9	1624.8	2185.0
Adsorbed O_2	182.0	6602.7	6361.4
f(O-Ce^{3+})	14.8%	82.5%	80.8%
f(O-Ce^{4+})	85.2%	17.5%	19.2%

The oxidation states of Ce can be alternatively quantified from O 1s core level spectra (Figure 5.4d). Three peaks were considered for deconvolution: 529.4 eV for O-Ce^{4+}, 531.5 eV for O-Ce^{3+} and 532.4 eV for adsorbed oxygen molecules or hydroxyl species.[29,61,63] C-eG has mostly O-Ce^{4+} (85.2%) with a small presence of O-Ce^{3+} whereas C-hG and C-cG have a much larger amount of O-Ce^{3+} bonding (C-hG: 82.5% and C-cG: 80.8%) than O-Ce^{4+}. This trend is overall aligned with the result from Ce 3d peaks in that C-hG and C-cG have much higher Ce^{3+} species than C-eG. On the other hand, the atomic ratio of Ce per C is quantified to be 29.8%, 10.3% and 11.3% for C-eG, C-hG and C-cG, respectively. The unexpectedly high concentration of Ce in C-eG is ascribed to a formation of ceria NP clusters without necessarily interfacing with each graphene flake leading to an unclear correlation between Ce content and ECSA.

High resolution transmission electron microscopy (HRTEM) images of the three CeO_2-fGO variants (Figure 5.6a-c) show that CeO_2 NCs of 2 – 4 nm in size are densely populated on graphene. CeO_2 NCs are nanocrystalline in the cubic phase. In particular, cubic (111) planes with the *d*-spacing of 3.1 Å are mostly visible with a relatively smaller number of (220) planes (*d*-spacing: 1.9 Å) in agreement with the XRD spectra presented in Figure 5.4b. A zoomed-out TEM image (Figure 5.6d) and its corresponding energy-filtered transmission electron microscopy (EFTEM) elemental maps (Figure 5.6e-g) on C-hG confirm that CeO_2 NCs are uniformly and densely anchored on graphene.

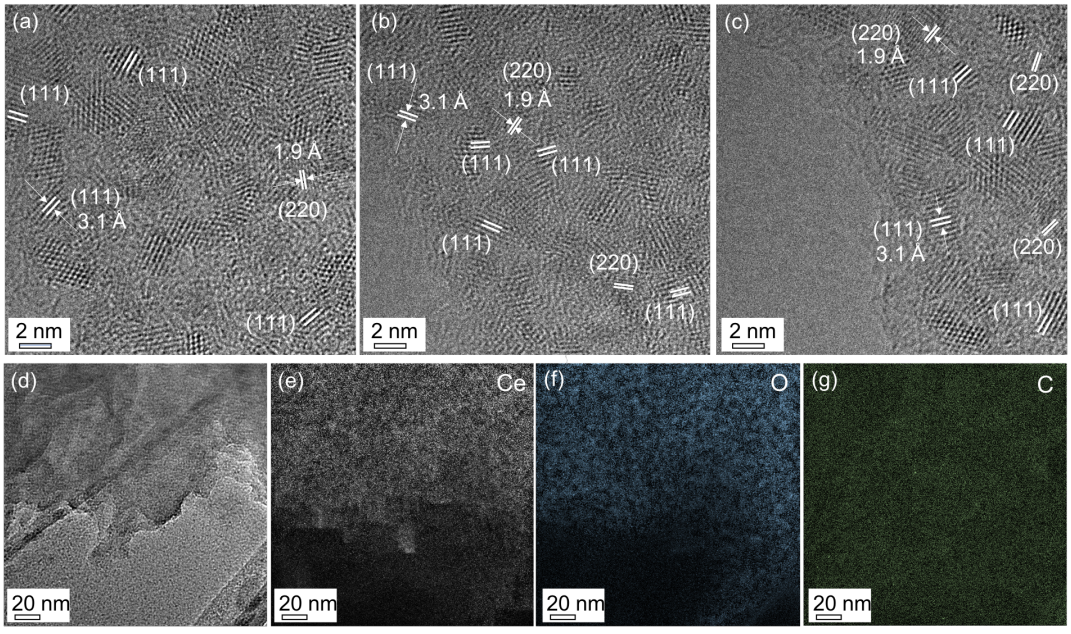

Figure 5.6: (a-c) HRTEM images of (a) C-eG, (b) C-hG, and (c) C-cG, revealing lattice fringes of cubic (111) and (220) planes in the majority of imaged CeO_2 nanoclusters. (d) A zoomed-out TEM image of C-hG and (e-g) their corresponding EFTEM elemental map of Ce, O and C, respectively.

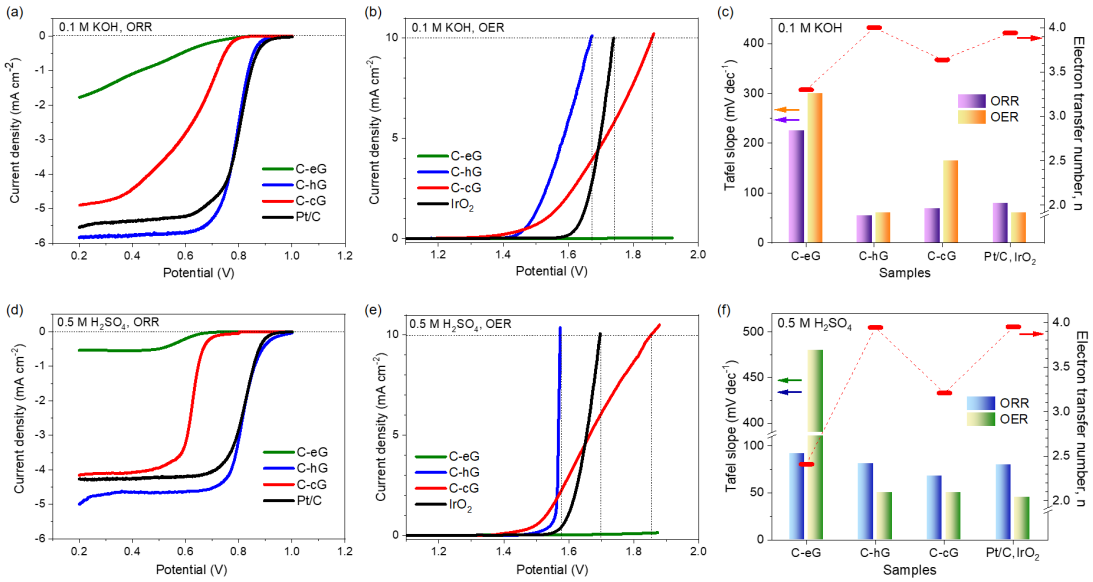

Figure 5.7: ORR voltammograms and processed data obtained in O_2-satured (a-c) 0.1 M KOH and (d-f) 0.5 M H_2SO_4. (a,d) LSV curves for ORR, (b,e) LSV curves for OER, (c,f) ORR/OER Tafel slopes and ORR electron transfer numbers (n). The electron numbers were obtained from RRDE measurements. All voltammograms were obtained at 1600 rpm.

5.3.2 Electrochemical properties of CeO2-fGO variants

The ORR performance of CeO_2-fGO hybrids was characterized in both alkaline (0.1 M KOH) and acidic (0.5 M H_2SO_4) media. All samples (including 20 wt.% Pt/C) used a solid loading of 0.18 mg cm^{-2}. In 0.1 M KOH, C-hG shows the best performance among the CeO_2-fGO variants for both ORR and OER (Figure 5.7a-c). The corresponding RRDE and Tafel plots voltammograms are provided in the Figure 5.8 and Figure 5.9, respectively.

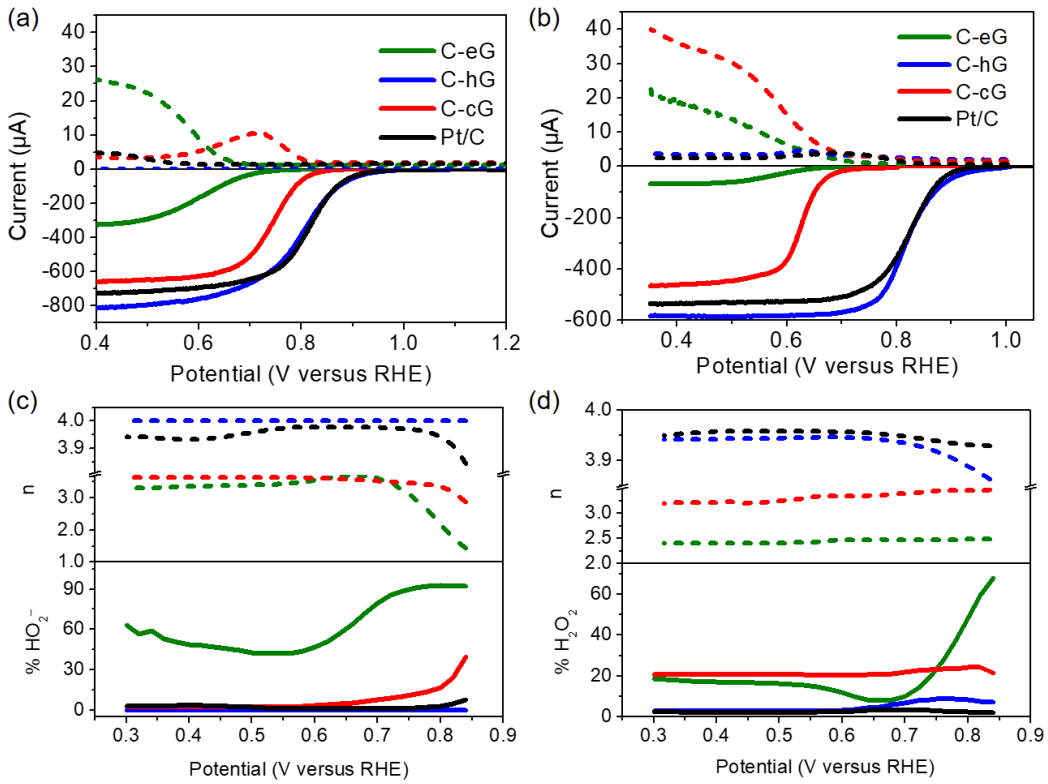

Figure 5.8: RRDE ring current (upper-dotted line) and disk current (lower-solid line) obtained at a disk sweep rate of 5 mV s^{-1} while the ring potential was fixed at 1.3 V (1600 rpm). Obtained in O_2-satured (a) 0.1 M KOH and (b) 0.5 M H_2SO_4. (c,d) The peroxide yield and electron transfer number obtained based upon the RRDE voltammograms.

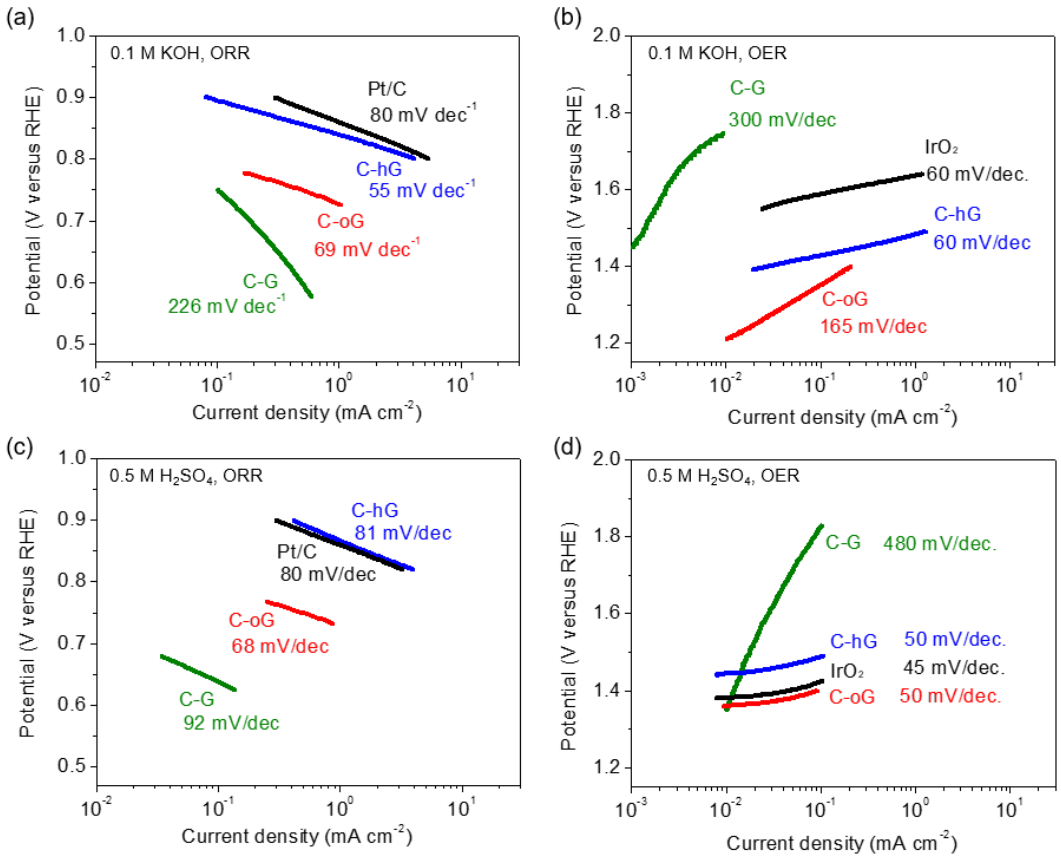

Figure 5.9: Tafel plots and Tafel slopes for ORR (a,c) and OER (b,d) measured in 0.1 M KOH (a,b) and 0.5 M H_2SO_4.

The ORR onset and half-wave potentials of C-hG (0.90 V and 0.79 V versus reversible hydrogen electrode, RHE; all potentials are versus RHE hereafter) are similar to those of Pt/C (0.92 V and 0.81 V), and the Tafel slope of C-hG (58 mV dec^{-1}) is even smaller than that of Pt/C (78 mV dec^{-1}). C-hG also exhibited higher current densities than Pt/C in the mass transport-limited region (5.78 versus 5.40 mA cm^{-2} at 0.3 V). Compared to the hydroxylated version, C-eG and C-cG show worse ORR performance (much lower onset and half-wave potentials). We also note that C-hG catalysts results in a dominant 4 e^- transfer process (n = 3.98 when averaged within the potential window of 0.3 – 0.85 V), while C-eG and C-cG are characterized as a mixed 2e^- and 4e^- process (averaged n = 3.28 and 3.55, respectively). As for OER in 0.1 M KOH solution (Figure 5.7b), the potential needed to reach 10 mA cm^{-2} (E_{10}) was 1.67 V for C-hG, significantly lower than the potential needed for IrO_2 (1.74 V). In addition, both C-hG and IrO_2 showed the OER Tafel slopes of 60 mV dec^{-1}, much smaller than those measured from C-eG and C-cG.

The promising ORR/OER performance of C-hG is not limited to alkaline media. Even in an acidic solution of 0.5 M H_2SO_4, C-hG exhibited excellent performance. For ORR, the onset and half-wave potentials of C-hG (0.94 and 0.83 V) are even more positive than those of Pt/C (0.92 and 0.82 V), and its Tafel slope (81 mV dec^{-1}) is nearly the same as Pt/C (78 mV dec^{-1}). Similar to the case in 0.1 M KOH, C-hG exhibited a dominant $4e^-$ ORR process (average n = 3.88) throughout the potential window of study (0.3 – 0.85 V) in the acid solution. For OER (Figure 5.3e,f), C-hG showed an E_{10} value of 1.58 V, significantly lower than those of IrO_2 (1.70 V), C-cG (1.90 V) and C-eG (> 2 V). The OER Tafel slopes of both C-hG and C-cG were quantified to be 50 mV dec^{-1}, slightly larger than that of IrO_2 (45 mV dec^{-1}). All linear sweep voltammetry (LSV) and corresponding Koutechy-Levich plots are provided in the Figures 5.10 and 5.11, and the ORR/OER performance is summarized in the Table 5.6. It is also noted that the ORR and OER activities of each of fGOs (i.e. eG, hG and cG) and CeO_2 themselves without interfacing each other is much worse than the hybrid catalysts; LSV curves in both 0.1 M KOH and 0.5 M H_2SO_4 are provided in Figure 5.10.

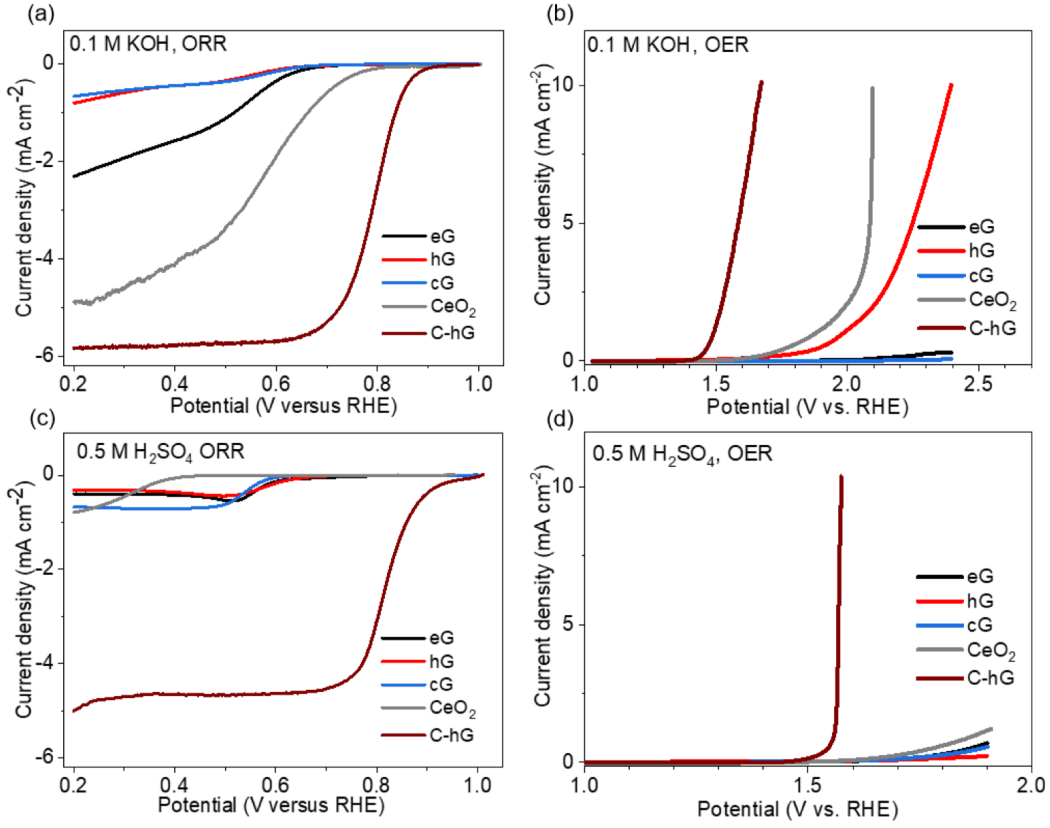

Figure 5.10: ORR voltammograms in (a) 0.1 M KOH and (c) 0.5 M H_2SO_4; OER voltammograms in (b) 0.1 M KOH and (d) 0.5 M H_2SO_4 for fGOs (eG, hG and cG) and CeO_2. The curves for C-hG are provided for comparison.

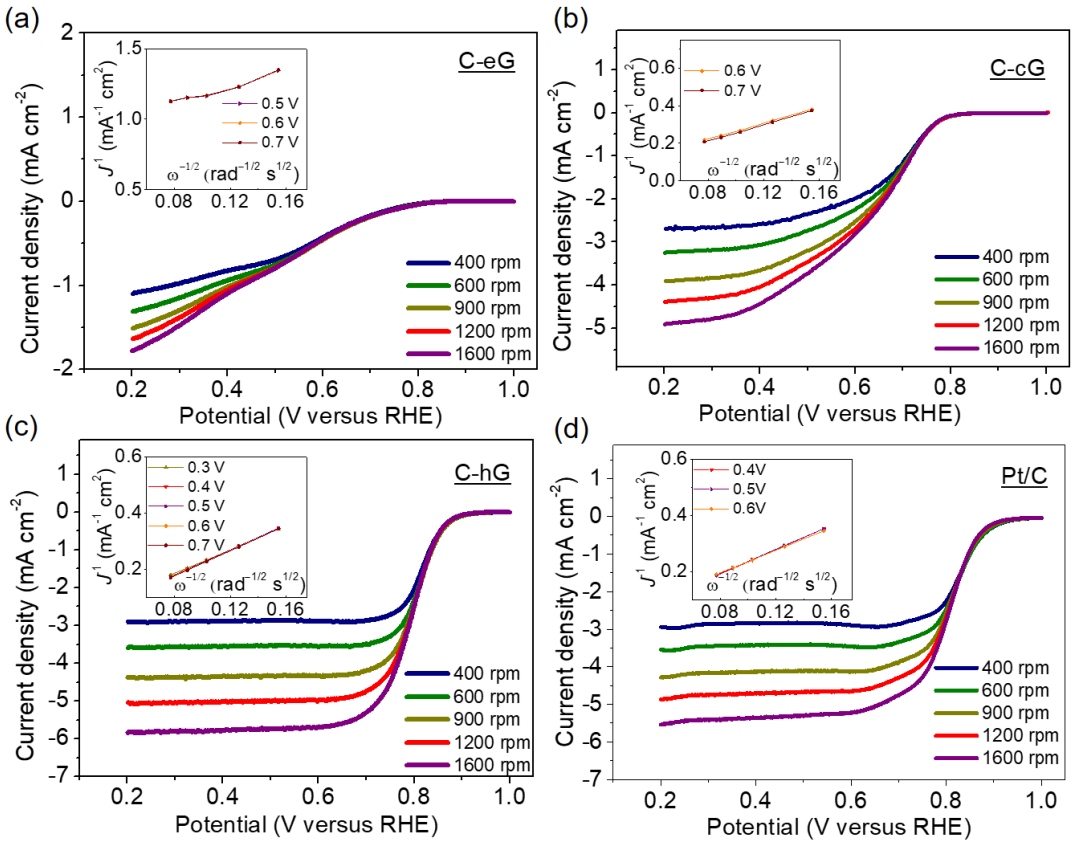

Figure 5.11: LSV curves in O_2-saturated 0.1 M KOH solution for (a) C-G (b) C-oG (c) C-hG (d) Pt/C obtained at various rotating speeds at a sweep rate of 5 mV s^{-1}. Inset: the corresponding Koutechy-Levich plot at various disk potentials. All voltammograms presented are IR-compensated.

Table 5.6: A summary of oxygen electrocatalytic performance quantified in 0.5 M H_2SO_4 (acidic) and 0.1 M KOH (alkaline) at a rotating rate of 1600 rpm.

	0.1 M KOH				0.5 M H_2SO_4			
	C-G	C-hG	C-oG	Pt/C	C-G	C-hG	C-oG	Pt/C
ORR onset potential[†] (V vs. RHE)	0.77	0.90	0.80	0.92	0.63	0.94	0.72	0.92
Half-wave potential (V vs. RHE)	< 0.5	0.79	0.64	0.81	0.57	0.83	0.62	0.82
Tafel slope, ORR (mV/decade)	266	58	69	78	92	81	68	78
Current density at 0.3 V[‡] (mA/cm^2)	1.48	5.78	4.77	5.40	0.51	4.81	4.09	4.28
Mass activity[§] (A/g) @ 0.90 V	0.06	3.1	0.89	2.44 (12.2)	0.03	2.74	0.003	2.42 (12.1)
Mass activity[§] (A/g) @ 0.85 V	0.09	10.5	0.73	11.3 (56.5)	0.031	9.95	0.01	11.0 (55.0)
Mass activity[§] (A/g) @ 0.80 V	0.21	25.2	4.71	47.0 (235.3)	0.04	24.7	0.34	46.4 (233.0)
Electron transfer number [*]	3.28	3.98	3.55	3.92	2.42	3.88	3.51	3.95
				IrO_2				IrO_2
OER potential at 10 $mA\ cm^{-2}$ (V vs. RHE)	N/A	1.67	1.85	1.74	N/A	1.58	1.90	1.70
Tafel slope, OER (mV/decade)	300	60	165	60	480	50	50	45

[†] Chosen to be the potential reaching 0.1 mA/cm^2.

[‡] IR-compensated current densities quantified at 0.2 V vs. RHE.

[§] Kinetic current per CeO_2/graphene or Pt/C mass (excluding additives such as Nafion and additional carbon black); 123.2 $\mu g/cm^2$ for all samples. The value in the parenthesis is based upon the mass of Pt only (24.6 $\mu g/cm^2$).

[*] Averaged values within the potential window of 0.35 – 0.75 V vs. RHE.

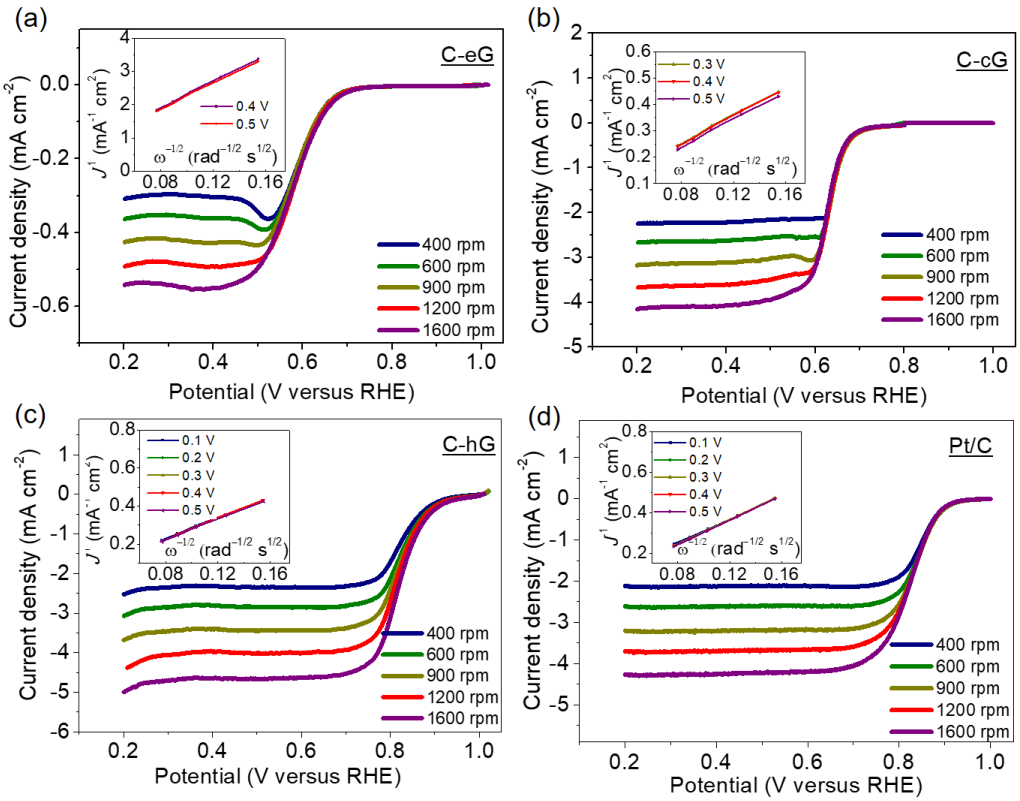

Figure 5.12: LSV curves in O_2-saturated 0.5 M H_2SO_4 solution for (a) C-G (b) C-oG (c) C-hG (d) Pt/C obtained at various rotating speeds at a sweep rate of 5 mV s^{-1}. Inset: the corresponding Koutechy-Levich plot at various disk potentials. All voltammograms presented are IR-compensated.

To the best of our knowledge, this level of performance (on par with noble metal-based benchmark) with versatility (bifunctional ORR/OER activity in both alkaline and acidic media) in oxygen electrocatalysis is unprecedented of non-noble metal-based systems. It is also noted that the excellent performance was realized without forming TM-N moieties (TM: transition metal) which has been considered almost as a prerequisite for a high-performance oxygen electrocatalysis in non-noble metal-based systems.[64,65] To further explore the origin of enhanced activity, we performed DFT calculations as discussed below.

5.3.3 Theoretical understanding of the activity of fGO and CeO_2-fGO hybrid systems

To rationalize the observed experimental activity of the fGO and CeO_2-fGO hybrid catalysts, we consider a number of possible electrochemically stable fGO and CeO_2-fGO systems as discussed further below. Given these systems, we then evaluate their theoretical ORR and OER activities (see Modeling and Computation section) at all possible active sites. This approach allows us to construct relative activity trends, particularly as a function of the activation groups (eG, hG, cG), and of the ceria (C)

support. The initial structures for graphene (G), epoxy-graphene (eG) and graphene hydroxide (hG) were chosen from original work of Wang *et al*.[66] The nanostructured model of mildly reduced GO (mrGO) was taken from Bukas *et al.*,[67] while ceria structural models were taken from our recent work on nickel-ceria CO_2RR catalysts,[41] both of which are included in the Catalysis-hub.org repository.[51] Finally, minimal cells representing the interface between GO and ceria surfaces were generated via MPInterfaces code.[68]

The most active structural models of graphene (G), fGO and CeO_2-fGO hybrid catalysts are shown in Figure 5.12a. This set includes two hydroxy-graphene (hG-model) and other reduced GO variants with different configurations of epoxy and hydroxyl groups: nanostripe structures, eG-edge and hG-edge. A nanostructured model of mrGO[67] (eG-patch) was also tested (not shown).

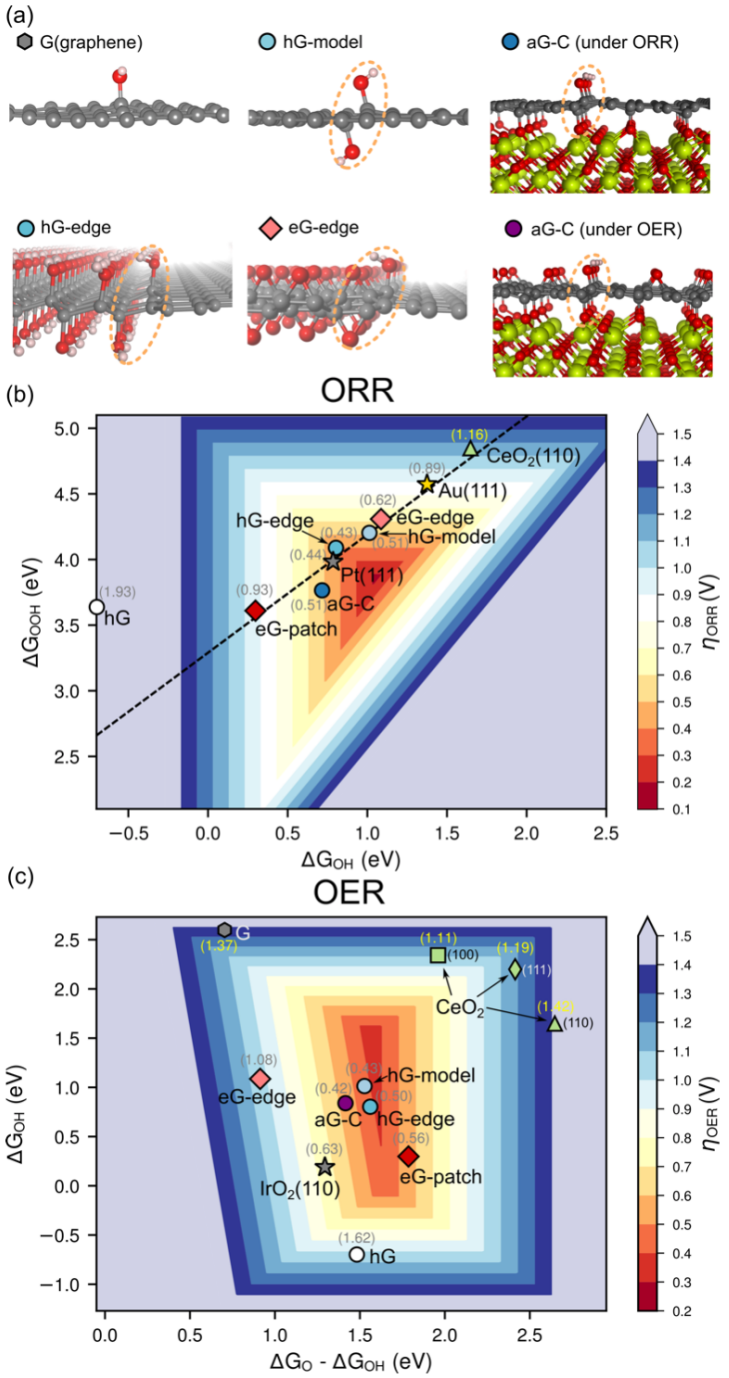

Figure 5.13: (a) Important structural models of GO-ceria hybrid system. The picture insets show rendered atomic structures with hydrogen, carbon, oxygen and ceria atoms are shown as pink, grey, red and lime-green spheres, respectively. The structure labels are introduced in text as: graphene (G) (with OH*), two hydroxy graphene (hG-model), hydroxylated graphene-graphene edge with OH* (hG-edge), and epoxy graphene-graphene edge with OH* (eG-edge). Supported and activated graphene structures on CeO_2(100)

(aG-C) have either low coverage of OH* (ORR), or high-coverage of O-epoxy (OER). The ellipses highlight a common structural motif. (b) Calculated ORR activity map as function of OH* and OOH* free energies of the above models. For comparison, the results for ceria-surfaces and Pt(111) and Au(111) benchmarks adapted from Ref.[43] are also shown. The dashed line indicates the OOH* vs. OH* linear scaling obtained in this study. (c) Similarly, the calculated OER activity map as function of O*-OH* and OH* free energies for the above models including the IrO_2(110) benchmark from Ref[69]. Symbols in brackets are numerical values of the obtained theoretical overpotentials for ORR (b) and OER (c) based on Equations 6 and 8.

Finally, we also highlight the structure of the "activated" form of functionalized graphene on ceria (100) (aG-C), which is a configuration where a covalent bonding is formed between ceria and fGO as discussed further below. Fully oxidized GO (i.e. GO fully covered with epoxy group; full eG) and fully hydroxylated GO (full hG) were also tested (not shown). To study the activity of ceria alone, the stochiometric (O-vacancy free) (111), (110) and (100) surfaces were also considered. Additionally, the computational benchmark catalysts Pt(111) and Au(111)[43] for ORR and IrO_2 (110)[69] for OER were also included for direct comparison with experiments.

Since the exact nature of the CeO_2-fGO interface is not known experimentally, an exhaustive search of all possible interfaces, orientations, lattice mismatches, and facets are not possible and are unlikely to provide fundamental insights. Instead, using MPInterfaces code,[68] we have narrowed down to the minimal common cells combining graphene variants (G, eG and hG) and ceria (C) facets, (111), (110) and (100). Such fully relaxed interfaces between graphene, full eG and full or half hG and a stoichiometric ceria (111) yielded very little interface formation energy and a very small charge transfer at the interface (shown in Figure 5.14). Other ceria surfaces yielded similar results.

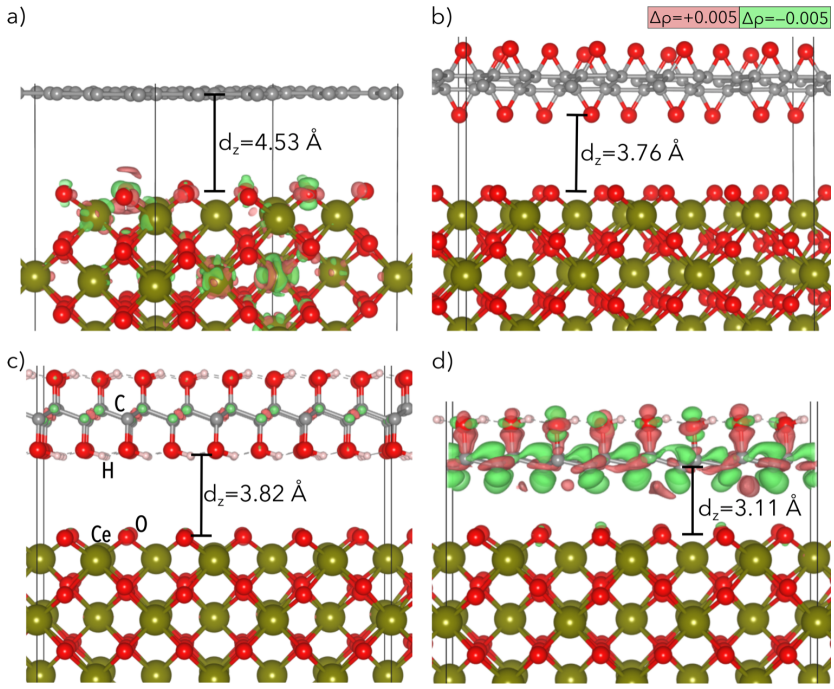

Figure 5.14: Weak support interaction and charge transfer values obtained for a non-activated graphene. GO on top of Ceria (111) for a) hydroxy free graphene, b) fully oxidized GO, c) fully hydroxylated GO, and d) top-half fully hydroxylated GO. The calculated GO-ceria interaction energies per (1x1) graphene are indeed very small: a) -0.003 eV, b) -0.002 eV, c) -0.007, and d) -0.048 eV. The colors indicate the isovalues for charge density difference plots after the formation of the interface.

For that reason, we have further investigated more reduced forms of the graphene variants supported on ceria. Particularly, for ceria (100), which had considerably better lattice matching between top-most oxygens of ceria and carbons in graphene, a covalent bond formation between ceria top-most oxygens and graphene is formed if hydroxyl groups were present. We refer to a configuration with covalently bonded functionalized graphene on ceria (100) as "activated" and name it aG-C. A number of possible combinations and coverages were tested using the surface Pourbaix analysis (Figure 5.2). The direct oxygen bonding of ceria with graphene in all aG-C hybrid models resulted in the presence of surface Ce^{3+} detected from DFT local magnetic moment analysis. Figure 5.13b shows a map of calculated theoretical ORR overpotentials (see Equation 6) as function of the two most important descriptors of ORR activity, the adsorption free energies of OH* and OOH*. Figure 5.14c features a similar map calculated for OER overpotential (see Equation 8), which is a function of O* and OH* adsorption free energies. It is noted that while the theoretical overpotentials are always calculated explicitly from OH*, O* and OOH*, the construction of the 2D maps takes advantage of O* or OOH* scaling vs. OH* for ORR and OER, respectively.

The ORR activity map (Figure 5.13c) show that energetics of all the systems (with the exception of full hG) closely follows the universal scaling relations between OOH* and OH* adsorption free energies,[48,70] $\Delta G_{OOH} = 0.9 \cdot \Delta G_{OH} + 3.29$ eV (shown as dotted line in Figure 5.13b). The main calculated trend in ORR activities is that only reduced forms of hG (hG-edge, hG-model) and the activated hybrid catalysts (aG-C) (η= 0.51 V) result in theoretical activities close to or better than Pt(111) (η=0.44 V). The reduced forms of eG are predicted to perform significantly worse when compared to reduced forms of hG, followed by pure ceria surfaces that have very low affinity to OH/O* groups. It is well known that ceria readily forms oxygen vacancies, but these, in turn, bind OH* too strongly (> -0.5 eV for single oxygen vacancy at CeO_2 (111)) to be catalytically relevant.

The OER activity map (Figure 5.13c) shows that reduced forms of hG (hG-edge, hG-model), activated hybrid (aG-C) and eG-patch contain favorable OER active sites, and all have overpotentials lower that IrO_2 (η= 0.63 V). Again, we do not find pure ceria surfaces to be a viable system for OER due too low affinity to OH*/O* groups. In the presence of oxygen vacancies on ceria surface, the affinity becomes too high.

From the aforementioned observations, it is worth highlighting that the highly active two-hydroxy-graphene structural motif of hG-model is essentially shared across all the active ORR and OER structures (highlighted with ellipses in Figure 5.13a). For that reason, we hypothesize that the bifunctional activity of hydroxylated CeO_2-fGO hybrid catalysts originates from the presence of activated forms of GO and that such activation shares a common structural motif.

A direct comparison of experimentally quantified performance to predictions of our theoretical models is shown in Figure 5.15. The measured ORR/OER overpotentials of the three CeO_2-fGO hybrid samples and benchmark catalysts (Figure 5.15a; directly quantified from data in Figure 5.8) are compared to calculated limiting potentials (Figures 5.16b,c; based on the results of Figure 5.13). We caution that such a comparison can only be made on a relative basis, and only if the precise chemical nature of the CeO_2-fGO hybrid catalysts is known at the operational conditions. Nevertheless, for ORR case, we find that the experimentally determined activity C-hG relative to Pt and other hybrid catalysts is well aligned with theoretical prediction based upon activated forms of reduced hG, particularly with the model of activated hybrid aG-C catalyst (Figure 5.15b). This is in agreement with the post e-chem analysis of C-hG samples, which indicate the presence of hydroxy groups.

For OER case, we also find that the high activity of C-hG also matches well with the theoretical prediction based upon activated forms of reduced hG and of the hybrid aG-C (Figure 5.15c). Under OER conditions, some epoxy surface species are present in the hybrid aG-C model (Figure 5.2) but the presence of hydroxy groups is simultaneously required to form an activated interface between the graphene and ceria. Post OER e-chem analysis of C-hG samples also show a high content of hydroxy groups.

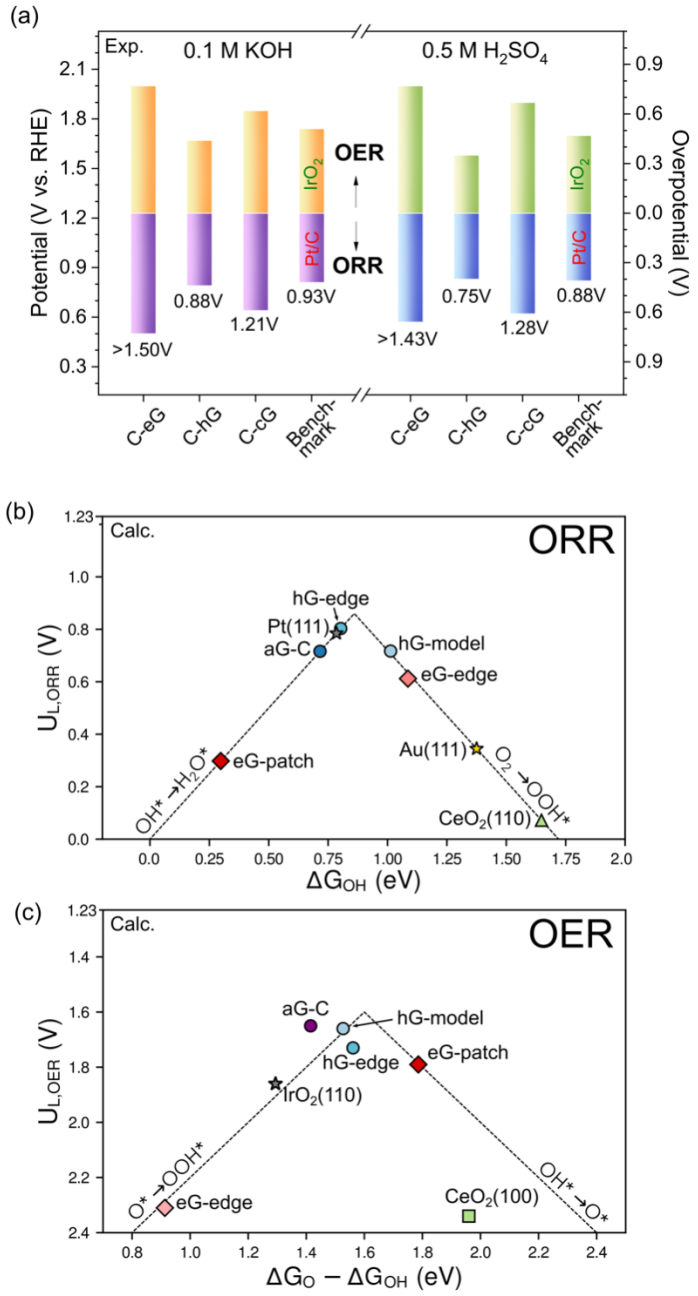

Figure 5.15: Direct comparison of the measured overpotentials (a) to calculated limiting potentials for ORR, $U_{L,ORR}$ (b) and for OER, $U_{L,OER}$ (c). The measured ORR overpotential is $E_{rev} - E_{1/2}$, and the OER overpotential is $E_{rev} - E_{10}$, which are based upon the results presented in Figure 5.3. The numbers inside the graph (a) are the sum of ORR and OER overpotentials; that is, $E_{10} - E_{1/2}$ values of each sample. The theoretical overpotentials are based on energetics of Figure 5.4.

5.3.4 Operational durability

The operational durability of C-hG was evaluated via potential cycling measurements in both 0.1 M KOH and 0.5 M H_2SO_4 (Figure 5.16). While the performance decay of C-hG during potential cycling in 0.1 M KOH was negligible, a dramatic degradation was observed in 0.5 M H_2SO_4. The sum of ORR and OER overpotentials (E_{10} - $E_{1/2}$) changed from 0.70 V (150 cycles) to 1.63 V (2000 cycles). This is not surprising because strong acids are expected to cause leaching of metal oxides.[71]

To probe possible impacts on durability by incorporating other functional groups on a carbon-based substrate, a composite of C-hG and activated carbon (AC) is considered. Since ACs have a high surface area and micro-porosity, they are widely used as the carbon support of oxygen electrocatalysts.[72] ACs are mixed with C-hG along with nitric acid (HNO_3) and sulfuric acid (H_2SO_4) mainly because acid treatment of ACs are expected to create various oxygen-containing functionalities.[72,73]

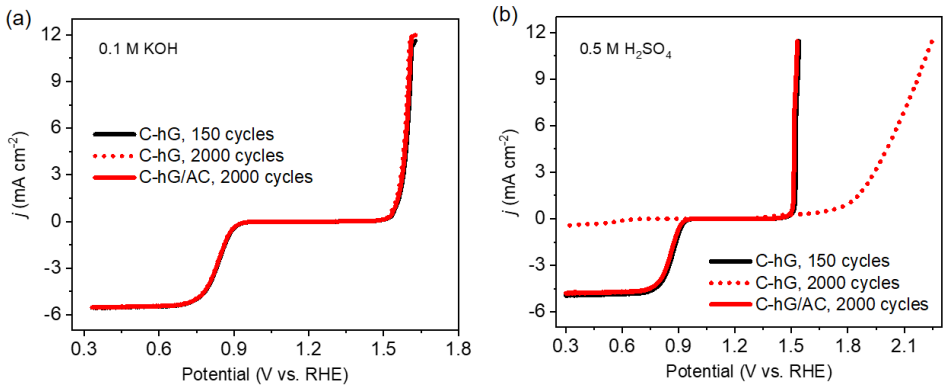

Figure 5.16: Cyclic durability test of C-hG in 0.1 M KOH (a) and 0.5 M H_2SO_4 (b) via potentiodynamic measurements at 50 mV s^{-1}. Only the AC treated sample maintained its activity in acid for 2000 cycles. Voltammograms are obtained during the 150th and 2,000th cycles between 0.0 V and 2.0 V with the compliance current of j = 12 mA cm^{-2}. All voltammograms presented were obtained at 1600 rpm.

The addition of AC proved highly effective in improving the operational stability of C-hG for both ORR and OER, especially in the acidic solution. As evident in Figure 5.16, AC-mixed C-hG (namely C-hG/AC) show little difference in the activity between the 150th and 2,000th cycles. To the best of our knowledge, this is the first demonstration of MO-based oxygen electrocatalysts stable in an acidic solution. It is noted that the ORR activity of AC itself is not impressive; the onset potential is 0.72 V, and electron transfer number spans between 2.2 and 3.3 in 0.1 M KOH as shown in Figures 5.17b-c. Therefore, the stability should originate from a specific type of chemical bonding between functionalized graphene and AC and/or between ceria and AC. The sulfonic group found in the AC as verified by an FTIR scan (at ~2490 cm^{-1}; Figure 5.17a) may be responsible

for the performance and stability because carbon with sulfonic groups acts as an active and stable heterogeneous acid catalyst.[74]

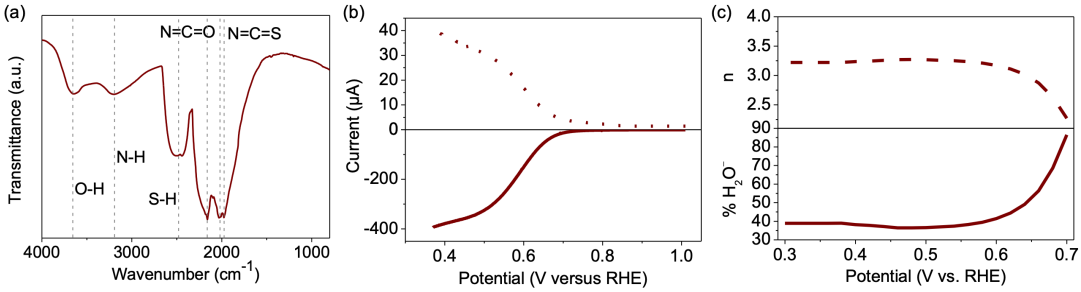

Figure 5.18: Characterization of activated carbon: (a) FT-IR spectra of AC, (b) RRDE voltammogram obtained in 0.1 M KOH, (c) the resulting electron transfer number (n) and HO_2^- production percentage.

5.4 Conclusions

In our previous work, we demonstrated that MO/graphene hybrids can be highly ORR-active even with ORR-inert MOs (TiO_2 and ZrO_2). We consider this behavior as an "MO-enabled activation of graphene for ORR," which is totally different from the conventional view on MO/graphene hybrids where graphene is regarded as a MO-anchoring template to enhance electronic transport and suppress MO agglomeration. Due to the promising properties exhibited by oxygen electrolysis this study was extended to include the application of CeO_2 to MO/graphene system with an expectation of further enhanced performance.

Consequently, this report demonstrates a highly active bifunctional oxygen electrocatalysis from the CeO_2-activated 2D carbon. CeO_2/hydroxylated graphene affords a surprisingly high ORR and OER performance, comparable to those of noble metal-based benchmark catalysts, in both alkaline and acidic media. This work presents a new approach of activating 2D carbon for excellent ORR/OER performance even without N-C or metal-N moieties, the widely accepted essential component for high catalytic activity in carbon structure-based systems. Our thermodynamic screening approach applied to GO, mrGO and hybrid CeO_2-fGO systems identifies the highest theoretical activities for reduced hydroxy-functionalized GO. The calculations also reveal an activation mechanism, by which ceria nanoparticles form strong interface with GO when hydroxyl groups are present. We further rationalize the bifunctionality of the CeO_2-fGO hydroxylated hybrid catalyst by the presence of previously unknown hydroxy-activated graphene structural motif. Finally, we briefly demonstrate a substantially enhanced stability of CeO_2/fGO hybrid catalysts in acidic media by incorporating activate carbon.

Reference

1. Wang, Y.-J. *et al.* Compositing doped-carbon with metals, non-metals, metal oxides, metal nitrides and other materials to form bifunctional electrocatalysts to enhance metal-air battery oxygen reduction and evolution reactions. *Chem. Eng. J.* **348**, 416–437 (2018).
2. Wang, H.-F., Tang, C. & Zhang, Q. A Review of Precious-Metal-Free Bifunctional Oxygen Electrocatalysts: Rational Design and Applications in Zn−Air Batteries. *Adv. Funct. Mater.* **28**, 1803329 (2018).
3. Wang, Y.-J. *et al.* Recent advancements in the development of bifunctional electrocatalysts for oxygen electrodes in unitized regenerative fuel cells (URFCs). *Prog. Mater. Sci.* **98**, 108–167 (2018).
4. Kim, J. S., Kim, B., Kim, H. & Kang, K. Recent Progress on Multimetal Oxide Catalysts for the Oxygen Evolution Reaction. *Adv. Energy Mater.* **8**, 1702774 (2018).
5. Li, Q., Cao, R., Cho, J. & Wu, G. Nanocarbon Electrocatalysts for Oxygen Reduction in Alkaline Media for Advanced Energy Conversion and Storage. *Adv. Energy Mater.* **4**, 1301415 (2014).
6. Xiao, J. *et al.* Surface Structure Dependent Electrocatalytic Activity of Co3O4 Anchored on Graphene Sheets toward Oxygen Reduction Reaction. *Sci. Rep.* **3**, 2300 (2013).
7. Mao, S., Wen, Z., Huang, T., Hou, Y. & Chen, J. High-performance bi-functional electrocatalysts of 3D crumpled graphene–cobalt oxide nanohybrids for oxygen reduction and evolution reactions. *Energy Environ. Sci.* **7**, 609–616 (2014).
8. Leng, M. *et al.* Enhanced oxygen evolution reaction by Co-O-C bonds in rationally designed Co_3O_4/graphene nanocomposites. *Nano Energy* **33**, 445–452 (2017).
9. Duan, J. *et al.* Mesoporous hybrid material composed of Mn_3O_4 nanoparticles on nitrogen-doped graphene for highly efficient oxygen reduction reaction. *Chem. Commun.* **49**, 7705–7707 (2013).
10. Wang, T. *et al.* Preparation of Porous Graphene@Mn_3O_4 and Its Application in the Oxygen Reduction Reaction and Supercapacitor. *ACS Sustain. Chem. Eng.* **7**, 831–837 (2019).
11. Bikkarolla, S. K. *et al.* A three-dimensional Mn_3O_4 network supported on a nitrogenated graphene electrocatalyst for efficient oxygen reduction reaction in alkaline media. *J. Mater. Chem. A* **2**, 14493–14501 (2014).
12. Wu, Z. *et al.* 3D nitrogen-doped graphene aerogel-supported Fe_3O_4 nanoparticles as efficient electrocatalysts for the oxygen reduction reaction. *J. Am. Chem. Soc.* **134**, 9082–5 (2012).
13. Gao, S. *et al.* N-doped-carbon-coated Fe_3O_4 from metal-organic framework as efficient electrocatalyst for ORR. *Nano Energy* **40**, 462–470 (2017).
14. Friebel, D. *et al.* Identification of Highly Active Fe Sites in (Ni,Fe)OOH for Electrocatalytic Water Splitting. *J. Am. Chem. Soc.* **137**, 1305–1313 (2015).
15. Zhao, Z., Schlexer Lamoureux, P., Kulkarni, A. & Bajdich, M. Trends in Oxygen Electrocatalysis of *3 d* -Layered (Oxy)(Hydro)Oxides. *ChemCatChem* **11**, cctc.201900846 (2019).
16. Wang, Y., Li, J. & Wei, Z. Transition-metal-oxide-based catalysts for the oxygen

reduction reaction. *J. Mater. Chem. A* **6**, 8194–8209 (2018).
17. Song, F. *et al.* Transition Metal Oxides as Electrocatalysts for the Oxygen Evolution Reaction in Alkaline Solutions: An Application-Inspired Renaissance. *J. Am. Chem. Soc.* **140**, 7748–7759 (2018).
18. Guo, S., Zhang, S., Wu, L. & Sun, S. Co/CoO Nanoparticles Assembled on Graphene for Electrochemical Reduction of Oxygen. *Angew. Chemie Int. Ed.* **51**, 11770–11773 (2012).
19. Liang, Y. *et al.* Co_3O_4 nanocrystals on graphene as a synergistic catalyst for oxygen reduction reaction. *Nat. Mater.* **10**, 780–6 (2011).
20. Liang, Y. *et al.* Oxygen Reduction Electrocatalyst Based on Strongly Coupled Cobalt Oxide Nanocrystals and Carbon Nanotubes. *J. Am. Chem. Soc.* **134**, 15849–15857 (2012).
21. Zhang, Y.-Q. *et al.* A strongly cooperative spinel nanohybrid as an efficient bifunctional oxygen electrocatalyst for oxygen reduction reaction and oxygen evolution reaction. *Appl. Catal. B Environ.* **236**, 413–419 (2018).
22. Wu, K.-H. *et al.* Structural Origin of the Activity in Mn_3O_4-Graphene Oxide Hybrid Electrocatalysts for the Oxygen Reduction Reaction. *ChemSusChem* **8**, 3331–3339 (2015).
23. Grewal, S. *et al.* Critical Impact of Graphene Functionalization for Transition Metal Oxide/Graphene Hybrids on Oxygen Reduction Reaction. *J. Phys. Chem. C* **122**, 10017–10026 (2018).
24. Zhao, S., Yan, L., Luo, H., Mustain, W. & Xu, H. Recent progress and perspectives of bifunctional oxygen reduction/evolution catalyst development for regenerative anion exchange membrane fuel cells. *Nano Energy* **47**, 172–198 (2018).
25. Paier, J., Penschke, C. & Sauer, J. Oxygen Defects and Surface Chemistry of Ceria: Quantum Chemical Studies Compared to Experiment. *Chem. Rev.* **113**, 3949–3985 (2013).
26. Zhao, D. *et al.* Enhancing Oxygen Evolution Electrocatalysis via the Intimate Hydroxide–Oxide Interface. *ACS Nano* **12**, 6245–6251 (2018).
27. Feng, J.-X., Ye, S.-H., Xu, H., Tong, Y.-X. & Li, G.-R. Design and Synthesis of FeOOH/CeO_2 Heterolayered Nanotube Electrocatalysts for the Oxygen Evolution Reaction. *Adv. Mater.* **28**, 4698–4703 (2016).
28. Sun, L., Zhou, L., Yang, C. & Yuan, Y. CeO2 nanoparticle-decorated reduced graphene oxide as an efficient bifunctional electrocatalyst for oxygen reduction and evolution reactions. *Int. J. Hydrogen Energy* **42**, 15140–15148 (2017).
29. Yu, Y. *et al.* Trivalent cerium-preponderant CeO_2 /graphene sandwich-structured nanocomposite with greatly enhanced catalytic activity for the oxygen reduction reaction. *J. Mater. Chem. A* **5**, 6656–6663 (2017).
30. Peng, W., Zhao, L., Zhang, C., Yan, Y. & Xian, Y. Controlled growth cerium oxide nanoparticles on reduced graphene oxide for oxygen catalytic reduction. *Electrochim. Acta* **191**, 669–676 (2016).
31. Masuda, T. *et al.* Role of Cerium Oxide in the Enhancement of Activity for the Oxygen Reduction Reaction at Pt–CeO_x Nanocomposite Electrocatalyst - An in Situ Electrochemical X-ray Absorption Fine Structure Study. *J. Phys. Chem. C*

116, 10098–10102 (2012).
32. Xu, F., Wang, D., Sa, B., Yu, Y. & Mu, S. One-pot synthesis of Pt/CeO_2/C catalyst for improving the ORR activity and durability of PEMFC. *Int. J. Hydrogen Energy* **42**, 13011–13019 (2017).
33. Liang, F., Yu, Y., Zhou, W., Xu, X. & Zhu, Z. Highly defective CeO_2 as a promoter for efficient and stable water oxidation. *J. Mater. Chem. A* **3**, 634–640 (2015).
34. Bagri, A., Grantab, R., Medhekar, N. V. & Shenoy, V. B. Stability and formation mechanisms of carbonyl- and hydroxyl-decorated holes in graphene oxide. *J. Phys. Chem. C* **114**, 12053–12061 (2010).
35. Perdew, J. P., Burke, K. & Ernzerhof, M. Generalized Gradient Approximation Made Simple. *Phys. Rev. Lett.* **77**, 3865–3868 (1996).
36. Kresse, G. From ultrasoft pseudopotentials to the projector augmented-wave method. *Phys. Rev. B* **59**, 1758–1775 (1999).
37. Kresse, G., Furthmüller, J. & Hafner, J. Ab initio molecular-dynamics simulation of the liquid-metal–amorphous-semiconductor transition in germanium. *Phys. Rev. B* **6**, 558–561 (1996).
38. Kresse & Hafner. Ab initio molecular dynamics for liquid metals. *Phys. Rev. B. Condens. Matter* **47**, 558–561 (1993).
39. Fabris, S., de Gironcoli, S., Baroni, S., Vicario, G. & Balducci, G. Reply to "Comment on 'Taming multiple valency with density functionals: A case study of defective ceria." *Phys. Rev. B* **72**, 237102 (2005).
40. Farra, R. *et al.* Promoted Ceria: A Structural, Catalytic, and Computational Study. *ACS Catal.* **3**, 2256–2268 (2013).
41. Skafte, T. L. *et al.* Selective high-temperature CO_2 electrolysis enabled by oxidized carbon intermediates. *Nat. Energy* (2019). doi:10.1038/s41560-019-0457-4
42. Nørskov, J. K. *et al.* Origin of the Overpotential for Oxygen Reduction at a Fuel-Cell Cathode. *J. Phys. Chem. B* **108**, 17886–17892 (2004).
43. Kulkarni, A., Siahrostami, S., Patel, A. & Nørskov, J. K. Understanding Catalytic Activity Trends in the Oxygen Reduction Reaction. (2018). doi:10.1021/acs.chemrev.7b00488
44. Montoya, J. H. *et al.* Materials for solar fuels and chemicals. *Nat. Mater.* **16**, 70–81 (2016).
45. Gu, X. *et al.* Efficient Oxygen Electrocatalysis by Nanostructured Mixed-Metal Oxides. *J. Am. Chem. Soc.* **140**, 8128–8137 (2018).
46. Sheng, H. *et al.* Electrocatalytic Production of H_2O_2 by Selective Oxygen Reduction Using Earth-Abundant Cobalt Pyrite (CoS_2). *ACS Catal.* **9**, 8433–8442 (2019).
47. Rossmeisl, J., Qu, Z.-W., Zhu, H., Kroes, G.-J. & Nørskov, J. K. Electrolysis of water on oxide surfaces. *J. Electroanal. Chem.* **607**, 83–89 (2007).
48. Man, I. C. *et al.* Universality in Oxygen Evolution Electrocatalysis on Oxide Surfaces. *ChemCatChem* **3**, 1159–1165 (2011).
49. Bajdich, M., García-Mota, M., Vojvodic, A., Nørskov, J. K. & Bell, A. T. Theoretical Investigation of the Activity of Cobalt Oxides for the Electrochemical

Oxidation of Water. *J. Am. Chem. Soc.* **135**, 13521–13530 (2013).
50. Barin, I. *Thermochemical data of pure substances*.
51. Winther, K. T. *et al.* Catalysis-Hub.org, an open electronic structure database for surface reactions. *Sci. Data* **6**, 75 (2019).
52. Chen, L. D. *et al.* Understanding the apparent fractional charge of protons in the aqueous electrochemical double layer. *Nat. Commun.* **9**, (2018).
53. Kirk, C. *et al.* Theoretical Investigations of the Electrochemical Reduction of CO on Single Metal Atoms Embedded in Graphene. *ACS Cent. Sci.* **3**, (2017).
54. Chen, S., Zhu, J., Wu, X., Han, Q. & Wang, X. Graphene oxide-MnO_2 nanocomposites for supercapacitors. *ACS Nano* **4**, 2822–30 (2010).
55. Xu, Y. & Shi, G. Assembly of chemically modified graphene: methods and applications. *J. Mater. Chem.* **21**, 3311 (2011).
56. Liu, Y., Deng, R., Wang, Z. & Liu, H. Carboxyl-functionalized graphene oxide-polyaniline composite as a promising supercapacitor material. *J. Mater. Chem.* **22**, 13619 (2012).
57. ASTM. Standard Test Method for Testing Polyurethane Raw Materials: Determination of Hydroxyl Numbers of Polyols (D4274). *ASTM Stand.* (2005). doi:10.1520/D4274-16
58. He, Z., Wang, Y., Zhao, T., Ye, Z. & Huang, H. Ultrasonication-assisted rapid determination of epoxide values in polymer mixtures containing epoxy resin. *Anal. Methods* **6**, 4257–4261 (2014).
59. Moghimi, A., Omrani, I., Nabid, M. R. & Mahmoodi, M. Quantification of hydroxyl group in polymers containing trace water by 19F NMR spectroscopy. *Eur. Polym. J.* (2013). doi:10.1016/j.eurpolymj.2012.09.019
60. De Marzi, L. *et al.* Cytotoxicity and genotoxicity of ceria nanoparticles on different cell lines in vitro. *Int. J. Mol. Sci.* **14**, 3065–3077 (2013).
61. Singh, P., Srivatsa, K. M. K., Barvat, A. & Pal, P. X-ray photoelectron spectroscopic studies of CeO_2 thin films deposited on Ni-W (100), c-Al2O3 (0001) and Si (100) substrates. *Curr. Appl. Phys.* **16**, 1388–1394 (2016).
62. Maslakov, K. I. *et al.* XPS study of ion irradiated and unirradiated CeO2 bulk and thin film samples. *Appl. Surf. Sci.* **448**, 154–162 (2018).
63. Liu, K. *et al.* Co_3O_4–CeO_2/C as a Highly Active Electrocatalyst for Oxygen Reduction Reaction in Al–Air Batteries. *ACS Appl. Mater. Interfaces* **8**, 34422–34430 (2016).
64. Martinez, U. *et al.* Progress in the Development of Fe-Based PGM-Free Electrocatalysts for the Oxygen Reduction Reaction. *Adv. Mater.* **31**, 1806545 (2019).
65. Peng, Y., Lu, B. & Chen, S. Carbon-Supported Single Atom Catalysts for Electrochemical Energy Conversion and Storage. *Adv. Mater.* **30**, 1801995 (2018).
66. Wang, L. *et al.* Stability of graphene oxide phases from first-principles calculations. doi:10.1103/PhysRevB.82.161406
67. Bukas, V. J. *et al.* Combining Experiment and Theory To Unravel the Mechanism of Two-Electron Oxygen Reduction at a Selective and Active Co-catalyst. *ACS Catal.* **8**, 11940–11951 (2018).
68. Mathew, K. *et al.* MPInterfaces: A Materials Project based Python tool for high-

throughput computational screening of interfacial systems. *Comput. Mater. Sci.* **122**, 183–190 (2016).

69. Strickler, A. L. *et al.* Systematic Investigation of Iridium-Based Bimetallic Thin Film Catalysts for the Oxygen Evolution Reaction in Acidic Media. *ACS Appl. Mater. Interfaces* acsami.9b13697 (2019). doi:10.1021/acsami.9b13697
70. Viswanathan, V., Hansen, H. A., Rossmeisl, J. & Nørskov, J. K. Universality in oxygen reduction electrocatalysis on metal surfaces. *ACS Catal.* **2**, 1654–1660 (2012).
71. Senanayake, G., Childs, J., Akerstrom, B. D. & Pugaev, D. Reductive acid leaching of laterite and metal oxides — A review with new data for Fe(Ni,Co)OOH and a limonitic ore. *Hydrometallurgy* **110**, 13–32 (2011).
72. Barazzouk, S., Lefèvre, M. & Dodelet, J.-P. Oxygen Reduction in PEM Fuel Cells: Fe-Based Electrocatalysts Made with High Surface Area Activated Carbon Supports. *J. Electrochem. Soc.* **156**, B1466 (2009).
73. Kobayashi, K., Nagao, M., Yamamoto, Y., Heo, P. & Hibino, T. Rechargeable PEM Fuel-Cell Batteries Using Porous Carbon Modified with Carbonyl Groups as Anode Materials. *J. Electrochem. Soc.* **162**, F868–F877 (2015).
74. Foo, G. S. & Sievers, C. Synergistic Effect between Defect Sites and Functional Groups on the Hydrolysis of Cellulose over Activated Carbon. *ChemSusChem* **8**, 534–543 (2015).

Chapter 6: 3D Interface-Engineered Transition Metal Oxide/MOF Hybrid Structures for Efficient Bifunctional Oxygen Electrocatalysis in Alkaline Environments

6.1 Introduction

The performance of representative electrochemical energy conversion and storage such as metal air batteries, fuel cells and electrolyzers relies largely on the catalysis of oxygen reduction reaction (ORR) and oxygen evolution reaction (OER).[321] To achieve a decent performance by overcoming the intrinsically sluggish nature of these reactions, researchers have employed noble-based catalysts such as platinum carbon (Pt/C) or IrO_2. However, due to its rarity, high cost and susceptibility to poisoning, many within the field have utilized heterogenous catalysts where a carbonaceous structure such as graphene oxide (GO) or metal-organic framework (MOF)-derived carbon is used as an electron-conducting matrix.[21,259,322] MOF is a type of supporting structure (framework) that links polyatomic clusters (secondary building blocks) using strong directional covalent bonds.[323–325] The catalytic performance of an electrocatalyst is determined by two factors: (1) the density of catalytically active sites and (2) the intrinsic activity of individual active sites.[65] Most metal-based catalysts consist of metal (or metal oxide) nanoparticles supported on a high-surface-area materials to provide electro-conducting pathways throughout the resulting catalyst.[326] Many pathways exist to increase both number of active sites and intrinsic activity of each site for bifunctional catalysis. One of them is the use of multiple metals and/or metal oxides interfacing each other. Bimetal-based catalysts have exhibited excellent catalytic activity[97,327–331] and in some cases, outperformed noble metal-based catalysts.[332] Bimetallics are such that, one metal ion acts as a support while the other acts as an active center for catalysis.[333] Examples of bimetallics include CoNiOOH and NiFeOOH that have shown higher activities than single metal core catalysts.[334–338] Li et al. fabricated four MOFs (NNU-21-24) based on Fe_2M (where M=Fe, Co, Ni, and Zn) clusters for OER in which all four catalyst based upon these metal ions outperformed the monometallic catalyst in terms of activity and durability.[339] It is believed that Fe cluster induce d-band centers to be close to the Fermi level, leading to a stronger binding interaction between O* intermediate and catalyst, thus aiding in the synergy electrocatalyst.[340] Zhu et al. demonstrated that a Ni-based MOF encapsulated by Fe-based MOF catalyst exhibit an overpotential of 265 mV at 10 mA cm^{-1} in 0.1 M KOH. DFT calculations also showed bimetal-based catalyst can afford a more optimal binding conditions for facilitated reactions.[341]

MOFs that solely use a single metal core, those containing Co, Ni, Mn, Ce, etc. has been widely applied for ORR/OER catalyst development. Among these metals, in my study, Co and Ce are chosen due to the bifunctionality of Co and high valence flexibility of Ce.[342–344] When both cerium and cobalt are combined to create a bimetallic catalyst, studies have shown enhanced activity for both ORR and OER.[345–347]

Structural integrity and enhanced performance is crucial, therefore, the use of ALD using metal-oxides is perferred.[348,349] Acid treatment using phosphoric acid should allow metal-oxides to better adsorb onto the surface of the MOF, which is advantageous in incurring potential synergies between metal and carbon. Nitrogen based functionalization

of ZIF based catalyst by acid treatment has been found effective in improving catalytic activity.[34–36] Phosphate functionalization can help with carbon substrates[37] although phosphate modification has been well-established in other oxide studies such as MCM-41 and SBA-15 by reaction with inorganic phosphoric acid. CeO_2 nanosheets (NSs) with trimethylphosphate (TMP) and a subsequent calcination, phosphate (PO_x)-modified CeO_2 NSs can be successfully prepared with controllable surface PO_x content and without impurity phases.[38–41] With phosphates present, metal oxides can adsorb onto the surface of the MOF, [42] possibly leading to an increased OER activity.[43–47]

Once these have formed, calcination can take place to allow not only further utilization of the metal oxides but introduce small quantities of nitrogen and oxygen into the MOF. Studies have shown that N-doped carbon structures with cobalt species exhibit excellence bifunctional performance.[48–52] Additionally, with the added small quantities of cobalt oxides, both ORR and OER has the potential to be enhanced. To the best of our knowledge, the introduction of second metal/metal oxide species by ALD on a metal/carbon hybrid catalyst derived from MOF is yet to be explored.

6.2 Experimental

Low temperature hydrothermal method was used to synthesize cobalt and cerium containing MOF framework. 2 mmol of $Co(NO_3)_2 \cdot 6H_2O$ and $Ce(NO_3)_3 \cdot 6H_2O$ were added into 8 mL of deionized water and 12 mL of ethanol. Then, 2 mmol of terephthalic acid (H_2BDC) was added into 12 mL of ethanol and subsequently added to the aforementioned solution to be stirred for 30 min for a uniform solution to form. The mixed solution was transferred into a 90 mL Teflon-sealed dry-oven for a hydrothermal reaction. The reaction was performed at 80°C for 24 h. Finally, the precipitate was washed repeatedly by ethanol and water in a 1:10 ratio respectively and named MOF. Once allowed to dry, the sample was treated with 2 mL of 0.1 M phosphoric acid and washed with the same ethanol-water combination and named pMOF. Allowed to dry overnight, the powder was placed inside a handmade copper box of a 4 cm x 4 cm dimension.

For ALD of zirconia and titania samples (termed Z-pMOF for zirconia incorporated phosphoric treated MOF and T-pMOF for titania incorporated phosphoric treated MOF), tetrakis(diethylamido)zirconium(IV)$[(C_2H_5)_2N]_4Zr$ and tetrakis(diethylamido)titanium(IV) $[(C_2H_5)_2N]_4Ti$ were used as the precursors while distilled water and nitrogen was used as co-reactant and purging gas, respectively. The canister temperatures for zirconia and titania were 250 °C and 200 °C with the chamber temperature of 250 °C. The pulsing time of 5 s was used for zirconia and titania precursor, and 0.5 s for water. Once completed, all samples were heated in air in a tube furnace at 400°C for 24 h.

6.3 Results and Discussion

6.3.1 Physicochemical properties of hybrid catalysts

In the FT-IR spectra Figure 6.1a, the H_3PO_4-treated sample (pMOF) shows distinct PO_4^{3-} stretching (1100 cm^{-1}) unlike the as-prepared MOF without such peak.

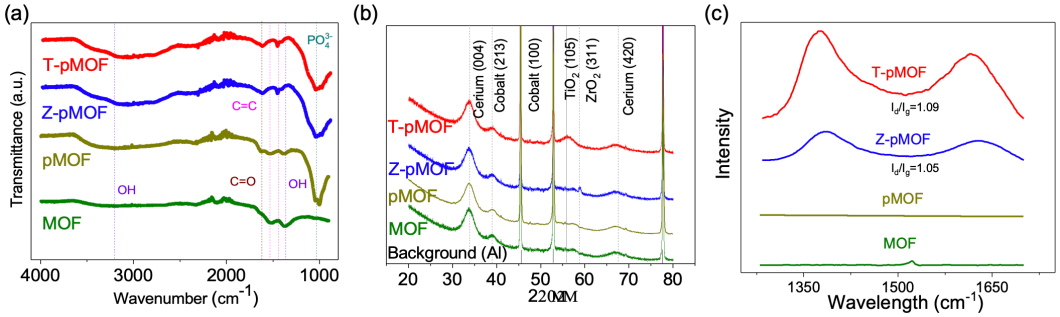

Figure 6.1: FT-IR (a) and XRD spectra (b) of MOF-Zr and MOF-Ti. Co Kα radiation (λ = 1.78897 Å) was used for XRD. (c) Raman data for MOF, Z-pMOF, and T-pMOF (c) CeO_2, and (d) CoO_2.

The uniform dispersion of phosphorus in the hybrid catalyst is also supported by the EFTEM elemental map of T-pMOF shown in Figures 6.2, 6.3 and 6.4. The XRD spectra (Figure 6.1b) indicates that CeO_2 (hexagonal) and CO_4 (cubic) crystals are already formed in both MOF and pMOF after heat treatment at 400 ºC. The formation of TiO_2 (anatase) in T-pMOF and ZrO_2 (monoclinic) in Z-pMOF are additionally confirmed by XRD. Peaks at 34º and 67º indicate the presence of cerium oxide for all MOF samples with their specific planes of (004), (213) and (420), respectively. All MOF samples show metallic Co peak at 46º. (Additionally, the system for T-pMOF is $CoTiO_3$ (rhombohedral). Scherrer equation was used to determine the particle size of cerium (47 nm), titanium (4.5 nm) and cobalt (4.7 nm).

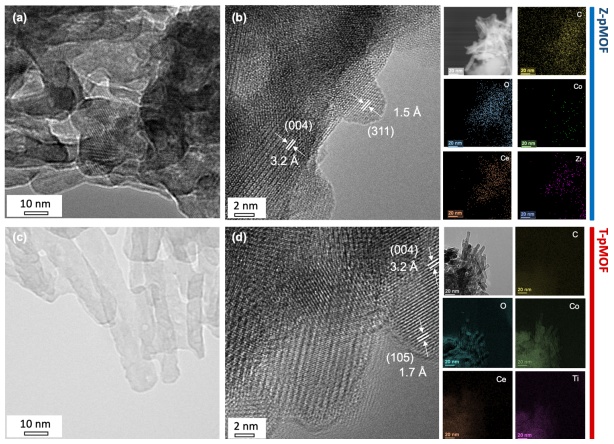

Figure 6.2: HRTEM images of (a) MOF (b) Z-pMOF, and (c) T-pMOF; revealing lattice fringes of (004) CeO_2 nanorods, (105) TiO_2 nanoclusters, and (311) ZrO_2 nanoclusters. (d) A zoomed-out TEM image of T-pMOF and (e-g) their corresponding EFTEM elemental map of Co, Ce and Ti, respectively. Circled in red is metallic cobalt nanoclusters.

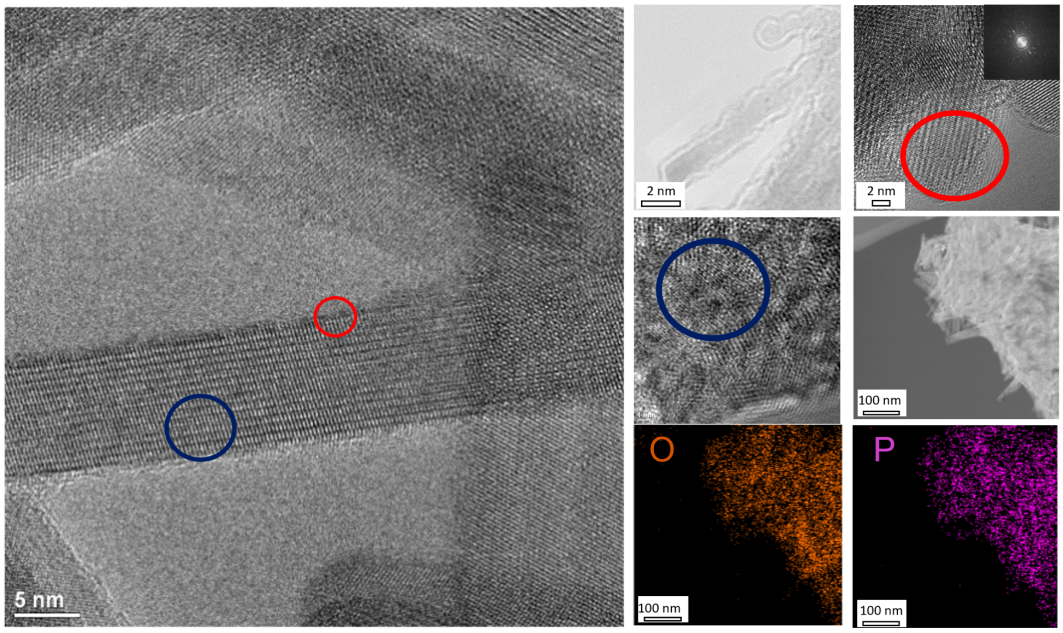

Figure 6.3: HRTEM, TEM, diffraction of titania, and EFTEM mapping for T-pMOF.

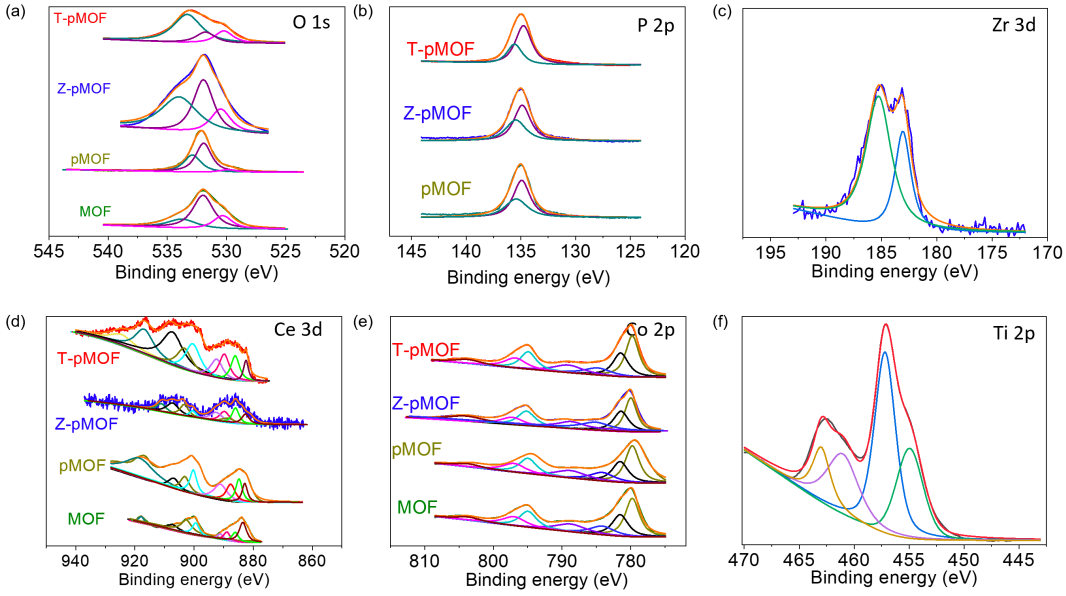

Figure 6.4: XPS data for T-pMOF, Z-pMOF, pMOF, and MOF for (a) O 1s, (b) P 2p, (c) Zr 3d, (d) Ce 3d, (e) Co 2p, and (f) Ti 2p.

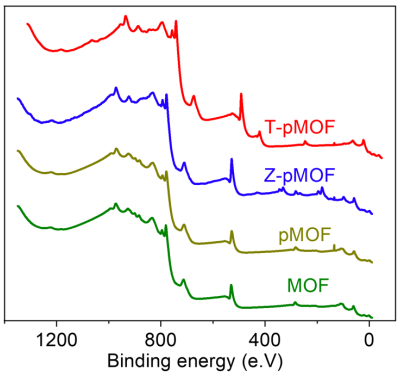

Figure 6.5: XPS survey data for MOF, Z-pMOF, and T-pMOF.

XPS data also confirms the presence of cerium oxide with further analysis of the valency states of cerium oxide as seen in Figure 6.4d. The binding energies of 882.7, 885.3, 889.2, 909.6, and 916.9 eV represent Ce^{4+}. The binding energies of 898.16 and 901.2 eV represent Ce^{3+}.[53] T-pMOF has more Ce^{4+} than Ce^{3+} in general than Z-pMOF or MOF alone. When looking at cobalt (Figure 6.4e), T-pMOF, Z-pMOF, pMOF, and MOF have the presence of Co^{3+} (779, 780, 784, 786 eV), Co^{2+} (794, 796, 800, and 802 eV), and metallic cobalt (788.8 eV).[54,55] Further analysis was made to confirm the presence of zirconia and titania as seen Figure 6.4c and Figure 6.4f. Additionally, a full survey of the XPS was also provided (Figure 6.5).

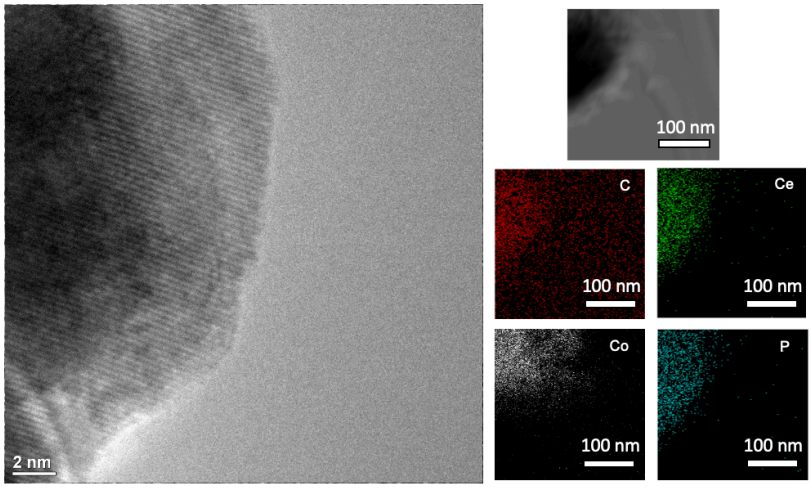

Figure 6.6: HRTEM, TEM, and EDS mapping of MOF sample.

TEM imaging and HRTEM was taken for all three samples MOF, T-pMOF and Z-pMOF to determine the crystallinity and size of TiO_2 and ZrO_2 nanoparticles. MOF amorphous structures are currently approximately 25 nm (Figure 6.6) compared to CeO_2 nanorods have a particle size of 50 nm for T-pMOF as seen in Figure 1d while the Z-pMOF

has an agglomerated particle size of 0.55 µm or amorphous particle size of approximately 5 nm as seen in Figure 6.2a. HRTEM in Figure 6.2b-c reveals how metallic cobalt nanoparticles resides within the CeO_2 nanorods and how TiO_2 particles of phase (101) (Figure 1e) or ZrO_2 particles of phase (103) (Figure 1b) "hang off" of the larger nanorod.

6.3.2 Electrochemical characterization of hybrid catalysts.

To characterize ORR performance of hybrid catalysts (and Pt/C for comparison), RDE and RRDE were performed in 0.1 M KOH aqueous solution. All samples including 20 wt.% Pt/C have a solid loading mass of 0.18 mg cm^{-2}. As shown in the LSV spectra (Figure 4a), T-pMOF exhibits an ORR activity even higher than that of Pt/C. The onset potential (E_{on}) of T-pMOF (0.92 V versus RHE; all potentials are presented versus RHE hereafter) is the same as that of Pt/C (E_{on} = 0.92 V), but the mass transport-limited current density (j_m) of T-pMOF (5.63 mA cm^{-2} at 0.2 V) compares rather favorably to Pt/C (5.54 mA cm^{-2}). MOF (E_{on} = 0.70 V and j_m = 1.42 mA cm^{-2}) and Z-pMOF (E_{on} = 0.78 V and j_m = 2.23 mA cm^{-2}) show poorer performances.

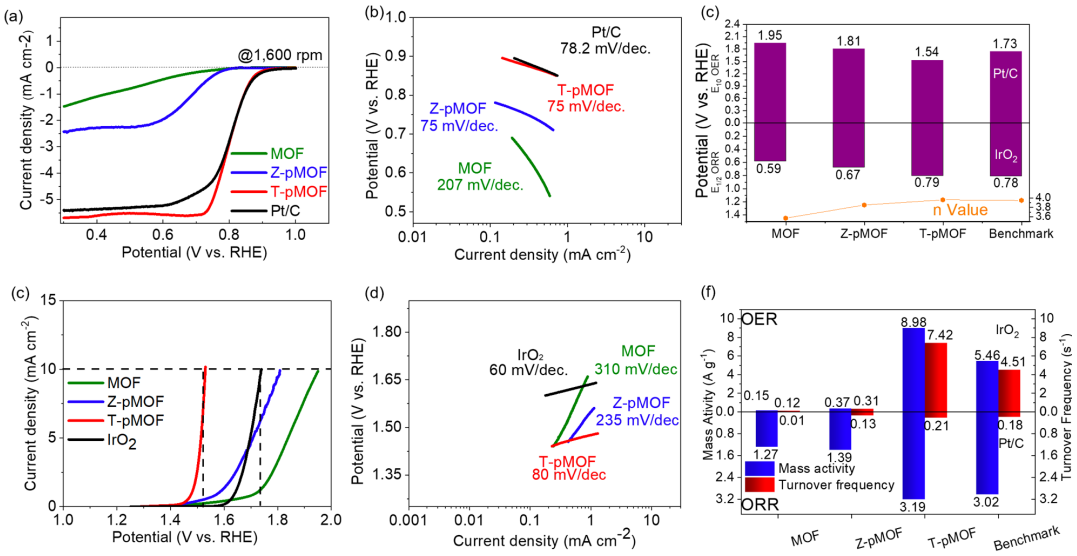

Figure 6.7: ORR voltammograms obtained in O_2-satured 0.1 M KOH. (a) LSV curves at 1600 rpm, (b) Tafel plot and Tafel slopes. OER characterization obtained in N_2-saturated 0.1 M KOH (a) LSV at 1600 rpm, (b,d) Tafel plot and Tafel slopes. (c) Half-wave potential with accompanying electron transfer and (f) Turnover frequency and mass activity for both ORR and OER.

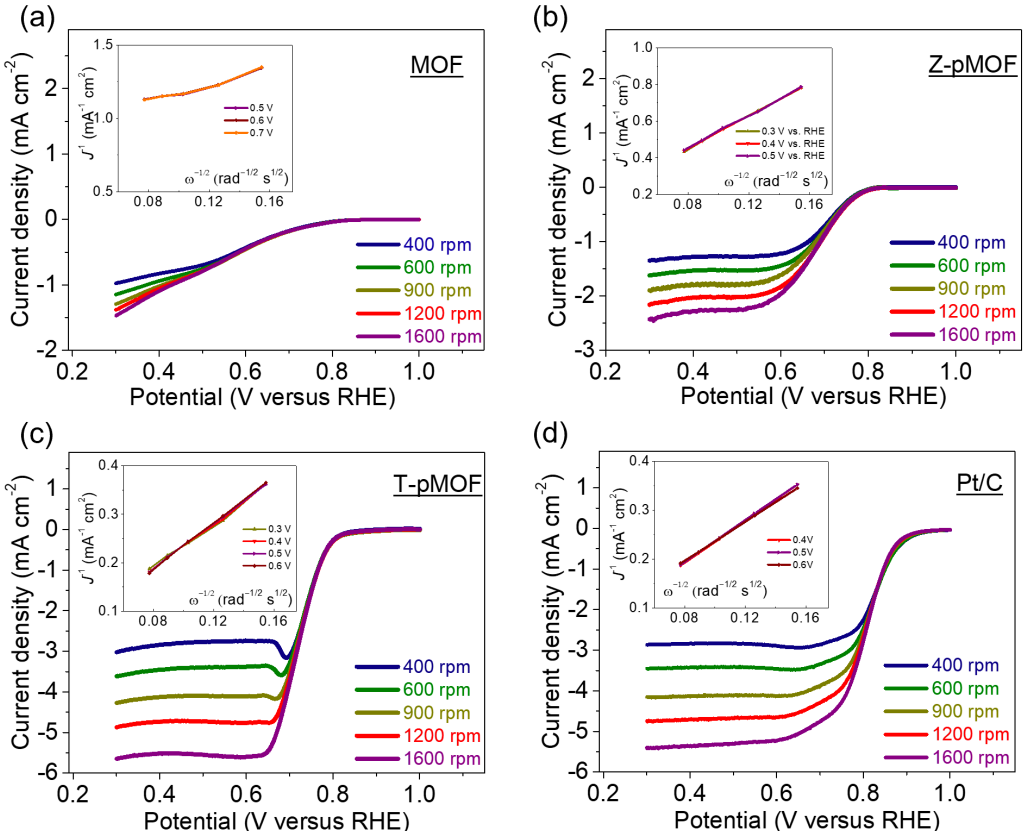

Figure 6.8: LSV curves in O_2-saturated 0.1 M KOH solution for (a) MOF (b) Z-pMOF (c) T-pMOF (d) Pt/C obtained at various rotating speeds at a sweep rate of 5 mV s^{-1}. Inset: the corresponding Koutechy-Levich plot at various disk potentials. All voltammograms presented are IR-compensated.

To further evaluate electrocatalytic activity, RRDE analysis was performed. Figure 6.9 shows linear sweep voltammetric (LSV) data, from both disk and ring, obtained from MOF, Z-pMOF, T-pMOF and Pt/C electrodes with various rotating rates. The phosphorylated MOF based sample (i.e., T-pMOF) again exhibited the highest onset potential (0.92 V versus RHE; all potentials versus RHE hereafter), half-wave potential (0.82 V) and current density (5.56 mA cm^{-2} at 0.4 V, respectively), close to those of Pt/C (0.92V, 0.80V, and 5.52 mA cm^{-2} at 0.4 V, respectively). The corresponding electron transfer number (n) value of T-pMOF was also larger (3.98) compared Z-pMOF (3.6) and MOF (3.2) when averaged for the potential window of 0.3 – 0.6 V. The LSV curves at different rotating speeds and corresponding Kouteckly-Levich (K-L) plots (insets) are shown in Figure 6.8. All the K-L plots exhibit linear slopes indicating a first-order ORR kinetics with respect to oxygen activity. The ORR kinetics were also quantified from the Tafel plots of mass transport-corrected kinetic currents for TMO/Co_xCeO_{x-2}-based nanorod hybrids (Figure 4b). The Tafel slope of T-pMOF is 75 mV per decade, better than Pt/C (78.2 mV dec^{-1}) and significantly smaller/equal than those of MOF and Z-pMOF (207 and 75 mV dec^{-1}, respectively).

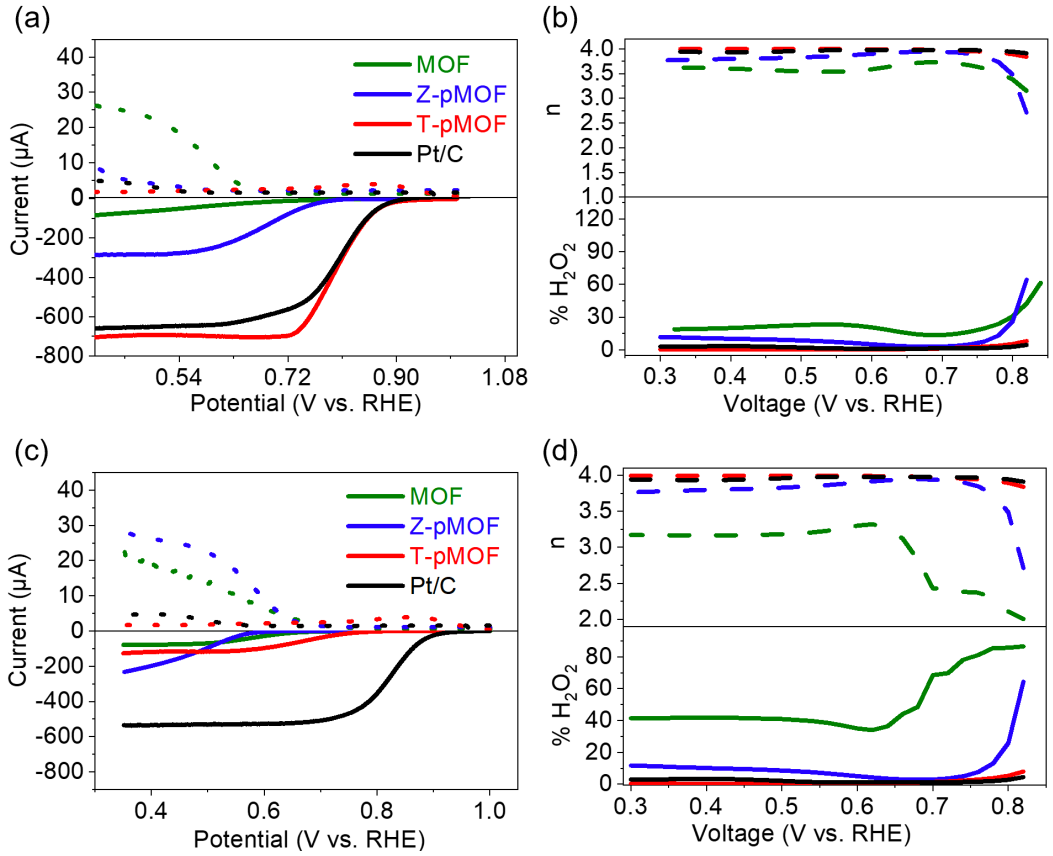

Figure 6.9: ORR voltammograms obtained in O_2-satured RRDE ring current (upper-dotted line) and disk current (lower-solid line) at 1600 rpm in (a) 0.1 M KOH, (c) H_2SO_4 and the resulting electron transfer number (upper-dotted) and hydrogen peroxide generation rate (lower-solid line) in (b) 0.1 M KOH and (d) 0.5 H_2SO_4. All voltammograms presented are IR-compensated.

Using Figure 6.9a, the peroxide yield and n values are represented based upon RRDE voltammograms obtained at a disk sweep rate of 5 mV s^{-1} while fixing the ring potential at 1.3 V. The hydrogen peroxide yield average was <5.2% for T-pMOF, <15% for Z-pMOF, and <25% for MOF and n average was 3.93 for T-pMOF, 3.41 for Z-pMOF, and 3.45 for MOF from 0.3 – 0.85 V vs. RHE according to Figure 6.9. This suggest that T-pMOF dominates a 4-electron ORR pathway. The good performance is attributed to the enhanced electrochemical surface area (ECSA) as seen in Figure 6.10 with T-pMOF having the largest area of 60.0 cm^2 compared to MOF, Z-pMOF, and Ni-foam (41.5, 43.7, Ni-foam 4.48 cm^2, respectively).

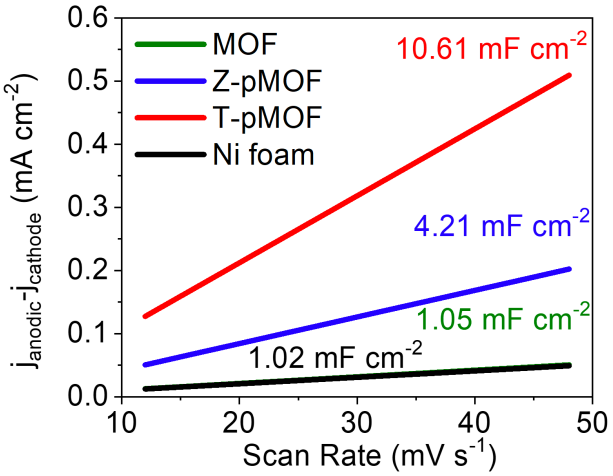

Area calculated using Figure 6.10 slopes.

Sample	Area (cm^2)
MOF	4.60
Z-pMOF	18.4
T-pMOF	46.4
Ni-foam	4.48

Figure 6.10: Plot of difference of anodic and cathodic current density as a function of scan rate for MOF, Z-pMOF, T-pMOF, and Ni-foam in 0.1 M KOH.

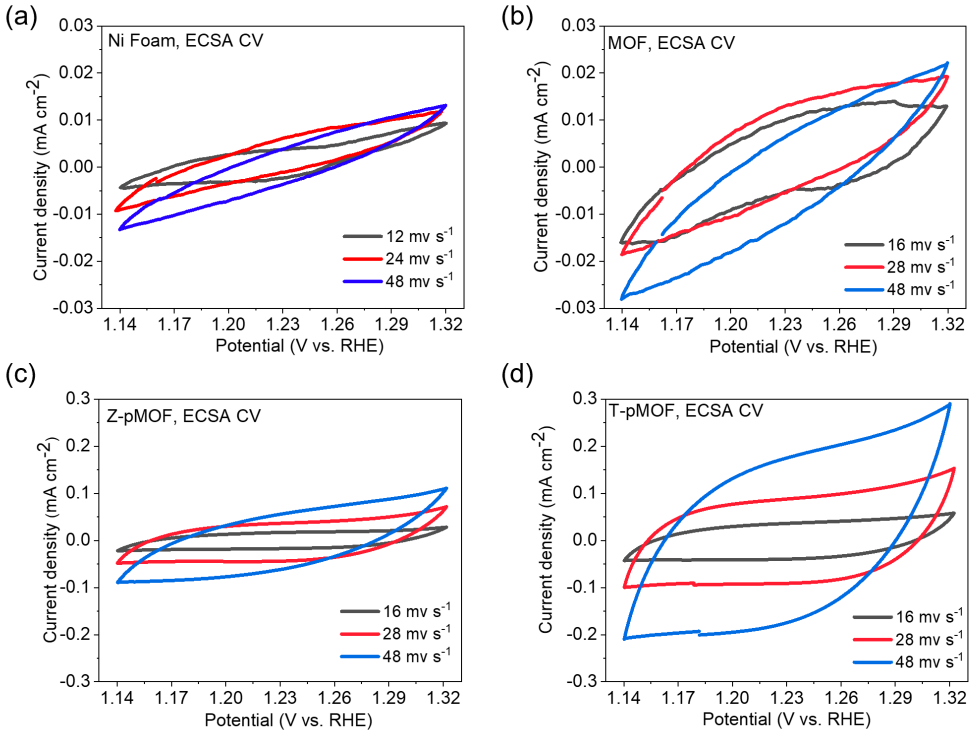

Figure 6.11: Cyclic voltammetry with various scan rates for the ECSA quantification (a) Ni Foam, (b) MOF, (c) Z-pMOF and (d) T-pMOF in 0.1 M KOH. For visual clarity, CV curves obtained at only 5 selected scan rates (12, 20, 28, 36 and 44 mV s^{-1}) are provided.

To fully test bifunctionality, OER measurements were taken in both 0.1 M KOH (Figure 4c) with corresponding Tafel plots as seen in Figure 6.4d. Onset potential in

alkaline media at 10 mV cm^{-2} for MOF, Z-pMOF, T-pMOF, and IrO_2 was 1.94, 1.78, 1.52, and 1.70 V vs. RHE. The T-pMOF strong performance was attributed to not only the aforementioned increase of cerium oxide. Further analysis was conducted on nickel foam for all samples including IrO_2 (Figure 6.12).

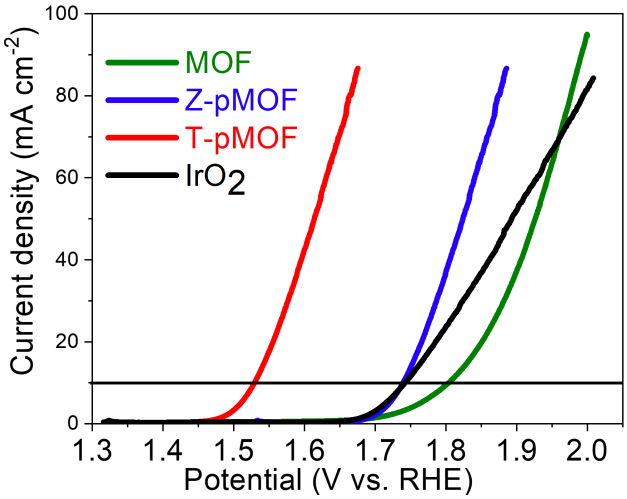

Figure 6.12: OER characterization using Ni-foam in 0.1 M KOH. LSV curves of metal oxide/MOF variants and IrO_2 in N_2-saturated. Dashed lines correspond to 10 mA cm^{-2}.

Durability test for both ORR and OER was performed for 2,000 cycles for T-pMOF in alkaline media as seen in Figure 6.13 and Figure 6.14. There was little to no difference between 150 and 2,000 cycles for T-pMOF in terms of both onset potential and current gain.

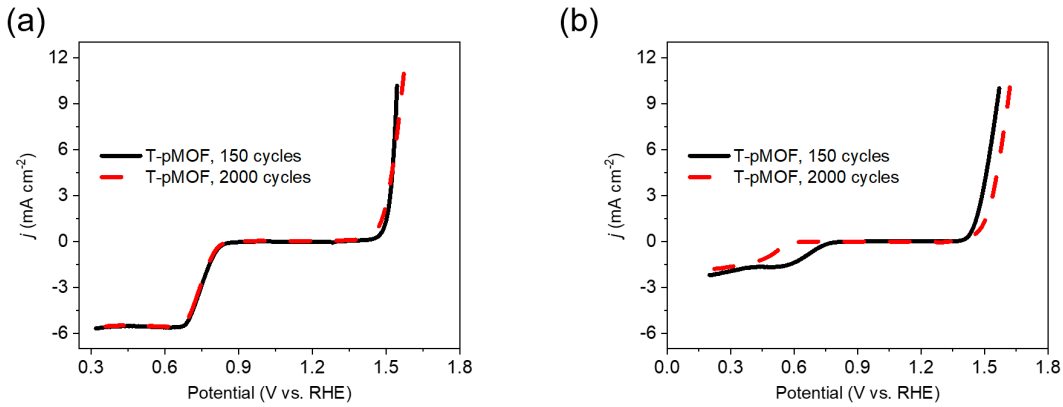

Figure 6.13: Cyclic durability test of T-pMOF in 0.1 M KOH (a) and 0.5 M H_2SO_4 (b) via potentiodynamic measurements at 50 mV s^{-1}. Voltammograms are obtained during the 150th and 2,000th cycles between 0.0 V and 2.0 V with the compliance current of j = 12 mA cm^{-2}. All voltammograms presented were obtained at 1600 rpm.

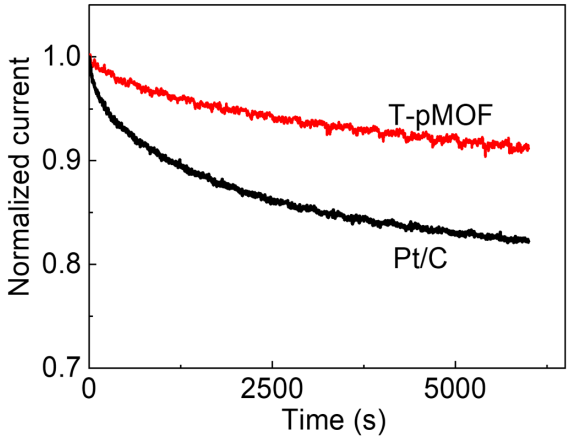

Figure 6.15: Chronopotentiometric measurements for T-pMOF and Pt/C.

Electrochemical tests were also conducted in acidic media (0.5 M H_2SO_4), but they were not as favorable as the alkaline performance. T-pMOF had ORR and OER activities of 0.79 V vs. RHE and 1.61 V vs. RHE, respectively (Figure 6.15). Other samples like Z-pMOF did not show any better performance (ORR: 0.62 V vs. RHE; OER: 1.69 V RHE). K-L plots (Figure 6.16) and Tafel plots (Figure 6.15b and 6.15d) also indicate poor kinetics for both T-pMOF (ORR: 80 mV dec^{-1}; OER: 60 mV dec^{-1}) and Z-pMOF (ORR: 80 mV dec^{-1}; OER: 60 mV dec^{-1}). However, RRDE data (Figure 6.9c-d) had favorable electron transfer number of (T-pMOF) 3.97 and (Z-pMOF) 3.5 between 0.3 – 0.8 V vs. RHE on average. A decrease OER and ORR durability for the T-pMOF sample as seen in Figure 6.15 (ORR 0.8 to 0.54 V vs. RHE; OER 1.57 to 1.62 V vs. RHE).

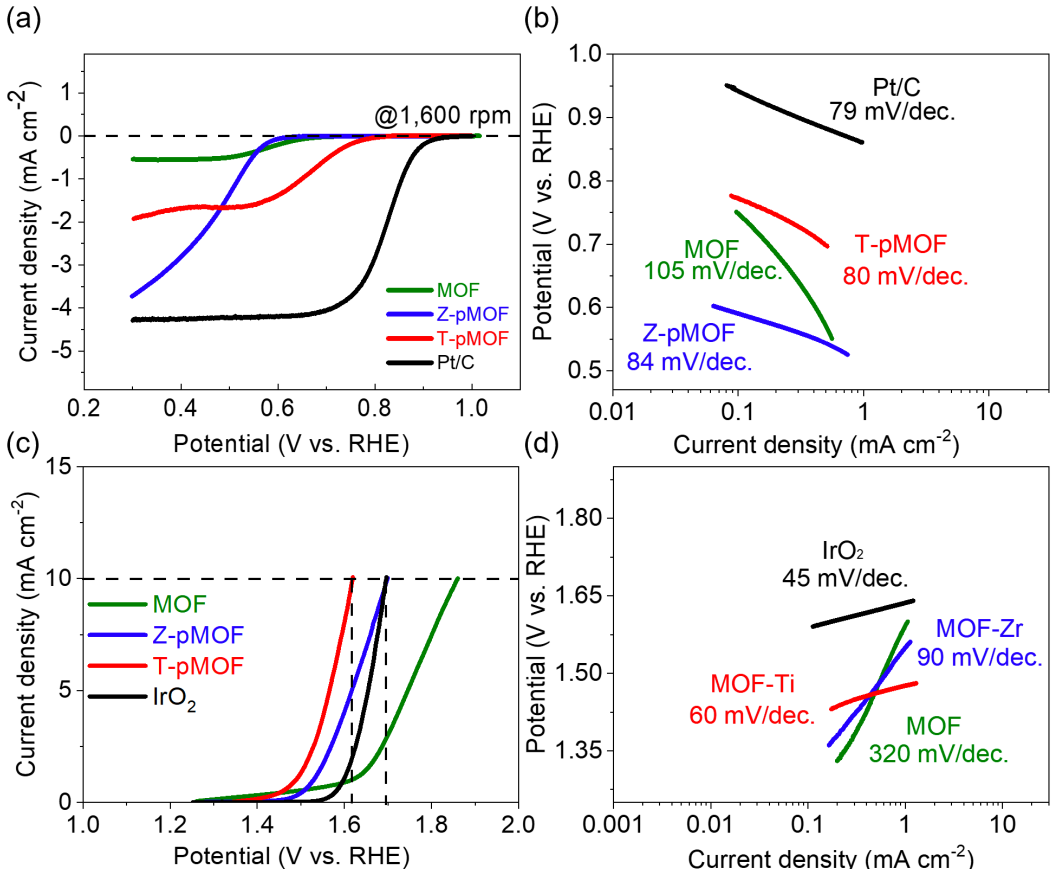

Figure 6.15: ORR voltammograms obtained in O_2-satured 0.5 M H_2SO_4. (a) LSV curves at 1600 rpm, (b) Tafel plot and Tafel slopes. OER characterization obtained in N_2-saturated 0.5 M H_2SO_4 (c) LSV at 1600 rpm, (d) Tafel plot and Tafel slopes.

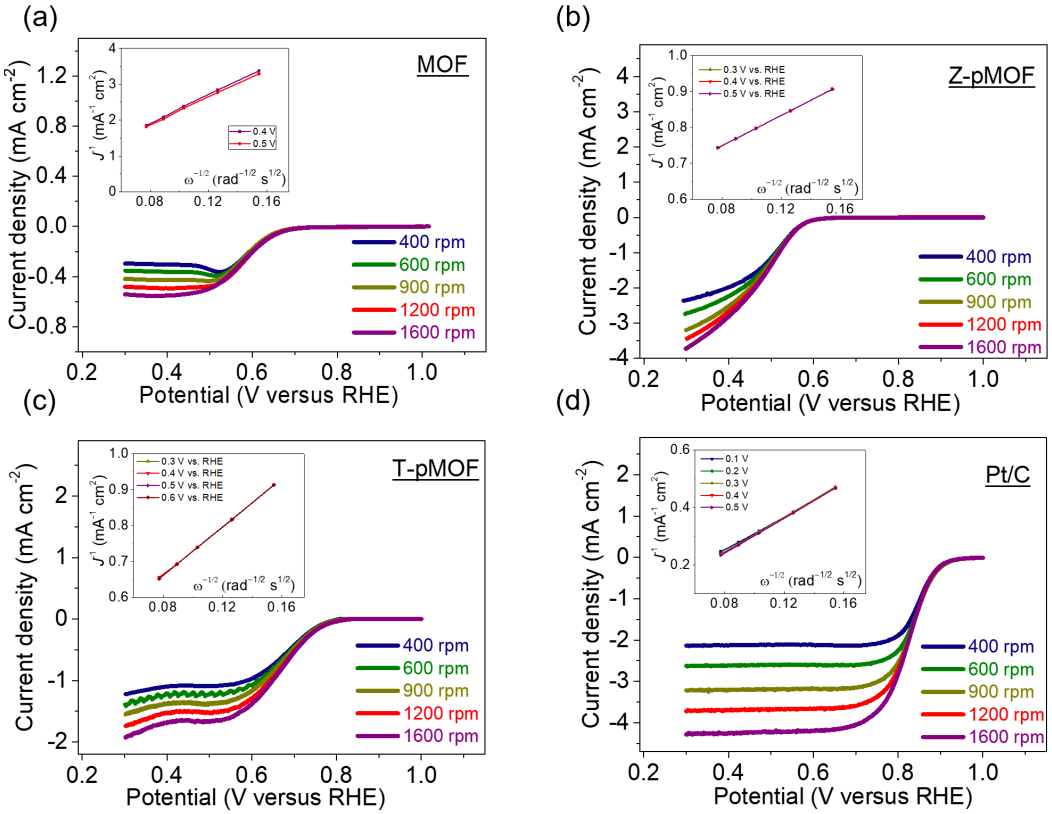

Figure 6.16: LSV curves in O_2-saturated 0.5 M H_2SO_4 solution for (a) MOF (b) Z-pMOF (c) T-pMOF (d) Pt/C obtained at various rotating speeds at a sweep rate of 5 mV s^{-1}. Inset: the corresponding Koutechy-Levich plot at various disk potentials. All voltammograms presented are IR-compensated.

6.3.3 Effects of heat treatment.

Pyrolysis is typically used to graphitize MOFs, however for our research, we have found that a simple heat treatment at 400°C in air for the T-pMOF sample has achieved graphitization. We found T-pMOF and Z-pMOF having a large Ig/Id ratio peak (1.09, 1.05 respectively) as seen in Figure 1c. The appearance of graphitization, as seen with a large Ig/Id ratio peak, indicates that the interfacing of TMO/MOF structure allows the formation of defects. The other samples in Figure 1c, pMOF and MOF, lacked any visible D or G band peaks.

Heat treatment at 400°C in air is critical for both ORR and OER performance. We found that catalysts that are heat treated below 400°C (e.g. 200°C for N_2 and O_2) display a large oxidation peak during positive LSV sweep (Figure 6.17). In Figure 6.18, the sample treated at 400°C in air is better than the other four samples in both ORR and OER indicating that our rather unconventional heat treatment leads to an unexpectedly favorable catalytic activity. Compared to T-pMOF, monometal-based catalysts slightly underperform, further supporting the favorable effect expected from bimetallic catalysts for both ORR and OER performance.

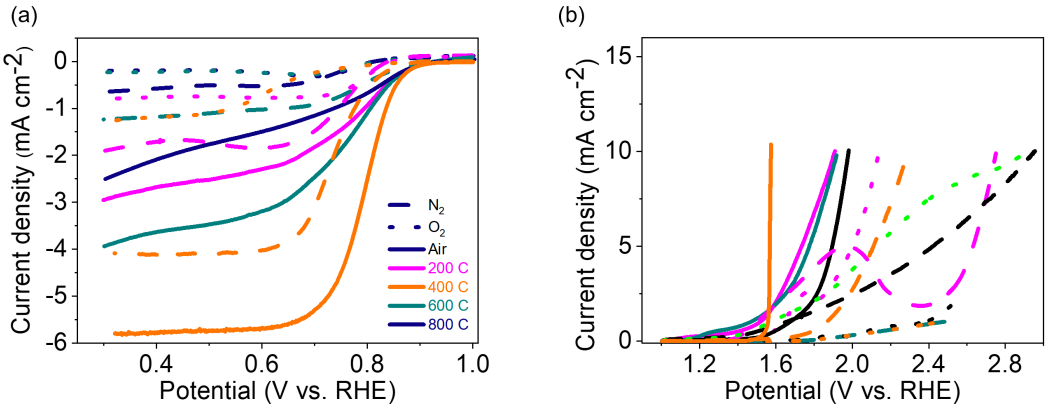

Figure 6.17: Voltammograms obtained in 0.1 M KOH LSV curves at 1600 rpm of various heating treatment (a) O_2-satured ORR and (b) N_2-satured OER.

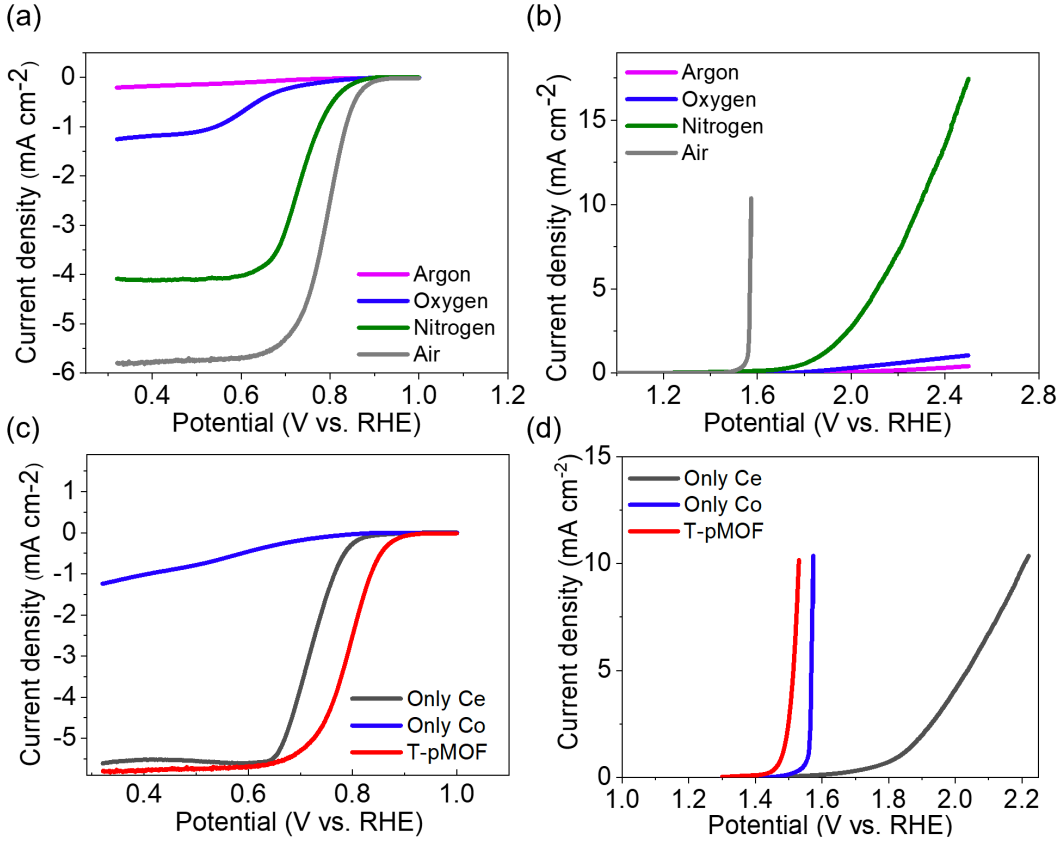

Figure 6.18: Voltammograms obtained in 0.1 M KOH LSV curves at 1600 rpm of various gasses and metal ions/compounds (a,c) O_2-satured ORR and (b,d) N_2-satured OER.

6.3.4 Quasi-operando XPS analysis

In the hope to observe the change in the chemical states of our catalysts during ORR and OER operation, we performed so-called *quasi-operando* XPS analysis, which is achieved by performing *ex situ* XPS after exposing the catalyst at a specific potential in an alkaline solution (Figure 6.19). We tested T-pMOF for Co 2p, O 1s, and Ce 3d after exposing the sample at a potential between 0.52 - 1.72 V. Co 2p spectra observed after performing ORR (0.52 – 0.92 V) and OER (1.32 – 1.72 V), the peaks of 797.05 and 804.83 eV of Co^{2+} peaks became smaller while Co^{3+} peaks got smaller. Ti 2p spectra after both ORR and OER, the peaks of 461.5 and 463.7 eV of Ti^{4+} got smaller while Ti^{3+} peaks got larger. This means the titanium for T-pMOF samples tends to be reduced as the potential increases while cobalt does the opposite. This indicates that both titanium and cobalt contribute synergistically towards the catalysis of T-pMOF.

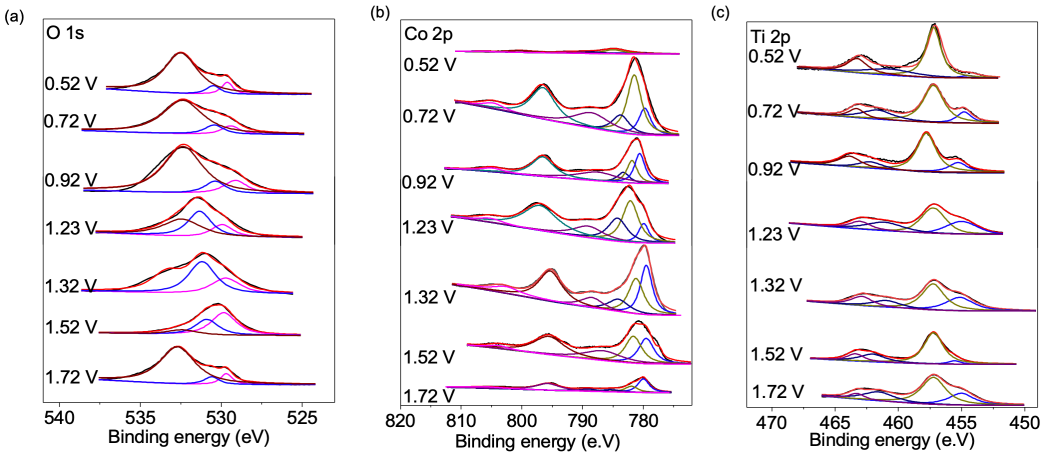

Figure 6.19: T-pMOF XPS data of voltages 0.52-1.72 V for (a) O 1s, (b) Co 2p, and (c) Ti 2p

6.4 Conclusion

We have demonstrated the critical impact of proper MOF functionalization on ORR and OER performance. Phosphoric acid treatment was performed on MOFs, which is made of Co and Ce precursors and organic linker, to induce more phosphate groups before anchoring TMO NPs (either TiO_2 or ZrO_2) using ALD. TiO_2 NPs/MOF hybrid, labeled as T-pMOF performed the best catalytic activity for both ORR and OER. T-pMOF have electron transfer number of nearly four and superior onset potentials (0.92 V vs. RHE for ORR and 1.52 V vs. RHE for OER) compared to other catalyst such as Z-pMOF and MOF. It is ascribed to the synergistic effect between TMOs and carbon mediated by phosphate groups, which provided a favorable environment for oxygen absorption upon the surface of the hybrid catalyst.

6.5 Experimental

6.5.1 Sample Preparations

Low temperature hydrothermal method was used to synthesize cobalt and cerium containing MOF structure. 2 mmol of $Co(NO_3)_2 \cdot 6H_2O$ and $Ce(NO_3)_3 \cdot 6H_2O$ were added into 8 mL of deionized water and 12 mL of ethanol. Then, 2 mmol of terephthalic acid (H_2BDC) was added into 12 mL of ethanol and subsequently added to the aforementioned solution to be stirred for 30 min for a uniform solution to form. The mixed solution was transferred into a 90 mL Teflon-sealed dry-oven for a hydrothermal reaction. The reaction was performed at 80°C for 24 h. Finally, the precipitate was washed repeatedly by ethanol and water in a 1:10 ratio respectively and named MOF. Once allowed to dry, the sample was treated with 2 mL of 0.1 M phosphoric acid and washed with the same ethanol-water combination. Allowed to dry overnight, the powder was placed inside a handmade copper box of a 4 cm × 4 cm dimension.

For zirconia and titania ALD, tetrakis(diethylamido)zirconium(IV) $[(C_2H_5)_2N]_4Zr$ and tetrakis(diethylamido)titanium(IV) $[(C_2H_5)_2N]_4Ti$ were used as the precursors while distilled water and nitrogen was used as co-reactant and purging gas, respectively. The canister temperatures for Zr and Ti were 250 °C and 200 °C, respectively while the chamber temperature was set at 250 °C. The pulsing time of 5 s was used to introduce Zr and Ti precursors, and 0.5 s was allowed for water. After 20 and 100 cycles (Zr and Ti precursors, respectively) of ALD processes, both samples were heated in air in a tube furnace at 400°C for 24 h. The products are named Z-pMOF and T-pMOF. Samples that did not have ALD deposition were termed MOF (MOF treated with phosphate was termed pMOF), both samples were subjected to subsequent heat treatment.

6.5.2 Material Characterization

The morphology of hybrid structures were characterized by transmission electron microscopy (TEM, Tecnai 200kV FEI monochromated F20 UT). The preparation for TEM samples was achieved by drop-casting the sonicated ethanol-suspended catalyst upon a 3 mm Lacey B Carbon 400 mesh grid from Ted Pella, followed by ambient drying. X-ray diffraction (XRD) patter was recorded by a PANalytical X'Pert PRO with Co Kα radiation (λ = 1.78897 Å) at a step size of 0.02º and scan rate of 0.04º s^{-1}. For XRD samples, 10 mg of catalyst in 5 mL of ethanol was drop-casted upon an aluminum disk and allowed to dry in oven at 40°C for 4 h. Fourier transform infrared spectroscopy (FT-IR) samples were dried under vacuum and placed between a diamond crystal and a Si wafer to ensure a flatness before being analyzed in a Nicolet 380 system (Thermo Fisher Scientific). X-ray photoelectron spectroscopy (XPS) analysis was performed in a Nexsa system using a focused, monochromatic micro-focused low power Al Kα X-ray (1486 eV) source for excitation and a spherical section analyzer (150 μm diameter X-ray beam incident to the surface normal; detector set at 45°). Sample preparation included a dispersion of the catalyst in ethanol and drop-cast onto a cleaned Si wafer.

6.5.3 Electrochemical characterization

The ORR activity of the catalysts was evaluated in 0.1M KOH or 0.5 M H_2SO_4 with ring-disk electrode (RDE; RRDE-3A, ALS Co.) in a three-electrode setup having

RRDE electrode as a working electrode, a graphite rod as a counter electrode, and an Ag/AgCl/KCl (3.5 M) electrode as the reference electrode. The working electrode was prepared by drop-casting each electrode ink onto a 4 mm RRDE glassy carbon disk electrode. The ink was prepared by immersing 15 mg of metal oxide/carbon hybrid catalysts into 2.21 mL of ethanol along with 3.75 mg of carbon black (Vulcan XC72) and 75 µl of 5 wt% Nafion (Nafion D-521, Alfa Aesar). For Pt/C electrode, a 15 mg ml^{-1} Pt/C suspension was prepared by using a commercial 20 wt% Pt supported on carbon black instead of the hybrid samples. Then, O_2 and N_2 saturated environment was implemented by flowing high-purity O_2 and N_2 gas at 32 sccm into 80 ml of electrolyte for >30 min. All electrochemical profiles are expressed with respect to reversible hydrogen electrode (RHE). ECSA was measured using a Ni-foam (geometric area of 0.35 cm^2) as the substrate. The Ni-foam was cleaned with 0.5 M HCl for 3 h and subsequently rinsed with 1:10 ethanol:water.

Reference

1. Ghosh, S. & Basu, R. N. Multifunctional nanostructured electrocatalysts for energy conversion and storage: current status and perspectives. *Nanoscale* **10**, 11241–11280 (2018).
2. Asefa, T. Metal-Free and Noble Metal-Free Heteroatom-Doped Nanostructured Carbons as Prospective Sustainable Electrocatalysts. *Acc. Chem. Res.* **49**, 1873–1883 (2016).
3. Shao, M., Chang, Q., Dodelet, J.-P. & Chenitz, R. Recent Advances in Electrocatalysts for Oxygen Reduction Reaction. *Chem. Rev.* **116**, 3594–3657 (2016).
4. Wang, H.-F., Tang, C. & Zhang, Q. A Review of Precious-Metal-Free Bifunctional Oxygen Electrocatalysts: Rational Design and Applications in Zn−Air Batteries. *Adv. Funct. Mater.* **28**, 1803329 (2018).
5. Ha, J., Lee, J. H. & Moon, H. R. Alterations to secondary building units of metal-organic frameworks for the development of new functions. *Inorg. Chem. Front.* **7**, 12–27 (2019).
6. Zhou, H. C. J. & Kitagawa, S. Metal-Organic Frameworks (MOFs). *Chem. Soc. Rev.* **43**, 5415–5418 (2014).
7. Tranchemontagne, D. J., Tranchemontagne, J. L., O'keeffe, M. & Yaghi, O. M. Secondary building units, nets and bonding in the chemistry of metal–organic frameworks. *Chem. Soc. Rev.* **38**, 1257–1283 (2009).
8. Kulkarni, A., Siahrostami, S., Patel, A. & Nørskov, J. K. Understanding Catalytic Activity Trends in the Oxygen Reduction Reaction. (2018). doi:10.1021/acs.chemrev.7b00488
9. Jöerissen, L. SECONDARY BATTERIES – METAL-AIR SYSTEMS | Bifunctional Oxygen Electrodes. in *Encyclopedia of Electrochemical Power Sources* (ed. Garche, J.) 356–371 (Elsevier, 2009). doi:https://doi.org/10.1016/B978-044452745-5.00920-5
10. Yin, P. *et al.* Single Cobalt Atoms with Precise N-Coordination as Superior Oxygen Reduction Reaction Catalysts. *Angew. Chemie* **128**, 10958–10963 (2016).
11. Chen, Y. *et al.* Isolated Single Iron Atoms Anchored on N-Doped Porous Carbon

as an Efficient Electrocatalyst for the Oxygen Reduction Reaction. *Angew. Chemie - Int. Ed.* **56**, 6937–6941 (2017).
12. Chen, W. *et al.* Single Tungsten Atoms Supported on MOF-Derived N-Doped Carbon for Robust Electrochemical Hydrogen Evolution. *Adv. Mater.* **30**, (2018).
13. Zhang, L. *et al.* Coordination of Atomic Co-Pt Coupling Species at Carbon Defects as Active Sites for Oxygen Reduction Reaction. *J. Am. Chem. Soc.* **140**, 10757–10763 (2018).
14. Du, C. *et al.* Metal organic framework for the fabrication of mutually interacted Pt–CeO2–C ternary nanostructure: advanced electrocatalyst for oxygen reduction reaction. *Electrochim. Acta* **266**, 348–356 (2018).
15. Osgood, H., Devaguptapu, S. V., Xu, H., Cho, J. & Wu, G. Transition metal (Fe, Co, Ni, and Mn) oxides for oxygen reduction and evolution bifunctional catalysts in alkaline media. *Nano Today* **11**, 601–625 (2016).
16. Wang, J. *et al.* Design of N-Coordinated Dual-Metal Sites: A Stable and Active Pt-Free Catalyst for Acidic Oxygen Reduction Reaction. *J. Am. Chem. Soc.* **139**, 17281–17284 (2017).
17. Chen, L., Wang, H.-F., Li, C. & Xu, Q. Bimetallic metal-organic frameworks and their derivatives. (2020). doi:10.1039/d0sc01432j
18. Tang, C. *et al.* Spatially Confined Hybridization of Nanometer-Sized NiFe Hydroxides into Nitrogen-Doped Graphene Frameworks Leading to Superior Oxygen Evolution Reactivity. *Adv. Mater.* **27**, 4516–4522 (2015).
19. Burke, M. S., Enman, L. J., Batchellor, A. S., Zou, S. & Boettcher, S. W. Oxygen Evolution Reaction Electrocatalysis on Transition Metal Oxides and (Oxy)hydroxides: Activity Trends and Design Principles. *Chem. Mater.* **27**, 7549–7558 (2015).
20. Liang, H. *et al.* Hydrothermal continuous flow synthesis and exfoliation of NiCo layered double hydroxide nanosheets for enhanced oxygen evolution catalysis. *Nano Lett.* **15**, 1421–1427 (2015).
21. Long, X. *et al.* A strongly coupled graphene and FeNi double hydroxide hybrid as an excellent electrocatalyst for the oxygen evolution reaction. *Angew. Chemie - Int. Ed.* **53**, 7584–7588 (2014).
22. Liu, J. *et al.* Confining ultrasmall bimetallic alloys in porous N–carbon for use as scalable and sustainable electrocatalysts for rechargeable Zn–air batteries. *J. Mater. Chem. A* **7**, 12451–12456 (2019).
23. Wang, Q. *et al.* FeNi-based bimetallic MIL-101 directly applicable as an efficient electrocatalyst for oxygen evolution reaction. *Microporous Mesoporous Mater.* **286**, 92–97 (2019).
24. Zhao, Z., DIng, J., Zhu, R. & Pang, H. The synthesis and electrochemical applications of core-shell MOFs and their derivatives. *Journal of Materials Chemistry A* **7**, 15519–15540 (2019).
25. Zhao, X., Liu, X., Huang, B., Wang, P. & Pei, Y. Hydroxyl group modification improves the electrocatalytic ORR and OER activity of graphene supported single and bi-metal atomic catalysts (Ni{,} Co{,} and Fe). *J. Mater. Chem. A* **7**, 24583–24593 (2019).
26. Tripathy, R. K., Samantara, A. K. & Behera, J. N. A cobalt metal-organic

framework (Co-MOF): A bi-functional electro active material for the oxygen evolution and reduction reaction. *Dalt. Trans.* **48**, 10557–10564 (2019).
27. Zhang, M., Dai, Q., Zheng, H., Chen, M. & Dai, L. Novel MOF-Derived Co@N-C Bifunctional Catalysts for Highly Efficient Zn–Air Batteries and Water Splitting. *Adv. Mater.* **30**, (2018).
28. Dou, S., Li, X., Tao, L., Huo, J. & Wang, S. Cobalt nanoparticle-embedded carbon nanotube/porous carbon hybrid derived from MOF-encapsulated Co3O4 for oxygen electrocatalysis. *Chem. Commun.* **52**, 9727–9730 (2016).
29. Li, X. *et al.* ZIF-67-derived Co_3O_4@carbon protected by oxygen-buffering CeO_2 as an efficient catalyst for boosting oxygen reduction/evolution reactions. *J. Mater. Chem. A* **7**, 25853–25864 (2019).
30. He, X. *et al.* Less active CeO2 regulating bifunctional oxygen electrocatalytic activity of Co_3O_4@N-doped carbon for Zn-air batteries. *J. Mater. Chem. A* **7**, 6753–6765 (2019).
31. Zhang, Z. *et al.* Co and CeO_2 co-decorated N-doping carbon nanofibers for rechargeable Zn-air batteries. *Nanotechnology* **30**, 0–8 (2019).
32. Ahn, S. *et al.* Stable Metal–Organic Framework-Supported Niobium Catalysts. *Inorg. Chem.* **55**, 11954–11961 (2016).
33. Lee, D. T., Zhao, J., Oldham, C. J., Peterson, G. W. & Parsons, G. N. UiO-66-NH_2 Metal–Organic Framework (MOF) Nucleation on TiO_2 , ZnO, and Al_2O_3 Atomic Layer Deposition-Treated Polymer Fibers: Role of Metal Oxide on MOF Growth and Catalytic Hydrolysis of Chemical Warfare Agent Simulants. *ACS Appl. Mater. Interfaces* **9**, 44847–44855 (2017).
34. Banerjee, R. *et al.* High-throughput synthesis of zeolitic imidazolate frameworks and application to CO_2 capture. *Science (80-91).* **319**, 939–943 (2008).
35. Lachawiec, A. J., Qi, G. & Yang, R. T. Hydrogen storage in nanostructured carbons by spillover: Bridge-building enhancement. *Langmuir* **21**, 11418–11424 (2005).
36. Song, Y. F. & Cronin, L. Postsynthetic covalent modification of metal-organic framework (MOF) materials. *Angewandte Chemie - International Edition* **47**, 4635–4637 (2008).
37. Liu, X., Li, J., Wang, X., Chen, C. & Wang, X. High performance of phosphate-functionalized graphene oxide for the selective adsorption of U(VI) from acidic solution. *J. Nucl. Mater.* **466**, 56–64 (2015).
38. Wang, T., Dai, Q. & Yan, F. Effect of acid sites on catalytic destruction of trichloroethylene over solid acid catalysts. *Korean J. Chem. Eng.* **34**, 664–671 (2017).
39. Li, D., Zheng, Y. & Wang, X. Effect of phosphoric acid on catalytic combustion of trichloroethylene over Pt/P-MCM-41. *Appl. Catal. A Gen.* **340**, 33–41 (2008).
40. Kawi, S., Shen, S. C. & Chew, P. L. Generation of Brønsted acid sites on Si-MCM-41 by grafting of phosphorus species. *J. Mater. Chem.* **12**, 1582–1586 (2002).
41. Dai, Q. *et al.* Phosphate-Functionalized CeO2 Nanosheets for Efficient Catalytic Oxidation of Dichloromethane. *Environ. Sci. Technol.* **52**, 13430–13437 (2018).
42. Islamoglu, T. *et al.* Cerium(IV) vs Zirconium(IV) Based Metal–Organic

Frameworks for Detoxification of a Nerve Agent. *Chem. Mater.* **29**, 2672–2675 (2017).
43. Zhao, S., Li, C., Huang, H., Liu, Y. & Kang, Z. Phosphate functionalized activated carbon as an efficient metal-free electrocatalyst for the oxygen reduction reaction. *New J. Chem.* **39**, 8881–8886 (2015).
44. Guo, R. *et al.* Phosphate-Based Electrocatalysts for Water Splitting: Recent Progress. *ChemElectroChem* **5**, 3822–3834 (2018).
45. Khrizanforova, V. *et al.* 3D Ni and Co redox-active metal-organic frameworks based on ferrocenyl diphosphinate and 4,4′-bipyridine ligands as efficient electrocatalysts for the hydrogen evolution reaction. *Dalt. Trans.* **49**, 2794–2802 (2020).
46. Tian, J., Liu, Q., Asiri, A. M. & Sun, X. Self-supported nanoporous cobalt phosphide nanowire arrays: An efficient 3D hydrogen-evolving cathode over the wide range of pH 0-14. *J. Am. Chem. Soc.* **136**, 7587–7590 (2014).
47. Liu, T. *et al.* CoP-Doped MOF-Based Electrocatalyst for pH-Universal Hydrogen Evolution Reaction. *Angew. Chemie - Int. Ed.* **58**, 4679–4684 (2019).
48. Osgood, H., Devaguptapu, S. V., Xu, H., Cho, J. & Wu, G. Transition metal (Fe, Co, Ni, and Mn) oxides for oxygen reduction and evolution bifunctional catalysts in alkaline media. *Nano Today* **11**, 601–625 (2016).
49. Chen, P. *et al.* Atomically Dispersed Iron-Nitrogen Species as Electrocatalysts for Bifunctional Oxygen Evolution and Reduction Reactions. *Angew. Chemie* **129**, 625–629 (2017).
50. Su, C. Y. *et al.* Atomic Modulation of FeCo–Nitrogen–Carbon Bifunctional Oxygen Electrodes for Rechargeable and Flexible All-Solid-State Zinc–Air Battery. *Adv. Energy Mater.* **7**, (2017).
51. Li, T. *et al.* Anchoring $CoFe_2O_4$ Nanoparticles on N-Doped Carbon Nanofibers for High-Performance Oxygen Evolution Reaction. *Adv. Sci.* **4**, (2017).
52. Amiinu, I. S. *et al.* Multifunctional Mo–N/C@MoS_2 Electrocatalysts for HER, OER, ORR, and Zn–Air Batteries. *Adv. Funct. Mater.* **27**, (2017).
53. Wang, B. *et al.* In Situ Growth of Ceria on Cerium–Nitrogen–Carbon as Promoter for Oxygen Evolution Reaction. *Adv. Mater. Interfaces* **4**, 1–8 (2017).
54. Lee, J.-M. *et al. X-ray Photoelectron Spectroscopy Study of Cobalt Supported Multi-walled Carbon Nanotubes Prepared by Different Precursors*. **8**, (2007).
55. Biesinger, M. C. *et al.* Resolving surface chemical states in XPS analysis of first row transition metals, oxides and hydroxides: Cr, Mn, Fe, Co and Ni. *Appl. Surf. Sci.* **257**, 2717–2730 (2011).

Chapter 7: Conclusion and Impact of Research

7.1 Conclusion

This Dissertation presented a series of experimental and theoretical studies (Chapters 4-6) having made an important contribution to the field (Chapter 1). Following from Chapter 1, 16 catalysts were tested to determine the most synergistic catalyst based upon three components: nanocarbon structures, functional oxygen groups, and transition metal oxides. After a series of tests of the graphene oxide series (Chapters 4 & 5) and metal-organic frameworks series (Chapter 6): T-cG, T-pMOF, and C-hG were the most optimal combinations of their respective functional oxygen groups. C-hG was the most effective catalysts in terms of onset potential, durability, and "binding conditions" (from density functional theory calculations). Using a systematic method, it was determined

Table 7.1: The structures that resulted from "**optimal**" adsorbed created enhanced "binding" performance compared to "non-optimal" adsorbed conditions.

NC	FOG	TMO
Graphene Oxide (G)	Epoxy (e) -eG	TiO_{2-x} (T) T-eG, **T-cG**, T-hG, and **T-pMOF**
Metal-Organic Framework (MOF)	Carboxyl (c) -cG	ZrO_{2-x} (Z) Z-eG, Z-cG, Z-hG, and Z-pMOF
	Hydroxyl (h) -hG	CeO_{2-x} (C) C-eG, C-cG, and **C-hG**
	Phosphate (p) -pMOF	

that sample preparation of graphene oxide and metal-organic frameworks samples allowed transition metal oxides to be adsorbed. This phenomenon of adsorption allowed for the study of the three classical combinations and lead to an increased knowledge of desirable combinations and understanding of oxygenated functionalization and how it can occur on nanocarbon structures. More importantly, the objectives outline in Chapter 1 were fulfilled:

(1) To study the effects of interfaces between nanocarbon structures and transition metal oxides on electrochemical performance and durability for oxygen reduction reaction and oxygen evolution reaction.

(2) To develop high-performance nanocarbon structures/transition metal oxide hybrid electrocatalysts for oxygen reduction reaction and oxygen evolution reaction based upon the studied property-performance correlation.

The assertion is justified because an increase in performance and durability as a result of effective interfacing between nanocarbon structures and transition metal oxides is presented. In addition, it was revealed that proper functionalization of nanocarbon

structures is critical in achieving high electrocatalytic activity by favoring an efficient 4-electron pathway. This is supported by the fact that interfacing nanocarbon structures with transition metal oxides, even with catalytically inert (against oxygen electrocatalysis e.g. TiO_2, ZrO_2), can still render an excellent oxygen reduction activity.

Interfacing with a catalytically active transition metal oxide (e.g. CeO_2) naturally resulted in an even more enhanced performance, indicating the non-negligible role of transition metal oxides in the catalytic activity of the resulting hybrid catalyst. However, the excellent activity was realized again only when a specific oxygen-containing functional group was formed before tethering the transition metal oxide, further supporting the critical role of functional groups in performance. It was also revealed that other important factors for electrocatalytic performance included the inhibition of graphene restacking, by which the catalytically active surface areas were conserved.

7.2 Impact of Research

TMO/NC hybrid catalysts have been synthesized mainly to complement low electronic conductivity and surface area of TMOs by placing them onto a high-surface-area electronic conducting NC. Recent studies focusing on the synergistic effect in catalytic activity between TMOs and NCs lack mechanistic understanding of the synergies. The work has mainly focused on the role of FOGs interfacing between TMOs and NCs in oxygen electrocatalysis, which has rarely been explored extensively. From a series of studies, it was revealed that TMOs can serve as an aid to functionalize the basal carbon surface in a way to maximize the catalytic activity. This is the case even with TMOs that are electrocatalytically inert.

This finding should enable a new route of developing non-noble metal-based oxygen electrocatalysts by engineering new interfaces to maximize electrocatalytic activity. The approaches, based upon the new understanding by using cost effective and abundant materials and processes, may facilitate a widespread deployment of fuel cells, electrolyzers, metal-air batteries and regenerative fuel cells. A large-scale production of these systems will enable hydrogen-based energy ecosystems, making the electric grid more accessible in a decarbonized way. The potential of the research is far-reaching beyond renewable energy technologies, as it can be applied to the wider field of nanotechnology.

7.3 Future of Work

The most immediate step in the research is the use of other NCs, FOGs, and TMOs. NCs also include fullerenes whose allotrope of single or double bonded carbon atoms can form fully or partially closed mesh of five to seven atoms fused rings with a hollow center in the shape of a tube, ellipsoid, sphere or etc. More specifically, the use of carbon nanotubes (graphene oxide in a tube shape) could significantly increase both surface area and catalytic performance. Another type of NCs could include highly oriented pyrolytic graphite (HOPG). HOPG is a form of highly ordered pure synthetic graphite, a periodical stack of two-dimensional (2D) graphene sheets long an axis. HOPG is preferred over natural graphite as the pyrolytic graphite is not only contains high purity, but the crystallographic orientation of the c-axes perpendicular to the surface is consistent, providing a well-defined carbon substrate for a systematic study of the

aforementioned catalysis of inorganic/carbon interfaces. Besides other NCs, other FOGs could be used such as sulfate, nitrate, ketones, aldehydes or etc. However, whenever using acid treatment to induce FOGs, the structural integrity of the NC (and TMOs) should be accounted for. Other TMOs should be used like other notorious ORR/OER-inert TMOs or, more catalytically active TMOs. Also, instead of using a NC, one could use boron-based nanostructures or cobalt corrins.

The principles illustrated by this research is that a catalyst components can be selected to achieve specific functional requirements. When fabricating said catalysts the influence of atomic density, facet, grain size and how these influencers are impacted by time/pressure/temperature, should be taken into account when combining any number of components.

For the immediate future C-hG, the best sample, should be assembled as a regenerative fuel cell for initial electrochemical testing, long-term durability, and subjected to different gas and thermal environments to gauge their usability range.